Experimental and Numerical Study of Dethridge Wheel for Pico-scale Hydropower Generation

Experimentelle und Numerische Untersuchung des Dethridge Rades zur Nutzung der Kleinwasserkraft

Zur Erlangung des akademischen Grades Doktor-Ingenieur (Dr.-Ing.)
genehmigte Dissertation von M.Sc. Shakun Paudel aus Kaski, Nepal
Tag der Einreichung: 14.09.2015, Tag der Prüfung: 03.12.2015
Darmstadt, 2016 — D 17

1. Gutachten: Prof. Dr.-Ing. habil. Boris Lehmann
2. Gutachten: Prof. Dr.-Ing. Nicole Saenger

TECHNISCHE UNIVERSITÄT DARMSTADT

Department of Civil and Environmental Engineering
Faculty of Hydraulic Engineering

Experimental and Numerical Study of Dethridge Wheel for Pico-scale Hydropower Generation
Experimentelle und Numerische Untersuchung des Dethridge Rades zur Nutzung der Kleinwasserkraft

Genehmigte Dissertation von M.Sc. Shakun Paudel aus Kaski, Nepal

1. Gutachten: Prof. Dr.-Ing. habil. Boris Lehmann
2. Gutachten: Prof. Dr.-Ing. Nicole Saenger

Tag der Einreichung: 14.09.2015
Tag der Prüfung: 03.12.2015

Darmstadt — D 17

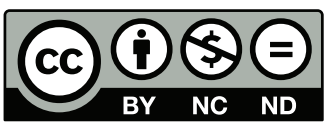

Erklärung zur Dissertation

Hiermit versichere ich, die vorliegende Dissertation ohne Hilfe Dritter nur mit den angegebenen Quellen und Hilfsmitteln angefertigt zu haben. Alle Stellen, die aus Quellen entnommen wurden, sind als solche kenntlich gemacht. Diese Arbeit hat in gleicher oder ähnlicher Form noch keiner Prüfungsbehörde vorgelegen.

Darmstadt, den 14th Sept. 2015

(S. Paudel)

Abstract

Hydropower sites with very low head are recently getting renewed interest with governments providing subsidies to meet the renewable energy targets. This study deals with the investigation of the Dethridge wheel, which was originally meant for flow measurement purposes, for developing power from very low head sites in open channel flow. Two different approaches are taken to assess the potential of the Dethridge wheel for electricity generation. The first is the experimental approach with a physical model of the wheel built and tested in the laboratory environment. The second approach is the three dimensional numerical modelling of the Dethridge wheel using a commercial Computational Fluid Dynamics (CFD) code Flow-3D.

The physical model tests show that at constant water levels the rotational speed of the wheel holds a linear relationship with torque as well as with flow rate. Using these linear regression models, full performance curves of the wheel are developed. Uncertainty analysis is carried out for all the measured data. The wheel housing, wheel to channel width ratio, blade numbers, channel transition shapes and the bottom clearance gap were experimentally investigated for their impact on the wheel performance. Original wheel housing is modified to allow side filling and emptying of the blade cells, which led to gain in efficiency. Performance of the wheel is observed to drop with increased number of blades. Wheel to channel width ratio plays vital role on the performance of the wheel. Two times wider channel is desired to allow for the side filling and emptying of the blade cells and thus improved efficiency. Effect of gradual transition is minimal on wheel performance suggesting no requirement of special channel transition profiles. Bottom clearance gap is identified to be important in controlling leakage losses and consequently wheel performance.

A three dimensional CFD model of Dethridge wheel is developed. The Renormalization Group (RNG) model is employed for modelling the turbulence. The wheel motion is modelled using the General Moving Object (GMO) model. Numerical model results are assessed for numerical and model uncertainties. Effect of surface roughness, turbulence model, advection scheme, blade thickness and domain symmetry is studied and validated against the physical model results. A rigorous approach of numerical uncertainty analysis called Grid Convergence Index (GCI) method is employed. Impact of blade shape and shroud shape modification is investigated on the numerical model. Modification of both blade and shroud shape led to the improvement in performance of the wheel. The computed results are in good agreement with the measured results. The development of a CFD model enhances our understandings of the complex hydrodynamics of the wheel.

The research findings has revealed that Dethridge wheel is a potential device for energy extraction from open channel flows. An efficiency of around 60% is achieved on the physical model tests. Given the simple and robust design of the wheel, this wheel could be implemented for decentralised pico-scale hydropower generation from very low head sites.

Kurzfassung

Um die hochgesteckten Ziele zum Schutz der Umwelt zu erreichen, unterstützt die Bundesregierung die Erneuerbaren Energien. Dabei rückt auch die Energiewandlung durch Kleinwasserkraft in den Fokus, die in dieser Arbeit am Dethridge Wasserrad untersucht wird. Das Dethridge Wasserrad wurde für die Abflussmessung in Bewässerungskanälen entwickelt und wird in dieser Arbeit zur Energiewandlung an Standorten mit sehr geringen Fallhöhen untersucht. Hier wird der sogenannte hybride Ansatz verfolgt: Zuerst wird ein physikalisches Modell zu Testzwecken in Laborumgebung aufgebaut und untersucht. Die zweite Methode ist die numerische Simulation der dreidimensionalen Strömung durch das Dethridge Rad mit der kommerziellen Software Flow-3D. Die Erkenntnisse aus beiden Methoden werden miteinander verglichen bzw. ineinander überführt.

Die Experimente zeigen, dass bei konstantem Wasserstand die Umdrehungsgeschwindigkeit des Wasserrads einen linearen Zusammenhang mit dem Drehmoment und dem Durchfluss durch das Wasserrad aufweist. Mit Hilfe dieses Zusammenhangs werden Leistungskurven und Wirkungsgrade dargestellt und detailliert analysiert. Eine Fehleranalyse wird für alle gemessenen Werte durchgeführt und diskutiert. Der Einfluss des Einhausung des Rades, des Verhältnisses zwischen Rad- und Kanalbreite, der Schaufelanzahl, der Geometrie im Zustrombereich des Rades und des Spaltmaßes zwischen Schaufel und Kanal wird im Hinblick auf Leistung und Wirkungsgrad untersucht. Um ein optimales Befüllen und Entleeren der Schaufelzellen zu ermöglichen wird die Geometrie der Einhausung verändert; eine Leistungssteigerung wird so erreicht. Ein Leistungsabfall wird bei größerer Schaufelanzahl beobachtet. Auch das Verhältnis zwischen Rad- und Kanalbreite hat einen großen Einfluss auf die Leistung. Hier sollte ein doppelt so breiter Kanal im Verhältnis zur Schaufelbreite geplant werden, um das leistungssteigernde Befüllen und Entleeren der Schaufelzellen zu begünstigen. Die Form des Übergangs von Zustromkanal zu Wasserradkanal hat keinen merklich Einfluss auf die Leistung des Rades. Wie erwartet führt ein geringeres Spaltmaßzu geringeren Verlusten.

Die Simulation der Strömung durch das Dethridge Wheel wird mit Flow-3D durchgeführt und Erkenntnisse mit den Ergebnissen des physikalischen Modells vergleichen. Zur Simulation der Turbulenzen wird das "Renormalization Group Modell (RNG)" verwendet, die bewegten Schaufeln werden mit dem "General Moving Object (GMO) Modell" abgebildet. Numerische Unsicherheiten werden detailliert untersucht. Die Effekte der Oberflächenrauheit, des Turbulenzmodells, des Advektionsschemas, und der Schaufeldicke werden mit den Ergebnissen der Experimente verglichen. Der "Grid Convergence Index (GCI)" wird verwendet, um die Unabhängigkeit von dem verwendeten Rechengitter und die Unsicherheiten der Konvergenz zu analysieren und zu bewerten. Verschiedene Schaufelgeometrie und Bodensegmentformen werden mit numerischen Simulationen untersucht. Veränderungen beider Geometrien führen zu einer Optimierung, also zu einer Leistungssteigerung des Wasserrads. Die Simulationsergebnisse stimmen sehr gut mit den experimentellen Erkenntnissen überein.

Das Dethridge Wasserrad hat das Potential zur Energiegewinnung in offenen Kanälen. Dabei wurde in den Experimenten ein Wirkungsgrad von über 60% gemessen. In Anbetracht des einfachen und robusten Designs des Wasserrads wird es für die dezentrale Energiewandlung bei sehr geringen Fallhöhen vorgeschlagen.

Table Of Contents

List of Figures **ix**

List of Tables **xiii**

1 Introduction **1**
- 1.1 Background . . . 1
- 1.2 Research objectives . . . 2
- 1.3 Research methodology . . . 3
- 1.4 Structure of the thesis . . . 3

2 Literature Review **5**
- 2.1 Potential of very low head hydropower . . . 5
- 2.2 Very low-head hydropower technologies . . . 6
- 2.3 History, use and evolution of Dethridge wheel . . . 11
- 2.4 Numerical modelling of energy extraction devices in open channel flow . . . 13

3 Experimental Approach **15**
- 3.1 The test rig . . . 15
  - 3.1.1 The model Dethridge wheel . . . 16
  - 3.1.2 The shroud . . . 16
  - 3.1.3 Measured variables and measurement system . . . 17
- 3.2 Methods of calculation and analysis . . . 19
  - 3.2.1 Comparison of experiment and CFD . . . 20
  - 3.2.2 Uncertainty analysis of experimental results . . . 21
- 3.3 Optimization study . . . 22
  - 3.3.1 Wheel housing . . . 22
  - 3.3.2 Blade number . . . 23
  - 3.3.3 Wheel to channel width ratio . . . 23
  - 3.3.4 Inlet and outlet transitions . . . 24
  - 3.3.5 Blade shape modification . . . 25
  - 3.3.6 Shroud shape modification . . . 25

4 Computational Fluid Dynamics (CFD) model **26**
- 4.1 CFD code Flow-3D . . . 26
- 4.2 Mass and momentum equations . . . 26

4.3 Turbulence modelling . . . 28
4.4 Free surface tracking . . . 30
4.5 Near-wall treatment and roughness modelling . . . 31
4.6 Equations of rigid body motion . . . 32
4.7 Numerical approximations . . . 33
4.8 Numerical stability . . . 34
4.9 Dethridge wheel CFD model development . . . 35
4.10 Uncertainty analysis of CFD model . . . 38
4.10.1 Quantification of numerical uncertainty . . . 38
4.10.2 Quantification of model uncertainty . . . 42

5 Results and Analysis **52**
5.1 Physical model results . . . 52
5.1.1 Wheel performance at different upstream water levels . . . 52
5.1.2 Wheel performance at different downstream water levels . . . 53
5.1.3 Wheel housing tests . . . 54
5.1.4 Blade number tests . . . 58
5.1.5 Wheel to channel width ratio . . . 61
5.1.6 Wheel performance at different transition shapes . . . 65
5.1.7 Analysis of leakage losses . . . 68
5.2 Numerical model results . . . 71
5.2.1 Numerical results of original Dethridge wheel . . . 71
5.2.2 Numerical results of curved blade shape BS1 . . . 83
5.2.3 Numerical results of modified shroud shape SS1 . . . 94
5.2.4 Summary . . . 104

6 Conclusions, Contributions and Future Work **106**
6.1 Conclusions . . . 106
6.2 Contributions . . . 108
6.3 Future work . . . 108

References **110**

Acknowledgements

I would like to express my sincere gratitude to Prof. Dr.-Ing. Nicole Saenger for her immense support from the PhD proposal phase to the completion of this thesis. Without her wisdom, encouragements and support, I wouldn't have been able to go through all the ups and downs and wouldn't be able to come this farther. I am grateful for the enormous time she invested in reading and correcting the manuscripts. My heartfelt appreciation for all her support, enthusiasm and generosity not only for offering her research expertise and supervision but also for the role she played as a guardian in every aspect of my stay in Germany.

I am grateful to Prof. Dr.-Ing. habil. Boris Lehmann for his guidance and encouragements on this work. I am thankful to him for agreeing to review and supervise the dissertation and for his support on all the administrative procedures.

Special thanks goes to Oliver Strohner for building up the model and for sharing his excellent ideas and skills. Thanks must also go to Markus Heim for his hard work to build up the model with high precision. I am thankful to my colleague Sven Bickelhaupt for all his technical support and specially for his prompt response and support whenever there were problems on the simulation computers.

I am indebted to my colleagues Matthias Von Harten, Olivier Schwyzer, Christopher Mook and Martin Weber for inspiring ideas, coffee breaks and lunch companion. A friendly and comfortable feeling in the lab wouldn't be possible without Barbara Kuhnke, Sabine Michling, Sabine Weinert, Lena Causemann, Thorsten Kraft, Prof. Iris Steinberg, Prof. Ulrich Drechsel, Prof. Stefan Krause, Prof. Ralf Mehler and Prof. Birte Frommer. I am thankful to Ursula Wicke, Silke Schneider and Veronica Hecht for helping me with all the administrative works at the university.

I am grateful to Dr. Nick Linton for his time and supervision at the University of Southampton during my visit as a postgraduate fellow. I am also very thankful to Dr. Gerald Müller for all his support throughout this study. The support from Frieder Semler and Dr. Matthias Todke from Flow Science is highly appreciated. I am grateful to all my great WG friends for their great company and making me feel home in a far away land. Thanks to family Ottmar for keeping me well during tough times as their family member in Erzhausen.

This work would be impossible without the support of my family members helping me to cope the hard time and stress. I am grateful to my brother-in-law, Milan Gyanwali, for spending tireless hours to proof read the draft. Special thanks to my parents for their encouragements, patience and belief in me and for letting me go farther than I actually thought.

Finally, I would like to gratefully acknowledge the financial support from the German Ministry of Education and Research (BMBF) and Schlumberger Foundation, Faculty for the Future program.

Nomenclature

Symbols	Description	Unit
α	Angular acceleration	rad/s^2
A	Cross-sectional area	m^2
b	Wheel width	m
B	Channel width	m
c	Courant number	–
ε	Turbulent dissipation	m^2/s^3
g	Acceleration due to gravity	m/s^2
h_1	Upstream water depth	m
h_2	Downstream water depth	m
H	Head	m
k	Turbulent kinetic energy	m^2/s^2
k_s	Roughness height	m
μ	Coefficient of dynamic viscosity	Ns/m^2
η	Efficiency	%
n	manning's roughness coefficient	$s/m^{1/3}$
N	Rotational speed	rpm
p	Pressure	Pa
P_{out}	Power output	Watts
Q	Flow rate	m^3/s
R_h	Hydraulic radius	m
ρ	Density	kg/m^3
r	radius	m
τ	Torque	Nm
t	Time	s
u_*	Wall shear stress velocity	m/s
v	Velocity	m/s
V	Volume	m^3
ω	Angullar velocity	rad/sec
y^+	Non-dimensional distance normal to the wall	–
x, y, z	Coordinates in 3D	m

Abbreviation	Description
BEP	Best Efficiency Point
BS	Blade Shape
CAD	Computer Aided Design
CFD	Computaional Fluid Dynamics
DLM	Dethridge Long Meter
GCI	Grid Convergence Index
GMO	General Moving Object
HPC	Hydrostatic Pressure Converter
HPM	Hydrostatic Pressure Machine
HPW	Hydrostatic Pressure Wheel
LDM	Large Dethridge Meter
RANS	Reynolds-averaged Navier-Stoke's equations
RNG	Renormalisation Group model
SDM	Small Dethridge Meter
SS	Shroud Shape
VOF	Volume of Fluid

List of Figures

2.1 Overshot water wheel (Loots et al., 2015) . . . 7
2.2 Zuppinger water wheel (Loots et al., 2015) . . . 7
2.3 Breastshot water wheel (Loots et al., 2015) . . . 8
2.4 Zuppingerrad (Senior, 2009) . . . 8
2.5 Aqualienne (www.h3eindustries.com) . . . 9
2.6 Staudruckmaschine (Brinnich, 2001) . . . 9
2.7 Different HPM designs (Linton, 2013; Schneider et al., 2011; Senior, 2009) . . . 10
2.8 Large (standard) Dethridge Meter (LDM) (www.pete-n-pam.com) . . . 11
2.9 Dethridge-Long Meter (ASTHC, 1988) . . . 11
2.10 Flow and head range for Dethridge wheel, after Linton (2013) . . . 12

3.1 Schematic sketch of the test facility . . . 15
3.2 Physical model . . . 16
3.3 Model wheel . . . 17
3.4 Shroud SS0 with side sealing (dimensions are in mm) . . . 17
3.5 Blade profile BS0 (dimensions in mm) . . . 18
3.6 Assembly of a torque transducer and braking system . . . 18
3.7 Original wheel housing . . . 23
3.8 Modified wheel housing . . . 23
3.9 Channel transition profiles (dimensions are in mm) . . . 24
3.10 Blade shape BS1 (dimensions are in mm) . . . 25
3.11 Shroud shape SS1 (dimensions are in mm) . . . 25

4.1 3D Model . . . 35
4.2 Computational Domain . . . 35
4.3 3D view of computational domain . . . 36
4.4 FAVORized view . . . 36
4.5 Nested meshing . . . 37
4.6 FAVORized blade (4 mm thickness) . . . 37
4.7 Time history development of key variables for eight sharp BS0 blades wheel . . . 39
4.8 Model output for different grid sizes used for GCI study . . . 42
4.9 Velocity profiles for different roughness heights at different x, $y = 0.065$ m . . . 43
4.10 Model output for different k_s values . . . 44

4.11 x-velocity contour and vectors for different roughness values, at $t = 30$ s. Flow direction is from left to right. . . . 45
4.12 Model output for different turbulence models . . . 46
4.13 Model output for different advection schemes . . . 47
4.14 Model output comparison between model with 2 mm and 4 mm thick blades . . . 49
4.15 Model output of axisymmetric half domain and full domain simulation . . . 50
4.16 x-velocity profiles for half domain and full domain simulations, at $t = 30$ s. Flow is from left to right. . . . 51

5.1 Power output and efficiency at different h_1 . . . 53
5.2 Power output and efficiency at different h_2 . . . 53
5.3 Definition diagram for operating upstream and downstream water depths (dimensions are in mm . . . 54
5.4 Performance curves at different wheel housings . . . 56
5.5 Fluctuation of rotational speed of the wheel in housings WH0 and WH1 (a) N fluctuation over time (b) Standard deviation of N . . . 57
5.6 Air entrainment in WH0 . . . 57
5.7 Air entrainment in WH1 . . . 57
5.8 Performance curves for different blade numbers . . . 60
5.9 Fluctuation of rotational speed for different blade numbers (a) N fluctuation over time for $Q = 14$ l/s (b) Standard deviation of N . . . 61
5.10 Performance curves at different wheel to channel width ratios . . . 63
5.11 Fluctuation of rotational speed for different $b : B$ (a) N fluctuation over time for $Q = 14$ l/s (b) Standard deviation of N . . . 64
5.12 Performance curves for different channel transition shapes . . . 67
5.13 Performance curves at different bottom gaps . . . 69
5.14 x-velocity contour and vectors for $N = 7.972$ rpm at different rotational angle. At every 45° rotation, new blade enters the water surface and the same cycle repeats. Flow is from left to right. . . . 72
5.15 Pressure distribution at different rotational positions for wheel with eight sharp blades BS0 at $N = 7.972$ rpm. Flow is from right to left. . . . 74
5.16 Model output for $N = 7.972$ rpm against simulation time. (a) Flow rates at the inlet and outlet boundary; (b) Outflow fluctuation and mean and standard deviation of Q; (c) Upstream and downstream water levels and the total head; (d) Total head fluctuation and its mean and standard deviation; (e) Total torque; (f) Torque ripple and its mean and standard deviation . . . 75
5.17 Torque versus rotational angle of the wheel for $N = 7.972$ rpm. . . . 76
5.18 x-velocity contour and vectors for $N = 25.181$ rpm at different rotational angle. The change in the flow field between rotational angle of $0° - 45^{\circ}$ is shown. Flow is from left to right. . . . 78
5.19 Pressure at different rotational positions for wheel with eight sharp blades BS0 at $N = 25.181$ rpm. Flow is from right to left. . . . 79

5.20 Torque versus rotational angle of the wheel for $N = 25.181$ rpm. 80
5.21 Model output for $N = 25.181$ rpm as a function of simulation time. (a) Flow rates at the inlet and outlet boundary; (b) Outflow fluctuation and mean and standard deviation of Q; (c) Upstream and downstream water levels and the total head; (d) Total head fluctuation and its mean and standard deviation; (e) Total torque; (f) Torque ripple and its mean and standard deviation. 81
5.22 Numerical and physical model results for eight BS0 blades wheel (a) Power output (b) Efficiency 82
5.23 x-velocity contour and vectors for blade shape BS1 for $N = 8$ rpm at different rotational angle. The change in the flow field between rotational angle of $0° - 60°$ is shown. Flow is from left to right. 84
5.24 Pressure distribution for wheel with six curved blade BS1 at $N = 8$ rpm at different rotational positions of the wheel. Flow is from right to left. 85
5.25 (a) Torque for blade BS1 at different rotational angles and (b) Torque comparison for wheel with eight BS0 and six BS1 blades. 86
5.26 Model output for BS1 for $N = 8$ rpm as a function of simulation time. (a) Flow rates at the inlet and outlet boundary; (b) Outflow fluctuation, mean and standard deviation of Q; (c) Upstream and downstream water levels and the total head; (d) Total head fluctuation and its mean and standard deviation; (e) Total torque; (f) Torque fluctuation, its mean and standard deviation. 87
5.27 x-velocity contour and vectors for blade shape BS1 for $N = 18$ rpm at different rotational angle. The change in the flow field between rotational angle of $0° - 60^{\circ}$ is shown. Flow is from left to right. 89
5.28 Pressure distribution for wheel with six curved blade BS1 at $N = 18$ rpm at different rotational positions of the wheel. Flow is from right to left. 90
5.29 Torque versus rotational angle for blade BS1 at $N = 18$ rpm. 91
5.30 Model output for BS1 for $N = 18$ rpm as a function of simulation time. (a) Flow rates at the inlet and outlet boundary; (b) Outflow fluctuation, mean and standard deviation of Q; (c) Upstream and downstream water levels and the total head; (d) Total head fluctuation and its mean and standard deviation; (e) Total torque; (f) Torque oscillation, its mean and standard deviation. 92
5.31 Numerical results comparison of six BS1 blades with physical model results of six BS0 blades wheel. The physical model refers to the wheel with six sharp BS0 blades and numerical results refers to the wheel with six curved BS1 blades (a) Power output (b) Efficiency 93
5.32 x-velocity contour and vectors for modified shroud shape SS1 and wheel with curved blade shape BS1 for $N = 8$ rpm at different rotational angles. The flow field is shown for rotational angle of $0° - 60^{\circ}$. Flow is from left to right. 95
5.33 Distribution of pressure for the modified shroud shape SS1 and wheel with six curved blade BS1 at $N = 8$ rpm at different rotational angles of the wheel. Flow is from right to left. 96

5.34 Torque versus rotational angle for wheel with shroud shape SS1 at $N = 8$ rpm 97
5.35 Model output for shroud shape SS1 with curved blade shapes BS1 at $N = 8$ rpm as a function of simulation time. (a) Flow rates at the inlet and outlet boundary; (b) Outflow fluctuation, mean and standard deviation of Q; (c) Upstream and downstream water levels and the total head; (d) Total head fluctuation and its mean and standard deviation; (e) Total torque; (f) Torque fluctuation, its mean and standard deviation. 98
5.36 x-velocity contour and vectors for modified shroud shape SS1 and wheel with curved blade shape BS1 for $N = 18$ rpm at different rotational angles. The flow field is shown for rotational angle of $0° - 60°$. Flow is from left to right. 100
5.37 Distribution of pressure for the modified shroud shape SS1 and wheel with six curved blade BS1 at $N = 18$ rpm at different rotational angles of the wheel. Flow is from right to left in this figure. 101
5.38 Torque versus rotational angle for wheel with shroud shape SS1 at $N = 18$ rpm 102
5.39 Model output for shroud shape SS1 and wheel with curved blade shapes BS1 at $N = 18$ rpm against simulation time. (a) Flow rates at the inlet and outlet boundary; (b) Outflow fluctuation, mean and standard deviation of Q; (c) Upstream and downstream water levels and the total head; (d) Total head fluctuation and its mean and standard deviation; (e) Total torque; (f) Torque fluctuation, its mean and standard deviation. . . . 103

List of Tables

3.1 Model Parameters . . . 17
3.2 Summary of data acquisition system . . . 19

4.1 Mesh details . . . 36
4.2 Manning's n values . . . 37
4.3 Grid details and computation time for GCI study . . . 40
4.4 Results of the grid convergence study . . . 41
4.5 Results from experiment and CFD for different models options . . . 48
4.6 Mean values of key variables for the 2 mm and 4 mm blade thickness . . . 48
4.7 Mean values of key variables for the half and full domain simulations . . . 49

5.1 BEP details of wheel housing WH0 and WH1 . . . 55
5.2 Performance comparison of wheel housings at different operating points . . . 55
5.3 BEP details of wheels with different number of blades . . . 59
5.4 Performance comparison of 6 and 8 blades wheel at different operating points . . . 59
5.5 BEP details of wheel at different channel widths . . . 62
5.6 Performance comparison between 1 : 2 and 1 : 4 width ratios at different operating points 64
5.7 BEP details of wheel at different transition shapes . . . 66
5.8 Performance comparison between sudden and gradual transition shapes at two different operating points . . . 66
5.9 BEP details of wheel at different bottom gaps . . . 69
5.10 Performance comparison between 2 mm and 1 mm gaps at two different operating points 70
5.11 Numerical model output for $N = 7.972$ rpm . . . 73
5.12 Numerical model output for $N = 25.181$ rpm . . . 80
5.13 Comparison of physical and numerical model results for eight BS0 blades wheel . . . 82
5.14 Numerical model output for blade BS1 for $N = 8$ rpm . . . 86
5.15 Numerical model output for curved blade BS1 for $N = 18$ rpm . . . 91
5.16 Comparison of numerical model results of six BS1 blades wheel with physical model results of six BS0 blades wheel . . . 93
5.17 Numerical model output for shroud shape SS1 and wheel with blade BS1 at $N = 8$ rpm . 97
5.18 Numerical model output for wheel with shroud shape SS1 and curved blade shape BS1 at $N = 18$ rpm . . . 102

Chapter 1

Introduction

1.1 Background

The growing concern for the global climate change calls for an active switch to the renewable technologies for electricity production to reduce the greenhouse gas emissions (Sims et al., 2007; Kosnik, 2008; Blindheim, 2015). Kyoto Protocol (1997) came into force to commit the industrialized countries to reduce emissions. The European Union directive 2009/28/EC has established a common framework for the use of renewable energy sources through the definition of national action plans to limit the greenhouse gas emissions before 2020. These policies have placed much emphasis on renewable energy sources including hydropower. Hydropower represents a reliable source of renewable energy with majority of global renewable energy production contributing over 16% of the global electricity production and accounting for 76% of total renewable electricity supply (World Energy Council, 2015). Only a third of a total world hydropower capacity has been developed and most of this growth and development is concentrated in developed countries specially in Europe (World Energy Council, 2015) where much of the large scale hydropower potential is either already developed or is currently stagnant due to their high financial risks as well as environmental, ecological and social impacts (Paish, 2002; Kosnik, 2008; Ansar et al., 2014). Thus focus is now shifted to the small scale hydropower development (Kosnik, 2010; Vowles, 2012).

Within the small scale hydropower sector, very low head sites below 5 m, formerly disregarded considering uneconomical for developing hydropower (Müller and Kauppert, 2002; Kosnik, 2010), are recently getting renewed interest with governments providing subsidies to meet the renewable energy targets (Vowles et al., 2014). Within the European Union's Seventh Framework Programme, 'Research Priorities for the Renewable Energy sector' has included the development of small turbines for very low heads below 5 m as one of its long term targets (Senior, 2009). There are abundant potential sites for small scale hydropower generation within the irrigation system, water treatment plants, old mills or weirs (Müller and Kauppert, 2004; Furukawa et al., 2010; Gensler and Kinzli, 2013; Tatsuki et al., 2013; Butera and Balestra, 2015; Loots et al., 2015). In less developed countries, apart from untapped large scale hydropower potential, there are ample opportunities to harness small-scale hydropower with power output less than 5 kW for cost-effective and environmentally sustainable rural electrification (Doig, 1999; Williams et al., 2000; Paish, 2002; Williams and Simpson, 2009) to improve the livelihood of the people (Mahat, 2004).

In order to develop these under utilised energy resources, conventional highly efficient low head hydraulic turbine technologies such as Kaplan or cross-flow turbines would be economically not viable because of the large size of the turbine required for very low head installations, requirement of special

flow control mechanism and the risk they impose on the environment (Müller and Kauppert, 2002; Senior et al., 2010). Furthermore, Kosnik (2010, pp.5513) reports that at current technologies and incurring costs, small scale hydropower resources are not worth developing. In developing countries this problem is even worsen by the inability to manufacture the hydraulic machinery of any size or design complexity (Basset, 1989). Technological development is therefore required to harness this very low head energy potential. Efforts has been made to develop technologies that suitably harness the very low head energy source. Ancient water wheels has been reassessed and optimised (Müller and Kauppert, 2002; Denny, 2004; Müller and Kauppert, 2004; Müller and Wolter, 2004; Pujol et al., 2011; Pelliciardi, 2015; Quaranta and Revelli, 2015b,a) and studies were undertaken to develop novel technologies such as hydrostatic pressure machine (HPM) (Senior et al., 2010; Müller et al., 2012; Linton, 2013; Paudel et al., 2013), Very Low Head (VLH) turbine (Juhrig, 2011), the Archemedes screw (Lyons and Lubitz, 2013; Nuernbergk, 2012; Nuernbergk and Rorres, 2014) and Staudruckmachine (Sternecker et al., 2013; Ulm, 2014) to name just a few. Although some developments have been made over the past few years, there still remains a potential for contributing towards the share of hydropower by developing new technology for utilising very low head sites.

This thesis investigates the potential of the Dethridge wheel for harnessing power from very low head sites in open channel flow with the aim of developing a low-cost hydropower converter for rural electrification. The Dethridge wheel is a type of water wheel invented for measuring flow in the irrigation canals. John Dethridge introduced them in Australia in 1910. Until today, this machine, being robust, cheap and simple to use, is widely used in Australia for flow measurement purposes. Being similar in working principle to the conventional water wheels, this wheel is believed to have significant potential to be used for electricity generation from very low head sites. This study explores the hydraulics and performance characteristics of the laboratory scale Dethridge wheel model and numerical model study of the wheel in commercial Computational Fluid Dynamics (CFD) code Flow-3D.

1.2 Research objectives

The main objective of this research is to investigate the potential of the Dethridge wheel for producing electricity from very low head sites in open channel flow. To meet this objective, following specific objectives are identified:

1. To design and build a physical scaled model of the original Dethridge wheel to test in the laboratory environment.
2. To study the performance of the same Dethridge wheel model numerically using the commercial Computational Fluid Dynamics (CFD) code Flow-3D.
3. To optimize the wheel performance by changing the wheel and channel geometry. This includes modification of the wheel housing, blade numbers, wheel to channel width ratio, channel transition shape as well as the analysis of clearance gaps.
4. To validate the numerical model using the results obtained from the physical model test.
5. To optimise the blade shape and shroud shape using the numerical approach.

1.3 Research methodology

The research is accomplished using two different research methodologies. The first one is the experimental approach which involves a laboratory scaled model of the Dethridge wheel. The model wheel is built and tested in the hydraulics laboratory of the Darmstadt University of Applied Sciences. The physical model of the Dethridge wheel, experimental test rig, measurement system and data analysis method are elaborated in Chapter 3.

The second method is numerical modelling. A numerical model reflecting the physical model of Dethridge wheel is studied in the commercial computational fluid dynamics (CFD) code Flow-3D. Flow-3D provides a highly precise time-dependent solution to three dimensional free surface problems. The Renormalization group (RNG) model is employed for modeling the turbulence. General Moving Object (GMO) model is used for modeling the wheel motion and calculating forces, torque and thus the power output and efficiency of the wheel. The physical model results are used to validate the numerical model. The CFD model is described in detail in Chapter 4.

1.4 Structure of the thesis

This thesis is structured into six chapters. Chapter 1 briefly outlines the background of the research, presents the objectives and research methodology of the thesis. In Chapter 2, a review of relevant literature is presented. An emphasis is given to the very low head hydropower. The status of very low head hydropower development and available technologies for harnessing pico hydropower are covered. These include conventional technologies such as water wheels as well as recently developed technologies. The history and use of the Dethridge wheel is presented. Literature on numerical modelling of energy extraction technologies in open channel flow is also reviewed.

The test rig, measurement system, measured variables, methods of calculation and analysis and uncertainty analysis of experimental results are presented in Chapter 3. The Dethridge wheel model, shroud and blade profiles are explained. In this chapter, wheel housing modification, wheel to channel width ratio, different number of blades considered, channel transition shapes, blade shape and shroud shape modification are illustrated.

Chapter 4 describes the CFD methodology including the governing equations, turbulence modelling, Dethridge wheel numerical model development, and validation and uncertainty analysis procedure for the numerical model results. The grid convergence index (GCI) method for assessing the numerical uncertainty of the CFD model is explained and GCI values are calculated in this chapter. Model uncertainty of the numerical model is assessed for different roughness, turbulence, momentum advection schemes, blade thickness and domain symmetry cases.

Results and analysis of both physical model results and numerical model results are presented in Chapter 5. Physical model results at different wheel housings, wheel to channel width ratios, blade numbers, and channel transition shapes are presented in separate sections. Effect of different bottom clearance gap on the wheel performance is evaluated. Numerical model results are described separately within the chapter. Physical and numerical model results are then compared and validated.

Finally, in Chapter 6, conclusions of the research are drawn. The contributions made by this thesis are summarised and some recommendations for future work are presented. Publications related to this research are attached in Annex 1.

Chapter 2

Literature Review

In this chapter, a brief literature review of the potential of very low head hydropower is presented. Technologies available for pico-scale very low head hydropower are also reviewed and discussed. Conventional and recently developed technologies such as water wheels, Archimedes screw, Staudruckmaschine and HPMs are covered. This review helped to establish the relative importance of the technology investigated in this thesis. The history and use of Dethridge wheel is presented. Current practice of numerical modelling of the open channel flow energy extraction devices are reviewed.

2.1 Potential of very low head hydropower

Hydropower schemes are generally categorised according to their power output and the head. However, the classification varies across countries as there is no internationally agreed definition (Paish, 2002). In this thesis, sites with power output below 5 kW and head below 3 m are defined as very low head pico hydropower source. Worldwide most part of the low head hydropower potential remains untapped since the existing technologies to harness these sites are not economically justified. In Europe, under utilised low head small hydropower potential is estimated to be 18 GW (Paish, 2002). The 2010 survey of UK low head hydropower including sites below 1 m head and below 25 kW estimated to have a development potential of 146 to 248 MW (DoECC, 2010), while in Germany the technically realisable remaining hydropower potential is calculated to be around 750 MW (ca. 3.3 TWh/a) (Anderer et al., 2010).

Most of the very low head sites for pico hydropower are within redundant mill sites, weirs, irrigation network, waste water network, barrages, streams and water distribution systems. These sites with existing civil infrastructure, predictable flow rate and useful head represent significant future development potential for low head hydropower development. Abandoned old will sites usually have existing diversion structure and suitable head for low head hydropower. As late as in 1925, more than 33,500 mill sites were licensed alone in Germany and there were around 25 to 30,000 mill sites in the UK. Reactivation of these resources could produce 600 MW in the UK and 500 MW in Germany (Müller and Kauppert, 2004). Flow in irrigation canal is usually diverted through a diversion canal, have a wide distributary network and are also often equipped with small drops to reduce the erosion problem. One such example is the study of Dimke et al. (2011). They examined the potential of hydropower in an existing irrigation network in Pakistan and recommended the suitable machines for power extraction. With predictable and almost constant flow rate, waste water networks are also highly potential for hydropower (Steuernagel et al., 2002). The outflow discharged into the river at the outlet of waste water treatment plant generally have $1-10$ m head difference (Loots et al., 2015) and predictable flow rate. These resources offer a considerable scope to produce low head pico hy-

dropower (Botto et al., 2010; Campbell, 2010; Gensler and Kinzli, 2013; Tatsuki et al., 2013; Loots et al., 2015). In the later section, the conventional and novel low head hydropower technologies suitable for these applications are explored.

2.2 Very low-head hydropower technologies

Conventional technologies such as water wheels represent significant opportunity for harnessing very low head sites. They are economically and ecologically interesting option for both industrialised and less developed countries to utilise small scale energy sources (Quaranta and Revelli, 2015b). In ancient times, water wheels were used as a primary source of power. Invention of highly efficient turbine technologies led to the disappearance of the water wheels in recent times. However, researchers are now focused on using existing very low head sites for producing power using conventional technologies (Denny, 2004; Müller and Kauppert, 2004; Müller and Wolter, 2004; Senior, 2009; Quaranta and Revelli, 2015b,a). Basset (1989) stated that for most rural power requirements of up to 10 kW, water wheels are perfectly suitable and as efficient as other hydraulic turbines. The simple design, easy maintenance and ability to easily handle foreign objects make the water wheels more suitable and an attractive source of power for rural electrification compared to the modern turbines and should not be overlooked. Some companies like Hydrowatts, Waterwheel factory, are again manufacturing the economical water wheels. A wide variety of horizontal and vertical axis water wheel models have been evolved throughout the history. Most commonly used water wheel types namely overshot, undershot, breastshot and stream wheels are discussed here.

Overshot water wheels (shown in Fig. 2.1) are driven by the gravitational force of the water contained in the buckets of the wheel. Water flows at the top of the wheel and fills into the buckets evenly distributed around the periphery of the wheel. These wheels are applicable in hilly areas with larger heads of $2-10$ m and can have high efficiency of around 70% (Basset, 1989). However, at higher heads due to their large size they become uneconomical, difficult to install and aesthetically unpleasant (Müller and Kauppert, 2002; Müller and Kauppert, 2004). John Smeaton's revolutionary work in 1759 formed the basis for water wheel design and demonstrated that overshot wheels are much more efficient than the undershot wheels (Basset, 1989; Capecchi, 2013). Efficiencies of over 85% were reported by Weidner (1913); Staus (1928); Meerwarth (1935). A novel approach to improve the torque and efficiency of the overshot waterwheel is presented by Wahyudi et al. (2013). A recent study of Quaranta and Revelli (2015a) presents a comprehensive theoretical model of power loss and comparison with experimental model test results of overshot water wheel. Efficiencies of more than 80% is reported over the wide range of flow. Similarly, Pelliciardi (2015) demonstrated the effective utilisation of overshot water wheel as cost-effective, efficient and ecological energy converter for mechanical power in remote areas of Nepal.

The first kind of horizontal axle water wheel was the undershot water wheel described by Vitruvius in 27 BC (Basset, 1989). Undershot water wheels could operate with very small head differences of $0.5-2$ m head so they constitute an attractive option for power generation at very low head sites in flat terrain near the settlement areas (Capecchi, 2013). Water enters below the axis of the undershot wheel and works mainly due to the impulsive force of the flowing water and very small potential

energy due to the backing up of water. If only the kinetic energy is utilised then it is referred as stream wheel. Initially, the undershot water wheel was able to exploit only around 30% of the theoretical power of the stream (Mead, 1915). Ponocelet's modifications of the form of buckets resulted in increased efficiency of undershot wheels and reached as much as 70% (Mead, 1915; Basset, 1989; Denny, 2004). The Charles Bossut's work on undershot water wheels looked at the performance of the wheel at different flume width and blade numbers. He found that efficiency depends on number of blades, showing the more blades the better. Flume width was found to have no impact on the wheel performance. Importance of shockless entry for higher efficiency of undershot water wheels is highlighted by Borda (Basset, 1989). The most efficient undershot water wheel commonly used today is the Zuppinger wheel designed by the Swiss engineer Zuppinger. Overshot and Zuppinger water wheels are depicted in Figures 2.1 and 2.2 respectively. Design details of different models of water wheels can be found in Bach (1886); Brüdern (2006); Nuernbergk (2013, 2014).

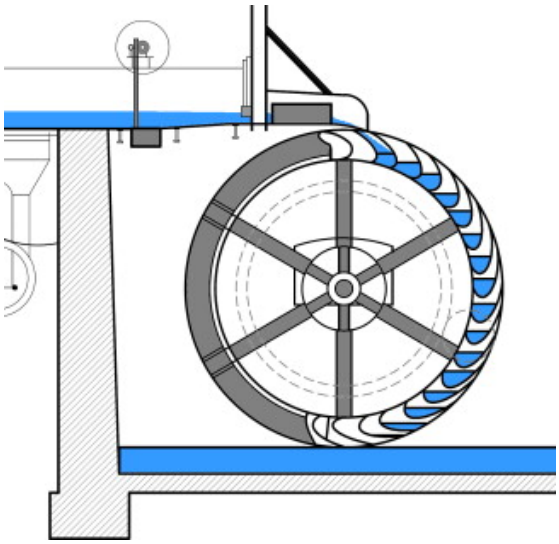

Figure 2.1: Overshot water wheel (Loots et al., 2015)

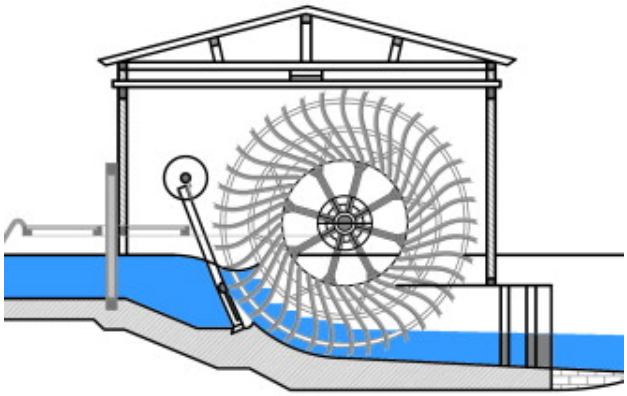

Figure 2.2: Zuppinger water wheel (Loots et al., 2015)

Following the work of Smeaton, breastshot water wheel (Fig. 2.3) was discovered as a result of optimisation of overshot and undershot water wheels to utilise the low head sites unsuitable for overshot water wheels mainly through the work of Fairbairn and Rennie (Mead, 1915; Denny, 2004; Quaranta and Revelli, 2015b). These wheels are applicable for head difference of 1.5−4 m (Senior, 2009) and the available head determines the height at which water strikes the blades (Basset, 1989). Even though these wheels perform better than the undershot wheels as they utilise both gravity and momentum torque (Basset, 1989; Denny, 2004), very little research has been done on this type of wheel (Müller and Wolter, 2004; Quaranta and Revelli, 2015b). Over 80% of efficiency is measured by Müller and Wolter (2004) in the model tests of a breastshot water wheel by optimising the inflow and outflow conditions. Quaranta and Revelli (2015b) presented a theoretical approach to estimate different types of losses on the breastshot water wheel and validated against the experimental model results. Efficiency of the wheel was measured as high as 96% in a 2 m diameter wheel. A distinct type of breastshot water wheel called Zuppinger'schen wasserrades with a central hub creating a damming effect was also

seen on the literature (Delabar, 1867). On this type of wheel, both upstream and downstream channel was wider than the wheel for cells to have open sides for easing cell filling and emptying process. The cells are completely filled with water so the rotational speed of the wheel is directly linked to the flow rate (Senior, 2009, pp. 50). We shall see later that the Dethridge wheel being geometrically similar to the Zuppinger'schen wasserrad (shown in Fig. 2.4) resembles identical characteristics.

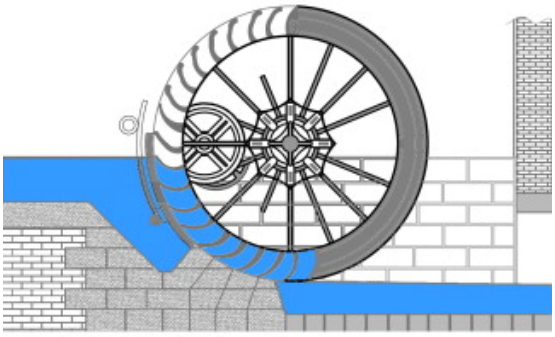

Figure 2.3: Breastshot water wheel (Loots et al., 2015)

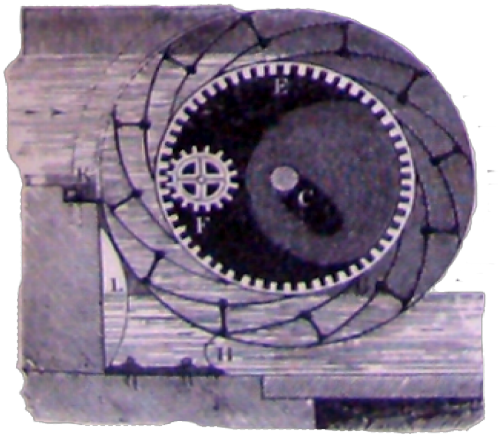

Figure 2.4: Zuppingerrad (Senior, 2009)

The stream wheels are driven directly by the river current and are able to convert only a small portion of the energy of the flowing stream (Mead, 1915). They are usually installed on shallow waters with their blades extended to the bottom of the flow in order to utilize the available kinetic energy of the flow. The typical efficiency achieved from these wheels is 30% (Müller et al., 2007). Tevata and Inprasit (2011) conducted tests on stream water wheel to quantify the effect of immersion ratio and the blade number on the wheel performance. Their results showed that as the immersion ratio increases, performance dropped down and the least number of blades performed better.

Apart from these conventional technologies suitable for very low head sites, there are modern-day technologies developed within the last few years. In Europe, recently Archimedes screws are widely used in reverse operation for utilising very low head energy resources (Müller and Senior, 2009; Lashofer et al., 2013; Nuernbergk and Rorres, 2013). Currently they represent commercially most successful modern-day low head hydropower technology (Senior, 2009, pp.58). These devices are claimed to be suitable for a $1-10$ m head. Efficiency of around 80% was reported in the literature(Brada, 1996, 1999; Lyons and Lubitz, 2013). The robust, simple and environmentally friendly design has encouraged the number of installations of the Archimedes screw within Europe in recent times (Nuernbergk and Rorres, 2013).

Aqualienne and Staudruckmaschine, shown in Figures 2.5 and 2.6, are other two interesting inventions patented in 2001 and 2004 in France and Austria respectively. The geometry and working principle of these machines are very similar to that of the Dethridge wheel. The cells of the both wheels are completely filled during operation maximising the flow delivering capacity of the wheel. Aqualienne is designed with a shroud structure to guide the flow and is suitable for head differences between $1-5$m. The inventor claimed an efficiency of 80% (Senior, 2009). The Staudruckmaschine is claimed

to be suitable for head range of $1-3$ m. The wheel works by creating a dam on the upstream and thus maintaining the upstream water level. It consists of a big hub with diameter equal to the head drop and diagonally mounted blades around its circumference, which enter and exit the water continuously across the width of the wheel. The blades are relatively longer, around two third of the radius of the wheel and are braced at both ends by a metal disks for stability (Brinnich, 2001; Senior, 2009). The big cells and flat flume bed allow sediment and other living organisms to pass through the wheel easily. Even though the inventor claimed more than 90% efficiency for wide range of flow conditions (Brinnich, 2001), model tests conducted by Senior et al. (2007) showed the maximum efficiency of only 40%. Modifications on the original Staudruckmaschine are patented by Sternecker et al. (2013) and Ulm (2014).

Figure 2.5: Aqualienne (www.h3eindustries.com)

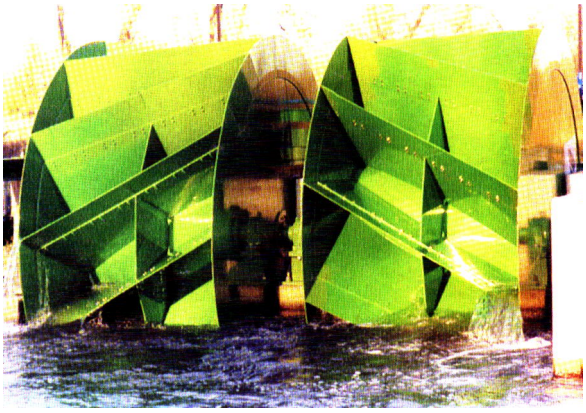

Figure 2.6: Staudruckmaschine (Brinnich, 2001)

The most recent development in the very low head hydropower technology is the Hydrostatic Pressure Converter (Fig. 2.7), which is developed as a result of further optimization of the Staudruckmaschine. Two major modifications to the wheel were the introduction of the shroud for minimizing leakage losses and the removal of side disks to allow cells to be filled and vented from the sides of the cells (Senior et al., 2007; Senior, 2009). Elaborated studies are conducted to determine the performance characteristics of the HPM and to optimise the wheel performance, which include prototype and field tests, for eg. Senior (2009); Senior et al. (2010); Schneider et al. (2011); Linton (2013). Senior (2009) developed a simplified theoretical model of these machines and verified by the scaled model tests. Based on these results full scale performance is estimated. The proposed designs of Hydrostatic Pressure Converter were found suitable for head differences below 2.5 m and found to have around 80% efficiency. In Senior et al. (2010), two different models of the wheel with different hub diameters namely Hydrostatic Pressure Wheel (HPW) and Hydrostatic Pressure Machine (HPM) are investigated. HPW is reported to be suitable for 0.2 to 1 m head differences while HPM is appropriate for 1 to 2.5 m head differences. The flexible rubber blade design and importance of side filling in HPM is discussed by Linton (2009). The study of Vowles (2012) on ecological impact of Hydrostatic Pressure Converters suggested design modifications of these machines such as increased gap and flexible rubber blades, which could however impact the hydroelectric performance of the wheel. Paudel et al. (2013) reported the importance of channel width for cell filling and emptying of the flexible rubber

blade HPM model. Schneider et al. (2011) investigated the effect of blade shape and channel width on the wheel performance and concluded that in such machines wider channel than the wheel are required for better performance. Model tests and full scale field tests of HPM on a 5 kW prototype HPM installed at a redundant mill site in Germany are carried out by Linton (2013). Several geometrical modification including the helical shape of blades and shroud modification were performed on the model study.

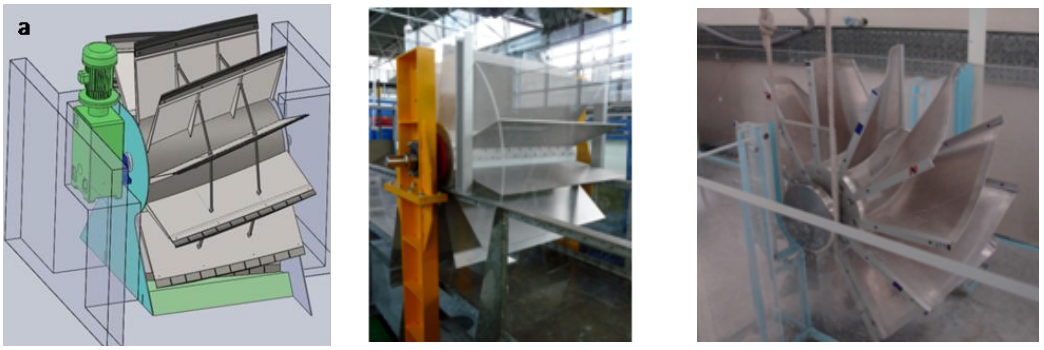

Figure 2.7: Different HPM designs (Linton, 2013; Schneider et al., 2011; Senior, 2009)

Further to the above discussed technologies, there are several other studies focused on utilising low head resources. Botto et al. (2010) discusses the regional scale power potential in irrigation canals using cross-flow type water wheels. Likewise, Ikeda et al. (2010) studied the nano overshot type of cross-flow turbine aimed at utilising the existing resources in irrigation canals to produce off-grid electricity for rural areas of Japan. Marine and hydrokinetic devices for harnessing energy from waves in oceans as well as from rivers and streams are equally getting popularity and possess significant potential to contribute to the share of future renewable energy supply (Kang et al., 2012; Kim et al., 2012; Marsh et al., 2015a). Even though there are wide range of technologies available for very low head hydropower development, the selection of technology for a particular case does not only depends on quantitative criteria such as head and flow rate but also on qualitative criteria like cost effectiveness and environmental requirements. Williamson et al. (2014) developed a multi-criteria method of choosing a low head pico hydropower turbine technology for $0.5 - 3.5$ m head range including factors such as environmental, regulatory context, location, cost etc. Elbatran et al. (2015) also provided a guidelines for selecting low head turbines including the economic analysis of low head turbine scheme and a case study of a cross flow turbine for very low head application. Linton (2013) provides a detailed review of very low head technologies and is recommended for further reading.

Above discussed brief review of the selected literature clearly demonstrates that there is a potential of harnessing very low head sites through utilisation of existing technologies and/or by developing new technologies that are economically justifiable and are environmentally sound. Basing upon these findings, the objective of this thesis is formed and a simple, low-cost technology, Dethridge wheel, is chosen for further investigation.

2.3 History, use and evolution of Dethridge wheel

The Dethridge wheel was invented in Australia in 1910 by John Dethridge for the purpose of measuring flow at the outlets of the irrigation canals. It is a type of water wheel placed on the curved shape shroud with only minimum practical clearance for the wheel to rotate. Being robust, and simple construction, accuracy over a wide range of flow rate, low head loss, ease of maintenance and relatively low cost, this wheel then was extensively used in Australia (ASTHC, 1988; Replogle and Kruse, 2007) and many other parts of the world including USA, Israel, India, Myanmar (Kraatz and Mahajan, 1975; ASTHC, 1988). Until 2008, there were approximately 60,000 of these wheels still under operation in Australian irrigation system (ANCID, 2002). The overall accuracy in flow measurement of this wheel was reported to be around ±3% for a wide range of upstream water depth when the wheel is operated within the design range. However due to the requirement of the modern irrigation water management practice and operational health and safety risk, these wheels are now slowly being replaced with the modern electronic flow measurement devices (Replogle and Kruse, 2007).

The design of the Dethridge meter has been continuously improved throughout the years with the use of new materials and construction methods but the essential aspects of the original hydraulic design remained almost unchanged (ASTHC, 1988). There are three different designs of the Dethridge wheel in practice: Small Dethridge Meter (SDM), Large (standard) Dethridge Meter (LDM) and Dethridge-Long Meter (DLM). SDM and LDM differs only on their size, SDM being the scaled down version. The LDM is the original Dethridge wheel used for irrigating area larger than 40 acres and has a capacity from 42 l/s to 140 l/s. SDM can handle discharge from 14 l/s to 70 l/s and was used for irrigating area up to 40 acres. SDM was invented later in 1920 for irrigating smaller land areas. On the optimised DLM, the blade shape, number of blades and the emplacement floor shape had been modified and is more efficient version of the Dethridge wheel (Ward and Alexander, 1992). The DLM was developed during the 1980s and was common in use in 1990s. The key dimensions and basic configuration of the DLM are same as that of LDM with only six vanes and elongated blade shapes to minimize splashes and flow restrictions. Figures 2.8 and 2.9 show a LDM and DLM in the farm outlet.

Figure 2.8: Large (standard) Dethridge Meter (LDM) (www.pete-n-pam.com)

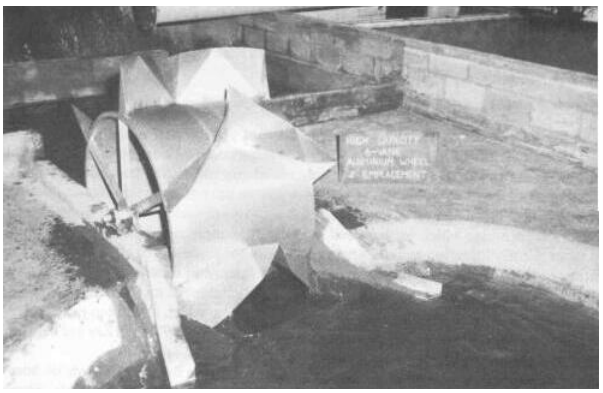

Figure 2.9: Dethridge-Long Meter (ASTHC, 1988)

The LDM and SDM design consists of a cylinder and eight externally attached blades of a mild steel sheet of 14 gauge (i.e. 2.03 mm) and is internally braced with steel spokes at the center and both ends

of the cylinder. A 25.4 mm galvanized pipe is used as an axle of the wheel. The blades are v-shaped with the apex leading to the direction of rotation and contain an air vent at the apex to allow emptying and filling of the adjacent compartments as they enter and leave the water passing under the wheel. The corners of the blades are chamfered to suit the fillets of the shroud. The shroud is designed to accommodate an arc of 70° of the circumference of the wheel. Detailed technical description of the LDM and SDM and their emplacements are given by Kraatz and Mahajan (1975). In this research, the dimension of the Small Dethridge Meter (SDM) is considered with a scale of 1 : 2 to the original wheel in laboratory scale model building. For practical simplicity, dimensions are rounded while converting from FPS to metric system. From here further, SDM is referred to as a Dethridge wheel.

As discussed earlier, the geometry and working principle of the Dethridge wheel is not that different from the ancient Zuppinger'sche wasserrad or recently developed Staudruckmachine, Aqualinne or Hydrostatic Pressure Converter, which are found suitable for very low head hydropower exploitation. To the best of our knowledge, until now no research has been done on the hydropower potential of the Dethridge wheel. When optimised for power, this simple technology can provide a low-cost solution for utilising very low head resources in rural areas of developing countries. An approximate estimate of operating range where the Dethridge wheel is intended to operate is shown in Fig. 2.10.

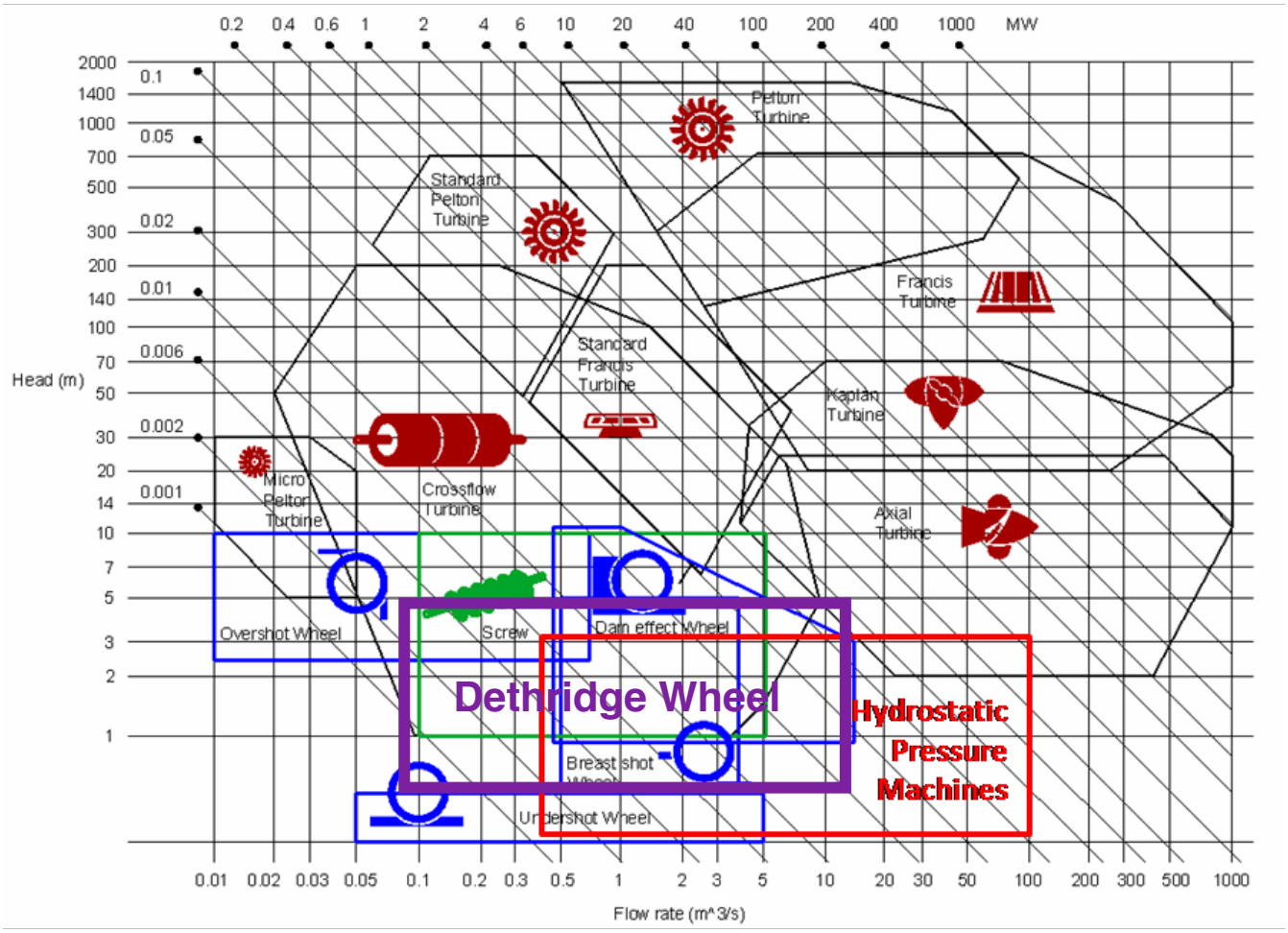

Figure 2.10: Flow and head range for Dethridge wheel, after Linton (2013)

Three dimensional modelling imposes increased level of simulation complexity and computational resources requirement. Simulation of a free surface flow problem involving the interaction of flow and moving object is a complicated three dimensional problem. Very few studies are found in the literature that focus on the hydrodynamic performance of a energy conversion device. Apparently much of the numerical modelling work has been found on the marine energy conversion technologies. Selected examples of numerical modelling of power extraction technologies in open channel flow are reviewed.

Pujol et al. (2015) studied the horizontal water wheel using the general purpose CFD STAR-CCM+ software to solve the unsteady mass and momentum energy conservation equations with an algebraic multi-grid algorithm. A rotating domain was used to simulate the moving water wheel. The realizable $\kappa - \varepsilon$ two-layer scheme turbulent model is adopted for modelling the turbulence. Similarly, Castro-García et al. (2015) carried out simulation on vertical water wheel using CFD software Autodesk Simulation CFD with the aim to determine the pressure exerted by the flow on the surface of the submerged blades. Moreover, Pujol and Montoro (2010); Pujol et al. (2010) have successfully used commercial CFD software to investigate the performance of ancient horizontal water wheels.

A three dimensional numerical study of an axial-flow marine hydrokinetic turbine mounted on the bed of a rectangular open channel is presented in Kang et al. (2012). The complex turbine geometry, including the rotating part is handled by employing the curvilinear immersed boundary (CURVIB) method. To model turbulence, Large Eddy Simulation (LES) approach with the dynamic Smagorinsky subgrid-scale model was used. The model predicted the torque and power generated by a turbine with reasonable accuracy.

Dai and Lam (2009) investigated the numerical model of straight bladed vertical-axis tidal turbine with a major focus on performance of the rotor and hydrodynamic loads for structural design. The hydrodynamic characteristics of straight and helical-bladed vertical axis turbines were investigated by Marsh et al. (2015a). Similarly, three dimensional simulation of three different geometries of straight bladed vertical axis turbine were performed by Marsh et al. (2015b). CFD analysis of bi-directional cross-flow tidal current turbine was carried out by Kim et al. (2012). The effect of channel area on the flow characteristics and the power output is studied. Ansys CFX was used for these three dimensional simulation with a moving mesh technique applied for the turbine rotation and the SST $\kappa - \omega$ model for the turbulence. In all of the above studies, CFD model was reported to be able to accurately predict the hydrodynamic characteristics of the rotor, torque and power output and the effects of geometrical changes.

The operational conditions for tidal energy extraction through a disk in a two and three dimensional domain is simulated by Sun et al. (2008). The commercial CFD software package FLUENT was used for the simulation. The simulation used a finite-volume method to solve the governing equations and standard $\kappa - \varepsilon$ for modelling the turbulence. To simulate the energy extraction device, an absorption zone was set in the numerical model by using the porous media model. Their CFD results showed that the tidal turbine interaction with the flow is a complicated three dimensional problem.

These selected examples show that three dimensional numerical modelling of a problem involving free surface and moving object has been successfully done to study the complex flow phenomena of free surface distortion and the interaction between flow and energy interaction device. Much of these studies are however on tidal energy extraction technologies. To the best of our knowledge, the CFD study presented in this thesis is novel for this particular type of energy extraction device. Part of this work has been published in Paudel and Saenger (2014) and attached in Annex 1.

Chapter 3

Experimental Approach

To test the Dethridge wheel in the laboratory, a test flume was built and the physical model and the measurement instruments were installed. The physical model, measurement equipments, methods of calculation and analysis, optimisation steps and method of uncertainty analysis for the measured data are described in this chapter.

3.1 The test rig

The test rig comprises of pumps, overhead tank, pipelines, flow meter, a flume, and the tail race tank. The flume is rectangular, 20 m long, 1 m wide and 1.5 m deep and houses a model of the Dethridge wheel with shroud, shaft, torque transducer, speed sensor, stilling tubes, an inlet tank at the upstream and a control weir at the downstream. Side walls of the flume are made up of a glass and the bottom is a smooth concrete floor. The slope of the channel is adjustable and in all test conducted in this research, the slope is kept at 0 °. The maximum flow rate the test set up could safely handle is around 35 l/s. Water was supplied through a pump of 50 l/s maximum capacity. The general layout of the test rig is shown in Fig. 3.1 and the physical model is shown in Fig. 3.2.

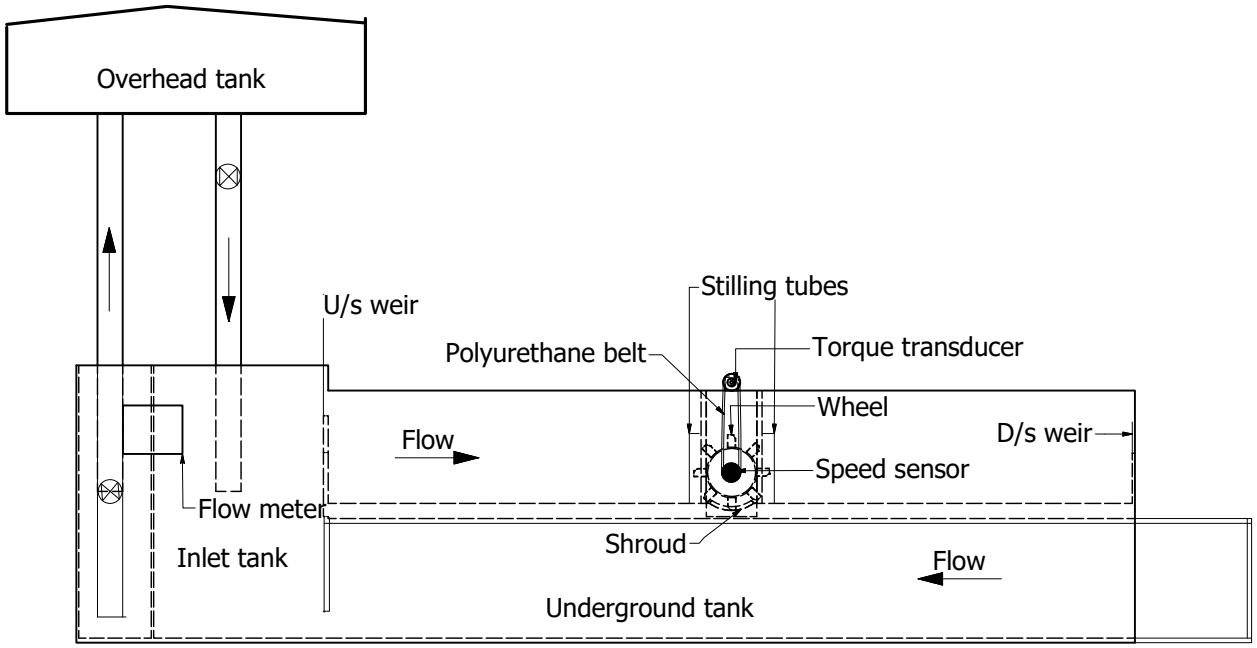

Figure 3.1: Schematic sketch of the test facility

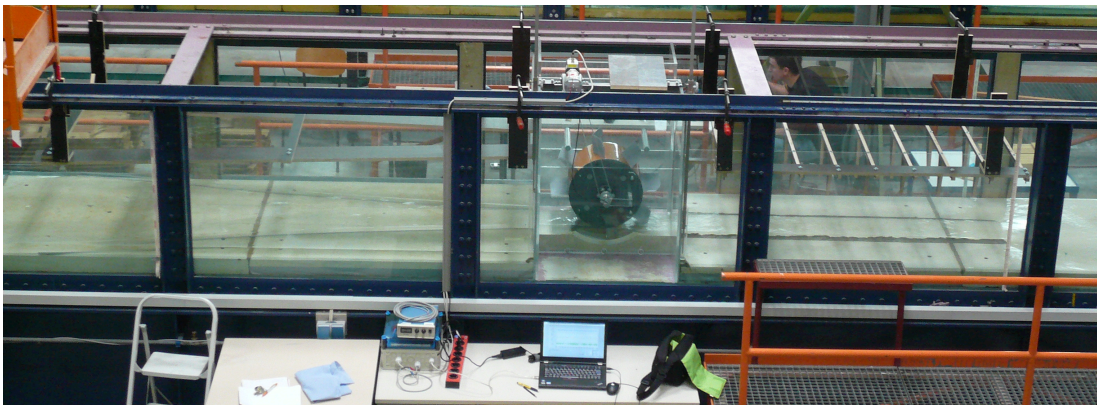

Figure 3.2: Physical model

3.1.1 The model Dethridge wheel

The model wheel is built in 1:2 scale to the original dimensions given in Kraatz and Mahajan (1975). Original dimensions were in FPS system, while converting to the SI system these dimensions are rounded off for practical purpose. The Dethridge wheel consists of a hub, blades and the side coverings. The hub of the wheel is made up of polyvinyl chloride (PVC) piping, which is 40 cm in diameter and 25 cm wide. The wheel is covered with a 20 mm thick PVC side covers on both sides to ensure the stability of the wheel and to avoid the accumulation of water inside the hub which would otherwise retard the wheel motion. The gap between the sides of the housing and the wheel and the bottom gap are minimised to 1 mm. Key dimensions of the model wheel are summarised in Table 3.1. The physical model of the Dethridge wheel is shown in Fig. 3.3.

Eight V-shaped steel blades of 2 mm thickness are mounted along the circumference of the hub. Blades are 10 cm long and are bent in V-shape to acquire an angle of 127 °. At the apex of each blade, an air vent is located to facilitate the filling and emptying of adjacent compartments as they enter and exit the water surface. The apex of the V is leading in the direction of rotation. Both sides of the blades are chamfered to match the fillets at the junction of the side walls and the floor. The blades are painted to reduce the surface roughness and to prevent corrosion. The geometry of the original blade (BS0) is shown in Fig. 3.5. A stainless steel shaft with a diameter of 20 mm and 45 cm long was used.

3.1.2 The shroud

The shroud profile was made by joining individual plexiglass profiles produced by laser cutting. The plexiglass profiles were joined together using a weld bonding method. On the side edges of the shroud curvature, a triangular curved profile is attached to reduce the gap losses between the chamfered blade corners and the shroud edges. These profiles are produced using rapid prototyping. The original shroud (SS0) is shown in Fig. 3.4 with the side seal profiles.

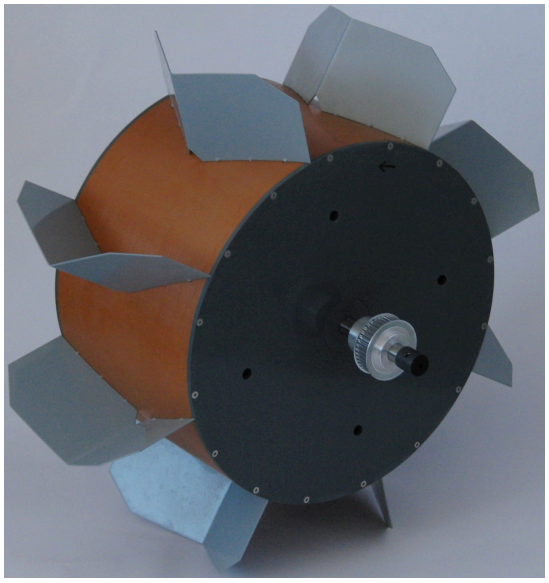

Figure 3.3: Model wheel

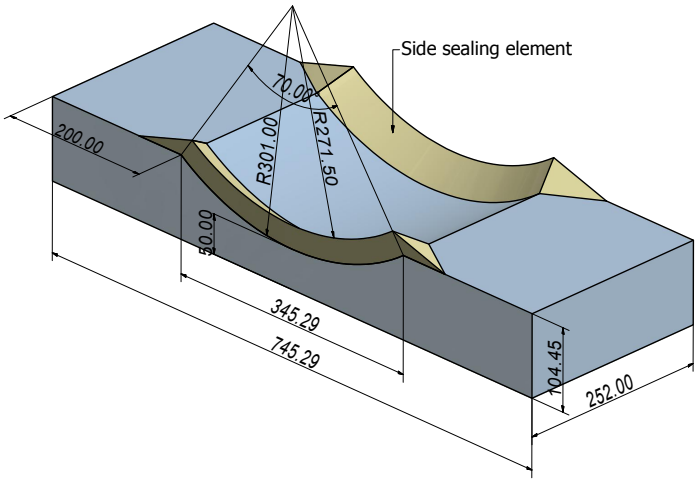

Figure 3.4: Shroud SS0 with side sealing (dimensions are in mm)

3.1.3 Measured variables and measurement system

The input variables to be measured are flow rate Q, total head acting on the wheel control volume H. The resulting variables are torque τ, and the rotational speed of the wheel N.

Flow (Q): This is a measure of volumetric mass flow rate through the wheel control volume including the amount of leakage flow through the side and bottom clearance gaps. Flow rate delivered to the test flume is measured using a magnetic flow meter which works according to the Faraday's law of electromagnetic induction. Voltage is induced when a conductive fluid moves through the magnetic field. The magnitude of this induced voltage is directly proportional to the velocity of the conducting fluid. The flow rate is then calculated using the flow velocity and the flow area.

Total head (H): The total head is calculated using the Bernoulli's principle. The total head acting on the wheel is a difference between pressure and velocity heads at the inlet and outlet of the wheel. The elevation head is 0. Water levels were measured at the immediate upstream and downstream of the

Table 3.1: Model Parameters

Geometry	Dimension
Model Scale	1:2
Hub diameter	400 mm
Blade length	100 mm
Overall diameter	600 mm
Wheel width	250 mm
Side gaps	1 mm
Bottom gap	1 mm
Number of blades	8
Weight of the wheel	19.71 kg

wheel control volume. To measure the water levels, two stilling tubes of diameter 20 cm were installed and depth gauges were used for the manual reading of the flow depth values. The mean velocity of the flow is then calculated from the known area of flow and the flow rate ($v = Q/A$). The total head H is therefore given by,

$$H = \left(h_1 + \frac{v_1^2}{2_g}\right) - \left(h_2 + \frac{v_2^2}{2_g}\right) \tag{3.1}$$

Torque (τ): The shaft torque is generated as a result of the energy transfer between the fluid and the rotating wheel. The shaft torque is transmitted to the torque transducer shaft through the Polyurethane synchronous belt drive. The measured torque therefore includes mechanical losses due to the bearings and the belt drive. The toque on the wheel shaft is measured using the torque transducer. The torque transducer works according to the principle of torsion theory. The angular deformation of the rotating element is a measure of a torque. The strain created by the torque is measured by the sensitive strain gauge and the signals are transmitted as a measure of the torque.

The top of the plexiglass frame on the sides of wheel (see Fig. 3.1) provided a mounting bay for the torque transducer shaft. In Figure 3.6 assembly of torque transducer shaft, couplings, gear box, brake and the belt pulley is shown.

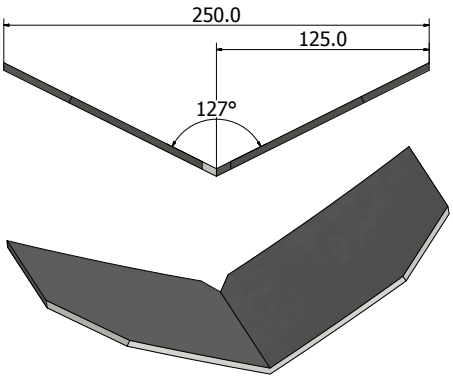

Figure 3.5: Blade profile BS0 (dimensions in mm)

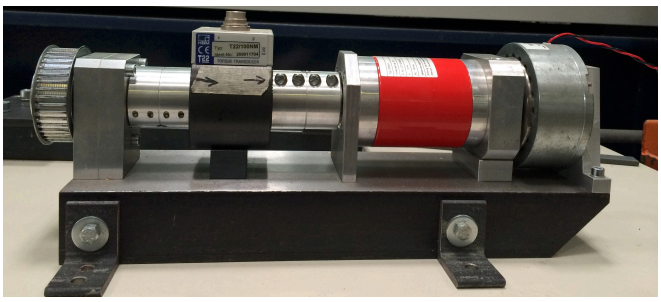

Figure 3.6: Assembly of a torque transducer and braking system

Speed (N): The speed is the rotational motion of the wheel which is measured using a solid shaft pulse encoder. The encoder transforms rotational movement into pulse sequences. The speed of the wheel is varied by applying load on the wheel through a Hysteresis braking system from Magtrol. The brake system operates at higher speed range so a gearbox from Bretzel GmbH was used to step up the shaft speed at the brake end. The brake is electrically operated through a power supply of Magtrol make model 5210.

Data acquisition system: Output signals from all the measurement instruments are collected into a junction box and fed to a computer using a LabView based program. For each constellation, data were acquired for approximately one minute and the mean value were taken. The summary of the data acquisition system is presented in Table 3.2.

Table 3.2: Summary of data acquisition system

Parameter	Make	Model	Accuracy	Range	Working principle
Flow rate (Q)	Krohne	IFC110	±1%	6 l/h − 86860 m^3/h	Faraday's law
Torque (τ)	HBM	T22	±0.1% of full scale	+/ − 100 Nm	Wheatstone bridge
Speed (N)	ifm	HB1015	±0.5 rpm	10000 rpm	Pulse encoder
U/s flow depth (h_1)	Ott	-	±1%	-	Point gauge
D/s flow depth (h_2)	Ott	-	±2%	-	Point gauge

3.2 Methods of calculation and analysis

The performance variables were measured for flow rates of 6 to 20 l/s. Beyond this flow rate, the test rig was not capable to accommodate the severe splashing occurred at the upstream by fast revolving wheel. The measured data showed that the speed of the wheel and flow rate has a linear relationship given by Eq. 3.2 at constant flow depths. The constants a_1 and b_1 in Eq. 3.2 are calculated from the measured results and the flow rates outside of the measured range including the minimum flow rate required to start the wheel into motion and maximum flow rate required for no-load speed are calculated using Eq. 3.2.

$$Q = a_1 N + b_1 \tag{3.2}$$

Similarly, the test results also revealed that speed and torque have a linear relationship of the form given by Eq. 3.3 at a constant flow depths. Speed-torque line was plotted from the measured data and the constants a_2 and b_2 were determined. Rest of the points on the curve outside the measured range including the stall torque and the no-load speed is calculated using the Eq. 3.3.

$$\tau = a_2 N + b_2 \tag{3.3}$$

By applying the Bernoulli's principle, the work done on the wheel shaft W_s by the water per unit mass flowing through the wheel is:

$$W_s = gH - \text{Losses} \tag{3.4}$$

where, H is the total head acting on the wheel control volume and is given by Eq. 3.1. The power delivered to the wheel shaft (P_{shaft}) is the the work done on the wheel shaft times the mass flow rate:

$$P_{\text{out}} = \rho Q(gH - \text{Losses}) \tag{3.5}$$

The power output is calculated from the known values of speed of the wheel (N) and the torque (τ) using Eq. 3.6. The measured power output (P_{out}) also includes the mechanical losses due to the bearings and the belt drive.

$$P_{\text{out}} = \rho Q(gH - gH_{\text{hyd. losses}} - gH_{\text{leakage}} - gH_{\text{mech. losses}}) = \omega\tau = \frac{2\pi N\tau}{60} \tag{3.6}$$

Total losses in the wheel control volume comprises of hydraulic losses, leakage losses and mechanical losses (Eq. 3.6). Hydraulic losses include the fluid friction losses, blade impact losses at the entry, exit losses, as well as complex losses within the blade cells such as flow separation, flow circulation and secondary flow which are difficult to quantify. Mechanical losses include losses due to belt drive and the bearings which is constant and assumed to be 5%.

Leakage losses are due to the clearance gaps between the wheel and the housing and through the air vent. Leakage flow can be quantified from the known volume of the blade cells and the measured speed of the wheel given that the cell compartments are completely filled.

$$Q_L = Q - V * N/60 \tag{3.7}$$

where, Q_L is the leakage flow rate, V is the volume of water occupied in the cells of the wheel which is calculated to be 38.84 l.

The shaft power can be measured without information on the losses. The mechanical efficiency of the wheel is therefore the ratio of shaft power output and the hydraulic power input and is given by Eq. 3.8. This efficiency combines the hydraulic efficiency, volumetric efficiency of the wheel and the mechanical efficiency of the bearings and belt drive system.

$$\eta = \frac{P_{\text{out}}}{P_{\text{in}}} = \frac{\rho Q(gH - \text{Losses})}{\rho QgH} = \frac{2\pi N\tau/60}{\rho QgH} \tag{3.8}$$

The analysis of change in performance at different modification stages is done by calculating the relative percentage change in performance variables. Percentage change in the variable of interest is calculated by Eq. 3.9:

$$\text{Percentage change} = \frac{\text{Modified case} - \text{Reference case}}{\text{Reference case}} \times 100\% \tag{3.9}$$

3.2.1 Comparison of experiment and CFD

The torque (τ) measured in the experiment is essentially a mechanical (shaft) torque whereas CFD only measures hydraulic (τ_{hyd}) torque excluding losses due to belt drive and bearings. In order to

compare these two results, the hydraulic torque from CFD must be corrected using Eq. 3.10. Flow rate Q does not require any correction since the leakage gap is same both in CFD and physical models.

$$\tau_{\text{CFD}} = \tau_{\text{hyd.CFD}} \eta_{mech} \tag{3.10}$$

3.2.2 Uncertainty analysis of experimental results

Uncertainty analysis of the measured data was done using constant odd combination method as described by Moffat (1988). Experimental data have both random (statistical) and bias (systematic or fixed) errors or uncertainty. Systematic errors associated with the measured variables, flow rate Q, head H, torque τ and speed N, are taken from manufacturer's specifications as presented in Table 3.2. Random error in the measured data is calculated by taking multiple measurements at each constellation. The standard deviation of the mean or the standard error is the measure of random errors in the measurements. The root sum square (RSS) of systematic and random errors gives an uncertainty bound on the measured variables.

The best estimate of the uncertainty in the use of linear regression models for $N-Q$ and $N-\tau$ in Eqs. 3.2 and 3.3 is calculated by Eq. 3.11 and 3.12:

$$\sigma_Q = \sqrt{\frac{1}{n-2}\sum_{i=1}^{n}(Q - a_1 N - b_1)^2} \tag{3.11}$$

$$\sigma_\tau = \sqrt{\frac{1}{n-2}\sum_{i=1}^{n}(\tau - a_2 N - b_2)^2} \tag{3.12}$$

where, σ_Q and σ_τ are the best estimates of uncertainties on the use of Eqs. 3.2 and 3.3 respectively, n is the total number of measurements, a_1, b_1 and a_2, b_2 are the constants for $N-Q$ and $N-\tau$ equations respectively, which are determined from the measured data.

The uncertainties on the main variables are used to calculate the overall uncertainty in derived quantities namely, total head, power output and efficiency given by Eqs. 3.13, 3.14, 3.15 respectively using the method of uncertainty propagation (Moffat, 1988). The dimensionless form of uncertainty on power output and efficiency in Eqs. 3.16 and 3.17 gives the relative uncertainty bound in power output and efficiency:

$$\delta H = \pm\left[(\delta h_1)^2 + (\delta h_2)^2 + \frac{Q}{g^2 b^4 h_1^4}\left\{\left(\frac{\delta Q}{Q}\right)^2 + \left(\frac{\delta h_1}{h_1}\right)^2\right\} + \frac{Q}{g^2 b^4 h_2^4}\left\{\left(\frac{\delta Q}{Q}\right)^2 + \left(\frac{\delta h_2}{h_2}\right)^2\right\}\right]^{\frac{1}{2}} \tag{3.13}$$

$$\delta P = \pm\left[\left(\frac{\partial P}{\partial N}\right)^2 (\delta N)^2 + \left(\frac{\partial P}{\partial \tau}\right)^2 (\delta \tau)^2\right]^{\frac{1}{2}} \tag{3.14}$$

$$\delta \eta = \pm\left[\left(\frac{\partial P}{\partial Q}\right)^2 (\delta Q)^2 + \left(\frac{\partial P}{\partial H}\right)^2 (\delta H)^2 + \left(\frac{\partial P}{\partial N}\right)^2 (\delta N)^2 + \left(\frac{\partial P}{\partial \tau}\right)^2 (\delta \tau)^2\right]^{\frac{1}{2}} \tag{3.15}$$

$$\frac{\delta P}{P} = \pm\left[\left(\frac{\delta N}{N}\right)^2 + \left(\frac{\delta \tau}{\tau}\right)^2\right]^{\frac{1}{2}} \tag{3.16}$$

$$\frac{\delta \eta}{\eta} = \pm\left[\left(\frac{\delta Q}{Q}\right)^2 + \left(\frac{\delta H}{H}\right)^2 + \left(\frac{\delta N}{N}\right)^2 + \left(\frac{\delta \tau}{\tau}\right)^2\right]^{\frac{1}{2}} \tag{3.17}$$

where, H, τ, Q, N, P and η are the total head, torque, flow rate, rotational speed, shaft power output and efficiency respectively. $g(= 9.81\ \mathrm{N/m^2})$ is the acceleration due to gravity, b is the channel width, h_1, h_2 are the upstream and downstream flow depths respectively.

3.3 Optimization study

In order to improve the overall performance of the wheel, the optimisation looked at the performance of the wheel at different wheel housings, numbers of blades, width of the channel, inlet and outlet transition shapes, different blade shape and shroud shape. In this section, the modifications carried out are presented in detail.

3.3.1 Wheel housing

As outlined in Chapter 2, the possibility of side filling and emptying of the blade cells is important for the performance of Hydrostatic Pressure Machines (HPMs) (Linton, 2009; Senior, 2009; Schneider et al., 2011; Paudel et al., 2013). For Dethridge wheels, being similar to the HPMs, the side filling is an important performance criteria which needs to be further investigated. The Dethridge wheel in Australian farm outlets is housed in such a way that the blade cells at the inlet and exit are both enclosed by the side walls. In the wheel housing study, the side enclosure of the wheel is modified and the performance of the wheel is measured.

The model wheel was tested in two different housing designs. The only difference in these two settings was side enclosure of the blade cells. On the original setting, the blade cells at the inlet and exit are

both enclosed by providing elongated plexiglas side walls. On the optimized housing, side enclosure is reduced to enclose only the hub of the wheel. Figures 3.7 and 3.8 show plan and sectional view of these two settings.

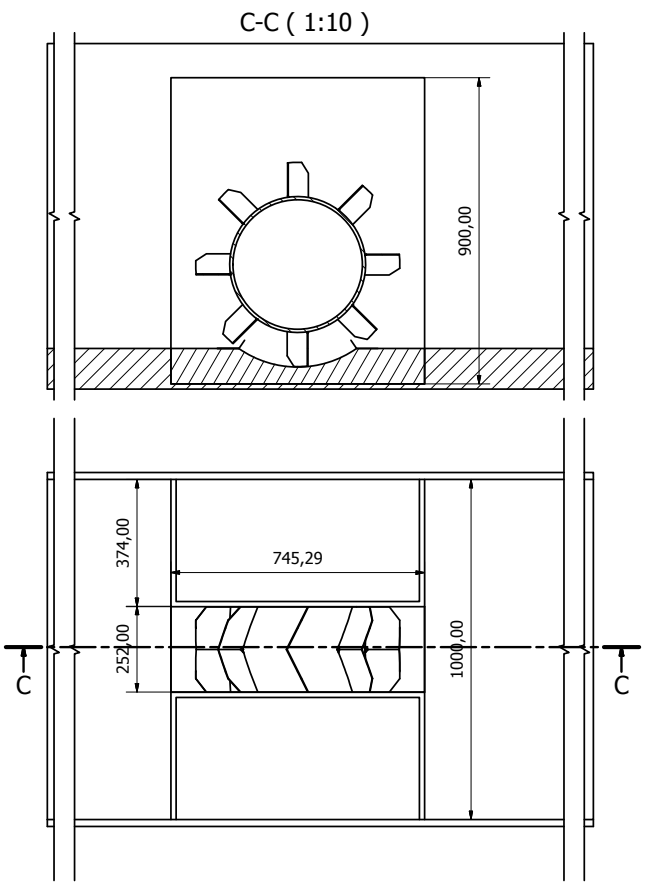

Figure 3.7: Original wheel housing

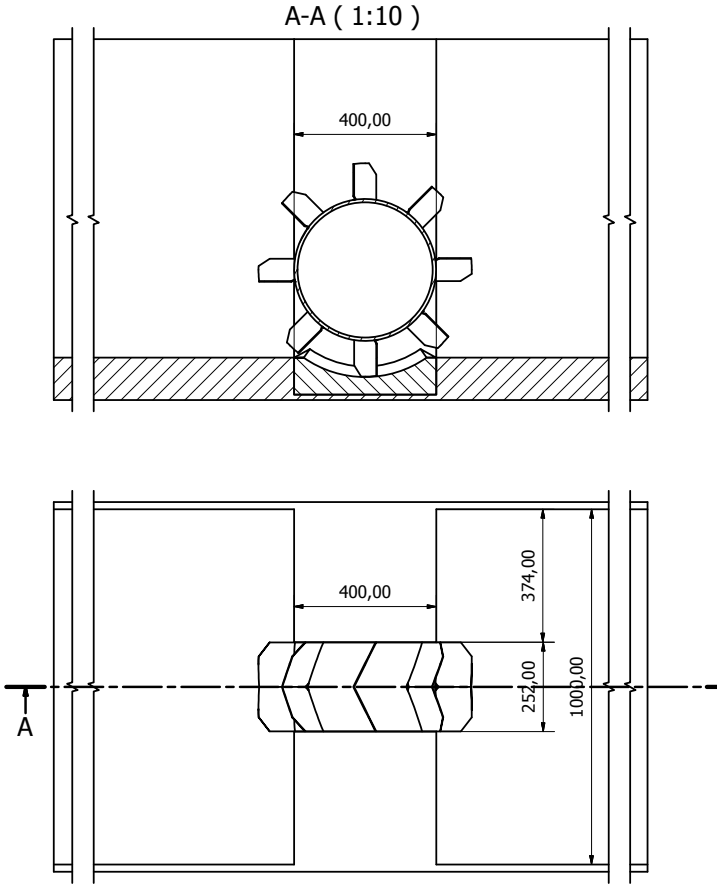

Figure 3.8: Modified wheel housing

3.3.2 Blade number

Blade number is an important geometrical design parameter for the optimal performance of water wheel. Blade number has an impact on friction losses, recirculation losses within the blade cells, rotational quality and stability of the wheel. Performance of the Dethridge wheel with different numbers of blades were measured on the physical model. The number of blades considered in the tests were $6, 8, 12$ & 16. The original sharp V-shaped BS0 blades shown in Fig. 3.5 were used for all blade number tests.

3.3.3 Wheel to channel width ratio

Wheel to channel width ratio is an important performance and economical criteria to be considered in the design of the Dethridge wheel. The review of literature on HPM in Chapter 2, (Linton (2009); Schneider et al. (2011); Paudel et al. (2013)), showed that channel width plays an important role on the performance of the wheel. Based on this evidence, tests on the Dethridge model wheel was carried out to identify the optimal wheel to channel width ratio. Wheel width (b) to channel width (B) ratios

of 1:4, 1:3, 1:2 and 1:1 were experimentally investigated on the physical model. Movable plexiglas walls were used to create the desired width of channel.

3.3.4 Inlet and outlet transitions

Transitions on the flow involve significant flow losses due to contraction, expansion and directional change losses. Smooth transition design where energy losses are minimal are desired at the inlet and outlet of the wheel. Different inlet and outlet forms are tested on the physical model. The contraction transition design on the upstream of the wheel follows a profile recommended by Swamee and Basak (1994). The length of the transition is governed by the side splay of 7:1. Eq. 3.18 below is used for the design of the contraction transition.

$$b = b_0 - (b_0 - b_L)\left[1.41 \times \left(\frac{1 - x/L}{x/L}\right)^{1.23} + 1\right]^{-0.924} \tag{3.18}$$

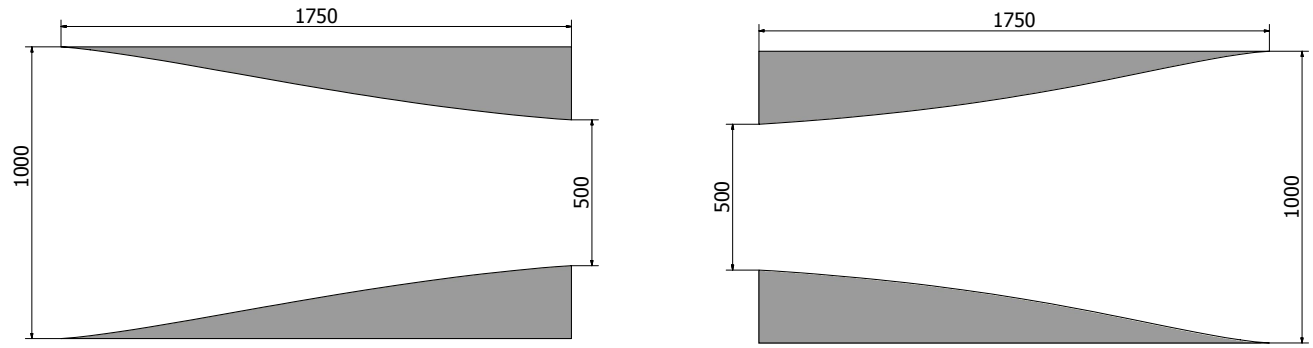

(a) Contraction profile

(b) Expansion profile

Figure 3.9: Channel transition profiles (dimensions are in mm)

To design the expansive transition at the outlet of the channel, a profile from Swamee and Basak (1993) was taken. Eq. 3.19 gives the optimal profile for the expansive transition. The length of the profile is governed by the splay of 7:1. This profile was experimentally tested and found to have the highest efficiency among the existing profiles (Basak and Alauddin, 2010). The contraction and expansion transition profiles are shown in Figures 3.9a and 3.9b respectively.

$$b = b_0 - (b_L - b_0)\left[2.52 \times \left(\frac{1 - x/L}{x/L}\right)^{1.35} + 1\right]^{-0.775} \tag{3.19}$$

where, $b_0 = 500$mm and $b_L = 1000$ mm are the channel width at $x = 0$ and $x = L$.

3.3.5 Blade shape modification

The blade shape plays a fundamental role on the performance of the wheel. The objective of the blade shape change are two folds. Firstly to increase the efficiency of the wheel by reducing the entry shock losses and turbulent disturbances at the flow blade interaction at the inlet and the reduction of the amount of flow driven upwards by the blades at the exit. Secondly, it aims to improve the torque fluctuation characteristics of the wheel. The three dimensional numerical model of the wheel with modified blades is simulated and analysed in Flow-3D

The original blade shape BS0 with sharp V-shape shown in Fig. 3.5 is modified to form a curvature while keeping the V-shape and the inner angle of 127 °. The new blade shape BS1 is shown in Fig. 3.10.

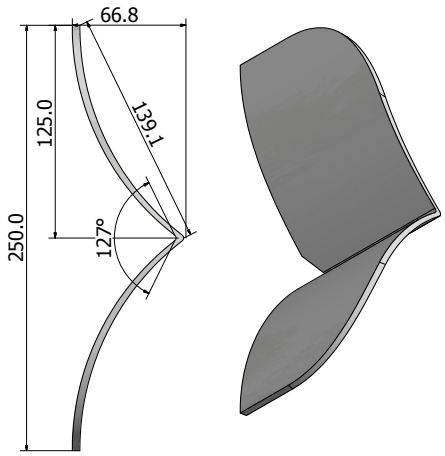

Figure 3.10: Blade shape BS1 (dimensions are in mm)

3.3.6 Shroud shape modification

The original shroud shape SS0 shown in Fig. 3.4 is modified to increase the total head acting on the wheel control volume. Performance of the wheel with different shroud shape is numerically studied in Flow-3D. The new shroud design is shown in Fig. 3.11. On the new shroud SS1, the downstream curved part of the shroud is removed and the curve only acquires 60 ° angle to the wheel enclosing one blade cell of six blade wheel at a time.

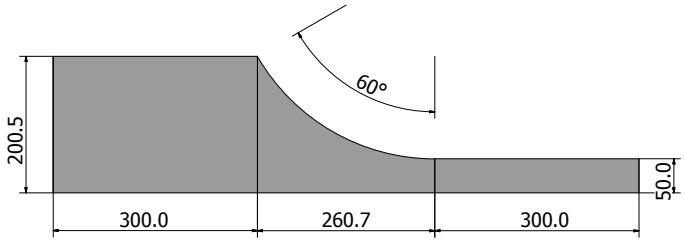

Figure 3.11: Shroud shape SS1 (dimensions are in mm)

Chapter 4

Computational Fluid Dynamics (CFD) model

Computational Fluid Dynamics (CFD) is a tool which provides solutions of governing equations of fluid flow. The governing partial differential equations of fluid flow commonly known as Navior-Stokes equations are discretized and solved over an area of interest with the known physically possible boundary conditions. CFD model was used to study the hydrodynamics of the Dethridge wheel model in this research.

4.1 CFD code Flow-3D

CFD commercial code Flow-3D (version 10.1.0.4) developed by Flow Science, Inc. was selected in this study. Flow-3D uses finite volume approach to solve the Reynolds-averaged Navier-Stoke's (RANS) equations over the computational domain. The computational domain is divided into a grid of variable-sized hexahedral cells. With each cell there are associated local average values of all dependent variables. For each cell values variables are solved at discrete times using a staggered grid technique (Versteeg and Malalasekera, 2007). The staggered grid places all dependent variables at the center of each cell except velocities and fractional areas, which are located at the center of the cell faces normal to the corresponding direction. Free surface of the flow is tracked using the Volume of Fluid (VOF) method developed by Hirt and Nichols (1981). Solid body is defined as an obstacle by the implementation of the Fractional Area/Volume Obstacle Representation (FAVOR) method where obstacles are embedded in a fixed grid by allowing them to block portions of grid cell faces and cell volumes. The geometry is therefore conveniently represented within the grid cells (Hirt and Chen, 1996). The FAVOR method is a porosity technique to define obstacles. The grid porosity value is 0 within the obstacle and one for cells without the obstacle. Cells only partially filled with an obstacle have a value between 0 and one (Hirt and Sicilian, 1985; Hirt, 1992).

4.2 Mass and momentum equations

The governing equations for fluid flow namely the continuity equation, the momentum equations, and the energy equation are derived from the fundamental physical principles of mass conservation, momentum conservation, and the first law of thermodynamics, respectively. This study is primarily concerned with an incompressible fluid flow for which only the mass and momentum equations are needed to be solved. Moreover, the moving object is present in the model. The modified form of continuity equation for moving obstacle problem therefore takes the form of Eq. 4.1.

$$\frac{\partial}{\partial x}(uA_x) + \frac{\partial}{\partial y}(vA_y) + \frac{\partial}{\partial z}(wA_z) = -\frac{\partial V_F}{\partial t} \tag{4.1}$$

where, V_F is the fractional volume of fluid in the cell i.e., $V_F = V_{open}/V_{cell}$. u, v, w and A are the fluid velocity components and fractional area of fluid in the x, y, and z directions.

The term on the right hand side of the Eq. 4.1 $-\partial V_F/\partial t$ is determined by using:

$$-\frac{\partial V_F}{\partial t} = \frac{S_{obj}}{V_{cell}}\vec{V}_{obj}.\vec{n} \tag{4.2}$$

where, S_{obj}, $\vec{V}_{obj}$ and $\vec{n}$ are the surface area, velocity and the unit normal vector of the moving object respectively. V_{cell} is the volume of the mesh cell.

However, in the momentum equation (Eqs.4.3–4.5) the presence of moving object doesn't make any difference to that of the equations involving stationary object. This is because in Flow-3D non-conservative form of the momentum equations are used, which are obtained by subtracting the continuity equation from the momentum equation in the conservative form. Therefore, terms containing the change of V_F with time are cancelled out. For more details see Anderson (2009) and Flow-3D (2011).

$$\frac{\partial u}{\partial t} + \frac{1}{V_F}\left\{uA_x\frac{\partial u}{\partial x} + vA_y\frac{\partial u}{\partial y} + wA_z\frac{\partial u}{\partial z}\right\} = -\frac{1}{\rho}\frac{\partial p}{\partial x} + G_x + f_x \tag{4.3}$$

$$\frac{\partial v}{\partial t} + \frac{1}{V_F}\left\{uA_x\frac{\partial v}{\partial x} + vA_y\frac{\partial v}{\partial y} + wA_z\frac{\partial v}{\partial z}\right\} = -\frac{1}{\rho}\frac{\partial p}{\partial y} + G_y + f_y \tag{4.4}$$

$$\frac{\partial w}{\partial t} + \frac{1}{V_F}\left\{uA_x\frac{\partial w}{\partial x} + vA_y\frac{\partial w}{\partial y} + wA_z\frac{\partial w}{\partial z}\right\} = -\frac{1}{\rho}\frac{\partial p}{\partial z} + G_z + f_z \tag{4.5}$$

In above equations, p is the pressure and ρ is a fluid density. G is the body accelerations and f is the viscous accelerations with their corresponding components represented by the subscripts x, y and z. For solving f, a turbulence model is required for closure.

The viscous accelerations for dynamic viscosity μ are defined by the following equations:

$$\rho V_F f_x = \tau_{bx} - \left\{\frac{\partial}{\partial x}(A_x\tau_{xx}) + \frac{\partial}{\partial y}(A_y\tau_{xy}) + \frac{\partial}{\partial z}(A_z\tau_{xz})\right\} \tag{4.6}$$

$$\rho V_F f_y = \tau_{by} - \left\{\frac{\partial}{\partial x}(A_x\tau_{xy}) + \frac{\partial}{\partial y}(A_y\tau_{yy}) + \frac{\partial}{\partial z}(A_z\tau_{yz})\right\} \tag{4.7}$$

$$\rho V_F f_z = \tau_{bz} - \left\{ \frac{\partial}{\partial x}(A_x \tau_{xz}) + \frac{\partial}{\partial y}(A_y \tau_{yz}) + \frac{\partial}{\partial z}(A_z \tau_{zz}) \right\} \tag{4.8}$$

$$\tau_{xx} = -2\mu \left\{ \frac{\partial u}{\partial x} - \frac{1}{3}\left(\frac{\partial u}{\partial x} + \frac{\partial v}{\partial y} + \frac{\partial w}{\partial z} \right) \right\} \tag{4.9}$$

$$\tau_{yy} = -2\mu \left\{ \frac{\partial v}{\partial y} - \frac{1}{3}\left(\frac{\partial u}{\partial x} + \frac{\partial v}{\partial y} + \frac{\partial w}{\partial z} \right) \right\} \tag{4.10}$$

$$\tau_{zz} = -2\mu \left\{ \frac{\partial w}{\partial z} - \frac{1}{3}\left(\frac{\partial u}{\partial x} + \frac{\partial v}{\partial y} + \frac{\partial w}{\partial z} \right) \right\} \tag{4.11}$$

$$\tau_{xy} = -\mu \left\{ \frac{\partial v}{\partial x} + \frac{\partial u}{\partial y} \right\} \tag{4.12}$$

$$\tau_{xz} = -\mu \left\{ \frac{\partial u}{\partial z} + \frac{\partial w}{\partial x} \right\} \tag{4.13}$$

$$\tau_{yz} = -\mu \left\{ \frac{\partial v}{\partial z} + \frac{\partial w}{\partial y} \right\} \tag{4.14}$$

In the above equations, τ_{bx}, τ_{by}, and τ_{bz} are the wall shear stresses which contain non-zero tangential velocity of the moving object boundary (Sicilian, 1990). In the absence of moving mesh or moving obstacle, wall shear stresses are modelled by assuming a zero tangential velocity on the portion area closed to flow. τ_{xx}, τ_{yy}, τ_{zz}, τ_{xy}, τ_{xz}, and τ_{yz} are the shear and normal stresses in the fluid, μ is the dynamic viscosity of the fluid. For turbulent flows, the wall shear stresses are evaluated assuming the law-of-the-wall velocity profile near the wall.

4.3 Turbulence modelling

For turbulence closure, a two-equation Renormalized Group (RNG) model is used. The RNG model is based on Re-Normalization Group (RNG) methods to renormalise the Navier-Stokes equation to account for the effects of the smaller scale motion and is suitable for flows with strong shear regions (Yakhot and Orszag, 1986; Yakhot and Smith, 1992). This approach applies statistical methods to the derivation of the averaged equations for turbulence quantities. The model consists of transport equations for both turbulent kinetic energy and dissipation. The constants in the RNG model are derived explicitly. The model uses transport equations similar to the standard $k-\varepsilon$ model. The transport

equation for turbulent kinetic energy (k) and turbulent dissipation (ε) in two-equation model is given as:

$$\frac{\partial k}{\partial t} + \frac{1}{V_F}\left\{uA_x\frac{\partial k}{\partial x} + vA_y\frac{\partial k}{\partial y} + wA_z\frac{\partial k}{\partial z}\right\} = P_T + D_k - \varepsilon \tag{4.15}$$

$$\frac{\partial \varepsilon}{\partial t} + \frac{1}{V_F}\left\{uA_x\frac{\partial \varepsilon}{\partial x} + vA_y\frac{\partial \varepsilon}{\partial y} + wA_z\frac{\partial \varepsilon}{\partial z}\right\} = C_{\varepsilon 1}\frac{\varepsilon}{k}P_T + D_\varepsilon - C_{\varepsilon 2}\frac{\varepsilon^2}{k} \tag{4.16}$$

where, the turbulent kinetic energy production P_T due to shearing forces is given by:

$$\begin{aligned} P_T \;=\; & \left(\frac{\mu}{\rho V_F}\right)\left\{2A_x\left(\frac{\partial u}{\partial x}\right)^2 + 2A_y\left(\frac{\partial v}{\partial y}\right)^2 + 2A_z\left(\frac{\partial w}{\partial z}\right)^2\right. \\ & + \left(\frac{\partial v}{\partial x} + \frac{\partial u}{\partial y}\right)\left[A_x\frac{\partial v}{\partial x} + A_y\frac{\partial u}{\partial y}\right] \\ & + \left(\frac{\partial u}{\partial z} + \frac{\partial w}{\partial x}\right)\left(A_z\frac{\partial u}{\partial z} + A_x\frac{\partial w}{\partial x}\right) \\ & \left. + \left(\frac{\partial v}{\partial z} + \frac{\partial w}{\partial y}\right) + \left(A_z\frac{\partial v}{\partial z} + A_y\frac{\partial w}{\partial y}\right)\right\} \end{aligned} \tag{4.17}$$

$$D_k = \frac{1}{V_F}\left\{\frac{\partial}{\partial x}\left(\nu_k A_x\frac{\partial k}{\partial x}\right) + \frac{\partial}{\partial y}\left(\nu_k A_y\frac{\partial k}{\partial y}\right) + \frac{\partial}{\partial z}\left(\nu_k A_z\frac{\partial k}{\partial z}\right)\right\} \tag{4.18}$$

$$D_\varepsilon = \frac{1}{V_F}\left\{\frac{\partial}{\partial x}\left(\nu_\varepsilon A_x\frac{\partial \varepsilon}{\partial x}\right) + \frac{\partial}{\partial y}\left(\nu_\varepsilon A_y\frac{\partial \varepsilon}{\partial y}\right) + \frac{\partial}{\partial z}\left(\nu_\varepsilon A_z\frac{\partial \varepsilon}{\partial z}\right)\right\} \tag{4.19}$$

The coefficient of dynamic viscosity μ is the sum of molecular and turbulent viscosities:

$$\mu = \rho(\nu + \nu_T) \tag{4.20}$$

The turbulent eddy viscosity ν_T is determined using:

$$\nu_T = C_\mu\frac{k^2}{\varepsilon} \tag{4.21}$$

In the above equations, ν_k and ν_ε is the diffusion coefficient of k and ε respectively and is computed based on the local value of turbulent viscosity. The coefficients $C_{\varepsilon 1}$, $C_{\varepsilon 2}$ and C_μ are the dimensionless turbulence parameters which can be adjusted by the users. The default value of $C_{1\varepsilon}$ and C_μ are 1.42 and 0.085 respectively in the RNG model. $C_{2\varepsilon}$ is computed from the turbulent kinetic energy k and

turbulent production P_T. D_k is the diffusion due to viscous losses within the turbulent eddies, D_ε is the diffusion of the dissipation, ν is the kinematic viscosity.

The maximum turbulent mixing length (TLEN) is used by the RNG turbulence model to limit the turbulent dissipation (ε) so that the turbulent viscosity (ν_T) in Eq. 4.21 does not become excessively large. Eq. 4.22 limits the value of the ε.

$$\varepsilon_{min} = C_\mu \sqrt{\frac{3}{2}} \frac{k^{\frac{3}{2}}}{TLEN} \tag{4.22}$$

The turbulent length and time scales are calculated as:

$$L = \frac{k^{\frac{3}{2}}}{\varepsilon} \tag{4.23}$$

$$T = \frac{k}{\varepsilon} \tag{4.24}$$

The recommended value of TLEN is 7% of the hydraulic diameter. However, for configurations with complex multi-scale features choosing this parameter is not simple. Flow-3D has an option to dynamically compute turbulent length and time scales, and their respective upper and lower bounds. The lower bounds of the turbulent length and time scales are based on the Kolmogorov scales and the upper bounds are based on the rapid distortion theory as shown in Eqs. 4.25 and 4.26 (Isfahani and Brethour, 2009; Flow-3D, 2011).

$$L_{min} = 70 \left(\frac{\mu}{\rho}\right)^{\frac{3}{4}} \left(\frac{1}{\varepsilon}\right)^{\frac{1}{4}}; \quad L_{max} = \frac{0.86}{C_\mu} \frac{\sqrt{k}}{S'} \tag{4.25}$$

$$T_{min} = 6\sqrt{\frac{\mu}{\rho \varepsilon'}}; \quad T_{max} = \frac{0.35}{C_\mu} \frac{1}{S'} \tag{4.26}$$

where, S' is the mean strain rate magnitude computed from the second invariant of the strain tensor. The length scale L in Eq. 4.23 subject to the limits by Eq. 4.25 is used to limit dissipation (ε) in Eq. 4.22. The inverse of the time scale T in Eq. 4.24 subjected to the limits by Eq. 4.26 is used to limit Eq. 4.16.

4.4 Free surface tracking

Flow-3D uses the Volume of fluid (VOF) method to locate and monitor the free surface. Free surface monitoring is important as the cells on the surface interface average the values of the fluid properties

at the interface which doesn't match to the real world problem (Flow-3D, 2011). Incorporating the presence of moving object, the modified equation for the free surface is:

$$\frac{\partial F}{\partial t} + \frac{1}{V_F}\left[\frac{\partial}{\partial x}(FA_x u) + \frac{\partial}{\partial y}(FA_y v) + \frac{\partial}{\partial z}(FA_z w)\right] = -\frac{F}{V_F}\frac{\partial V_F}{\partial t} \tag{4.27}$$

where, F represents the volume fraction of liquid occupied by the fluid ($= V_{\text{liquid fraction}}/V_{\text{cell}}$). The value of F ranges from 0 to one. Cells having a value of one are completely filled with liquid and cells with a value of 0 are voids. Voids are regions without liquid that have uniform pressure assigned to them and represent regions filled with air having insignificant density relative to the fluid density. Therefore, the governing equations for air is not included in the calculation. The term on the right hand side of the Eq. 4.27 is calculated by using Eq. 4.2.

4.5 Near-wall treatment and roughness modelling

Wall surfaces are represented by a no-slip condition meaning that there is no relative motion between the fluid and the wall at the interface. Modelling of the flow near wall possess difficulty due to the requirement of fine cells close to the walls to adequately resolve the viscous sub-layer and turbulent boundary layer. The most common approach to account for the near wall effects while avoiding the necessity of fine cells near boundary is by adopting the wall functions. Wall functions are designed to be used with coarse near-wall grids. The wall function approach assumes that for all flows, the near wall velocity profile obeys the law of the wall (Kalitzin et al., 2005; Sotiropoulos, 2005). The law of the wall divides the boundary layer into three layers:

$$\frac{u}{u_*} = \begin{cases} y^+ & \text{for } y^+ < 5 \quad \text{viscous sublayer} \\ y^+ - e^{-\kappa B}\left\{e^{-\kappa U^+} - 1 - \kappa U^+ - \frac{(\kappa U^+)^2}{2} - \frac{(\kappa U^+)^3}{2}\right\} & \text{for } 5 < y^+ < 30 \quad \text{transition} \\ \frac{1}{\kappa}\ln(y^+) + B & \text{for } y^+ > 30 \quad \text{fully turbulent} \end{cases} \tag{4.28}$$

where, $y^+ = yu_*/\nu$ is the non-dimensional distance normal to the wall. $U^+ = u/u_*$, u is the mean flow velocity, u_* is the wall shear stress velocity, von Karman constant $\kappa = 0.418$ and $B = 5.45$. The first cell near the wall gets its velocity according to the logarithmic profile corresponding to the log-law region. The first cell close to the wall must be sized in such a way that it is located well within the fully turbulent region, typically $30 < y^+ > 500$ (Lane et al., 2002; Versteeg and Malalasekera, 2007). Boundary conditions are applied at this first layer away from the wall by assuming that the mean velocity field is logarithmic. Boundary conditions for k and ε are obtained by assuming equilibrium between turbulence production and energy dissipation. This assumption results in following boundary conditions (Sotiropoulos, 2005; Souders and Hirt, 2002):

$$\frac{u}{u_*} = \frac{1}{\kappa}\ln(y^+ + B); \quad k = \frac{{u_*}^2}{\sqrt{C_\mu}}; \quad \varepsilon = \frac{{u_*}^3}{\kappa y} \tag{4.29}$$

These boundary conditions are valid for smooth wall and need to be modified for a rough wall. In Flow-3D, rough wall boundary condition is incorporated by combining the smooth and rough wall expressions for the near-wall logarithmic velocity profiles by introducing a modified viscosity at the boundary that reflects the enhanced momentum exchange due to the roughness (Eq. 4.30). Local shear stress close to the boundaries is calculated from this modified velocity profile. The value of k and ε is then calculated using shear stress velocity. Wall shear stresses obtained from the logarithmic velocity profile are also included in the momentum equations for the mean flow velocity (Souders and Hirt, 2002).

$$\frac{u}{u_*} = \frac{1}{\kappa}\ln\left(\frac{\rho u_* y}{\mu + \rho a u_* k_s}\right) + 5.0 \tag{4.30}$$

Above equation is iterated to solve for the shear velocity u_*, where $a = 0.246$ and k_s is the roughness height. The term $\rho a u_* k_s$ represents an effective viscosity due to the effect of the rough boundary. In the above equation, when roughness is 0, only molecular viscosity is acting and the profile becomes valid for smooth wall. If the roughness value becomes much larger than the molecular viscosity the logarithmic profile reduces to the widely accepted expression for rough wall:

$$\frac{u}{u_*} = \frac{1}{\kappa}\ln\left(\frac{y}{k_s}\right) + 8.5 \tag{4.31}$$

For a surface with uniform roughness, the relationship given by Chow (1959) between Manning's n value and the roughness height k_s is used to calculate the value of k_s for the corresponding value of n (Eq. 4.32). In this equation hydraulic radius R_h and roughness height k_s are in feet. This value of k_s is input into the component property to represent the surface roughness of the component:

$$\log\frac{R_h}{k_s} = \frac{0.046}{n}R_h^{\frac{1}{6}} - 1.088 \tag{4.32}$$

4.6 Equations of rigid body motion

The motion of the wheel is solved by using the equations of rotational motion. The fixed-axis rotational motion of the wheel is a planar motion with one degree of freedom. Angular velocity and thus torque of a rotating body has only one non-zero component in the axis of rotation and can be calculated by solving:

$$\sum \tau = I\alpha \tag{4.33}$$

where, τ is the total torque, I is the moment of inertia and $\alpha(= d\omega/dt)$ is the angular acceleration about the rotation axis in the body system. For any point on the rigid body, its motion is 1-D rotation about the fixed axis and is calculated by:

$$V = \omega r \tag{4.34}$$

where, ω is the angular velocity, r is the distance of any point on the rigid body from the axis of rotation. The axis of rotation, which in this case is y, must be parallel to the y-axis of the space coordinate system. The body system is set up with y-axis coinciding with the rotation axis and the x and z axes are parallel to those of the space system. x and z coordinates of the body system origin are thus the same as those of the rotation axis, and the y coordinate is set equal to 0.

4.7 Numerical approximations

To transform the continuous description of the governing equations into a discrete numerical approximations, the flow domain is divided into a mesh of fixed rectangular cells forming finite number of control volumes around each dependent variable location. Velocities and pressures are located at staggered locations within the cell. As such, velocities (u, v, w) and fractional areas (A_x, A_y, A_z) are placed at the centres of cell-faces normal to the corresponding direction and pressures (p), fluid fractions (F), fractional volumes (V_F), density (ρ), viscosity (μ) and other dependent variables are located at the cell centres.

Most of the terms in the governing equations are calculated explicitly i.e., using the current time-step values of the local variables with an exception to the pressure forces. Pressures and velocities are coupled implicitly in order to maintain the incompressibility of the fluid and stability of the solution by using time-advanced pressures in the momentum equations and time-advanced velocities in the mass continuity equation. As described by Flow-3D (2011), the procedure for advancing a solution through one increment in time follows three basic steps:

- Explicit approximations of the momentum equations are used to compute the first guess for new time-level velocities using the initial conditions or previous time-level values for all advective, pressure, and other accelerations.
- When the implicit option is used the pressures are iteratively adjusted in each cell and the velocity changes induced by each pressure change are added to the velocities computed in the first step to satisfy the mass continuity equation. An iteration is required here because the change in pressure in one cell will affect the six adjacent cells.
- Final step is to update the free surface and turbulent quantities by using the VOF method to give the new fluid configuration.

These steps are repeated through desired time interval or until the user prescribed steady state conditions are met. Suitable boundary conditions must be imposed at all mesh, obstacles, and free surfaces at each time step.

4.8 Numerical stability

The maximum stable time step Δt for the simulation is dynamically computed based on the stability criteria. Following stability criteria are met while choosing the time steps:

- The first criterion is that fluid must not be permitted to flow across more than one computational cell in one time step. This advective transport is known as the Courant-Friedrichs-Lewy (CFL) condition and depends not only on the velocity but also on the fractional area/volume open to the flow (Eq. 4.35). This stability limit also ensures that the moving object does not move more than one computational cell in a single time step for accuracy and stability of the solution. Therefore, the speed of the moving objects during computation also limits the time step.

$$\Delta t < c \cdot \min\left(\frac{V_F \delta x_i}{A_x u}, \frac{V_F \delta y_j}{A_y v}, \frac{V_F \delta z_k}{A_z w}\right) \tag{4.35}$$

  where, u, v, w are velocity magnitudes, A is the fractional area open to flow. $\delta x, \delta y, \delta z$ are the cell size in corresponding directions. The quantity c is referred to as the flow Courant number. It should be less than one for accurate results and for numerical stability when using explicit computational methods. The default value for c in Flow-3D is 0.45.

- The presence of free-surfaces introduces another type of stability condition associated with the propagation of surface waves. In this case as well the surface waves should not propagate more than one cell in one time step. This time step limiting condition is given by:

$$\Delta t < 0.5 \frac{\min\left\{\delta x_i, \delta y_j\right\}}{\sqrt{\delta z_k \cdot \mathrm{ACCZ}}} \tag{4.36}$$

  where, ACCZ is the normal acceleration where z direction is normal to the free surface. Similar limits must be applied in the x and y directions as well for each cell containing a free-surface.

- A non-zero value of dynamic viscosity means that the time step is further limited by the condition given by Eq. 4.37 so that no quantity should diffuse more than approximately one cell in one time step.

$$\Delta t = \frac{0.25}{\max\left[\mathrm{RM} \cdot \frac{\mu}{\rho}\left(\frac{1}{\mathrm{DXS}} + \frac{1}{\delta y_j{}^2} + \frac{1}{\delta z_k{}^2}\right)\right]} \tag{4.37}$$

where, DXS $= \delta x_i^2(1 - 0.334 \cdot \text{CYL})$. RM is the maximum multiplier used on μ for all types of diffusion processes including turbulent, fluid fraction, density, and turbulent energy diffusion.

- Another stability limit which controls the relative amounts of donor-cell and centred differencing used for the momentum advection terms is introduced by:

$$\Delta t \cdot \max\left(\frac{|u|}{\delta x_i}, \frac{|v|}{\delta y_j}, \frac{|w|}{\delta z_k}\right) < \alpha \leq 1.0 \tag{4.38}$$

In the above condition if $\alpha = 1$ is used, the above three stability considerations are sufficient. In no case should α be more than 1.

4.9 Dethridge wheel CFD model development

A 3D CAD model is prepared using Autodesk Inventor® 2014 from Autodesk, Inc and imported as stereo-lithography (STL) files to be read and interpreted by Flow-3D. The wheel, shroud and flume are imported as separate files after checking and fixing them for errors using miniMagics[1], Pyadmesh and Netfabb[2]. The computational domain was then defined by using the nested meshing. Keeping the available computational resources and time into consideration, only the symmetrical half of the model is simulated. The 3D model and the computational domain is shown in Fig. 4.1 and 4.2

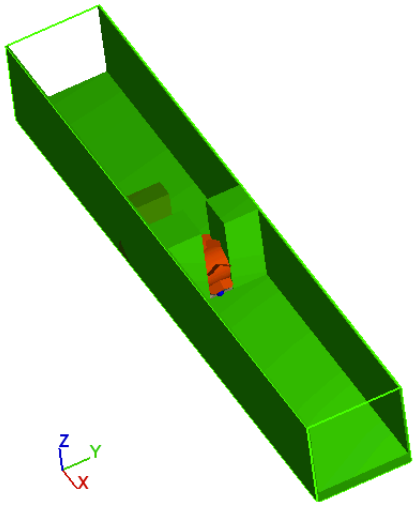

Figure 4.1: 3D Model

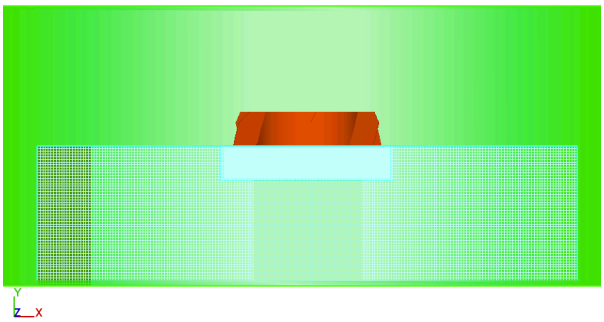

Figure 4.2: Computational Domain

The resolution of the geometry was visualized iteratively using the FAVORize tool in Flow-3D until a good resolution of the geometry was achieved. The 3D view of the computational domain and the FAVORized view of the domain is shown in Figures 4.3 and 4.4 respectively. In this case, the 2 mm thick wheel blades, the complex geometry of the wheel and shroud combined with the nature of orthogonal meshing meant that very small cell sizes were required to resolve the complex geometry. The 2 mm blade thickness thus imposed a modelling challenge with a requirement of very fine meshing

[1] Tools available within Flow-3D
[2] Netfabb basic is freely available at: http://www.netfabb.de

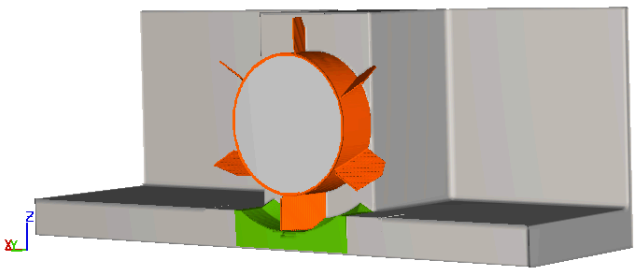

Figure 4.3: 3D view of computational domain

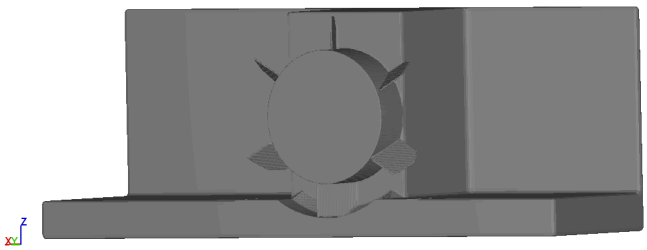

Figure 4.4: FAVORized view

and consequently resulting in significantly longer simulation time i.e., months to finish a single simulation, overtopping the computational resources available for this research. Therefore, the blades in the CAD model were thickened to 4 mm to achieve a required resolution. The uncertainty associated with this change in blade thickness is presented in section 4.10. Ultimately, three nested mesh blocks of cell size 10 mm, 5 mm and 2.5 mm as shown in Fig. 4.5 are used to embed the geometry into the computational domain. The details of the mesh used in this study is shown in Table 4.1. The origin $(0,0,0)$ is the center of the wheel. The nested meshing on the symmetrical half of the geometry allowed the area around the wheel to be refined and thereby reduced the computational effort to a great extent. The resolved geometry of the modified 4 mm blades is shown in Fig. 4.6. The half of the v-shaped air vent at the apex of the blade and the chamfered corner of the half blade are adequately resolved on this image.

The next step was to specify the boundary and initial conditions to correctly define the physical processes. Volume flow rate was prescribed as inflow by creating a bottom inlet. At the downstream, pressure boundary condition with a stagnation pressure condition and prescribed fluid elevation was defined. The sides of the domain and top boundary were defined as symmetry boundaries as fluid is not in contact at these boundaries. The fluid is in contact with the solid geometry of the model. A no-slip boundary condition was prescribed at all solid surfaces. The law of the wall de-

Table 4.1: Mesh details

Block	Cell size (mm)	No. of cells	Extents (m)	
1	10	208000	$x_{min} = -1.00$ $y_{min} = -0.52$ $z_{min} = -0.36$	$x_{max} = 1.00$ $y_{max} = 0.00$ $z_{max} = 0.31$
2	5	201600	$x_{min} = -0.32$ $y_{min} = -0.13$ $z_{min} = -0.31$	$x_{max} = 0.32$ $y_{max} = 0.00$ $z_{max} = 0.31$
3	2.5	991440	$x_{min} = -0.31$ $y_{min} = -0.125$ $z_{min} = -0.30$	$x_{max} = 0.31$ $y_{max} = 0.00$ $z_{max} = 0.30$

scribed in section 4.5 was used to define the shear stress and the y^+ criteria was met in all cases viz. ($30 < y+ < 500$). Surface roughness for the flume and the wheel were calculated based on the Manning's n value presented in Table 4.2 and Eq. 4.32 for the given hydraulic radius. Uniform pressure distribution and fluid initialization with fluid elevation were used as initial conditions for the model. The fluid was defined as water at 20°C with a density of 1000 kg/m^3 and a dynamic viscosity of 0.001 N $-$ s/m^2.

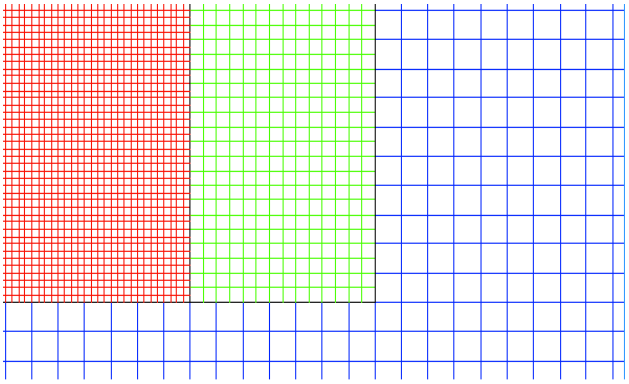

Figure 4.5: Nested meshing

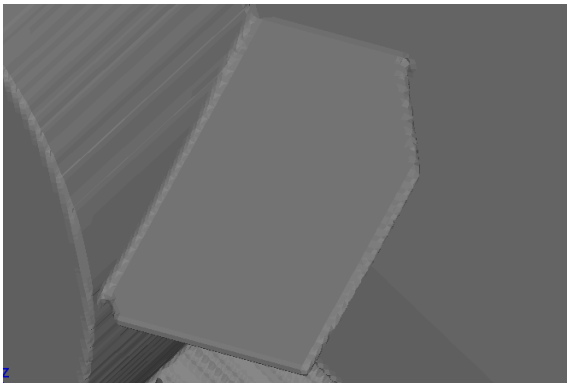

Figure 4.6: FAVORized blade (4 mm thickness)

Additional models used in this study are the gravity, viscosity and turbulence model, and the General Moving Object (GMO) Model. The gravity model was activated with a gravitational acceleration of 9.81 m/s^2 acting in the negative z-direction. The RNG turbulence model was used for modelling the turbulence with the dynamically computed maximum turbulent mixing length option and no-slip wall shear boundary condition. The choice of the RNG model is done based on the fact that it provides improved predictions of near wall flows, separated flows as well as flows in curved geometries (Biswas, 2002, pp.358). It was difficult to estimate the location and magnitude of the maximum turbulent mixing length. Therefore, the option dynamically computed is chosen to calculate the maximum turbulent mixing length (TLEN) which is automatically computed as a function of time and space (Eqs. 4.22–4.26). The value of the turbulent mixing length is automatically calculated as 7% of the smallest domain dimension (which is 0.52 m in this case). The wheel was categorised as moving object using the GMO model. Moving object motion can be a coupled or prescribed motion. Coupled motion was used to simulate the free wheel motion under no load condition whereas prescribed motion was used to calculate the speed and torque for the given flow rate and flow depths.

As discussed earlier, different numerical options are available in Flow-3D to solve the governing equations. In this study, default numerical settings were used unless a change was required. The time step

Table 4.2: Manning's n values

Component	Surface	Manning's n		
		Minimum	Normal	Maximum
Flume bed	Cement	0.010	0.011	0.013
Flume side walls	Glass	0.009	0.010	0.013
Wheel hub	PVC	0.009	0.010	0.011
Wheel blades	Steel	0.011	0.012	0.014

for the simulation was computed dynamically based on the numerical stability criteria described in section 4.8. For incompressible flow, only an implicit solver option is available for the pressure solver. The Generalized Minimal Residual Method (GMRES) is the default solver option for the pressure. The GMRES solver is a highly accurate and efficient method for a wide range of problems (Brethour, 2009). It possesses good convergence, symmetry and speed properties and handles complex geometries well (Flow-3D, 2011). GMRES method was used as it is best suited to solve the complex flow field involved in this research. The density of the moving object is much smaller than the fluid density, so for coupling the moving object and fluid, an implicit scheme was used. The VOF-advection is modelled as one fluid with free surface since the influence of air on the free surface is neglected. For momentum advection, a first-order scheme was used. The first-order scheme showed better results and performed significantly faster than higher order schemes (for details see section 4.10.2). A 64 bit 12 processors Intel (R) core I7 3.2 GHZ, with 16GB RAM was used for simulations.

4.10 Uncertainty analysis of CFD model

Uncertainty of a CFD model is an estimation of error involved in the simulation results. Freitas (2002) describes uncertainty as the estimated amount or percentage by which an observed or calculated value may differ from the true value. Roache et al. (1986) discussed the importance of assessing the uncertainty of the numerical simulation. A systematic CFD uncertainty evaluation process described in Roache (1994, 1997, 1998) is adopted in this study which is recommended and adopted in several journal's editorial policy for systematic and uniform reporting of CFD results.

Sources of errors and uncertainties in CFD can be divided into three distinct sources: input, model and numerical uncertainty (Freitas, 2002). Input uncertainty results from the values input by the user to model the physical processes. It might be eliminated or made a second-order effect through improved definition of the input parameters (Freitas, 2002). In this study, input uncertainties were sourced from measured parameters such as flow depths, speed of the wheel, flow rate and torque from the physical model. The uncertainties associated with these parameters are discussed in chapter 3. Numerical and model uncertainties are discussed in detail in the following sections.

4.10.1 Quantification of numerical uncertainty

Numerical uncertainty is due to the errors involved in numerical modelling of Navier-Stokes equations and includes the influence of discretization, round-off and iterative convergence errors (Chen et al., 2002; Freitas, 2002; Roy, 2005; Eça and Hoekstra, 2009, 2014). Numerical uncertainty can not be eliminated but can be minimized or bounded in the simulation. It is therefore vital to minimize and quantify the numerical uncertainty (Freitas, 2002; Roy, 2005; Eça and Hoekstra, 2009). Systematic grid refinement studies are the most common approach used in assessing numerical uncertainties of a simulation (Roache, 1994, 1997; Roy and Blottner, 2006). The procedure of solution verification through quantification of numerical uncertainty is discussed below.

Before assessing the numerical uncertainties, an initial assessment of overall convergence in the calculations was performed by studying the time history development of the main variables (Fig. 4.7).

The finish time of 30 s was enough for most of the simulations to reach the convergence. The variation of the quantities has shown a reducing oscillations until reaching a statistically stationary value, with some very small and regular variations about the mean value. The data are analysed using Matlab® curve fitting tool and outliers are excluded while taking the mean value. The average value of these variables was taken from the converged solution between 20 s to 30 s of the simulation time. Using these mean values of main variables from converged solution for each grid, the numerical uncertainties of computational results are quantified by using the Grid Convergence Index (GCI) methodology advocated by Roache (1994, 1997, 1998).

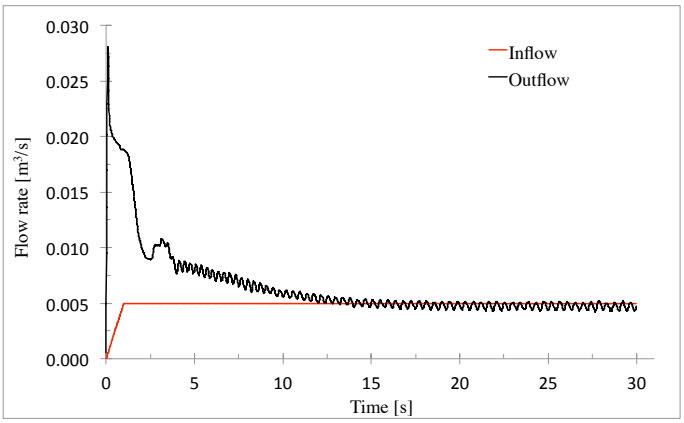

(a) Flow rates

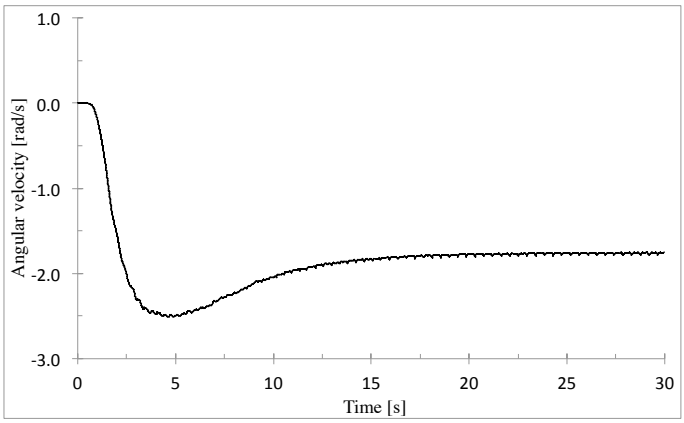

(b) Angular velocity of the wheel

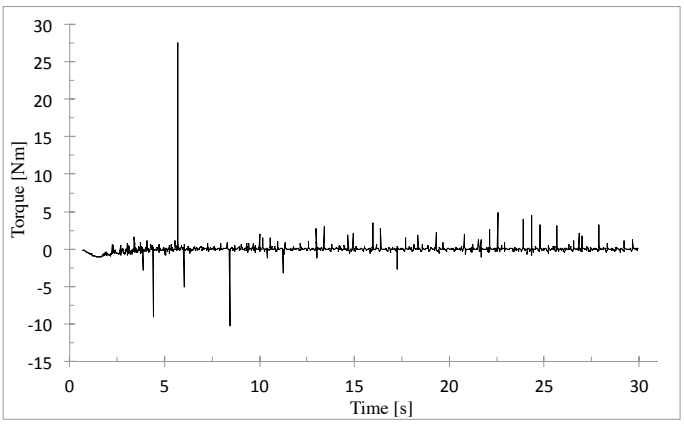

(c) Torque

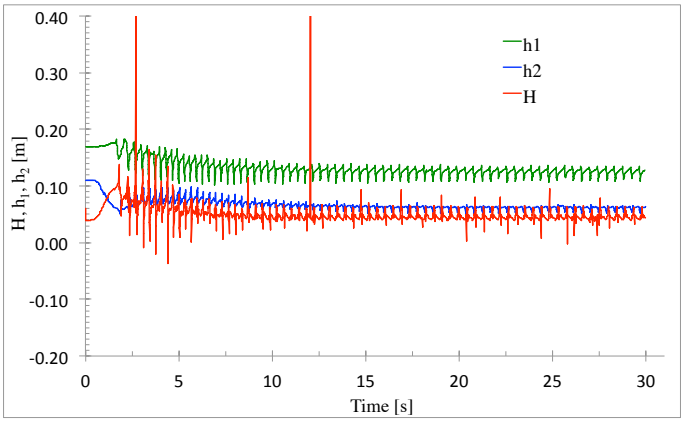

(d) Total head (H) and upstream and downstream flow depths (h_1, h_2)

Figure 4.7: Time history development of key variables for eight sharp BS0 blades wheel

The GCI is based on the generalized theory of Richardson extrapolation and involves the comparison of discrete solutions at different grid resolutions. It is a measure of a percentage the computed value is away from the value of the asymptotic numerical value. It indicates an error band on how far the solution is from unknown exact solution and consequently gives an indication of how much further grid refinement would change the numerical solution. A small value of GCI indicates that the computation is within the asymptotic range. To calculate the GCI in the present study, three grids of size fine (t_1), medium (t_2) and coarse (t_3) were used with a constant refinement ratio ($r = t_2/t_1 = t_3/t_2$) in the three coordinate directions. The y^+ criteria was met for all these grids by adding the fixed mesh

plane at the wall boundaries. The details of the grids used for the GCI study is shown in Table 4.3. The computational domain was resolved using three nested mesh blocks in each case. A constant refinement ratio $r = 1.25$ was used.

Table 4.3: Grid details and computation time for GCI study

Grid	Grid spacing (mm)	Total cells	Solver elapsed time
Coarse	$10 \times 5.0 \times 2.5$	1571103	09 days 21:25:44
Medium	$8.0 \times 4.0 \times 2.0$	3012260	19 days 13:27:10
Fine	$6.4 \times 3.2 \times 1.6$	5776613	41 days 14:21:23

The GCI measure for a key variable f over the fine and medium grid solution is given as:

$$\mathrm{GCI}_{12} = \frac{F_s}{r^p - 1}\left|\frac{f_2 - f_1}{f_1}\right| \times 100 \tag{4.39}$$

GCI for a medium and coarse grid numerical solution is:

$$\mathrm{GCI}_{23} = \frac{F_s}{r^p - 1}\left|\frac{f_3 - f_2}{f_2}\right| \times 100 \tag{4.40}$$

For constant grid refinement ratio r, the observed order of convergence p is:

$$p = \frac{\ln((f_3 - f_2)/(f_2 - f_1))}{\ln r} \tag{4.41}$$

For the asymptotic solution for the cell size t approaching 0, the Richardson extrapolation is generalized for any p-th order approximations and the mesh refinement ratio r as:

$$f_{t=0} \cong f_1 + \frac{f_1 - f_2}{r^p - 1} \tag{4.42}$$

where, f is a measure of a key variable with a subscript 1, 2 and 3 for the fine, medium and coarse grid solution respectively. F_s is a factor of safety which is empirically determined parameter which represents 95% confidence for the uncertainty estimate (Roache, 1994). Roache (1997) suggested $F_s = 3$ for comparison of two grids and 1.25 for comparison over three grids or more. Following Oberkampf and Roy (2010), a safety factor (F_s) of 1.25 is used.

The value of $\alpha = 1$ below gives an indication of a grid level yielding solutions in the asymptotic range of convergence:

$$\alpha = \frac{r^p \mathrm{GCI}_{12}}{\mathrm{GCI}_{23}} \tag{4.43}$$

The convergence conditions of the system is evaluated with the convergence ratio R:

$$R = \frac{f_1 - f_2}{f_2 - f_3} \tag{4.44}$$

The possible convergence conditions are:

- If $0 < R > 1$ monotonic convergence
- If $R < 0$ oscillatory convergence
- if $R > 1$ divergence

The numerical output of the key variables for three different grids described in Table 4.3 are compared in Fig. 4.8. Converged solution is achieved at the simulation time of around 15 s in all cases. The average value of the variables from each of these solutions on the fine, medium and coarse grids are used in the grid convergence study in the following paragraph.

Table 4.4 shows the results of the grid convergence study. Using the mean value of variables on coarse, medium and fine grids, observed order of convergence, asymptotic solution and the global GCI values for the main variables namely angular velocity ($\omega = 2\pi N$), torque (τ), total head (H), flow depths (h_1& h_2) and flow rate (Q) are calculated. The analysis shows that the results are in the asymptotic range because the obtained values for α are close to unity. Flow rate, upstream and downstream flow depths show oscillatory convergence with negative R values while the convergence of angular velocity, torque and total head is monotonic as the ratio R is between 0 and one. There is a reduction in the GCI value for the successive grid refinements (i.e. $\mathrm{GCI}_{12} < \mathrm{GCI}_{23}$) which indicates that the dependency of the numerical results on the cell size has been reduced and a grid independent solution has been achieved. The asymptotic values provide the best approximation and the GCI values give an error bound. Further refinement of the grid will not result in significant change of the values.

Table 4.4: Results of the grid convergence study

Variables	Coarse (f_3)	Medium (f_2)	Fine (f_1)	p (Eq. 4.41)	$f_{t=0}$ (Eq. 4.42)	GCI_{12}% (Eq. 4.39)	GCI_{23}% (Eq. 4.40)	α (Eq. 4.43)	R (Eq. 4.44)
Ang. vel. (ω, rad/s)	1.767	1.761	1.757	1.82	1.749	0.57	0.85	1.00	0.67
Torque (τ, Nm)	0.043	0.040	0.039	4.11	0.038	2.14	5.21	1.03	0.4
Flow rate (Q, l/s)	4.74	4.92	4.77	0.82	0.004	19.65	22.87	1.03	−0.83
U/S depth (h_1, cm)	12.51	12.42	12.44	6.74	0.124	0.06	0.26	1.00	−0.22
D/S depth (h_2, cm)	6.11	6.05	6.07	4.92	0.061	0.21	0.62	1.00	−0.33
Total head (H, cm)	4.61	4.92	4.99	7.36	0.050	0.36	1.89	0.99	0.19

Principally, the above grid convergence study must be repeated for any other simulation with changing geometry and boundary conditions. However, looking at the computational time required (see

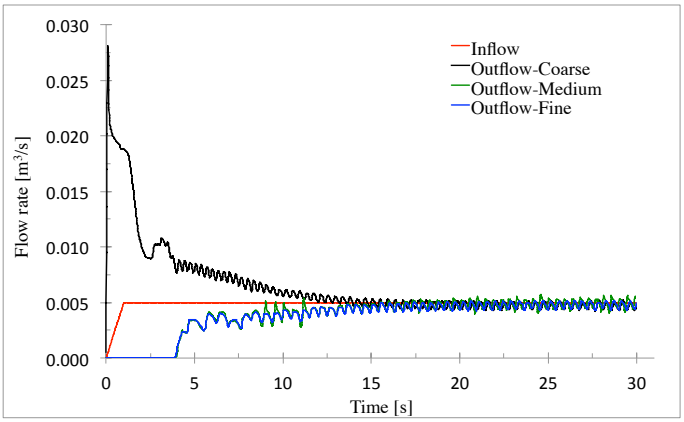

(a) Flow rates

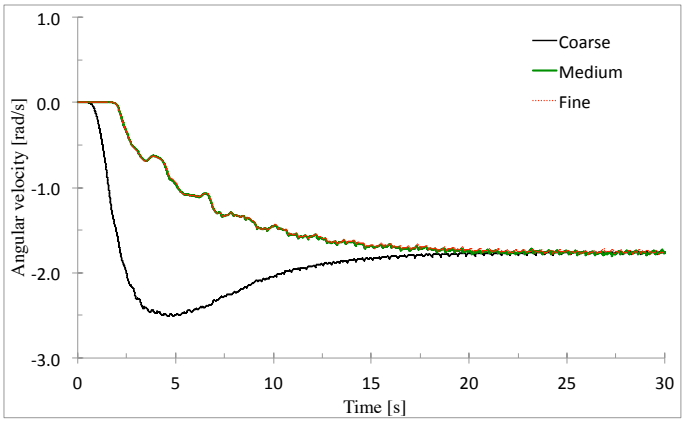

(b) Angular velocity of the wheel

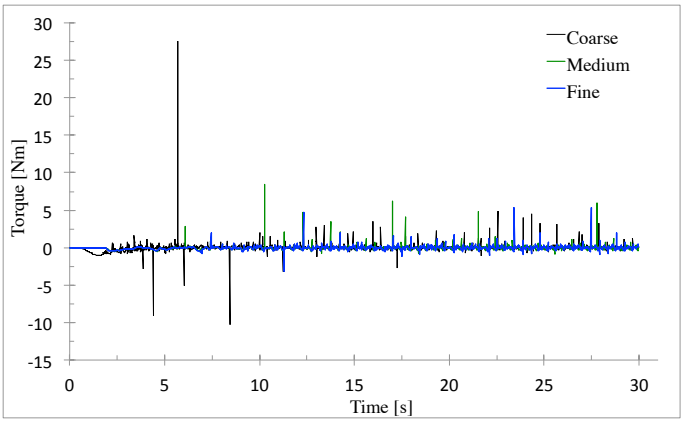

(c) Torque

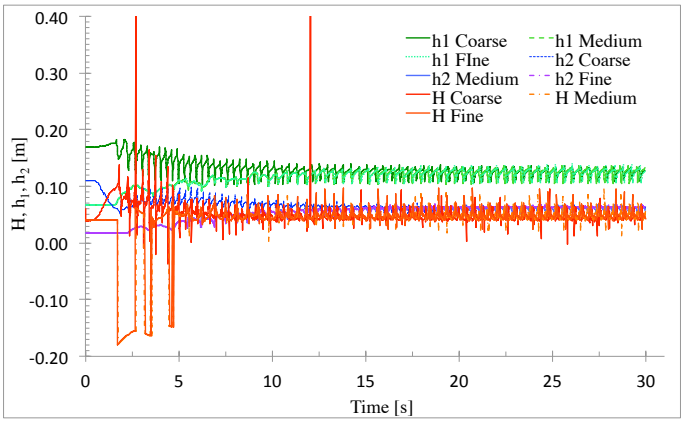

(d) Total head and flow depths

Figure 4.8: Model output for different grid sizes used for GCI study

Table 4.3) for these simulations, it was not possible to accomplish this study for each of the simulations within the research time frame. The above presented results thus provided a quantitative measure of the numerical uncertainty and gave guidelines for analysing any discrepancy between measured and computed results. Therefore, the nested mesh block with 10 mm, 5.0 mm and 2.5 mm was considered appropriate for the purpose of this research and was used for the rest of the simulations in this study.

4.10.2 Quantification of model uncertainty

Model uncertainty is associated with the approximations in the mathematical formulation of the physical problem (Roache, 1997; Stern et al., 1999; Freitas, 2002). Even though, computer codes use the same formulation for a given model with similar discretization schemes, each code implements these models differently which produces differences in the results (Freitas, 2002). Model uncertainty can be minimized, or potentially eliminated by the use of an enhanced or improved model. In the present study, current best practices in hydrodynamic modelling are followed in choosing the different available model options to solve the given problem. Some of the studies are essentially focused on the model validation and provide confidence on the choice of specific model for given application,

for eg. Souders and Hirt (2002); Wei (2005a,b, 2006); Isfahani and Brethour (2009); Brethour (2009); Hasan (2012). Following validation studies are deemed necessary in the present study:

Roughness: In open channel flow modelling, roughness height is commonly used as a calibration parameter to tune the model outputs to the measured data (Nicholas, 2001; Lane, 2005; Nicholas, 2005; Kim and Park, 2005; Morvan et al., 2008). As described in section 4.5, roughness in 3D modelling appears in the boundary condition rather than as a term in the governing equations. The impact of roughness value on the solution is therefore much more localised and limited (Morvan et al., 2008). However, Morvan et al. (2008) argue that even though in less significant way than in 1D and 2D models, roughness still serves as a calibration parameter in 3D models. But, even so, roughness alone can not compensate for errors in 3D models. Other effects have to be considered in addition to the roughness(Morvan et al., 2008).

Test simulation run with k_s values of 0 (hydraulically smooth), 0.8 and 3 mm based on Manning's n range given in Table 4.2 were accomplished. In Fig. 4.9, x-velocity profiles for different values of roughness are shown at randomly chosen sections on the upstream and downstream of the wheel. In the ordinate, the depth above the flume bed (z) is normalised by the total flow depth (h) and the abscissa is flow velocity in x-direction (u) normalised by the maximum velocity (u_{max}). On the upstream of the wheel (i.e. at $x = -0.715$ & -0.425 m; origin $(0,0,0)$ = center of the wheel), the difference in velocity profile is negligible. However, on the downstream of the wheel (at $x = 0.425$ & 0.465 m) there is noticeable difference in flow velocity with different roughness values between $z/h = 0.3$ to 0.6. However, this downstream flow velocity has no influence on the main variables of interest.

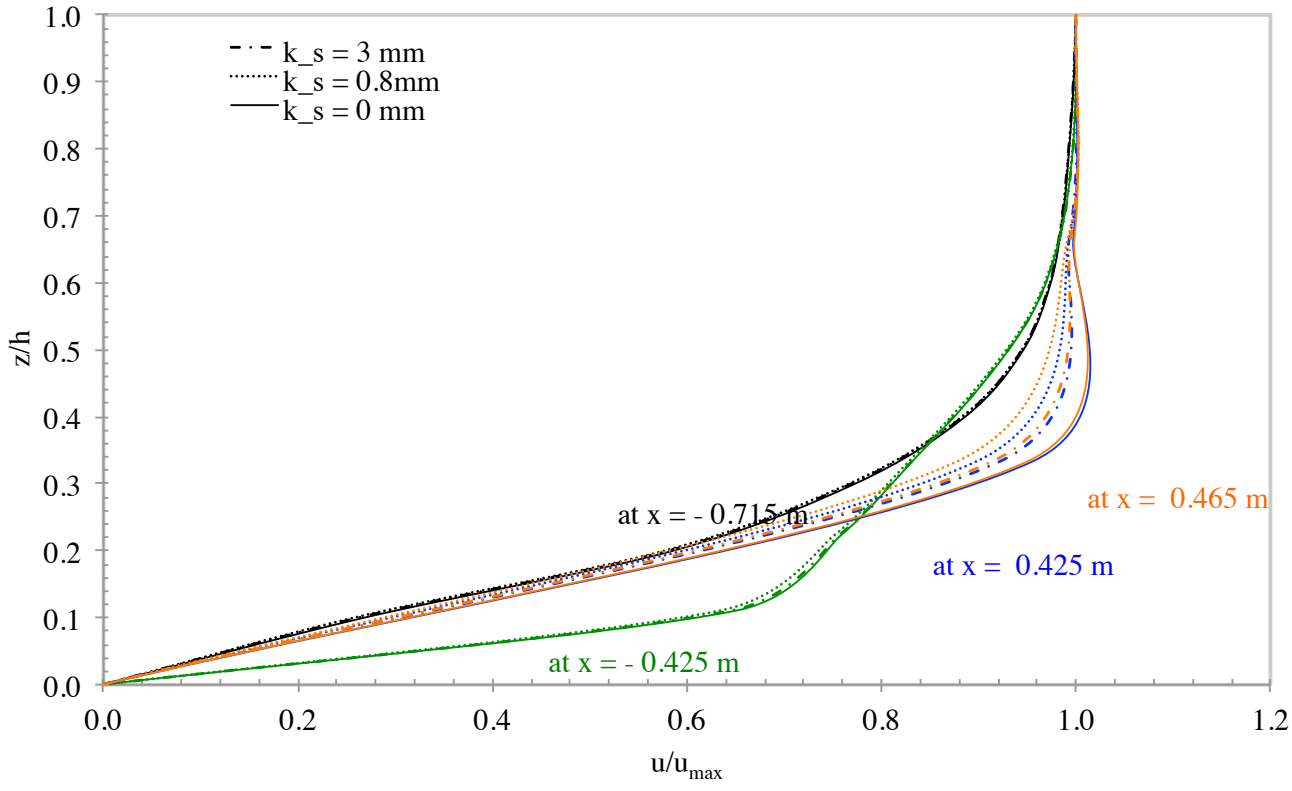

Figure 4.9: Velocity profiles for different roughness heights at different x, $y = 0.065$ m

The angular velocity, torque, total head, upstream and downstream flow depths, and the flow rates are compared in Fig. 4.10. As seen, there is a negligible difference on the key variables and the solution overlaps. A converged solution is achieved at about 15 s of simulation time in all cases. x-velocity contours and vectors for three different cases are also shown in Fig. 4.11. Based on these results, we can conclude that errors due to the surface roughness effect are insignificant. Hence, further model runs were accomplished with $k_s = 0$ mm.

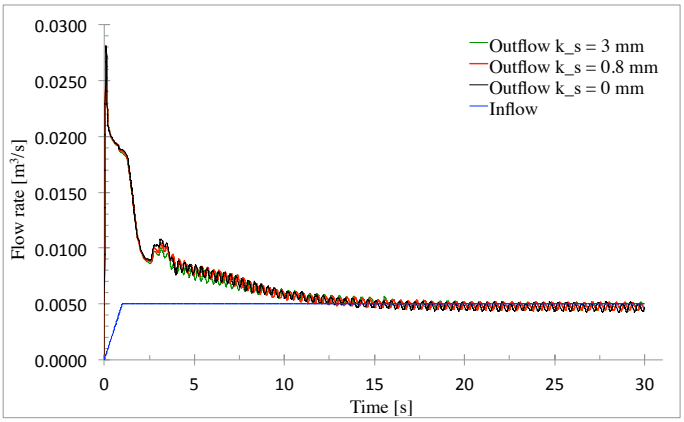

(a) Flow rates

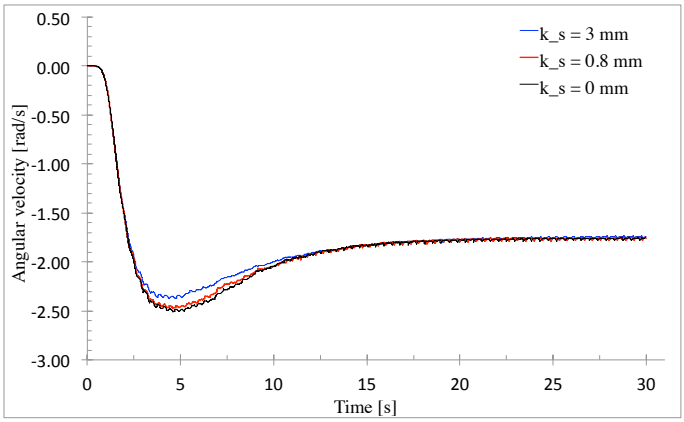

(b) Angular velocity of the wheel

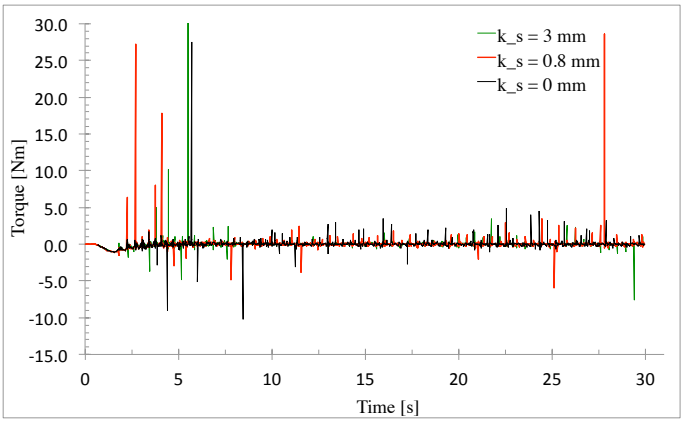

(c) Torque

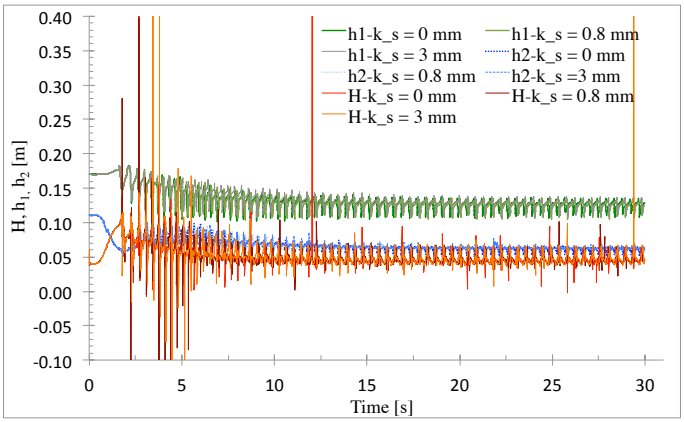

(d) Total head and flow depths

Figure 4.10: Model output for different k_s values

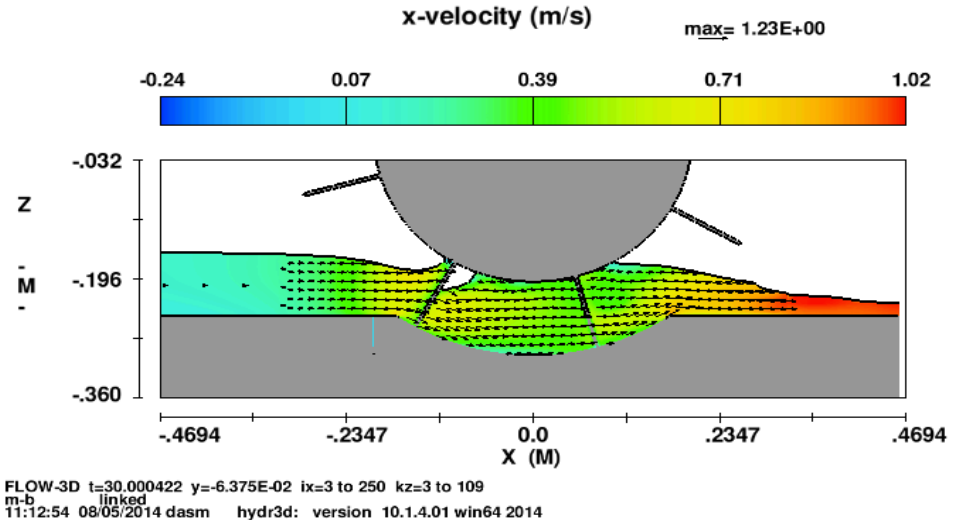

(a) $k_s = 0$ mm

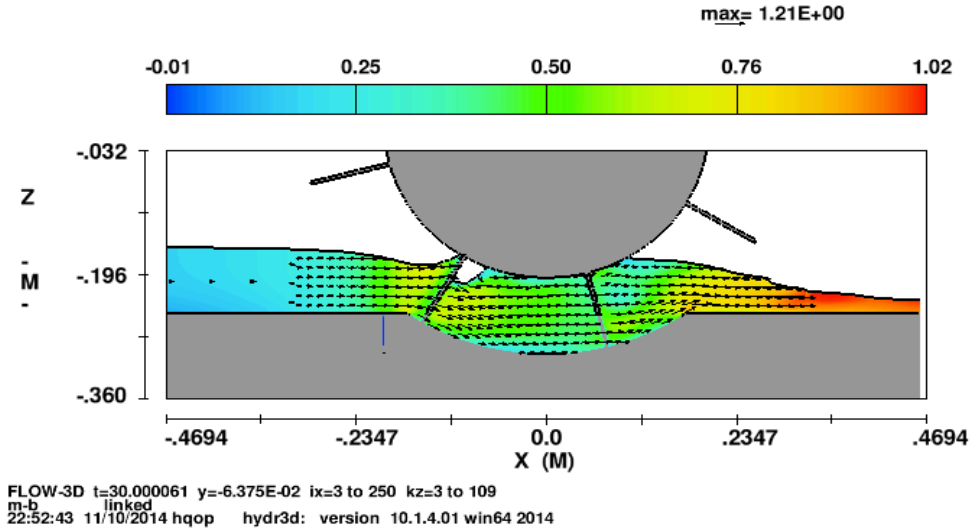

(b) $k_s = 0.8$ mm

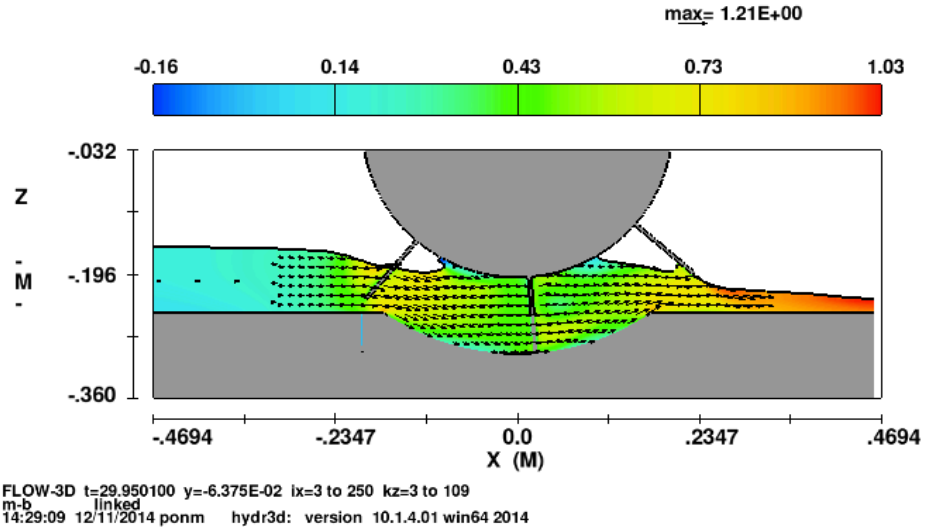

(c) $k_s = 3$ mm

Figure 4.11: x-velocity contour and vectors for different roughness values, at $t = 30$ s. Flow direction is from left to right.

Turbulence model: One of the models with highest uncertainty is the turbulence model (Roy and Blottner, 2006). This uncertainty was examined by running simulations with two different turbulent models: RNG $k-\varepsilon$ and standard $k-\varepsilon$ turbulent models. The dynamically computed turbulent length option was used for both RNG and standard $k-\varepsilon$ models. In Fig. 4.12 flow rates, torque, total head, flow depths and angular velocity is compared. These results clearly show that both turbulence models yielded quantitatively similar predictions. This suggests that the uncertainties owing to the turbulence models are small and can be ignored. The results presented in the remainder of this thesis were therefore produced using the RNG model.

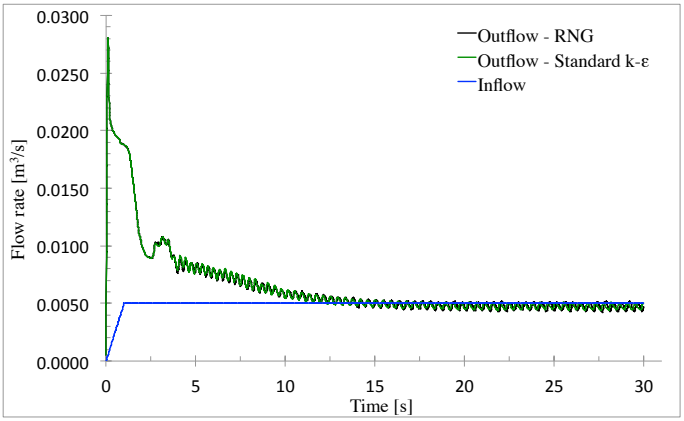

(a) Flow rates

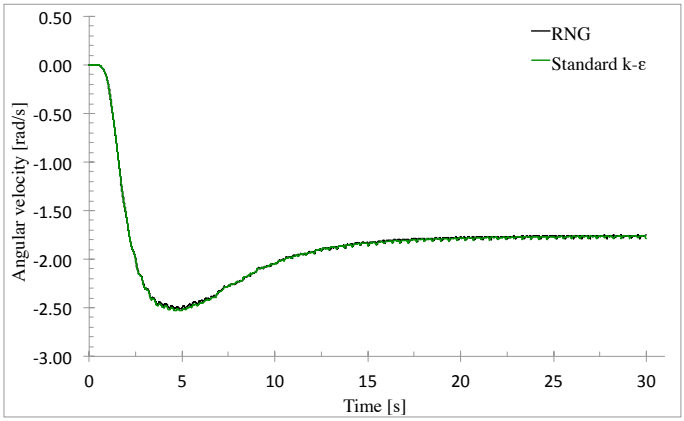

(b) Angular velocity of the wheel

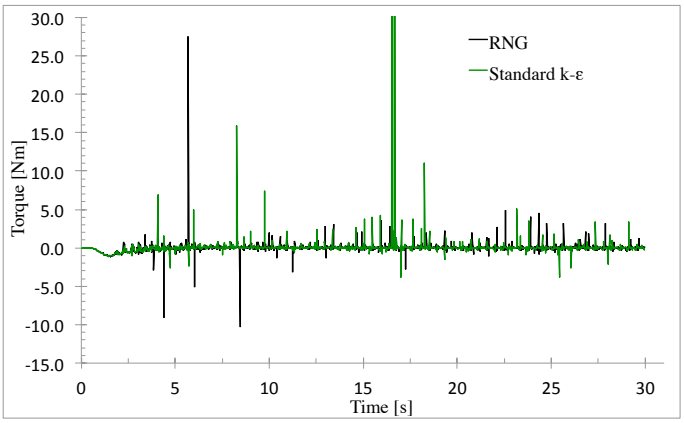

(c) Torque

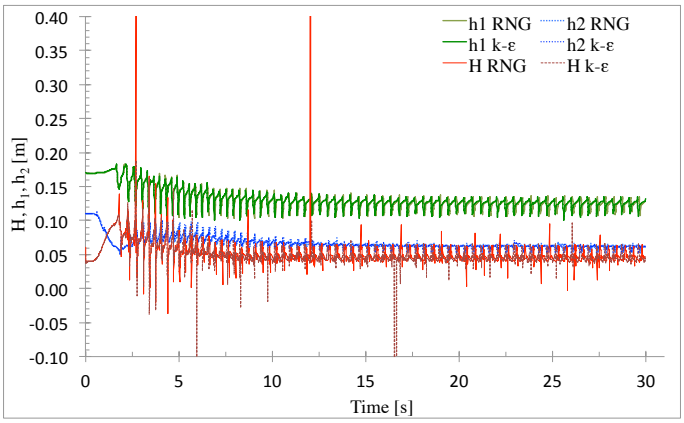

(d) Total head and flow depths

Figure 4.12: Model output for different turbulence models

Momentum advection scheme: Simulation with first order and second order monotonicity preserving momentum advection schemes were performed. Flow rate, torque, total head, upstream and downstream flow depths and angular velocity with different advection schemes are compared in Fig. 4.13. The statistically stationary solution is achieved at around 20 s of simulation time in both cases. First order scheme showed better results with a faster solution time. Therefore, for the rest of the simulations first order momentum advection was adopted.

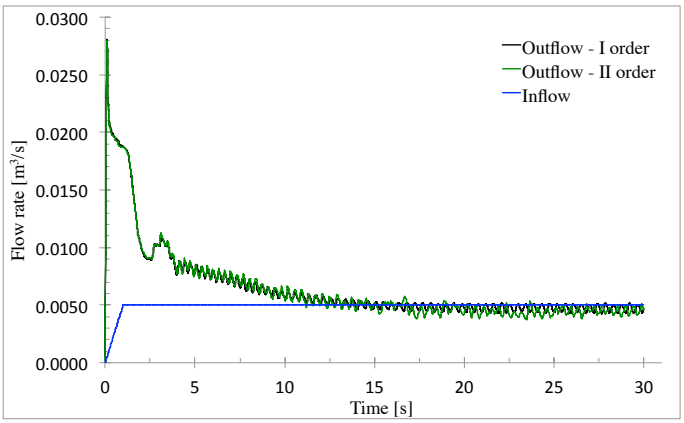

(a) Flow rates

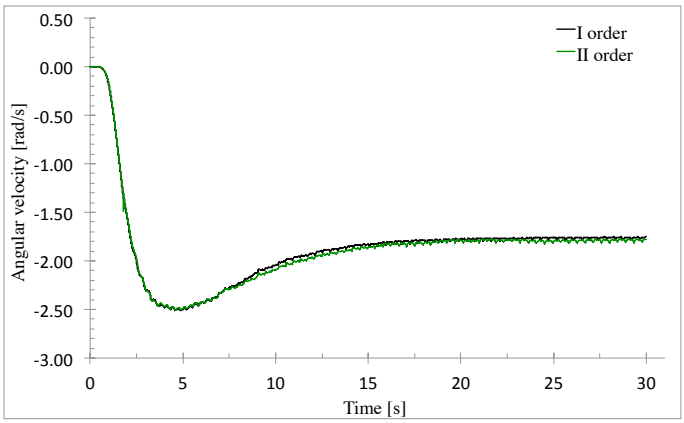

(b) Angular velocity of the wheel

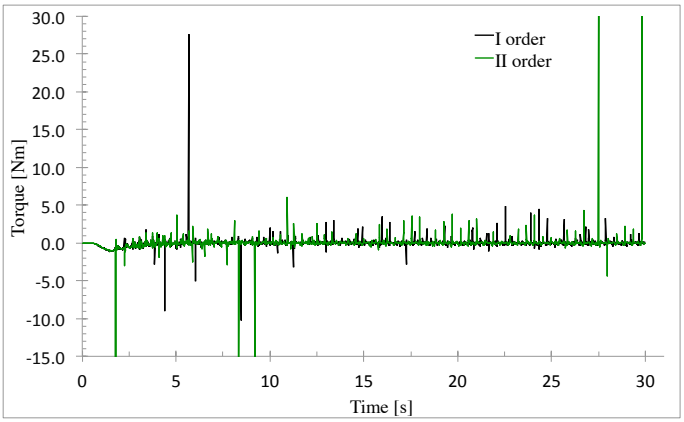

(c) Torque

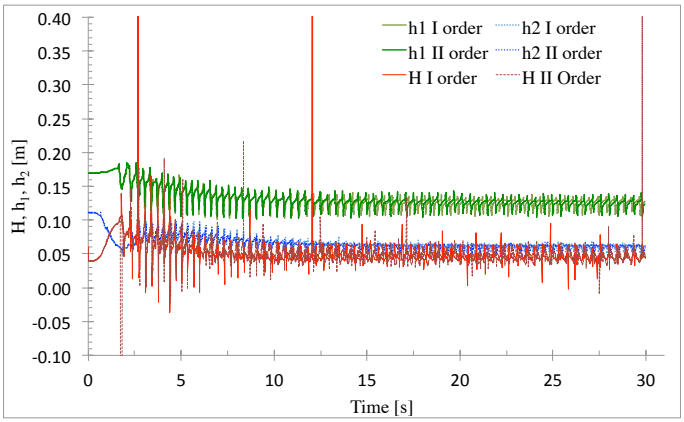

(d) Total head and flow depths

Figure 4.13: Model output for different advection schemes

Above discussed results with different roughness values, turbulence models and advection schemes are presented in Table 4.5 with their corresponding experimental values. The case used above in accessing these uncertainties is the free wheel (no-load) condition for which small amount of no-load torque is present in the physical model. In the numerical model results, torque is fluctuating around the 0 mean value with some unusual high peaks.

Table 4.5: Results from experiment and CFD for different models options

	Angular velocity (ω, rad/s)	Flow rate (Q, l/s)	Total head (H, cm)	Upstream depth (h_1, cm)	Downstream depth (h_2, cm)
Experiment	1.529	5.00	4.36	10.10	5.63
$k_s = 0$ mm	1.767	4.74	4.61	12.51	6.11
$k_s = 0.8$ mm	1.764	4.75	4.65	12.49	6.06
$k_s = 3$ mm	1.752	4.83	4.74	12.72	6.17
Advection I order	1.767	4.74	4.61	12.51	6.11
Advection II order mono.	1.791	4.47	5.08	12.49	5.99
RNG model	1.767	4.74	4.61	12.51	6.11
Standard $k-\varepsilon$	1.773	4.75	4.62	12.47	6.05

Error due to blade thickness: Another important validation question in this study is the increased thickness of the blades. As described earlier, due to the requirement of huge numbers of cells to resolve the 2 mm blade geometry and thus increased solution time, the blades in the numerical model are thickened to 4 mm. The uncertainty associated due to this change in the thickness of the blades is evaluated by simulating a single case of 2 mm thick blade profile using three nested blocks of finer mesh of 5.0 mm, 2.5 mm and 1.25 mm mesh.

Flow rate, torque, total head, flow depths and angular velocity is monitored for the case of 2 mm blades. These results are then compared with the performance of 4 mm blade in Fig. 4.14. The mean value of these parameters were obtained once a statistically stationary flow was observed and summarised in Table 4.6. As the mean value of the key variables show negligible amount of difference, it can be concluded that the effect of blade thickening has negligible effect on the model results and all further simulations refer to 4 mm blade thickness.

Table 4.6: Mean values of key variables for the 2 mm and 4 mm blade thickness

Variable	2 mm	4 mm
Flow rate (Q, l/s)	4.74	4.74
Ang. vel. (ω, rad/s)	1.751	1.767
U/S depth (h_1, cm)	12.41	12.51
D/S depth (h_2, cm)	6.03	6.11
Total head (H, cm)	4.89	4.61

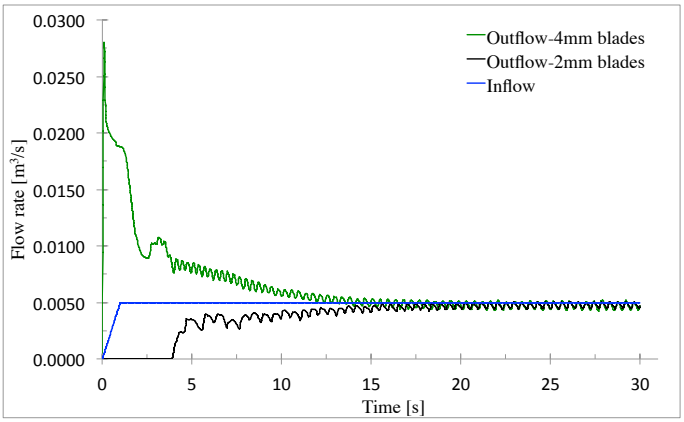

(a) Flow rates

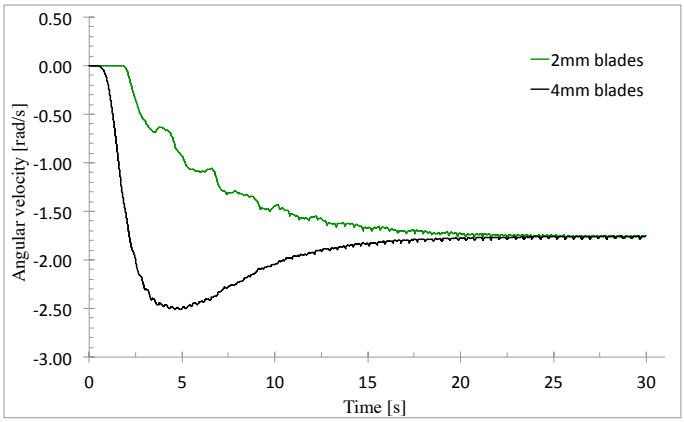

(b) Angular velocity of the wheel

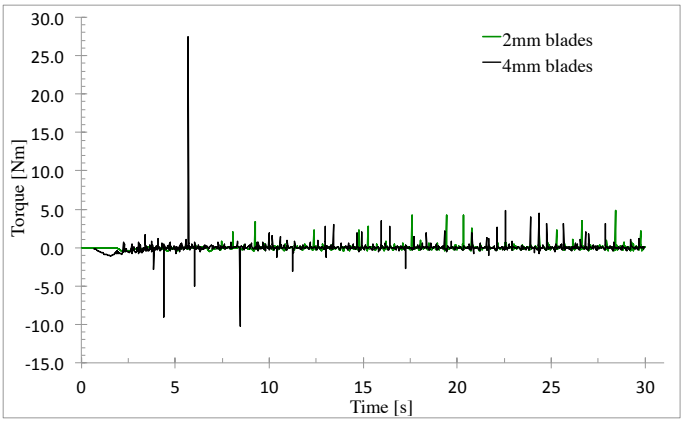

(c) Torque

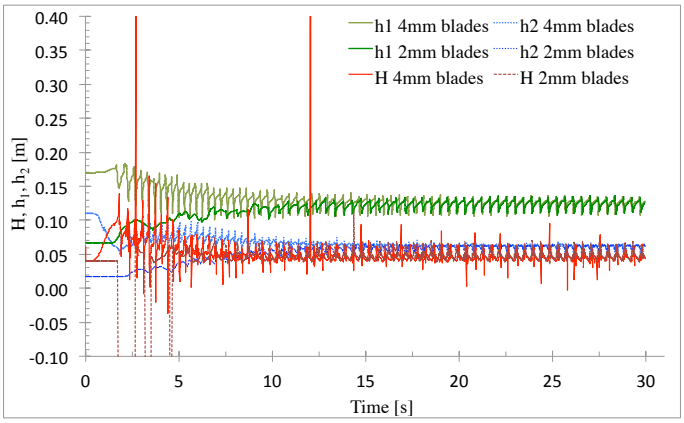

(d) Total head and flow depths

Figure 4.14: Model output comparison between model with 2 mm and 4 mm thick blades

Validation of the domain symmetry: As described earlier, to save the computational time only a symmetrical half of the model is simulated. The error due to this assumption of axisymmetric flow field is investigated by running a single simulation over the entire width of the flow domain. In Fig. 4.15, the time history development of key variables for the symmetrical half and full width flow fields are shown. Flow rates for the symmetrical half case is doubled for comparison with the full width case. As seen, both solutions overlap in case of all key variables and solution becomes statistically stationary after 20 s of simulation time. The mean values of all the key variables for both cases are taken from 20 to 30 s of simulation time and are compared in Table 4.7. Both cases produce apparently same results with negligible difference in mean values of the key parameters.

Table 4.7: Mean values of key variables for the half and full domain simulations

Variable	Half domain	Full domain
Flow rate (Q, l/s)	9.487	9.485
Ang. vel. (ω, rad/s)	1.767	1.768
U/S depth (h_1, cm)	12.51	12.55
D/S depth (h_2, cm)	6.11	6.13
Total head (H, cm)	4.61	4.59

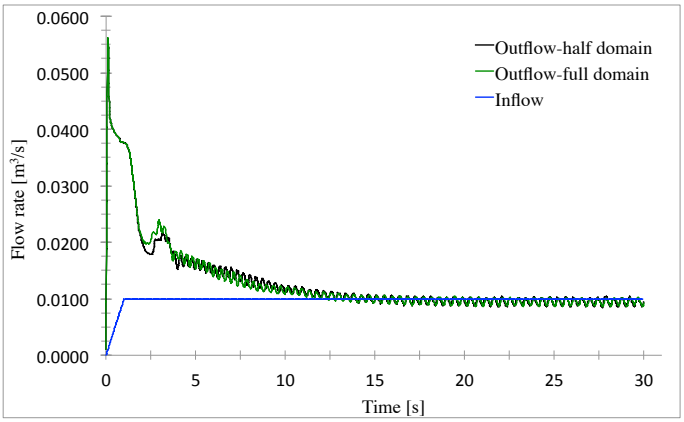

(a) Flow rates

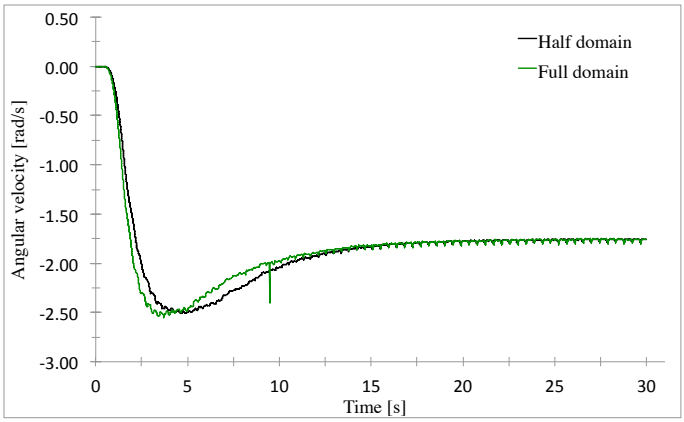

(b) Angular velocity of the wheel

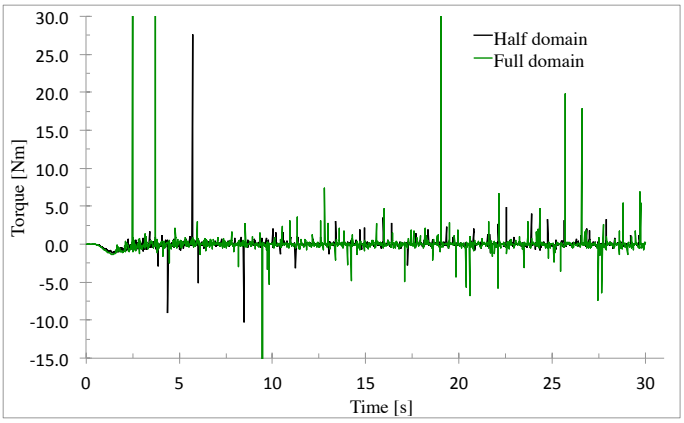

(c) Torque

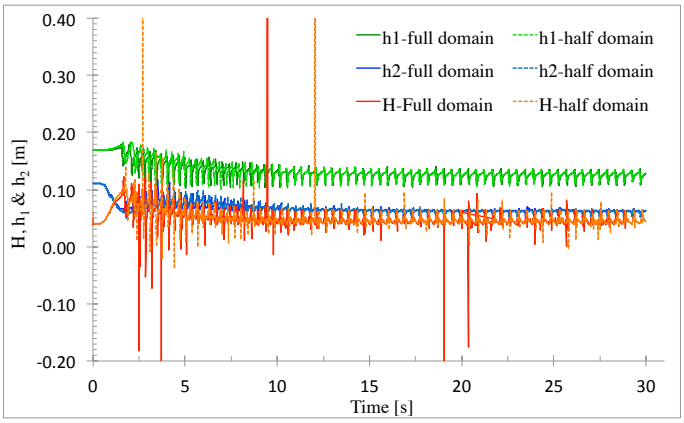

(d) Total head and flow depths

Figure 4.15: Model output of axisymmetric half domain and full domain simulation

The x-velocity profiles for both cases are shown in Fig. 4.16 at the simulation time of 30 s. The results show minimal difference in the velocity distribution with the difference in fraction of fluid at the immediate downstream of the wheel. However, the velocity distribution in both cases matches very well. As the output of the key variables doesn't differ between the half and full domain cases (see Table 4.7), model results demonstrate that they are not affected by the assumption of axisymmetric flow field and the results are validated. This validation provided confidence in using the symmetrical half computational domain and saved computational time to a great extent.

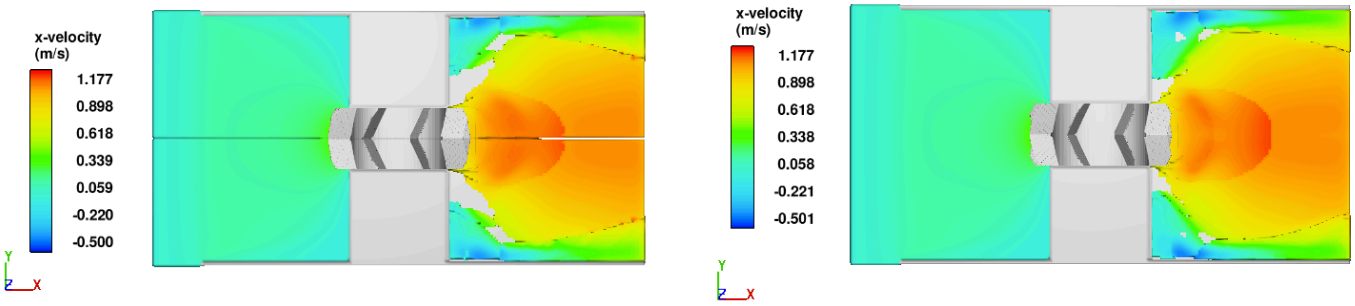

(a) Simulated and mirrored half domains

(b) Full domain

Figure 4.16: x-velocity profiles for half domain and full domain simulations, at $t = 30$ s. Flow is from left to right.

Chapter 5

Results and Analysis

In this chapter, the results from the physical model and numerical model are presented and discussed. Firstly, the results of the optimisation study from the physical model are presented, followed by the numerical model results of the wheel with eight sharp BS0 blades. The numerical model results of the wheel with BS0 blades are then compared with the physical model results. The numerical model performance of the wheel with new curved shape blades BS1 and shroud shape SS1 are then analysed. Detailed discussion and analysis of each optimisation steps are presented.

5.1 Physical model results

Physical model test results are presented in this section. It begins with the results of the wheel performance at different upstream and downstream water levels. These results provided the rational for fixing operating upstream and downstream water levels for further tests on the physical model. This is followed by the results and discussion on wheel housing, blade number, wheel to channel width ratio, and inlet and outlet transition tests. Uncertainty bounds on the power output and efficiency are calculated following the methodology described in Chapter 3, Section 3.2.2. Leakage losses are discussed at the end of this section.

5.1.1 Wheel performance at different upstream water levels

The wheel is partially submerged into the water at normal operating condition. The upstream and downstream water levels are the determinants of the hydrodynamics of the wheel. The number of blades at work at any given time is determined by the depth of upstream and downstream water levels h_1 and h_2. The upstream water level depends on the flow rate, the rotational speed of the wheel and on the downstream water level. The downstream water level however varies very little with the speed of the wheel and the flow rate. In Figures 5.1a and 5.1b, the power output and efficiency are plotted against the rotational speed of the wheel with their uncertainties at different upstream water levels. The downstream water level in these tests was kept at minimum possible constant value with the help of the downstream adjustable weir and the tests were done in wheel housing WH0 (see Fig. 3.7). The power output continually increases and the efficiency decreases with increasing upstream water level. Uncertainty bounds for the efficiency curves are relatively large, however change in efficiency with changing h_1 can be noticed. Following Eq. 3.6, increase in power output at higher h_1 at any rotational speed is resulted from increased total head acting on the wheel. Efficiency reduces as a result of increased amount of leakage and hydraulic losses with increasing h_1 (Eq. 3.8). While choosing an operating upstream water level h_1, a compromise was made between the efficiency and power output and h_1 was fixed to be 44.65 cm for further tests which refers to the top of the hub.

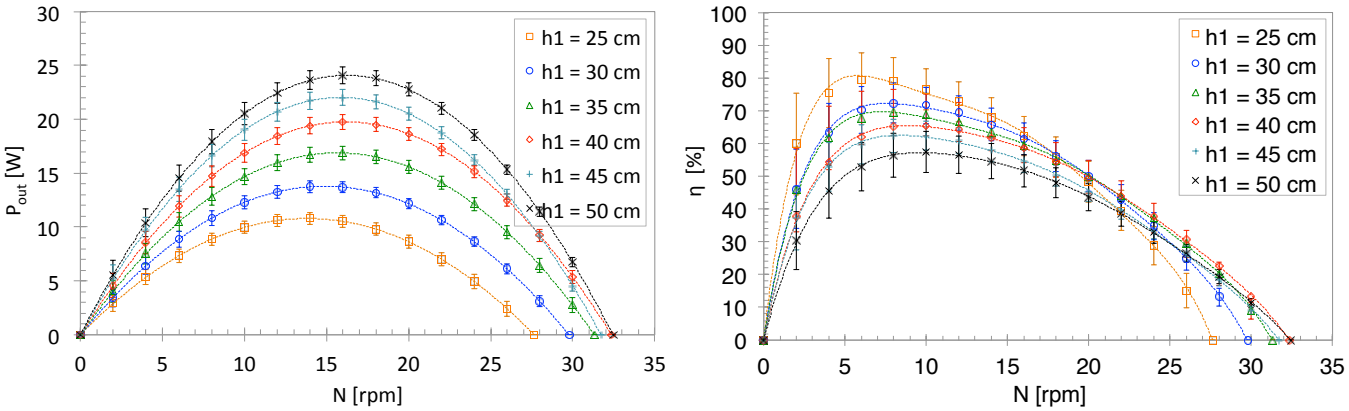

(a) Power output (b) Efficiency

Figure 5.1: Power output and efficiency at different h_1

5.1.2 Wheel performance at different downstream water levels

Different downstream water levels were tested while keeping the upstream water level constant at 44.65 cm in the wheel housing WH1 (see Fig. 3.8). Higher downstream water level results in smaller total head acting on the wheel. The hydraulic power input delivered to the wheel therefore reduces with increasing downstream depth. The power output and efficiency curves at different downstream water levels are shown in Figures 5.2a and 5.2b. Power output and efficiency both reduce with increasing downstream water level h_2. The uncertainties in efficiency around the best efficiency point (BEP) region overlap making it difficult to conclude of any change in the efficiency. At higher rotational speeds, it is clear that efficiency dropped with increasing h_2. This drop in efficiency is contributed by the reduced total head and possibly due to the increased amount of hydraulic losses at higher h_2.

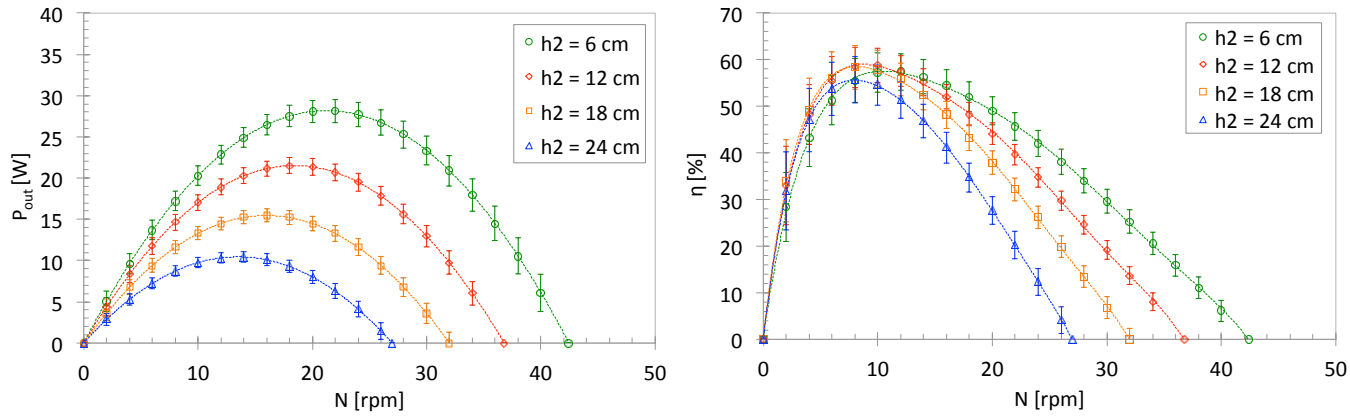

(a) Power output (b) Efficiency

Figure 5.2: Power output and efficiency at different h_2

Based on the above results, upstream and downstream water levels ($h_1 = 44.65$ cm, $h_2 = 6.18$ cm) as shown in Fig. 5.3 were kept fixed for all further tests carried out in this research in order to be able to compare data at different optimisation steps and with the numerical model results. The velocity

head term in Eq. 3.1 is very small and therefore the total head acting on the wheel is dominated by the pressure head term.

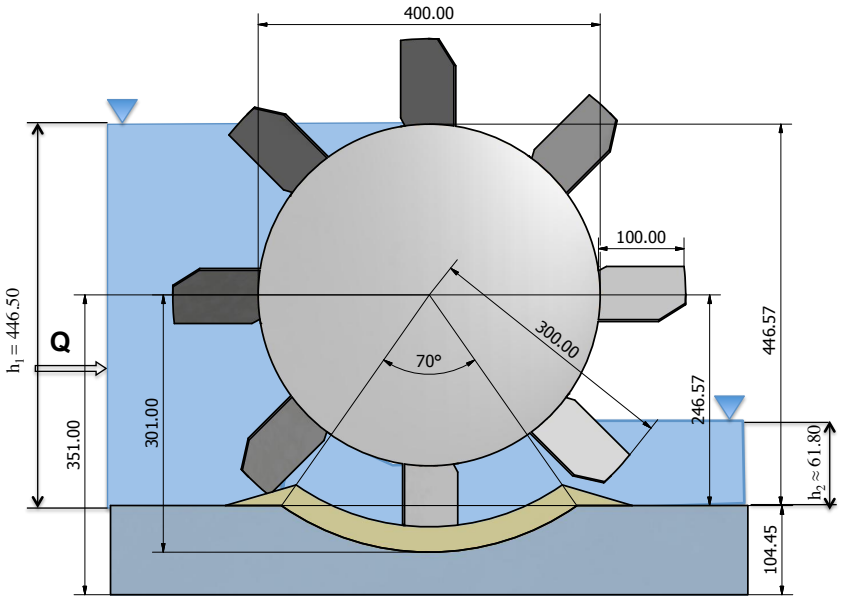

Figure 5.3: Definition diagram for operating upstream and downstream water depths (dimensions are in mm

5.1.3 Wheel housing tests

Two different wheel housings WH0 and WH1, shown in Figures 3.7 and 3.8, are tested. As described in Chapter 3, section 3.3, the original wheel housing WH0 provided an enclosure for the blade cells. On the modified wheel housing WH1, the length of the side enclosure is reduced to cover only the hub of the wheel. The results of the modification on the wheel housing on wheel performance is plotted in Fig. 5.4. Torque, flow rate, total head, power output and efficiency for both settings are plotted against the rotational speed of the wheel. As mentioned previously, these tests are done with constant upstream and downstream flow depths.

Torque at different speed of the wheel for both settings is compared in Fig. 5.4a. The no-load speed is increased from 31.7 rpm in WH0 to 42.4 rpm in WH1. The stall torque is reduced from 26.5 Nm in WH0 to 25.35 Nm in WH1. The torque in WH1 only starts to increase beyond 5 rpm speed and shows a significant gain at higher rotational speed.

As shown in Fig. 5.4b, the rotational speed of the wheel and the flow rate acquire a linear relationship at a constant flow depths. The flow rate at 0 rotational speed is increased from 2.45 l/s in WH0 to 3.55 l/s in WH1 but the slope of both lines remains the same. Moreover, it is clearly seen that the no-load speed in WH0 was at about 21 l/s which is increased to about 29 l/s in WH1. This shows that in WH1 wider operation range is possible than in WH0. The leakage flow Q_L (calculated using Eq. 3.7) is reduced with increasing rotational speed in both settings and is higher in WH1.

The total head for both settings is compared in Fig. 5.4c. The inlet and exit flow area was increased in WH1 giving smaller flow velocities. The total head acting on the wheel is higher and remains almost

constant in WH1 due to the decrease in velocity head which is a negative term in Eq. 3.1. This increase becomes more apparent at higher wheel speeds, viz., higher flow rates.

The power output and efficiency for both cases are compared in Figures 5.4d and 5.4e. The total uncertainty involved in power output and efficiency for both cases are also shown simultaneously. The maximum power gain is at half of the no-load speed and about half of the stall torque. The power output starts to increase only beyond 5 rpm speed and shows substantial gain at higher rotational speed. The best efficiency point (BEP) of $63.55 \pm 5.57\%$ in WH0 is at 8 rpm, which is shifted to 12 rpm speed and reduced to $57.35 \pm 3.88\%$ in WH1. The details of the BEP for both cases are presented in Table 5.1.

Table 5.1: BEP details of wheel housing WH0 and WH1

Setting	η (%)	P_{out} (W)	N (rpm)	τ (Nm)	H (m)	Q (l/s)
WH0	63.55 ± 5.57	16.61 ± 1.05	8	19.83	0.374	7.1
WH1	57.35 ± 3.88	22.85 ± 1.11	12	18.18	0.383	10.6

The relative change in head, flow rate, power output and efficiency is plotted in Fig. 5.4f. The change in head and flow rate is positive through out. The change in power output is positive only beyond 5 rpm speed and shows excessive gains at higher rotational speed. Following Eq. 3.6 the increase in power output is either due to increase in total head and/or due to decrease in hydraulic losses. Since the leakage flow rate is proportionately increased with respect to the total flow rate (see Fig. 5.4b), the net flow rate effectively utilized for the energy transfer remains the same for both cases. The percentage increase in power output at higher flow rates is up to five folds greater than the increase in head which indicates that hydraulic losses are greatly reduced at $N \geqq 5$ rpm. The change in efficiency however starts to be positive only beyond 15 rpm. Despite the higher amount of leakage losses in WH1, positive change in efficiency at higher rotational speeds signifies the reduction of hydraulic losses. The negative change in efficiency at $N < 15$ rpm suggests that losses are high in the low speed range.

Two additional operating points are chosen visually on the performance curve to compare the performance of the wheel at different housings: one point below the BEP rotational speed and the other one above the BEP rotational speed. The percentage change in head, flow rate, power output and efficiency at these operating points are calculated using Eq. 3.9 and are summarized in Table 5.2. At $N = 4$ rpm, the negative change in power output and efficiency ascertains that losses are highly increased in comparison to the increase in the head. The increase in power output and efficiency at $N = 24$ rpm is considerable. The gain in power output and efficiency reached 70.54% and 11.47% respectively.

Table 5.2: Performance comparison of wheel housings at different operating points

Operating point	H	Q	P_{out}	η
$N = 4$ rpm	+1.09%	+23.35%	−0.92%	−11.19%
$N = 24$ rpm	+13.60%	+7.10%	+70.54%	+11.47%

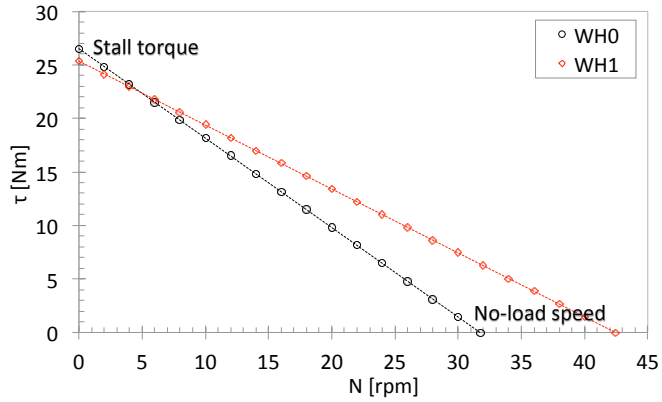

(a) Torque

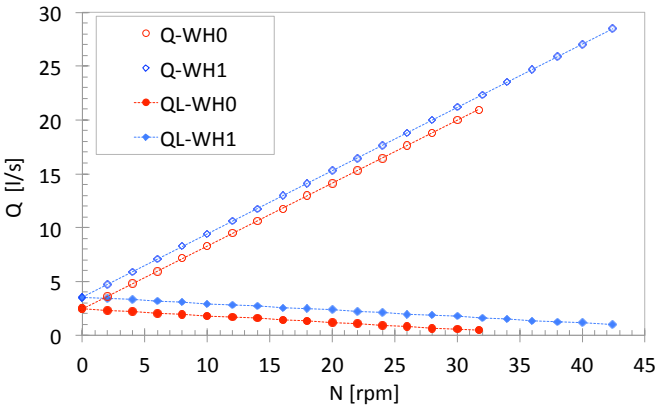

(b) Flow rate

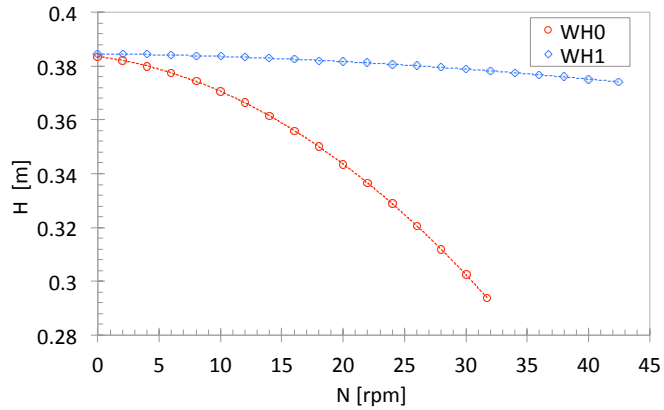

(c) Total head

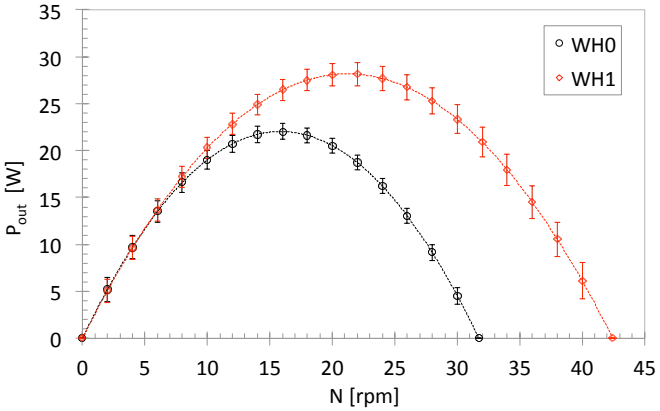

(d) Power output

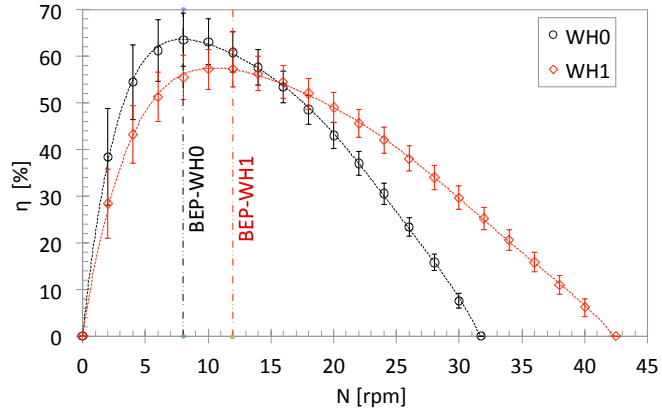

(e) Efficiency

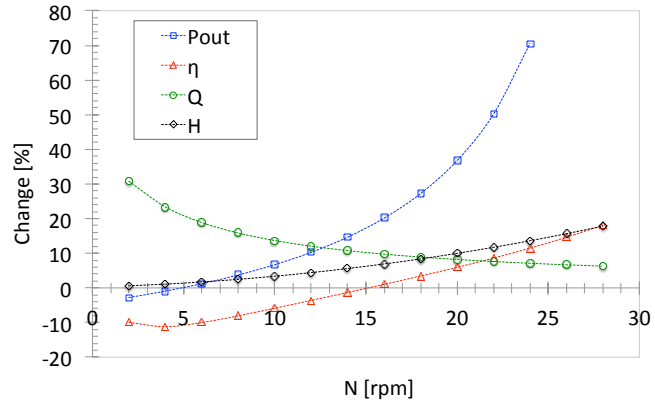

(f) Percentage change in performance between different wheel housings

Figure 5.4: Performance curves at different wheel housings

Moreover, the rotational uniformity of the wheel is important from the operational point of view. The periodic emptying of the blade cell at the exit of the wheel created fluctuation on the upstream head creating pulsation on the wheel motion. The amplitude of the waves generated at the upstream due to the blade and flow interaction at the free surface was observed to be reduced in WH1 due to the possibility of the sideways flow through side openings of the blade cells. Fluctuation on the rotational

speed of the wheel at two different flow rates are compared in Fig. 5.5a for both cases. In Fig. 5.5b, the standard deviation of N for both housings are shown. The magnitude of pulsation is reduced in case of WH1.

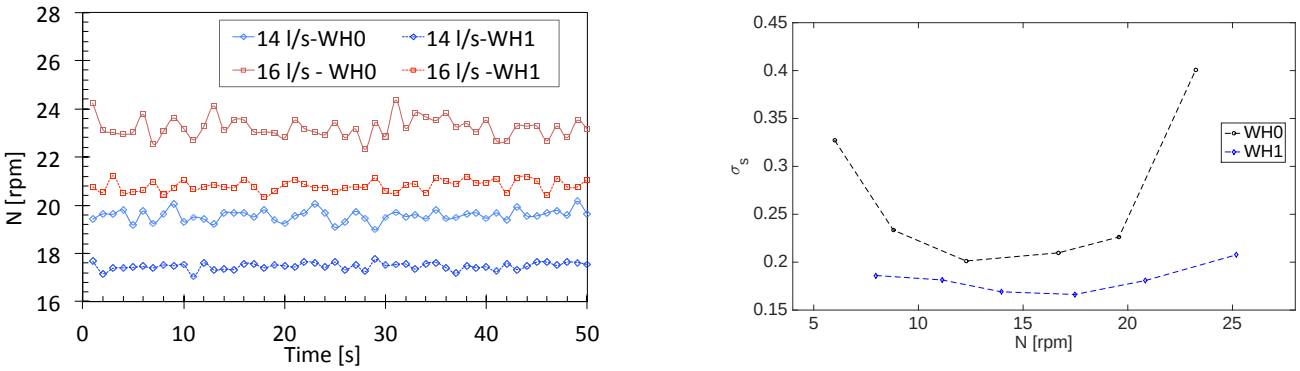

(a) (b)

Figure 5.5: Fluctuation of rotational speed of the wheel in housings WH0 and WH1 (a) N fluctuation over time (b) Standard deviation of N

From the above analysis it can be concluded that the effect of wheel housing modification has overall a mixed effect on the wheel efficiency. The performance shows improvement in efficiency only at higher rotational speeds indicating a drop in the losses in the wheel control volume. Power output is however greatly improved. Air entrainment raised from turbulent disturbances at the free surface due to blade and flow interaction was observed to be increased with increasing rotational speed. The amount and size of air bubbles entrapped inside the blade cells in WH0 was much higher than in WH1 (see Figures 5.6 and 5.7). The splashing behaviour at the blade entry, the amplitude of the upstream waves was also observed to be reduced in WH1. Water was carried upward by the blades at the exit in WH0 and was prominent at higher rotational speed. In WH1, the side openings of the blade cells permitted the water filled inside the blade cell to be emptied earlier. The amount and size of the entrapped air bubbles and the amount of water carried upward at the exit has clearly a negative effect on the wheel performance, which contributed to the under performance of wheel in WH0 at high rotational speeds. The wheel housing WH1 will be kept for all further investigations in this study.

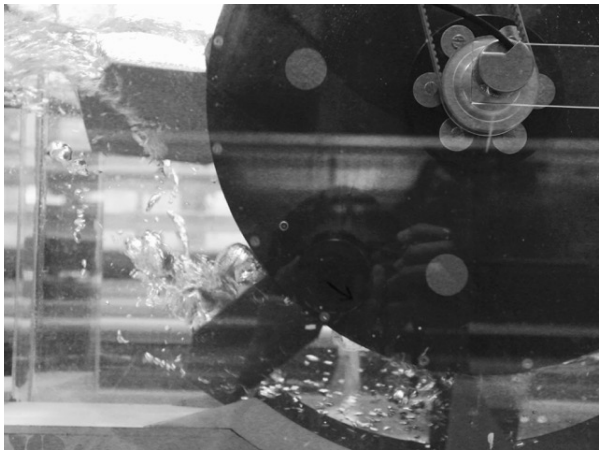

Figure 5.6: Air entrainment in WH0

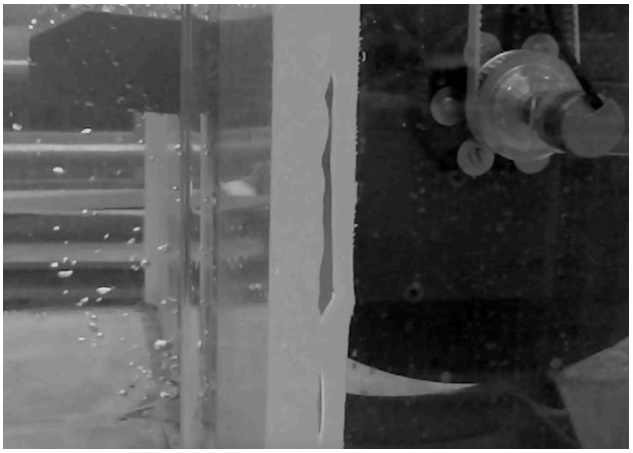

Figure 5.7: Air entrainment in WH1

5.1.4 Blade number tests

Four different blade numbers 6, 8, 12 & 16 were tested in the blade number test. The performance of the wheel with different number of blades is shown in Fig. 5.8. All these tests are done at constant upstream and downstream water levels as described earlier. On the original wheel, eight numbers of sharp V-shaped BS0 blades were mounted. The output torque, total head, flow rate, power output and efficiency are plotted against the rotational speed of the wheel in Figures 5.8a to 5.8e. A relative change in performance is studied between six and eight number of blades (Fig. 5.8f).

Torque at different speed of the wheel for all combination of blades is compared in Fig. 5.8a. The wheel with 12 and 16 number of blades showed significant reduction in torque at higher rotational speed compared to the original eight blades wheel. The no-load speed reduced from 42.4 rpm on the original eight blades wheel to 36.2 rpm with 12 blades wheel and 33.2 rpm with 16 blades wheel giving a very narrow range of operation. The wheel with six number of blades performed better with higher gain in torque at higher speed. The no-load speed is increased to 51 rpm in six blades wheel. The stall torque remained almost the same in all blade number variations.

The flow rates for all cases are plotted in Fig. 5.8b along with the leakage flow rate Q_L calculated using Eq. 3.7 for each case. The flow rate shows very small increase in case of six number of blades, no change in case of 12 number blades and slight decrease in 16 blades case in comparison to the 8 blades case. The flow rate at the no-load speed decreased from 28.47 l/s to 24.98 l/s in 12 blades case and 22.13 l/s in 16 blades. In six blades wheel, the maximum flow rate at no-load speed increased to 33.82 l/s giving wider range of possible flow rates for wheel operation. The leakage flow is the function of rotational speed and the total flow rate (Eq. 3.7) therefore shows similar trend as the flow rate.

The total head for all cases is compared in Fig. 5.8c. Since the flow area remains constant in all four cases in blade number tests, the total head in Eq. 3.1 is only a function of the flow rate. The flow rate in case of six blades is slightly higher than in eight blades wheel which created negligible drop in the total head. In case of 16 blades (see Fig. 5.8b), flow rate is slightly dropped which causes the head to slightly increase due to the decreased velocity head term in Eq. 3.1. At 12 number of blades, the head curve remains the same as that of an eight blade wheel. As the flow rate increases at higher rotational speeds, the total head becomes smaller owing to the increase in the velocity head.

Figure 5.8d shows the power output for all number of blade cases and their corresponding uncertainty values. The maximum power gain is always at half of the no-load speed and about half of the stall torque. Up to 5 rpm speed the power output remains almost the same and shows a substantial gain in six blades wheel at higher rotational speeds. The power output in 12 and 16 blades wheel is significantly reduced in comparison to the original eight blades case.

The efficiency of the wheel with different numbers of blades is compared in Fig. 5.8e with their corresponding uncertainty values. The six blades case shows highest efficiency while the 12 and 16 blades drop in performance as compared to the original eight blades wheel. The best efficiency point (BEP) of six blades wheel and eight blades wheel coincide at 12 rpm speed and at 10 rpm in case of 12 and 16 blades wheel. The details of the BEP for all four cases are presented in Table 5.3.

Table 5.3: BEP details of wheels with different number of blades

No of blades	η (%)	P_{out} (W)	N (rpm)	τ (Nm)	H (m)	Q (l/s)
6	59.57 ± 3.48	24.20 ± 1.11	12	19.26	0.3831	10.80
8	57.35 ± 3.91	22.85 ± 1.17	12	18.18	0.3832	10.60
12	54.71 ± 3.37	19.48 ± 1.09	10	18.60	0.3835	9.46
16	53.40 ± 4.21	18.37 ± 1.15	10	17.54	0.3836	9.14

The overall improvement in performance of the wheel with six numbers of blades in comparison to the eight blades wheel is studied using the plot of relative change in power output, efficiency, head and flow rate as shown in Fig. 5.8f. The change in total head is negative but remains very small and negligible. The flow rate remains positive though out with 1 to 5% increase. The change in power output remains also positive and shows impressive gains at higher rotational speed. Since the head was nearly constant in both cases, this increase in power output is mainly contributed by the reduction in hydraulic losses, important among others is the friction losses due to the decreased surface area of the blades. The gain in power output increases exponentially and reaches more than 200% at 40 rpm speed. There is up to 1% drop in efficiency below 6 rpm from where it continuously increases and shows maximum gain of up to 16.5% at 40 rpm.

The performance of the six and eight blades wheels is compared in two different operating points away from BEP: one point below the BEP speed ($N = 4$ rpm) and other one above the BEP speed ($N = 24$ rpm). These points are chosen visually on the efficiency curves in Fig. 5.8e. The relative change in head, flow rate, power output and efficiency at these operating points are summarized in Table 5.4. At $N = 4$ rpm, change in power output is positive indicating hydraulic losses are slightly reduced in six blades wheel. Change in efficiency is still negative due to the increased leakage losses in case of six blades wheel despite reduction in hydraulic losses. At $N = 24$ rpm both power output and efficiency show a substantial gain of 21.06% and 8.17% respectively.

Table 5.4: Performance comparison of 6 and 8 blades wheel at different operating points

Operating point	H	Q	P_{out}	η
$N = 4$ rpm	−0.007%	+3.20%	+1.06%	−0.89%
$N = 24$ rpm	−0.029%	+1.39%	+21.06%	+8.17%

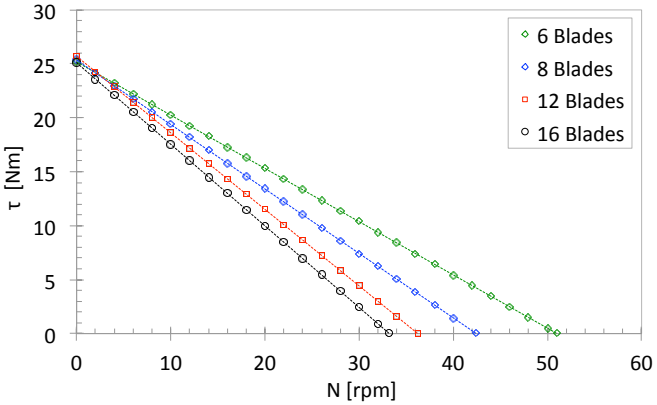

(a) Torque

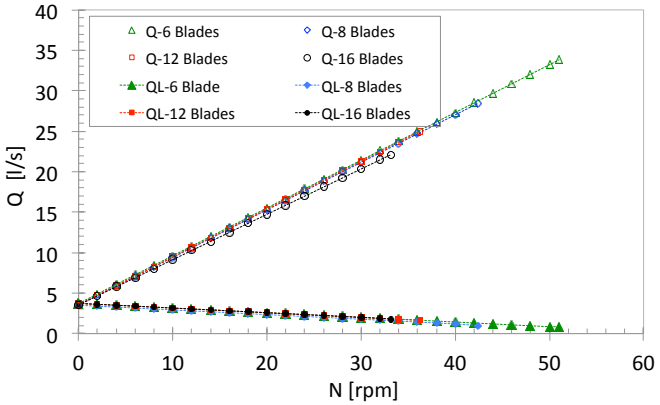

(b) Flow rate

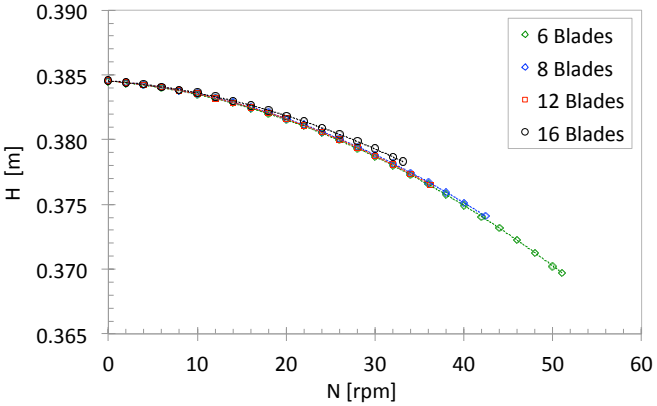

(c) Total head

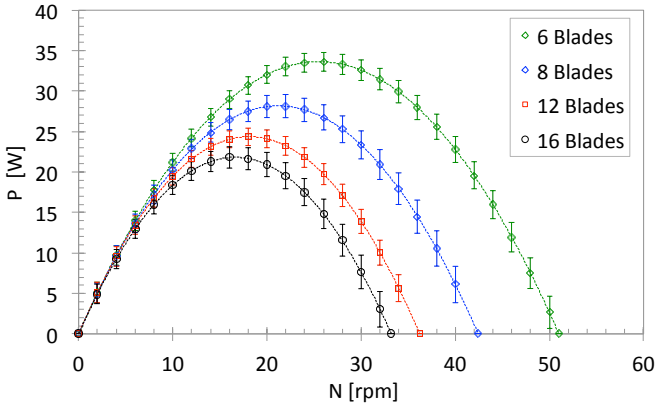

(d) Power output

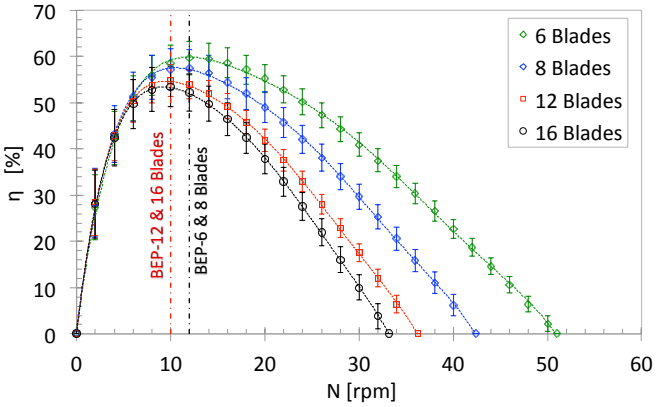

(e) Efficiency

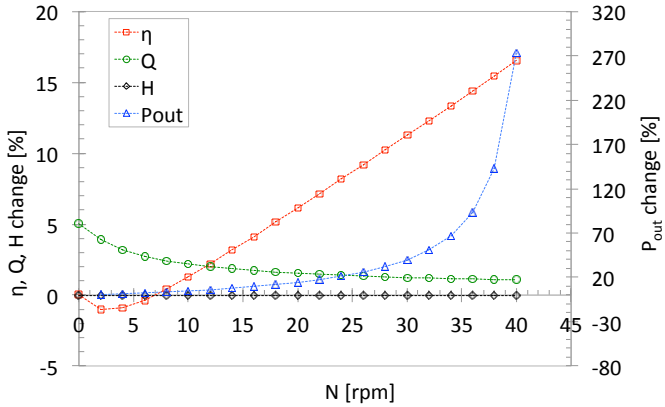

(f) Percentage change in performance between six and eight blades wheel

Figure 5.8: Performance curves for different blade numbers

With increased numbers of blades, the uniformity of rotation is expected to increase. However, in Fig. 5.9a no significant difference in rotational quality is observed on the wheel with increased numbers of blades at $Q = 14$ l/s. The standard deviation of N for different numbers of blades is compared in Fig. 5.9b. At low speed, the six blade wheel showed a large deviation in speed. However, at higher rotational speeds ($N \geq 10$ rpm) reduction in the blade numbers didn't necessarily result in large pulsation on the wheel rotation.

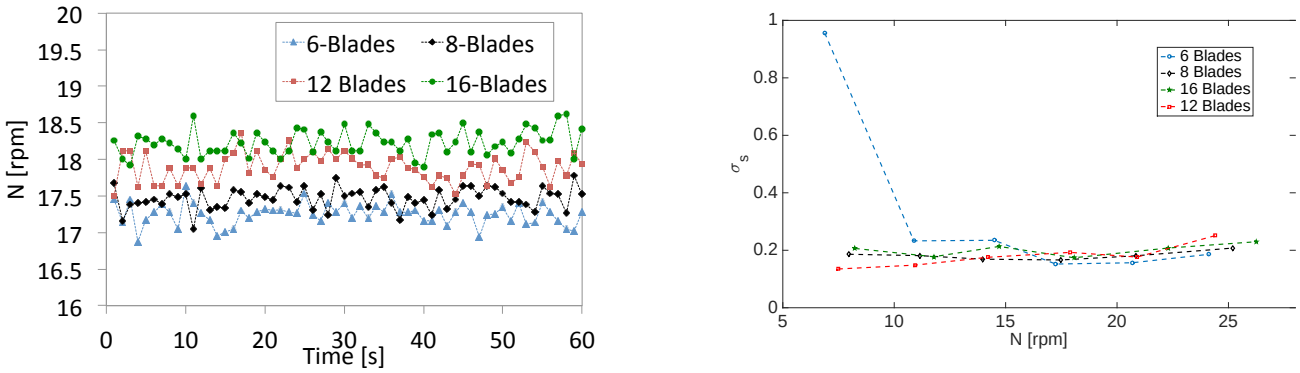

(a) (b)

Figure 5.9: Fluctuation of rotational speed for different blade numbers (a) N fluctuation over time for $Q = 14$ l/s (b) Standard deviation of N

To summarise, the wheel performance with six number of blades shows improvement with efficiency rise of 2.2% at BEP. Beyond 6 rpm, the six blades wheel shows positive gain in power output and efficiency. This increase in power output and efficiency with reduced number of blades is expected to be partly contributed by the decrease in friction losses with decreased number of blades. Moreover, the amount of fluid displacement caused by the blade at the entry is observed to be reduced with decreased number of blades. This energetic displacement of water could represent significant amount of loss. The exit losses are also reduced with lower number of blades. As the frequency of the blade entering and exiting the water surface reduces, the frequency at which the water is carried upward with the blade on the downstream also reduces thus contributing to the increased power output and efficiency. Other complex hydraulic losses inside the blade cells due to flow circulation and eddies are thought to be low in bigger cells, i.e. at lower blade numbers. The numerical model results discussed in section 5.2 show an evidence of reduced flow circulation losses at lower number of blades. For further tests, the wheel with six number of blades is used.

5.1.5 Wheel to channel width ratio

The performance of the wheel at different channel widths involved the test with four different wheel width (b) to channel width (B) ratios: $1:4, 1:3, 1:2$ and $1:1$. The model wheel is 25 cm wide and the existing flume is 100 cm wide. Temporary plexiglass walls were installed on the upstream and downstream sides of the wheel to build the desired width ratios. The performance curves at different wheel to channel width ratios ($b:B$) is plotted in Fig. 5.10. Torque, flow rate, total head, power output and efficiency are plotted against the rotational speed of the wheel. A relative change in performance is used to study the change in performance at two different settings.

Figure 5.10a shows the torque at different speed of the wheel for all $b : B$ values. At $b : B = 1 : 1$, the torque shows significant drop beyond 10 rpm in comparison to the 1 : 4 width ratio. The no-load speed is reduced from 51 rpm in the case 1 : 4 to 39 rpm in 1 : 1 ratio giving a very narrow range of operation. Torque on both wheel to channel width ratio of 1 : 3 and 1 : 2 showed improvement over the 1 : 4 setting with increased no-load speed of 53.4 rpm and 52.8 rpm respectively.

The flow rates for all tested $b : B$ ratios are shown in Fig. 5.10b along with the leakage flow rate Q_L for each case. There is only slight difference in the flow rates between all four cases. At 1 : 1 ratio, the no-load flow rate reduces to 26.86 l/s from 33.82 l/s in 1 : 4 width ratio. In 1 : 3 and 1 : 2 width ratios the no-load flow rate slightly increased to 33.88 l/s and 34.66 l/s respectively. The leakage flow also shows the similar trend as the flow rates for all four cases.

In Figure 5.10c total head for all four $b : B$ values are shown. In this case, the flow area changes with changing channel width while the flow depth remains the same. The total head in Eq. 3.1 is therefore a function of the flow rate as well as the channel width. It is clear that the 1 : 1 width ratio has highest drop in the head due to increased velocity head term (-ve term in Eq. 3.1) and vice versa. At higher rotational speeds, i.e. at higher flow rates the difference in total head becomes more obvious.

Power output for all four cases are presented in Fig. 5.10d along with their uncertainty values. The power output in case of 1 : 3 and 1 : 2 both show gain in comparison to the 1 : 4 width ratio. The 1 : 1 case shows significant drop beyond 10 rpm. Power output in case of 1 : 3 and 1 : 2 width ratios remained same up to $N = 26$ rpm. At higher speed, the 1 : 3 width shows slight gain. However, uncertainties in power output for both 1 : 2 and 1 : 3 case are partly overlapped making it difficult to judge.

Similarly, the efficiency of the wheel at different wheel to channel width ratios is shown in Fig. 5.10e with the uncertainty bound. The efficiency remains highest in case of $b : B = 1 : 2$ above 10 rpm speed. The 1 : 1 setting showed highest performance among all four test cases up to 10 rpm and beyond 20 rpm shows lowest performance amongst all. Around the BEP region, the uncertainties are high and partly overlapped. The efficiency of 1 : 2 and 1 : 3 width ratios didn't differ much at higher rotational speeds. The BEP details for all four cases are presented in Table 5.5.

Table 5.5: BEP details of wheel at different channel widths

Wheel to channel width ratio ($b : B$)	η (%)	P_{out} (W)	N (rpm)	τ (Nm)	H (m)	Q (l/s)
1 : 4	59.57 ± 3.48	24.20 ± 1.11	12	19.26	0.3831	10.80
1 : 3	61.09 ± 3.48	27.59 ± 1.10	14	18.82	0.3813	12.07
1 : 2	62.14 ± 2.93	27.74 ± 1.07	14	18.92	0.3770	12.06
1 : 1	61.98 ± 4.00	23.79 ± 1.14	12	18.93	0.3604	10.86

The effect of wheel to channel width ratio on the wheel performance is studied using the percentage change plots in Fig. 5.10f. The relative change in performance between 1 : 2 and the 1 : 4 width ratios is calculated using Eq. 3.9. The change in total head is negative and reaches up to −11% at highest speed. The change in flow rate is positive for $N \leq 24$ rpm. At higher speed, it becomes negative with maximum change of −0.5%. The change in power output remains positive through out and shows

exponential gain with increasing rotational speed. Despite the decrease in total head, this increase in power output illustrates that the hydraulic losses are reduced. Change in efficiency is also positive with maximum of up to 5.66% at 38 rpm. This increase in efficiency is attributed to the combined effect of reduced leakage and hydraulic losses.

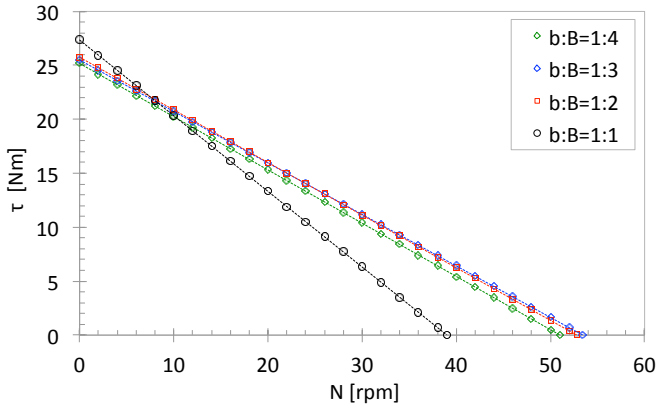

(a) Torque

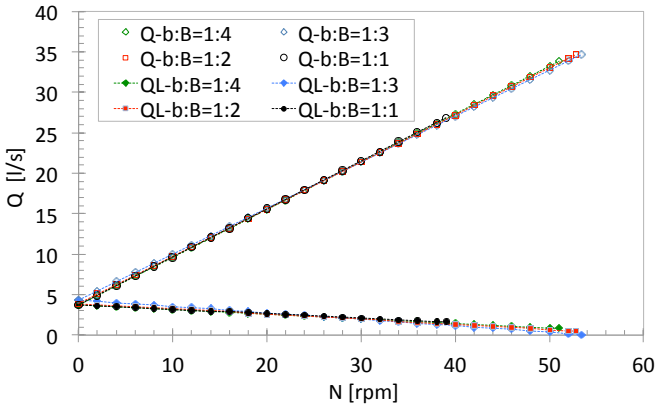

(b) Flow rate

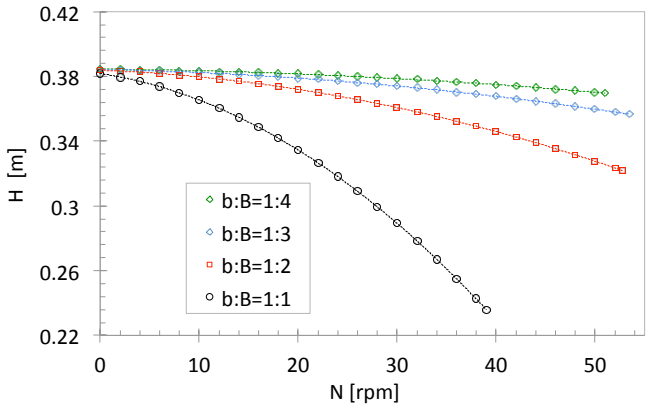

(c) Total head

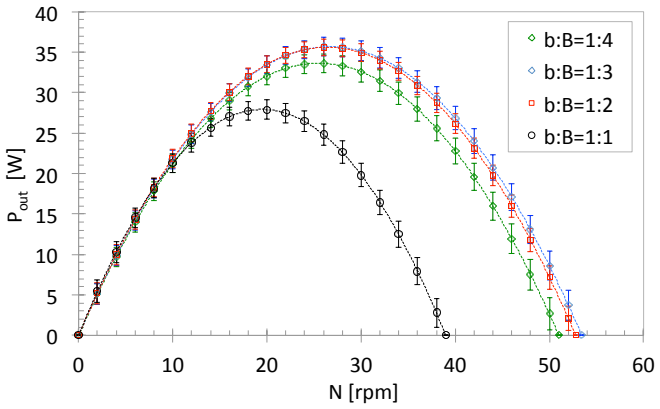

(d) Power output

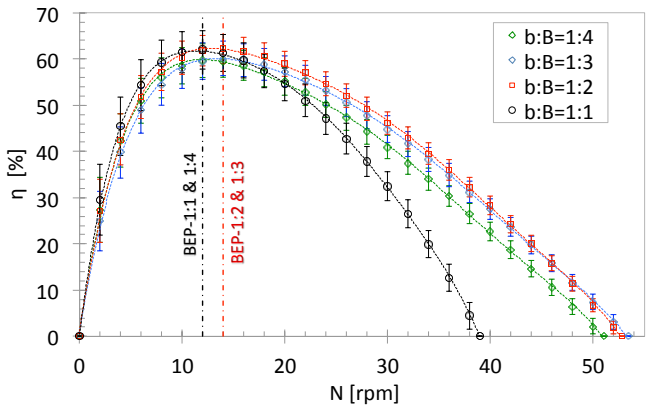

(e) Efficiency

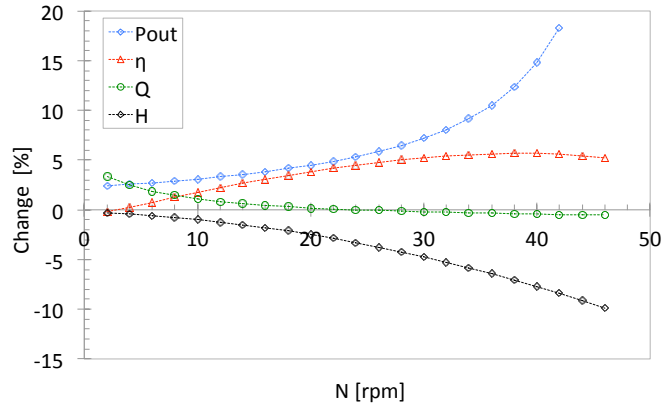

(f) Percentage change in performance between 1 : 2 and 1 : 4 width ratios

Figure 5.10: Performance curves at different wheel to channel width ratios

In Figure 5.10e, two operating points away from BEP are selected in order to compare the performance of the 1 : 2 and 1 : 4 cases. These points correspond to $N = 6$ rpm and $N = 30$ rpm respectively. The relative change in head, flow rate, power output and efficiency at these operating points for both cases are summarized in Table 5.6. At both points, change in power output is positive despite negative change in total head indicating reduced hydraulic losses in case of 1 : 2 width ratio. Change in efficiency at 6 rpm is positive despite increased leakage losses, i.e. hydraulic losses at this point is dominating. At $N = 30$ rpm, efficiency shows even higher gain due to the combined effect of reduced leakage and hydraulic losses.

Table 5.6: Performance comparison between 1 : 2 and 1 : 4 width ratios at different operating points

Operating point	H	Q	P_{out}	η
$N = 6$ rpm	−0.56%	+1.86%	+2.73%	+0.73%
$N = 30$ rpm	−4.73%	−0.19%	+7.19%	+5.22%

Rotational quality of the wheel for all wheel to channel width ratios are compared in Fig. 5.11a for the flow rate of 14 l/s. The standard deviation of N for all $b : B$ ratios are plotted in Fig. 5.11b. High deviation is noticed at low speed in all cases, at higher speed there is only small variation on the deviation of N.

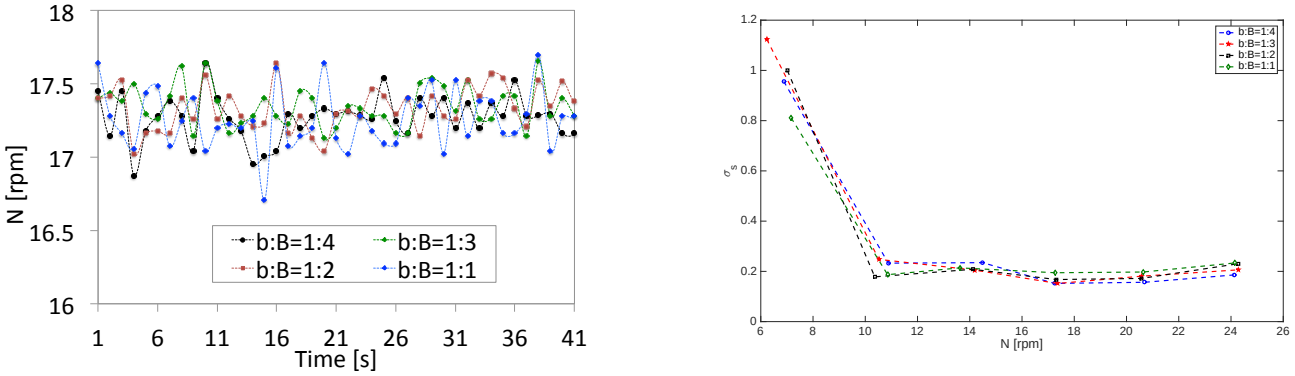

(a) (b)

Figure 5.11: Fluctuation of rotational speed for different $b : B$ (a) N fluctuation over time for $Q = 14$ l/s (b) Standard deviation of N

Above results show that the wheel to channel width ratio is an important performance and economical criteria for Dethridge wheel operation. In the 1 : 1 width ratio, the total head sharply dropped creating a decrease in power output. Moreover, hydraulic losses increased and contributed to the decrease in both power output and efficiency. Flow rates didn't change much, therefore the leakage losses also remained the same (Eq. 3.7). The increase in hydraulic losses could be attributed to the high amount of splashing, high amplitude waves on the upstream due to blade and flow interaction; and the amount of air entrainment. At the exit, the water was driven upward in the blade cells like in the case of wheel housing WH0. The splashing, size and amount of air bubbles and amount of water driven upward at the exit increased with the increasing speed. The performance of 1 : 2 and 1 : 3 width ratios was better in comparison to the 1 : 4 case. Beyond 12 rpm speed, the 1 : 2 width ratio

showed highest efficiency among others. By having a wheel to channel width ratio of 1 : 2, i.e. channel width two times greater than the width of the wheel, the efficiency of the wheel can be increased by 2.6% at BEP and at higher speed range to about 5%.

5.1.6 Wheel performance at different transition shapes

Converging and diverging transition shapes as shown in Fig. 3.9 are tested on the wheel housing WH1 with six number of sharp V-shaped blades BS0 model wheel. The performance of the wheel with this transition are compared with the performance of the wheel with wheel to channel width ratio, $b : B = 1 : 2$, which is the case of sudden contraction from 100 cm channel width to 50 cm on the upstream and sudden expansion on the downstream. In Fig. 5.12, torque, flow rate, total head, power output and efficiency against the rotational speed of the wheel are compared for sudden and gradual transition profiles. Overall performance of both settings are studied using the percentage change in variables between the two cases.

The torque for the parabolic and straight transitions are compared in Fig. 5.12a. There is a very small drop in torque below 20 rpm speed in case of gradual transition. For $N \geq 36$ rpm, the torque becomes slightly higher than the sudden transition. The no-load speed in gradual transition increases only marginally and reaches 53.45 rpm from 52.8 rpm in case of sudden transition profiles.

The flow rates and the respective leakage flow for both cases are shown in Fig. 5.12b. Below 24 rpm speed, the flow rate increased in case of gradual transition which means more hydraulic power input is delivered to the wheel for the same rotational speed. The flow rate starts to drop beyond 30 rpm than in sudden transition profile. The flow rate at no-load speed remains almost equal in both cases. The leakage flow decreases with increasing speed and is proportional to the total flow rate through the wheel.

The total head in case of gradual transition profile showed a negligible drop in head due to the increase in flow rate as shown in Fig. 5.12c. As the flow rate drops beyond 30 rpm, the head starts to increase again since the velocity head is a negative term in Eq. 3.1. However, the difference remains very small. The flow area at the inlet and exit remains the same for both cases. But due to the change in flow rate, the approach and exit velocity changes creating a difference in the total head.

Power output for both cases are compared in Fig. 5.12d. The difference in power output between the two settings is negligible. Maximum power output appears at half of the no-load speed in both cases. This insignificant increase in power output at higher speed in case of gradual transition is explained by the increase in head and possible drop in the hydraulic losses. At < 20 rpm speed, the change in power output lies within the uncertainty bounds in power output.

The efficiency of the wheel for both transition profiles are plotted in Fig. 5.12e with their corresponding uncertainties. As shown, efficiency in case of gradual transition only starts to increase beyond 22 rpm speed. At higher speed, there is decrease in total flow rate (see Fig. 5.12b). So the leakage flow rate in case of gradual expansion also dropped with increasing rotational speed giving rise to the efficiency. There is a drop in efficiency for $N \leq 22$ rpm including the BEP. The increased flow rate, therefore the increased leakage flow rate and the hydraulic losses at the wheel control volume de-

scribes this drop in the efficiency. The BEP in both cases is attained at 14 rpm. The performance at BEP is summarized in Table 5.7.

Table 5.7: BEP details of wheel at different transition shapes

Transition	η (%)	P_{out} (W)	N (rpm)	τ (Nm)	H (m)	Q (l/s)
Gradual	59.8 ± 2.28	27.47 ± 1.13	14	18.74	0.3766	12.42
Sudden	62.14 ± 2.93	27.74 ± 1.07	14	18.92	0.3770	12.06

The relative change in performance between the gradual and sudden transition is calculated using Eq. 3.9 and plotted in Fig. 5.12f. As described earlier, the flow rate is positive until 24 rpm speed with maximum of 20% increase at $N = 0$ rpm. Beyond $N = 24$ rpm, it remains in the negative quadrant and reaches up to -2.6%. Owing to this change in flow rate, the head changes similarly and stays negative for $N \leq 20$ rpm and the rest positive with maximum value of 0.9%. Change in power output is negative until 28 rpm speed. For the rest of the operating range, it stays in positive quadrant and shows an exponential gain with increasing speed. Efficiency change is negative $N \leq 26$ rpm with the drop of -2.31% at BEP. At higher speeds, change in efficiency is positive and reaches of up to $+1.6\%$.

The performance of the wheel with sudden and gradual transition profiles is compared at two points outside the BEP. These two points refer to the $N = 8$ rpm and $N = 32$ rpm speed which are below and above the BEP speed respectively. These points are chosen visually on the performance curve. The relative change in variables between the different settings are summarized in Table 5.8. At $N = 8$ rpm, increase in flow rate in gradual transition is suggestive of the decrease in efficiency. The drop in head due to the increased flow rate following Eq. 3.1 and probable hydraulic losses describes the negative change in power output. However, at $N = 32$ rpm change in power output and efficiency both are positive with a small change of $+0.46\%$ and $+0.57\%$ respectively. The change in head is positive due to decreased flow rate.The negative change in flow rate means proportionally reduced leakage flow at this operating point (Eq. 3.7). Since the change in power output in both of these operating points is very small, there is no significant change in hydraulic effects due to the change in transition designs. The drop in efficiency at $N = 8$ rpm is however noticeable and is predominantly contributed by the increased amount of leakage flow. At the same time, uncertainty bounds are large at lower speed. Therefore, it is not clear whether performance really changed between these settings.

Table 5.8: Performance comparison between sudden and gradual transition shapes at two different operating points

Operating point	H	Q	P_{out}	η
$N = 8$ rpm	-0.13%	$+6.49\%$	-1.18%	-4.05%
$N = 32$ rpm	$+0.15\%$	-1.01%	$+0.46\%$	$+0.57\%$

The test with different transition profiles showed that efficiency doesn't necessarily improve with gradual transition profile. The hydraulic losses are lower than in case of sudden transition profile, which means more hydraulic power input is transferred to the wheel. This became apparent up to 24 rpm speed where more flow rate is required in gradual transition for the same rotational speed of the wheel inferring increased leakage losses and consequently drop in efficiency of the wheel. As

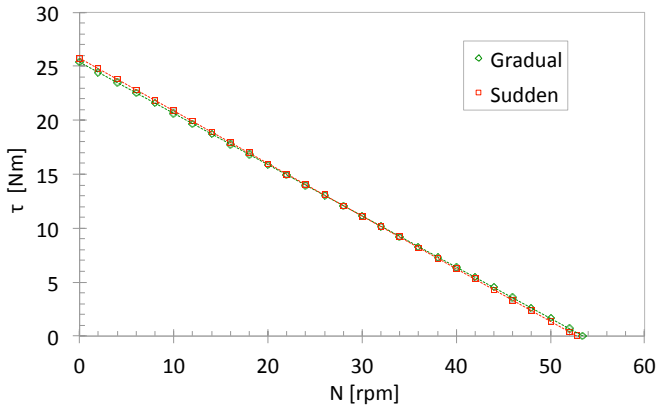

(a) Torque

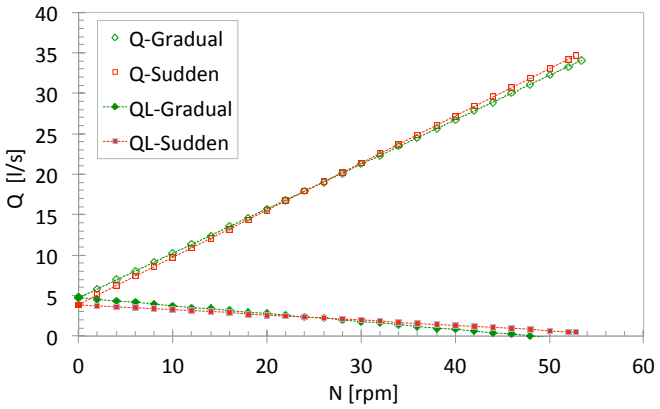

(b) Flow rate

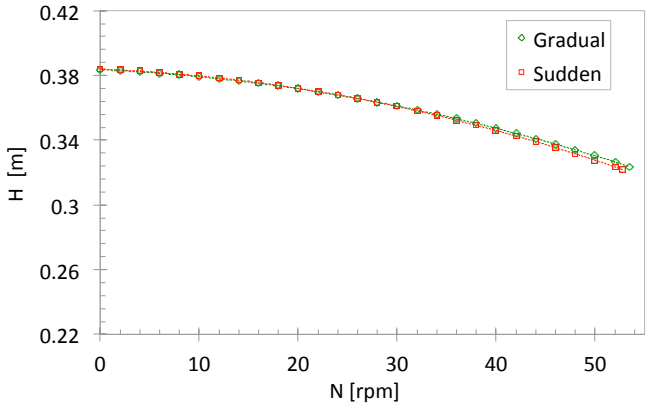

(c) Total head

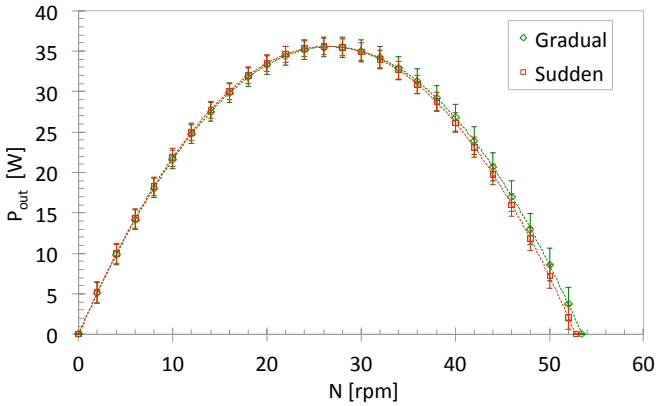

(d) Power output

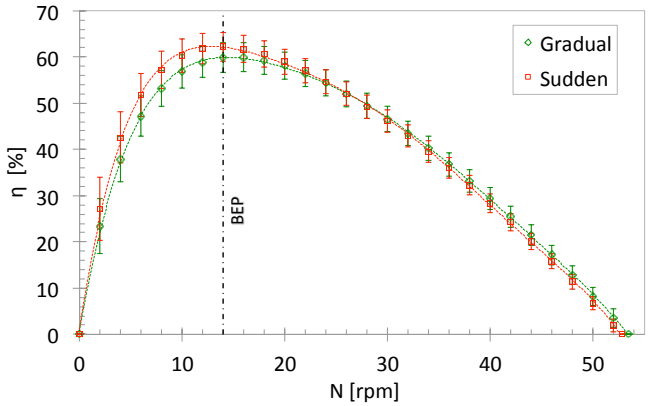

(e) Efficiency

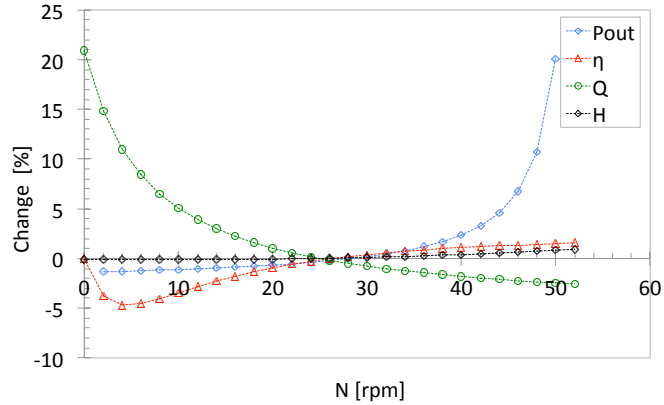

(f) Percentage change in performance between gradual and sudden transitions

Figure 5.12: Performance curves for different channel transition shapes

the rotational speed increased, the leakage flow became smaller and the head slightly increased in gradual transition than in sudden transition profiles contributing to the increase in power output and efficiency. However, performance change is insignificant at higher speed and lies within the defined uncertainty bounds.

5.1.7 Analysis of leakage losses

The dependency of the wheel performance on the clearance gap is studied by setting the bottom clearance gap to three different values: 1 mm, 2 mm and 4 mm. These tests are done on the wheel with 6 blades, wheel to channel width ratio $b : B = 1 : 4$ and in the wheel housing WH1. The behaviour of torque, flow rate, total head, power output and efficiency is plotted in Fig. 5.13.

As seen in Fig. 5.13a, the decrease in torque is noticeable in case of 2 mm and 4 mm gaps until $N =$ 20 rpm. At higher rotational speeds 2 mm shows highest torque among all the three cases. However, there is no remarkable difference in torque at different clearance gaps. The no-load speed in case of 2 mm and 4 mm gaps increased to 53.07 rpm and 52 rpm respectively from 51.02 rpm in case of 1 mm gap.

The total flow rate through the wheel is obviously highest at the 4 mm gap i.e, more flow passes through the increased gap. The leakage flow is proportional to the flow rates in each case and decreases with increasing rotational speed of the wheel. The maximum leakage flow in case of 1 mm gap is 3.7 l/s, which is increased to 5 l/s in case of 4 mm bottom gap. The flow rate at the no-load speed is increased from 33.83 l/s at 1mm gap to 35.5 l/s at 2 mm and 37.2 l/s in case of 4 mm gap. Flow rate and leakage flow for all three cases are plotted in Fig. 5.13b.

The head remains the same in all three variations of clearance gap until 20 rpm speed as shown in Fig. 5.13c. Beyond this speed, the head in 2 mm and 4 mm shows slight drop. Since the flow area remained constant in all three settings, the increased flow rate, i.e. the decreased total head in Eq. 3.1 at high rotational speed is responsible for the drop in the head at higher gaps.

Power output for all bottom gaps are plotted in Fig. 5.13d. The uncertainty bounds on the power output are plotted simultaneously. The performance of 1 mm gap remains highest up to 20 rpm, then the 2 mm gap takes over and shows maximum gain in power output at high speed range. Power output in case of 4 mm gap is the lowest up to 34 rpm speed, beyond which it shows higher output than the 1 mm case but lower than the 2 mm gap. Contrary to the drop in head, increase in power output at high speed range in case of 2 mm and 4 mm in comparison to the 1 mm bottom gap indicates that hydraulic losses are reduced at higher rotational speed (see Eq. 3.6).

Figure 5.13e shows efficiency curves with uncertainty bounds for different bottom gaps. Efficiency in the BEP region and throughout the low speed range is dominated by the 1 mm gap setting. For $N > 30$ rpm, efficiency in case of 2 mm gap is higher than 1 mm and 4 mm gaps. The BEP for all three cases are summarised in Table 5.9. The BEP in case of 2 mm and 4 mm gaps shifted to 14 rpm. There is an efficiency drop of about 9% between 1 mm and 4 mm gaps at BEP. This shows that how a small change in bottom gap can greatly influence the performance of the wheel. The increased amount of leakage flow in 4 mm is the major contributor for this drop in the efficiency.

Table 5.9: BEP details of wheel at different bottom gaps

Bottom gap (mm)	η (%)	P_{out} (W)	N (rpm)	τ (Nm)	H (m)	Q (l/s)
1 mm	59.57 ± 3.48	24.20 ± 1.11	12	19.26	0.3831	10.80
2 mm	55.24 ± 2.49	26.47 ± 0.97	14	18.05	0.3825	12.76
4 mm	50.82 ± 2.42	26.14 ± 1.02	14	17.83	0.3822	13.72

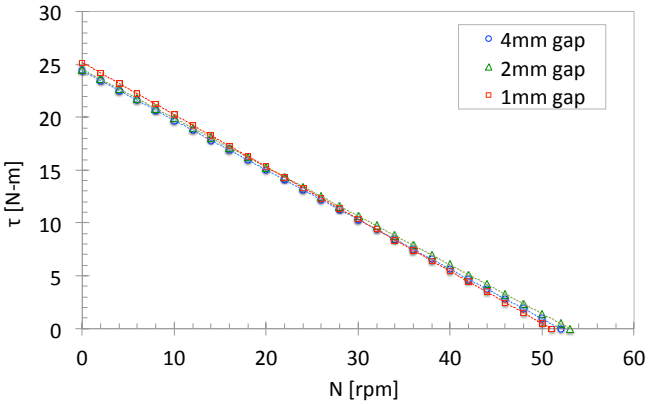

(a) Torque

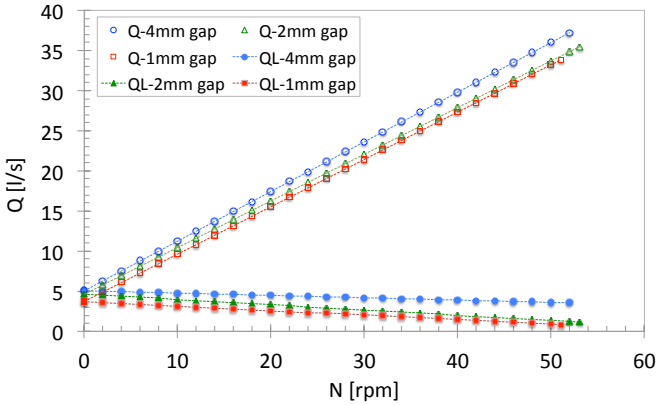

(b) Flow rate

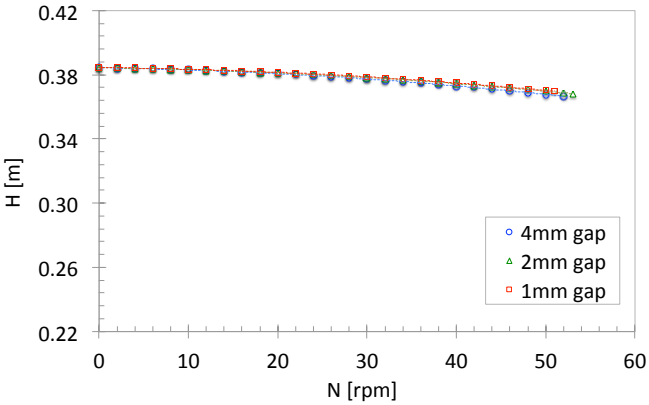

(c) Total head

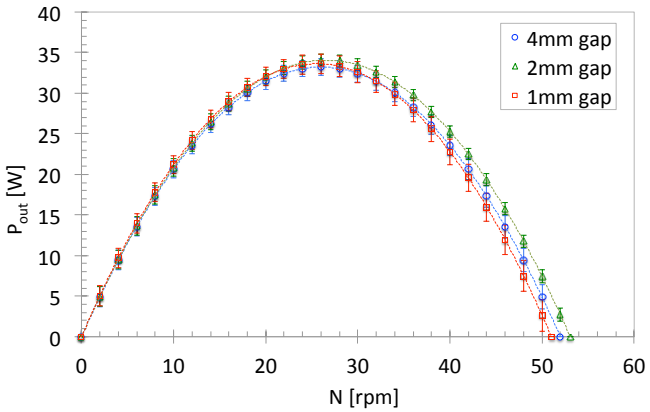

(d) Power output

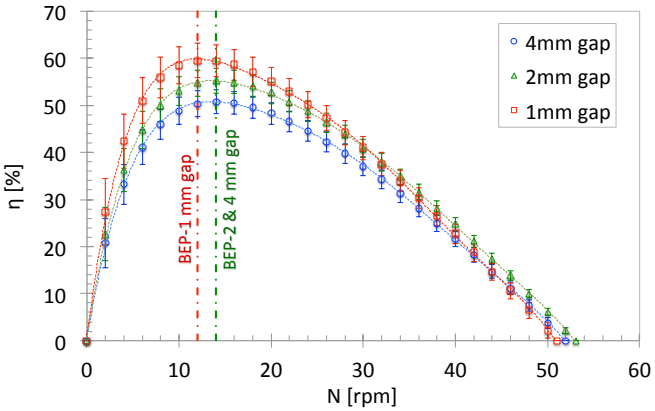

(e) Efficiency

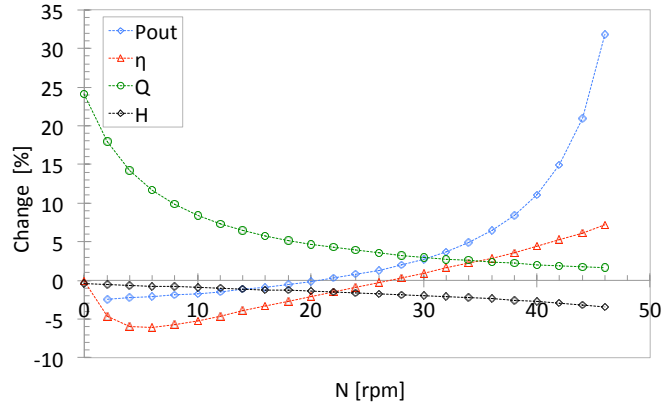

(f) Percentage change between 1 mm and 2 mm gap

Figure 5.13: Performance curves at different bottom gaps

The percentage change in variables between the 2 mm and 1 mm bottom clearance gap is calculated using Eq. 3.9 and plotted in Fig. 5.13f. As seen in the figure, the flow rate is increased and remains positive throughout the operating range. There is only negligible negative change in the total head which is described by the increased amount of flow in case of 2 mm gap and remains negative throughout. Change in power output is negative until 20 rpm speed then at higher speeds it shows exponential rise. Change in efficiency remains negative for $N < 30$ rpm. At higher speeds, it shows a gain in efficiency of up to 4%. This increase in power output and efficiency at increased gap at higher speeds clearly indicates that there are reduced hydraulic losses. Losses within the blade cells such as flow recirculation losses (visualised in the numerical model results in section 5.2) might have been reduced at 2 mm gap at higher rotational speed.

Two operating points on the efficiency curve are selected in order to compare the performance of the 2 mm and 1 mm bottom clearance gaps away from BEP. These points represent $N = 6$ rpm and $N = 40$ rpm respectively. At these operating points, the relative change in head, flow rate, power output and efficiency are analysed in Table 5.10. At $N = 6$ rpm, change in power output is negative indicating increased hydraulic losses. Efficiency is reduced by −6.26% due to combined effect of increased leakage flow rate and hydraulic losses in 2 mm gap. At $N = 40$ rpm, both power output and efficiency are positive with +11.05% +2.03% rise respectively, i.e. gain in 2 mm gap at higher speed. This gain describes that hydraulic losses are greatly reduced at higher speed in case of 2 mm gap. Moreover, difference in leakage losses between 1 mm and 2 mm gap also reduces at higher speed as shown in Fig. 5.13b.

Table 5.10: Performance comparison between 2 mm and 1 mm gaps at two different operating points

Operating point	H	Q	P_{out}	η
$N = 6$ rpm	−0.04%	+11.66%	−2.10%	−6.26%
$N = 40$ rpm	−0.11%	+2.04%	+11.05%	+2.03%

In summary, clearance gap is an important parameter for the hydroelectric performance of the Dethridge wheel. A larger gap would be desired for sediment transport and for ecological reasons in such machines. However, performance of the wheel is highly dependent on the clearance gap. As discussed above, for most of the area on the operating range, the least provision of bottom clearance gap (1 mm) showed highest performance. For $N \geq 32$ rpm, however 2 mm performed well. Despite higher leakage losses, the performance improvement at higher speed in 2 mm gap implies that there is reduction in the hydraulic losses. The actual hydraulic loss mechanisms that might be present such as flow recirculation and looses due to secondary flow are however difficult to visualize. Further increase in bottom gap to 4 mm showed drop in performance in most of the operating region and BEP efficiency drop of up to 9%.

5.2 Numerical model results

In this section, the numerical model result of the eight sharp V-shaped blades (BS0) wheel model in wheel housing WH1 and the resulting flow field is presented and discussed. These results are compared with the corresponding physical model results. Following the analysis of these results, the numerical model results for the wheel with six curved blade shape BS1 are analysed and compared with the physical model results of six sharp V-shaped blades BS0. The numerical model results of the modified shroud shape SS1 are interpreted at the end.

5.2.1 Numerical results of original Dethridge wheel

A numerical model of the original Dethridge wheel with eight sharp V-shaped blades (BS0) in the wheel housing WH1 is numerically computed and compared with the experimental results. In addition to the uncertainty analysis of the numerical model presented in Chapter 4, the study presented here will supplement the validation of the numerical model at distinct boundary conditions.

Two points referring two different rotational speeds within the operating range is taken for simulation. The torque, flow depths, total head and flow rates are acquired at the prescribed rotational speeds of $N = 7.972$ rpm and $N = 25.181$ rpm. The distribution of eight blades produces 45° angle between two subsequent blades.

Model output for $N = 7.972$ rpm

The velocity contours and vectors around the wheel at various angular positions of 0° to 45° revolution for $N = 7.972$ rpm are shown in Figures 5.14a-5.14f. These are the computed flow fields for time steps of 28.2, 28.4, 28.6, 28.8, 29 and 29.15 s respectively and corresponds to a angular positions of 0°, 8.7°, 18.3°, 27.85°, 37.42° and 45° respectively. The same cycle repeats as the rotational angle increases and completes the one full revolution of the wheel in eight cycles. The flow field around the rotating wheel is complicated. The flow exhibits an oscillatory behaviour. The area at the inlet zone shows the region where the x-velocity is negative indicating the region of flow recirculation, separation due to the blade and flow interaction. As the blade completely intrudes into the water (Figures 5.14c and 5.14d), the flow circulation and the vortex becomes clearly visible. This vortex continues to travel downstream until the next blade enters into the upstream water surface. The flow velocity within the cell continuously increases as it moves downstream. At the exit zone, another minor recirculation of the flow within the blade cell becomes visible. The flow velocity of the wake at the downstream of the wheel is obviously the highest. The flow velocity is in the range between −0.68 to 4.5 m/s with a maximum velocity occurring at an angular position of 37.42°. The recirculation of flow impacts the blade motion and contributes to the losses reducing the efficiency of the wheel.

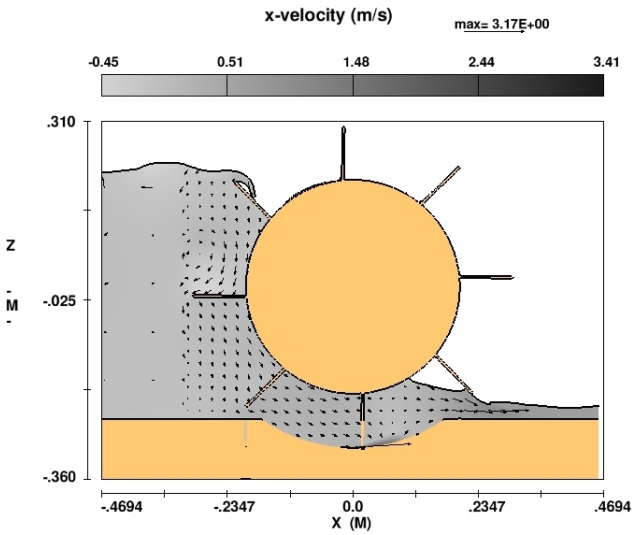

(a) $0^{\circ}, t = 28.2$ s

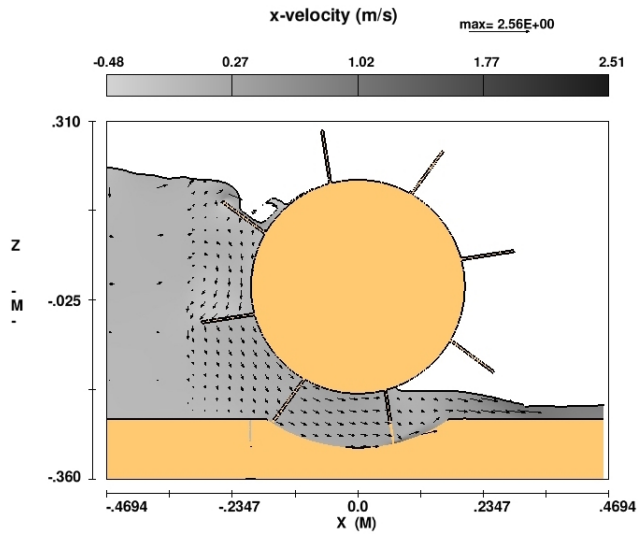

(b) $8.7^{\circ}, t = 28.4$ s

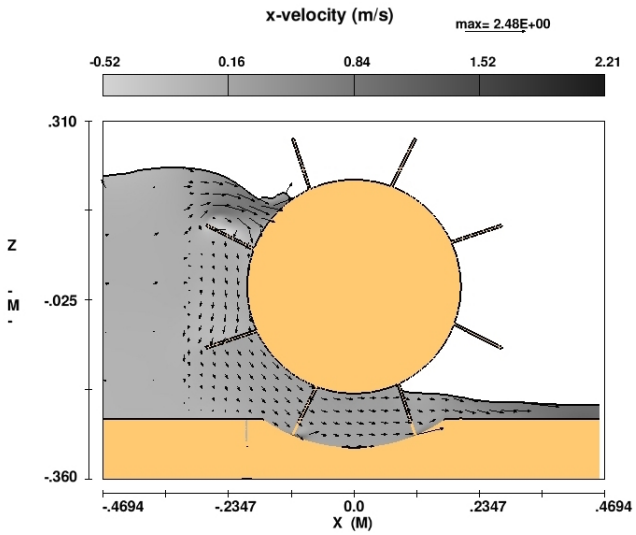

(c) $18.3^{\circ}, t = 28.6$ s

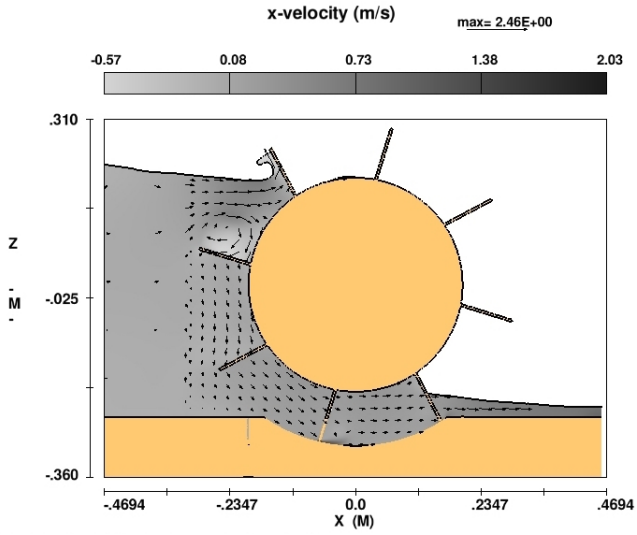

(d) $27.85^{\circ}, t = 28.8$ s

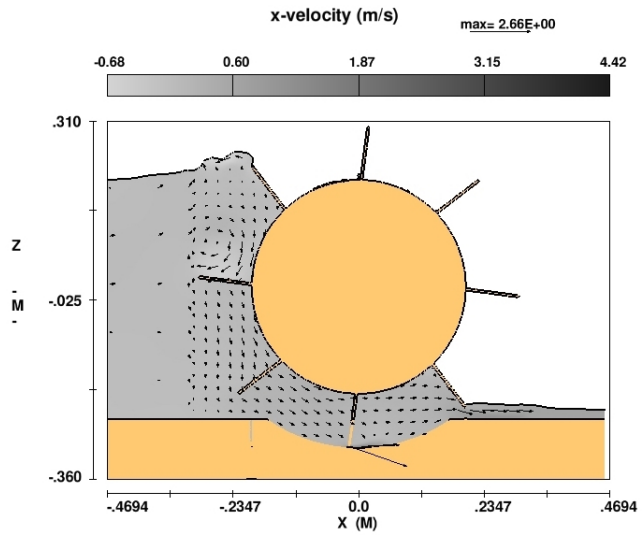

(e) $37.42^{\circ}, t = 29.0$ s

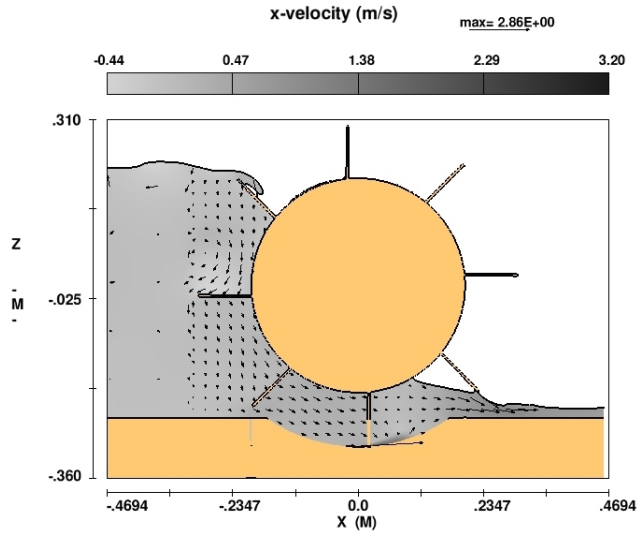

(f) $45^{\circ}, t = 29.15$ s

Figure 5.14: x-velocity contour and vectors for $N = 7.972$ rpm at different rotational angle. At every 45° rotation, new blade enters the water surface and the same cycle repeats. Flow is from left to right.

Figure 5.15 depicts the three dimensional flow field around the wheel at various angular positions of 0° to 45° for $N = 7.972$ rpm. These angular positions also refer to 0°, 8.7°, 18.3°, 27.85°, 37.42° and 45° at time steps of 28.2, 28.4, 28.6, 28.8, 29 and 29.15 s respectively. The contours are coloured by the pressure distribution. The wheel blades experience high fluid pressure at the upstream side of the wheel. The pressure drops as the blade moves downstream. Force is imparted by the fluid on the wheel blades creating pressure difference between the upstream and downstream side of the wheel. Notable amount of leakage flow through the V-shaped air vent, similar to that of physical model, can be visualised in Figures 5.15c, 5.15d and 5.15e. Disturbance at the upstream free surface at the blade entry and the surface waves are also clearly visible.

The numerical model output for $N = 7.972$ l/s is plotted in Fig. 5.16. The temporal development of main variables, i.e. flow rate (Q), upstream flow depth (h_1), downstream flow depth (h_2), the total head (H) and the torque (τ) are monitored over the simulation time of 30 s. The mean value of these variables from 20 s to 30 s is calculated by using the smoothing spline model of the curve fitting tool in Matlab®. The outliers in the data are excluded in the fitted model and the mean and the standard deviation (σ_s) of the variables are computed and presented in Table 5.11.

The upstream free surface interaction with the wheel blades produce large fluctuations on the variables. The periodic evacuation of the blade cell at the exit and fluid displacement by the blade at the entry creates oscillation of the free surface and generate surface waves and pulsating loading forces on the wheel. As a result, the wheel experiences significant cyclic torque oscillations (see Fig. 5.16f). These oscillations, if the amplitude is significant, could lead to structural damage of the wheel.

Table 5.11: Numerical model output for $N = 7.972$ rpm

Parameter	Mean	$\pm\sigma_s$
Q (l/s)	6.93	±1.56
τ (Nm)	20.70	±1.19
h_1 (cm)	47.53	±3.48
h_2 (cm)	5.23	±0.80
H (cm)	40.45	±1.34

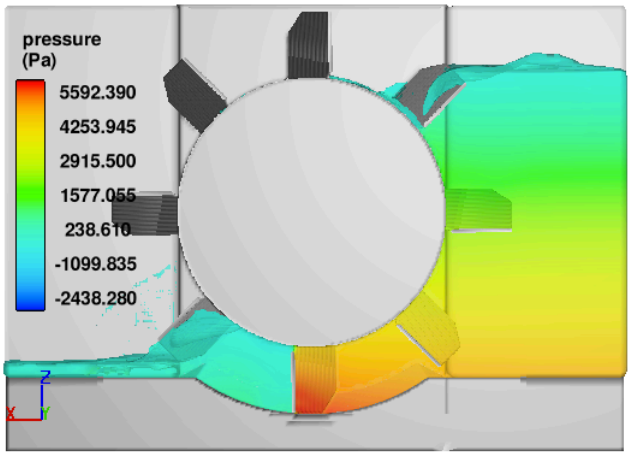

(a) 0°, $t = 28.2$ s

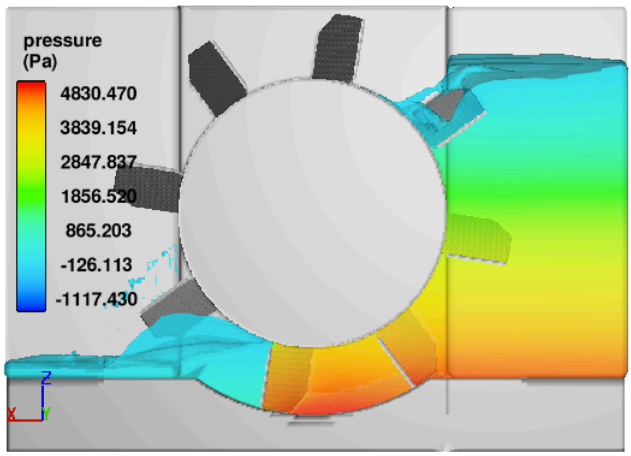

(b) 8.7°, $t = 28.4$ s

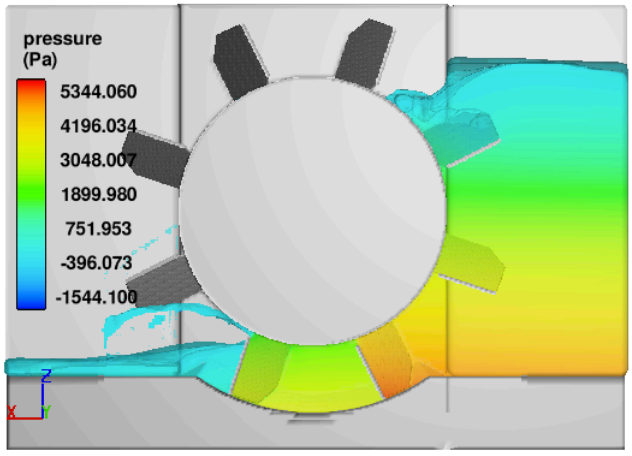

(c) 18.3°, $t = 28.6$ s

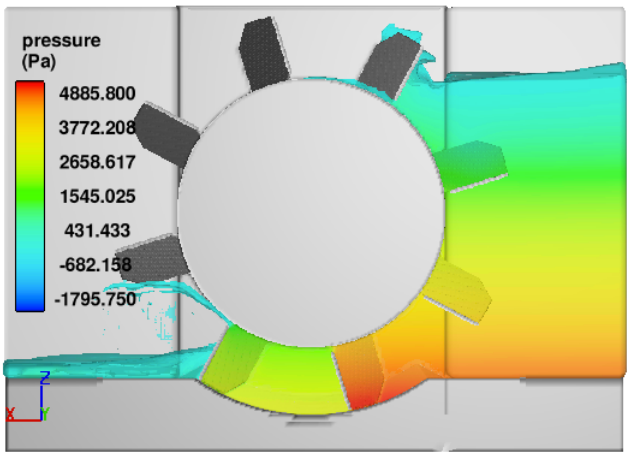

(d) 27.85°, $t = 28.8$ s

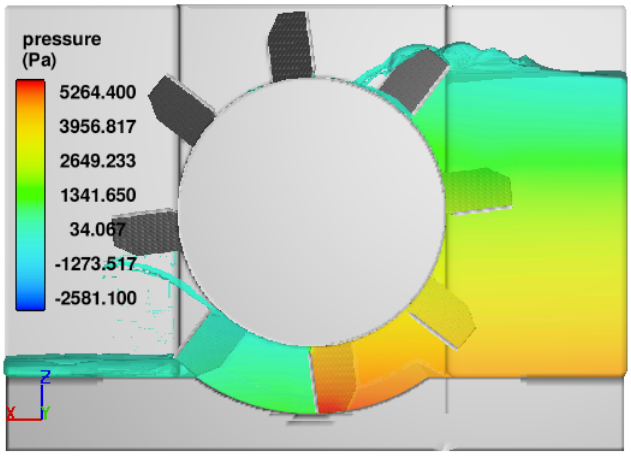

(e) 37.42°, $t = 29$ s

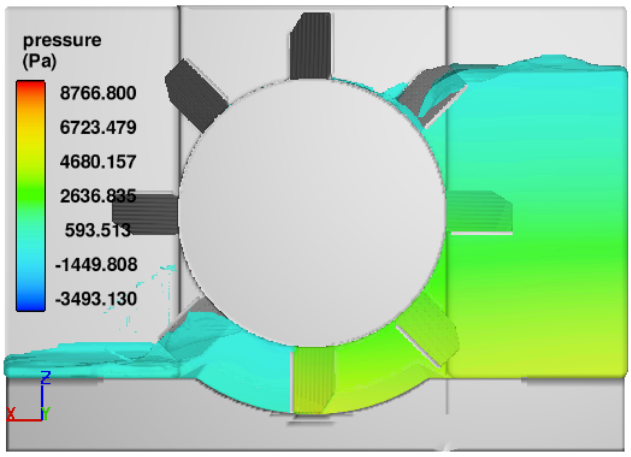

(f) 45°, $t = 29.15$ s

Figure 5.15: Pressure distribution at different rotational positions for wheel with eight sharp blades BS0 at $N = 7.972$ rpm. Flow is from right to left.

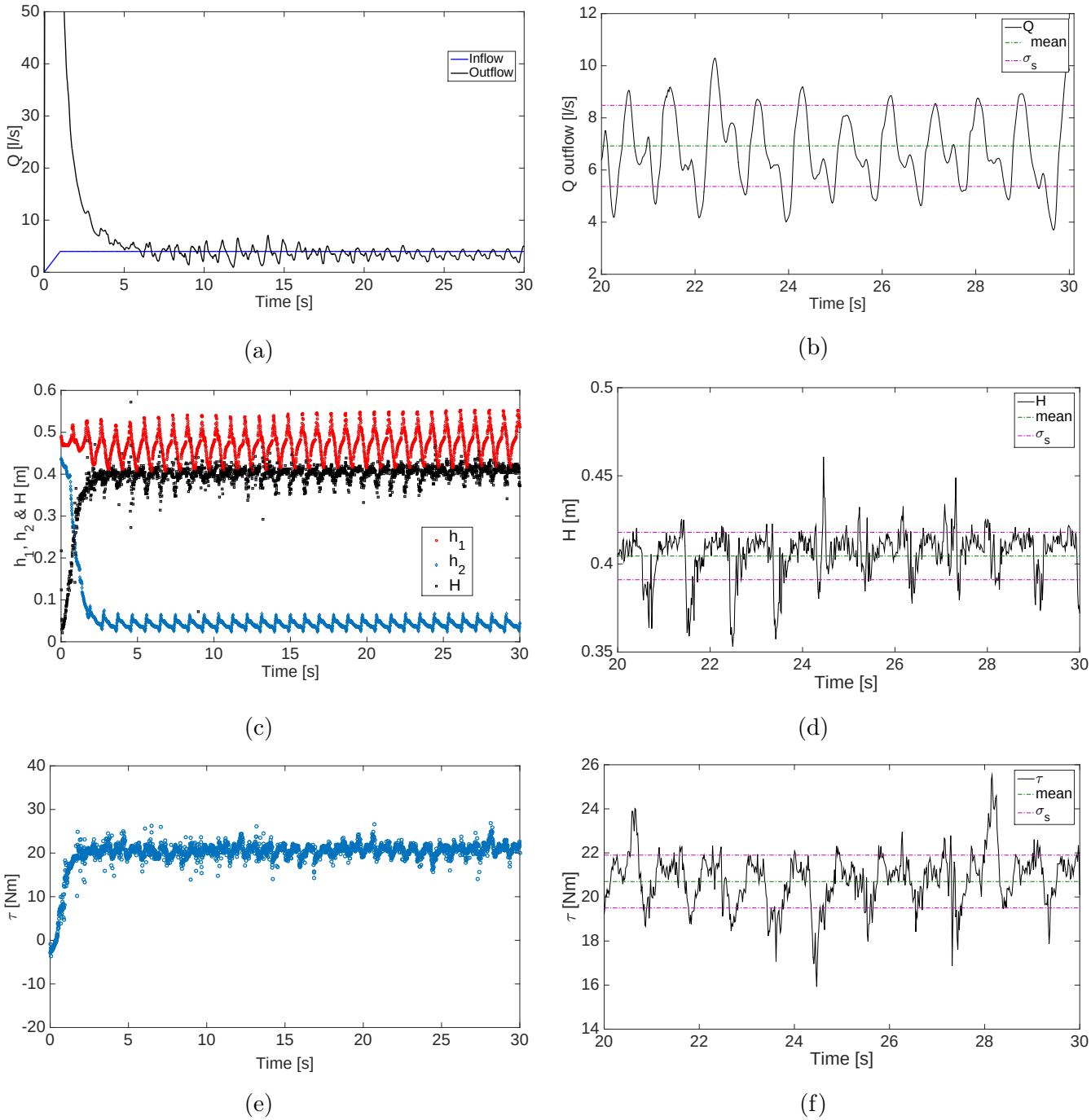

Figure 5.16: Model output for $N = 7.972$ rpm against simulation time. (a) Flow rates at the inlet and outlet boundary; (b) Outflow fluctuation and mean and standard deviation of Q; (c) Upstream and downstream water levels and the total head; (d) Total head fluctuation and its mean and standard deviation; (e) Total torque; (f) Torque ripple and its mean and standard deviation

The fluctuation of the total torque of the wheel in one complete revolution ($0° - 360°$) is shown in Fig. 5.17. The torque fluctuation has a period of 45° which is the angle between the two blades in eight blades wheel. The torque oscillation characteristics is therefore a function of blade distribution around the rotational axis. This resulted in eight cycles of torque oscillation in one revolution of the wheel. The maximum torque occurs at every 22.5° interval and minimum torque occurs around every 45° interval. In one revolution, there are two events of peak and dip torque; the maximum is 25.92 Nm at angular position of 271.5° and the minimum is 15.58 Nm at angular position of 90.69°.

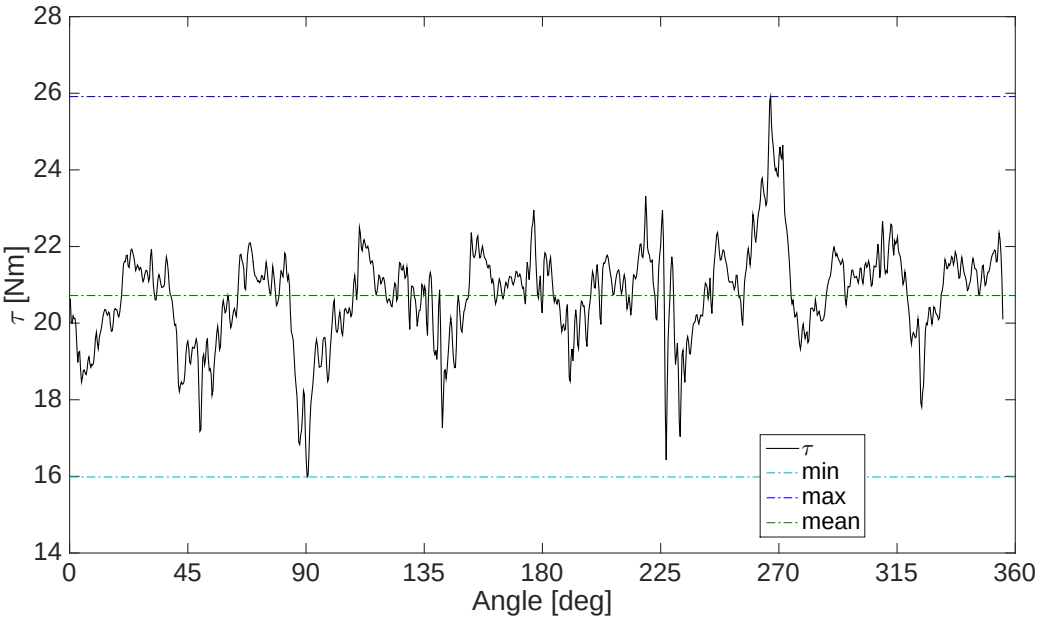

Figure 5.17: Torque versus rotational angle of the wheel for $N = 7.972$ rpm.

Model output for $N = 25.181$ rpm

The wheel model with eight sharp V-shaped BS0 blades is simulated at another operating point of $N = 25.181$ rpm rotational speed. Two dimensional flow field at various rotational angles of $0° - 45°$ for $N = 25.181$ rpm are shown in Figures 5.18a-5.18f corresponding to $0°, 6°, 21.2°, 28.74°, 36.3°$ and $45.35°$ rotational angle of the wheel at time step $26.2, 26.25, 26.35, 26.40, 26.45$ and 26.50 s respectively. The contours show the x-velocity distribution. After each 45° rotation of the wheel, the identical cycle repeats with the new blade entering the water surface. In comparison to the previous case, the higher speed of the wheel resulted in a substantial fluctuation on the upstream water depths with high amplitude upstream waves. This fluctuation on the water depth and the blade distribution around the rotational axis caused increased periodic loading on the wheel producing large amplitudes on the wheel torque. Fluid displacement caused by the entry of the blades is substantial as captured in Figures 5.18c and 5.18d. The formation of the vortex, flow separation and recirculation zone inside the blade cell is clearly noticed in Fig. 5.18b. The velocity distribution resulted in between -3.0 to 3.5 m/s.

In Figure 5.19, corresponding 3D pressure field is depicted for $N = 25.181$ at different rotational angles of 0°, 6°, 21.2°, 28.74°, 36.3° and 45.35° at the simulation time step of $26.2, 26.25, 26.35, 26.4, 26.45$ and 26.5 s respectively. Since the angle between two subsequent blades is 45°, the new blade enters the fluid and the similar phenomena occurs after every 45° rotation. A area of low pressure is distinguished on the upstream side around the tip of the blade in Figures 5.19a and 5.19b. The increased speed of the wheel created free surface distortion, large amount of splashing and fluid displacement at the entry as seen in Figures 5.19b, 5.19c and 5.19d. The fluid taken upward by the blades at the exit is remarkable. These observations are identical to the observations in the physical model at higher rotational speeds, i.e. free surface distortion, splashing, high amplitude waves on the upstream, fluid displacement by the blades on the upstream and the fluid taken upwards by the blades at the exit. The pressure drops as the blade moves downstream. As the fluid moves downstream imparting force on the wheel blades, pressure difference is created between the upstream and downstream side of the wheel.

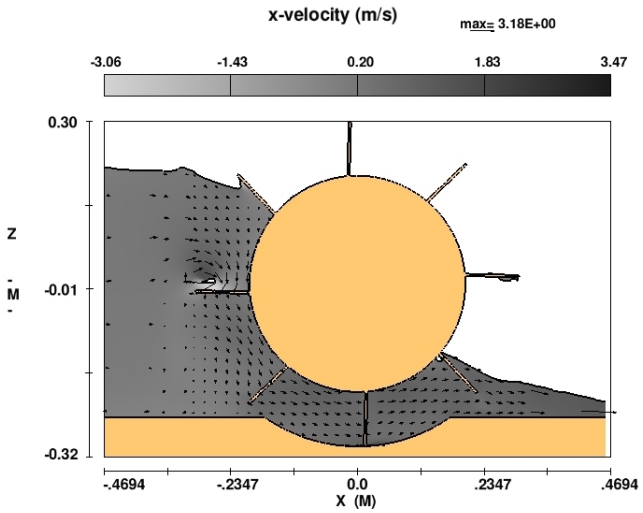

(a) $0^{\circ}, t = 26.20$ s

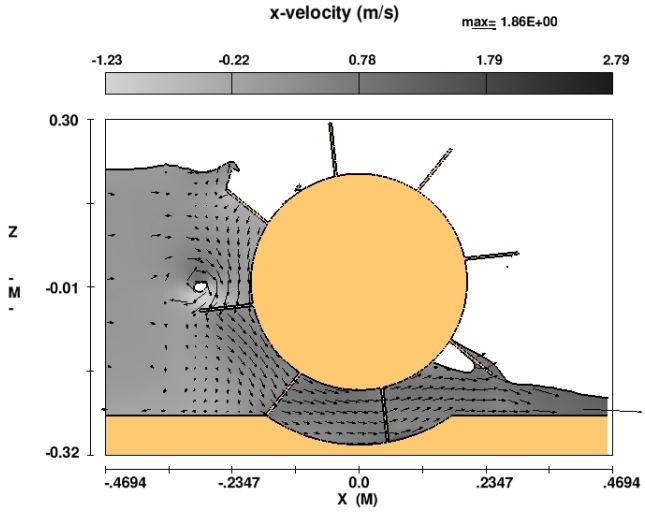

(b) $6^{\circ}, t = 26.25$ s

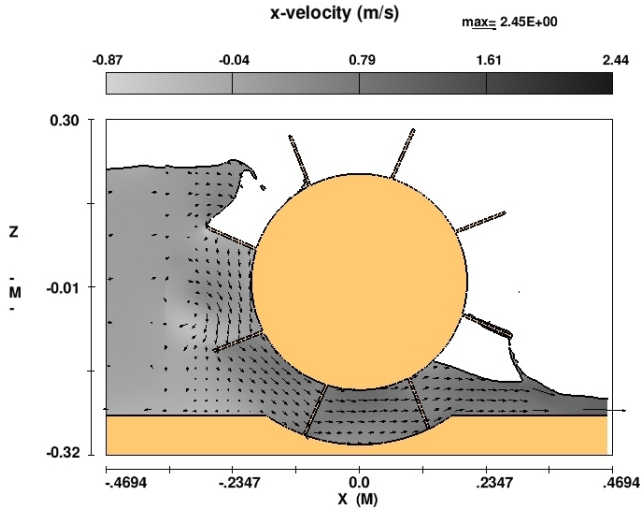

(c) $21.2^{\circ}, t = 26.35$ s

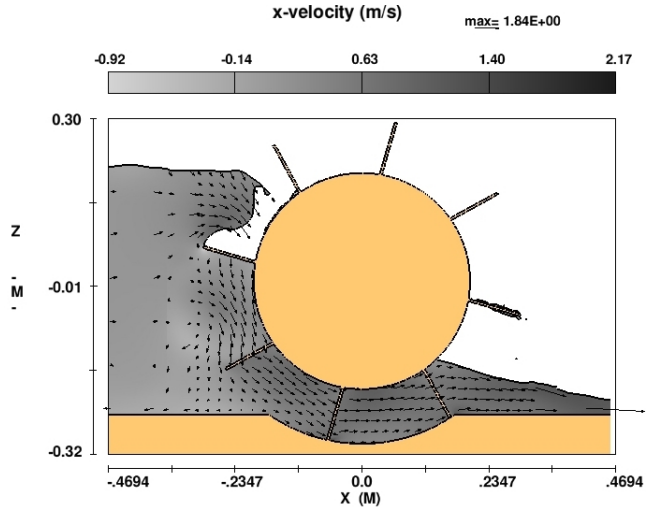

(d) $28.74^{\circ}, t = 26.4$ s

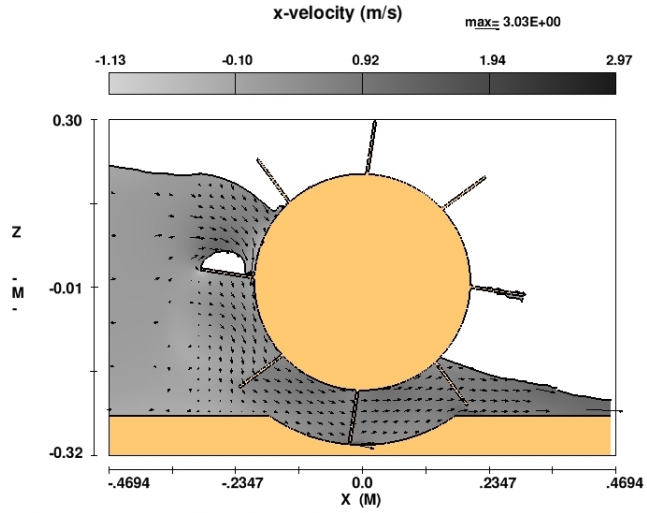

(e) $36.3^{\circ}, t = 26.45$ s

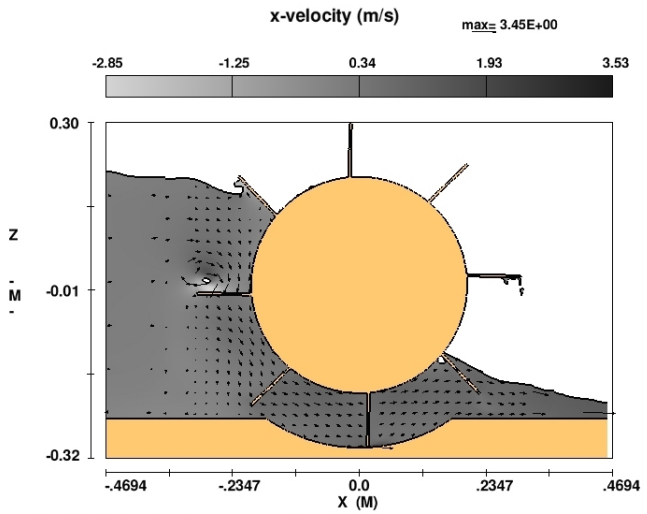

(f) $45.35^{\circ}, t = 26.5$ s

Figure 5.18: x-velocity contour and vectors for $N = 25.181$ rpm at different rotational angle. The change in the flow field between rotational angle of $0° - 45^{\circ}$ is shown. Flow is from left to right.

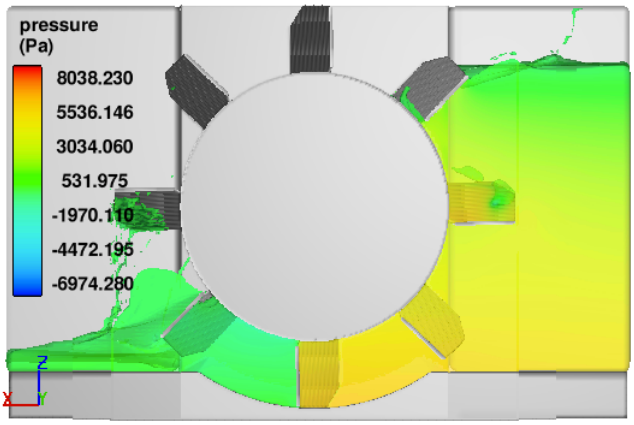

(a) 0°, $t = 26.2$ s

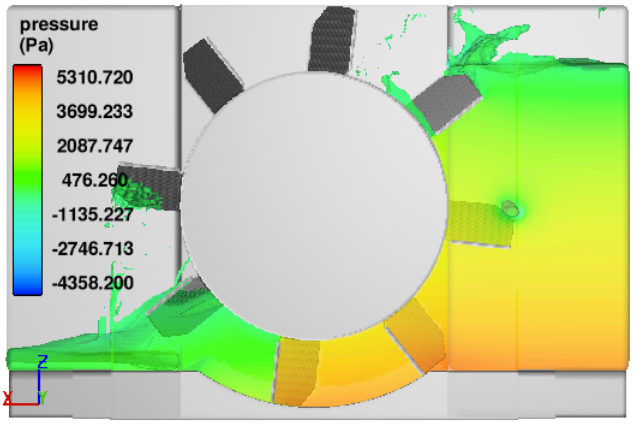

(b) 6°, $t = 26.25$ s

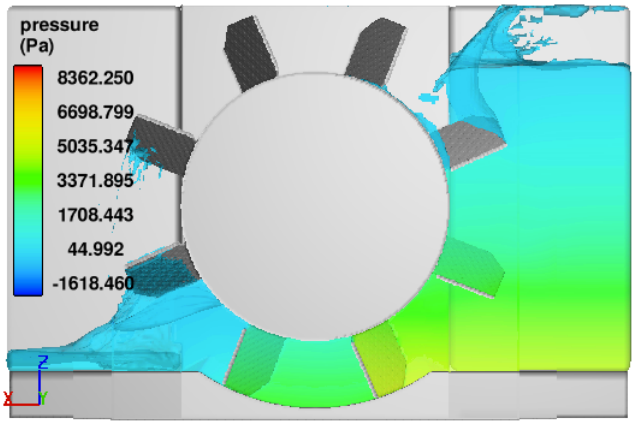

(c) 21.2°, $t = 26.35$ s

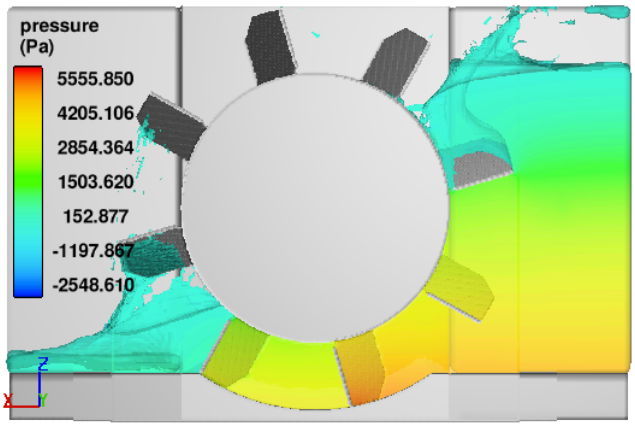

(d) 28.74°, $t = 26.4$ s

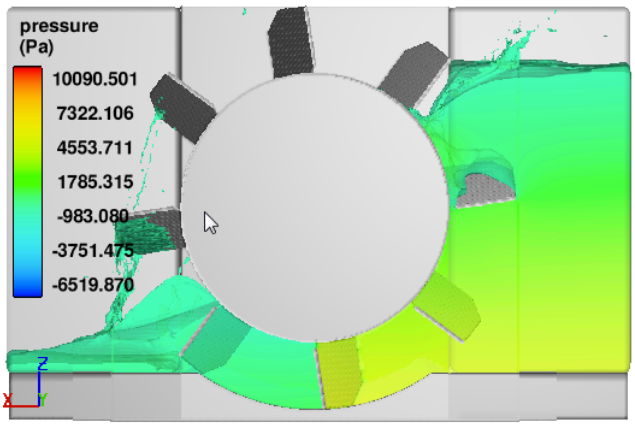

(e) 36.3°, $t = 26.45$ s

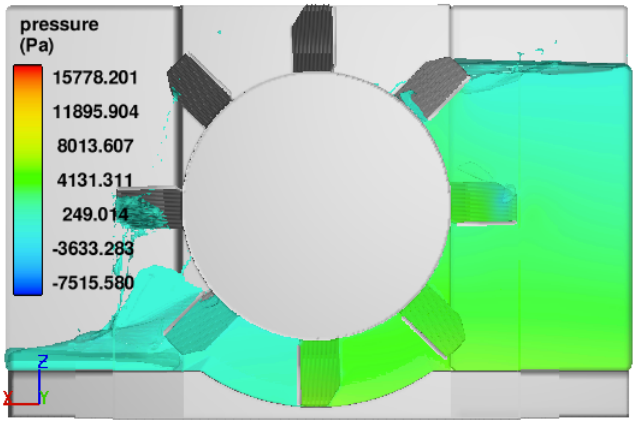

(f) 45.35°, $t = 26.5$ s

Figure 5.19: Pressure at different rotational positions for wheel with eight sharp blades BS0 at $N = 25.181$ rpm. Flow is from right to left.

The quality of total torque for one complete revolution of the wheel, (0° − 360°), is shown in Fig. 5.20 for the rotational speed of $N = 25.181$ rpm. As noticed in the previous case, the cycle of the torque remains at 45°. Within one cycle, there is a reoccurrence of intermittent regular ripples of same magnitude. The amount of torque within one cycle fluctuates noticeably for the mean value of 12.27 Nm with standard deviation of 2.27 Nm. The amplitude of the fluctuation in one revolution of the wheel remained nearly uniform in all cycles except the peak and the dip torque of 20.15 and 0.76 Nm noticed at the rotational positions of 267.5° and 270.5° respectively.

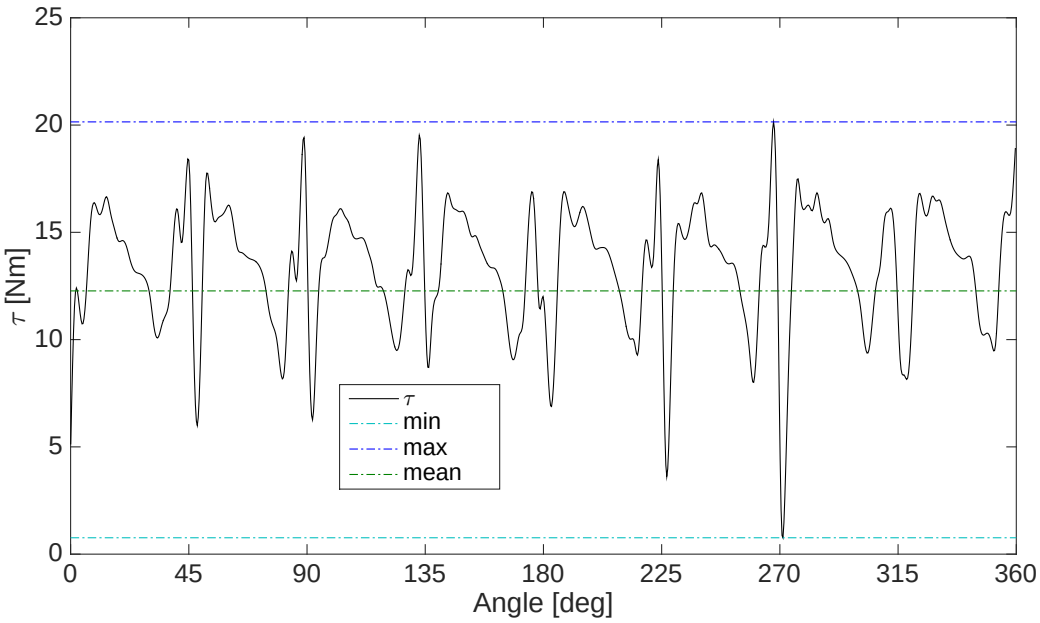

Figure 5.20: Torque versus rotational angle of the wheel for $N = 25.181$ rpm.

The output of the main variables for $N = 25.181$ rpm are presented in Fig. 5.21 with their corresponding mean and standard deviation. The simulation ran for 30 s and the mean was taken from 20 to 30 s of simulation time. These results show that the fluctuation of the variables about the mean value is significant at higher rotational speed as compared to the previous case of $N = 7.971$ rpm (see Table 5.11). The upstream water depth shows highest fluctuation with standard deviation of ±3.90 cm. The mean value of the variables and their corresponding standard deviation for $N = 25.181$ rpm are summarised in Table 5.12.

Table 5.12: Numerical model output for $N = 25.181$ rpm

Parameter	Mean	$\pm\sigma_s$
Q (l/s)	16.79	±0.90
τ (Nm)	12.27	±2.27
h_1 (cm)	45.41	±3.90
h_2 (cm)	6.59	±0.73
H (cm)	37.98	±2.83

Above described cases are further analysed to predict the full performance curve of the numerical model. As described previously, the rotational speed and torque as well as the rotational speed and

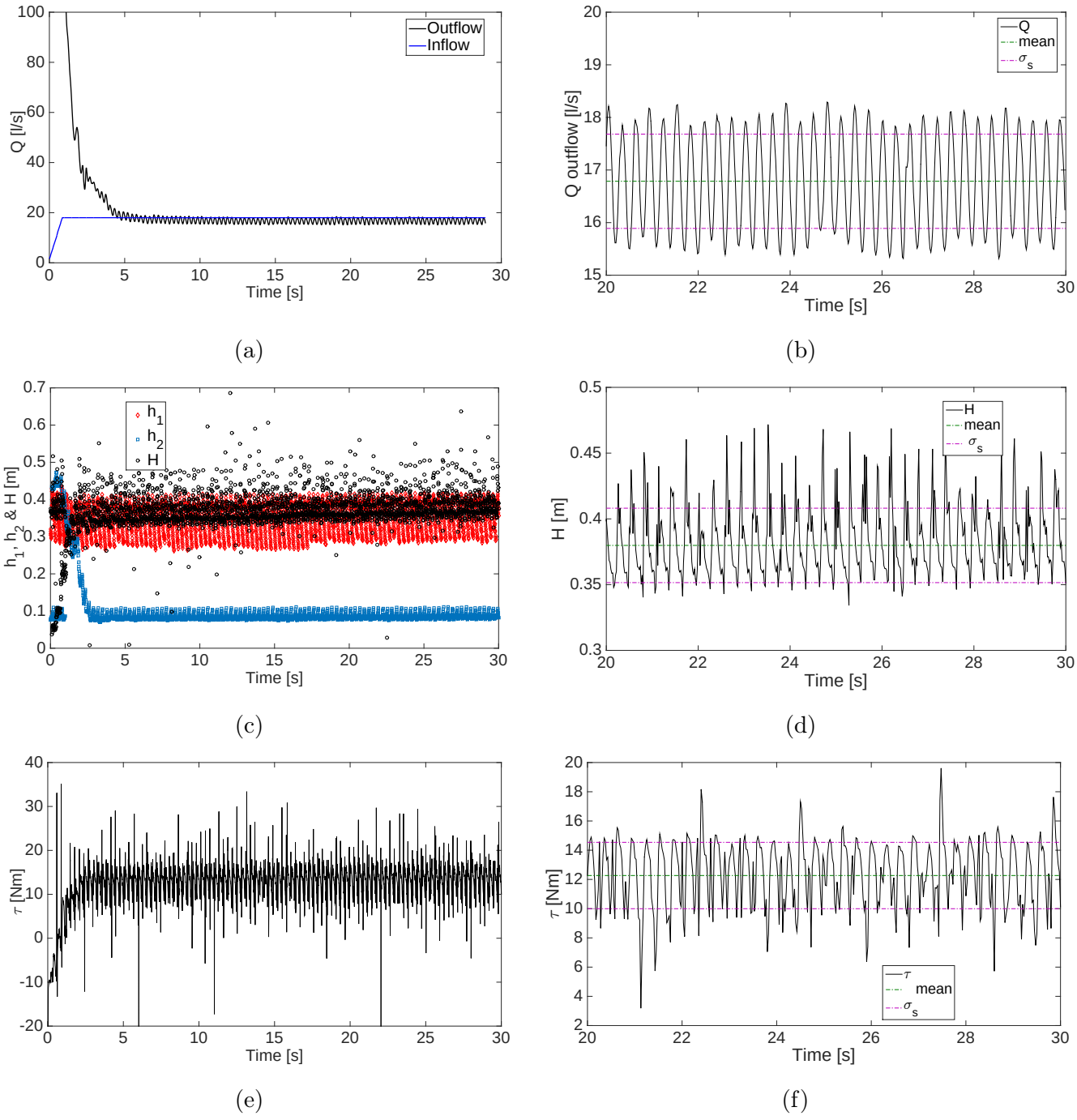

Figure 5.21: Model output for $N = 25.181$ rpm as a function of simulation time. (a) Flow rates at the inlet and outlet boundary; (b) Outflow fluctuation and mean and standard deviation of Q; (c) Upstream and downstream water levels and the total head; (d) Total head fluctuation and its mean and standard deviation; (e) Total torque; (f) Torque ripple and its mean and standard deviation.

flow rate acquire linear relationship at constant water depths. By having the equation of these linear models, the power output and efficiency at different rotational speeds can be calculated. In Figures 5.22a and 5.22b, the numerical and physical model results are compared with corresponding uncertainties in both physical model and numerical model results. The total uncertainty of the numerical model is evaluated using the Grid Convergence Index (GCI) in Chapter 4. The numerical

model results appear to be in good agreement with the measured values. Although the numerical model over predicts both the power output and the efficiency at higher rotational speeds, the computed results lie within the defined uncertainty bounds around the BEP region.

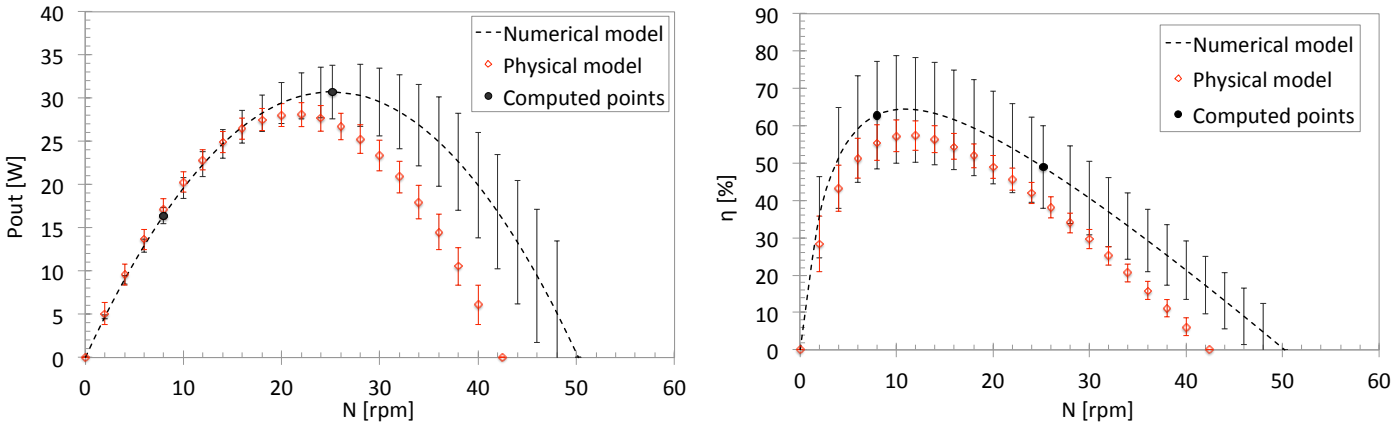

(a) (b)

Figure 5.22: Numerical and physical model results for eight BS0 blades wheel (a) Power output (b) Efficiency

The power output and efficiency at the computed points from the numerical model and measured values on the physical model are summarised in Table 5.13 along with their corresponding uncertainty values. As noticed the measured and computed power output and efficiency values are within the defined uncertainty bounds. High uncertainty in efficiency values, i.e. 14.15% and 10.83% are depicted in the numerical model results at $N = 7.971$ rpm and $N = 25.181$ rpm respectively. As described by the Eq. 3.17, the uncertainty bound in efficiency is the propagation of uncertainties in total head, flow rate, rotational speed and the torque.

Table 5.13: Comparison of physical and numerical model results for eight BS0 blades wheel

Parameter	$N = 7.971$ rpm		$N = 25.181$ rpm	
	Measured	Computed	Measured	Computed
P_{out} (W)	17.18 ± 1.17	16.42 ± 0.97	27.18 ± 1.54	30.73 ± 3.13
η (%)	55.46 ± 4.72	61.58 ± 14.15	39.74 ± 2.79	47.96 ± 10.83

5.2.2 Numerical results of curved blade shape BS1

The results for wheel with eight sharp V-shaped blades BS0 has shown that the sharp blades produce high amount of torque fluctuation due to cyclic nature of loading on the wheel, which is not desirable for the structural safety of the wheel. Simulations on wheel with curved blade shapes BS1 shown in Fig. 3.10 are done at two different rotational speeds of 8 rpm and 18 rpm. The nested mesh described in Chapter 4 with a size of 10 mm, 5 mm and 2.5 mm was too coarse to resolve the blades BS1 due to the curvature on the blade geometry. The mesh size of the three nested mesh blocks is therefore reduced to 8 mm, 4 mm and 2 mm. This created substantial increase on the simulation time to around 21 days for 20 s of simulation time compared to 9 days for 30 s simulation time in case of sharp V-shaped BS0 blades. The quality of the total torque output and other main variables for both cases is studied thoroughly.

Model output for $N = 8$ rpm

The flow field of the wheel with curved blade shape BS1 at the rotational speed of $N = 8$ rpm is shown in Fig. 5.23. Number of blades is reduced to six following the results of the blade number tests on the physical model for sharp blades BS0. The angle between two blades is now increased to 60°. Velocity contours and vector fields are shown for rotational positions of $0° - 60°$. The rotational positions refers to 0°, 12°, 24°, 36°, 48° and 60° at time step of 15, 15.25, 15.50, 15.75, 16 and 16.25 s respectively. Another five same cycles continue in one complete revolution of 360°. The recirculation of flow appears at the angular position of 12° (Fig. 5.23b) and continues to exists up to 36° position (Fig. 5.23d). A closer look at the flow field reveals that the circulation of flow in all angular positions seems to be reduced in comparison to the sharp blades case of $N = 7.972$ rpm shown in Fig. 5.14. Region of very low velocity is also noticed at the blade exit area at 48° and 60° positions (Fig. 5.23e and 5.23f). The flow velocity ranges from -0.5 m/s to 2.3 m/s.

A three dimensional flow fields for $N = 8$ rpm for the wheel with BS1 blades are shown in Fig. 5.24. These pressure fields corresponds to 0°, 12°, 24°, 36°, 48° and 60° at time steps of 15, 15.25, 15.50, 15.75, 16 and 16.25 s. The curved shape of the blades allowed smoother entry into the fluid at the upstream and therefore less disturbances on the free surface. Although the surface disturbance and waves on the upstream side of the wheel tends to be reduced due to the curved shape of the blades, the curved chamfered blade edges enhanced leakage losses through the side clearance as seen in Figures 5.24b, 5.24c and 5.24d. The leakage flow through the v-shaped air vent is also clearly visible. Due to the curved shape of the blades, the blade cells are emptied easily at the exit. The pressure difference between the upstream and downstream side of the wheel creates force on the wheel blades. The pressure reaches maximum as the blade reaches the lowermost point in the curvature of the shroud and drops as the blade exit at the downstream.

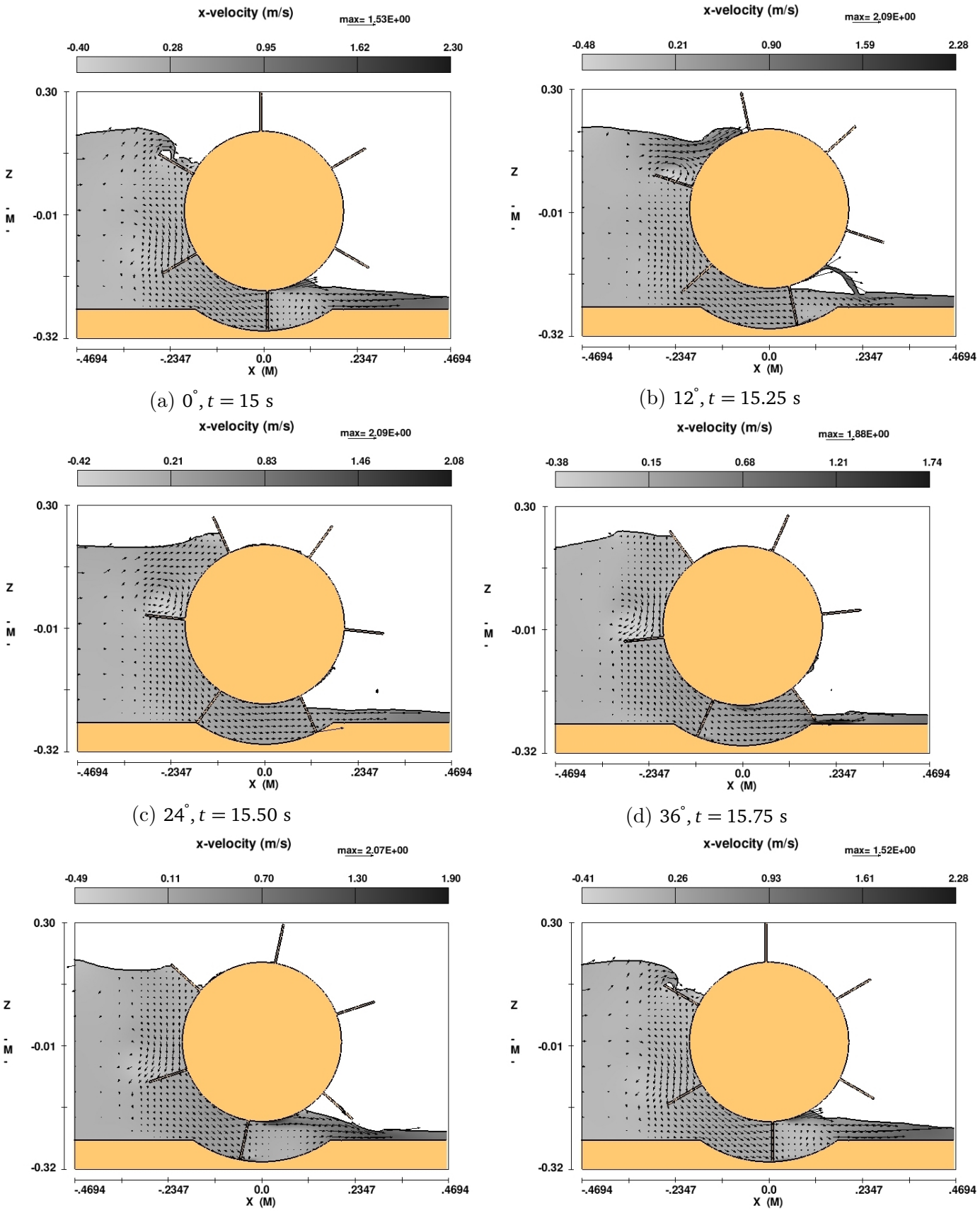

(a) $0^{\circ}, t = 15$ s

(b) $12^{\circ}, t = 15.25$ s

(c) $24^{\circ}, t = 15.50$ s

(d) $36^{\circ}, t = 15.75$ s

(e) $48^{\circ}, t = 16$ s

(f) $60^{\circ}, t = 16.25$ s

Figure 5.23: x-velocity contour and vectors for blade shape BS1 for $N = 8$ rpm at different rotational angle. The change in the flow field between rotational angle of $0° - 60°$ is shown. Flow is from left to right.

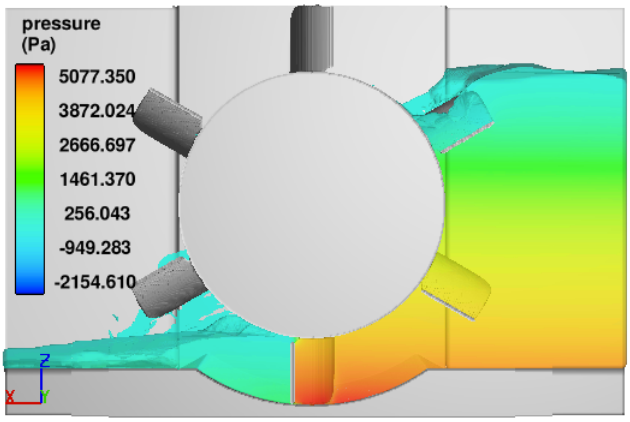

(a) 0°, $t = 15$ s

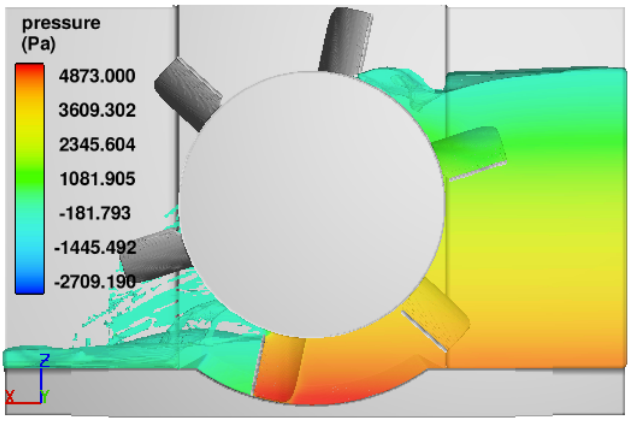

(b) 12°, $t = 15.25$ s

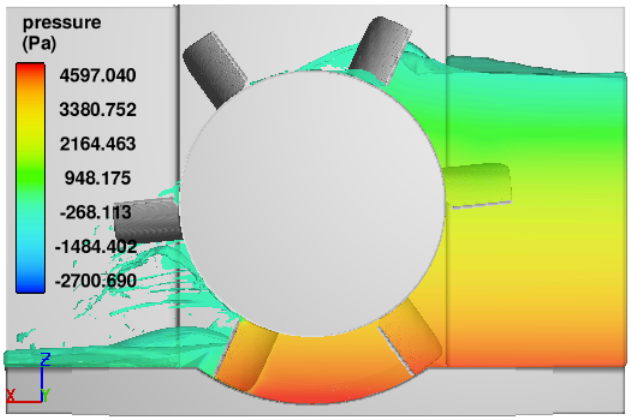

(c) 24°, $t = 15.50$ s

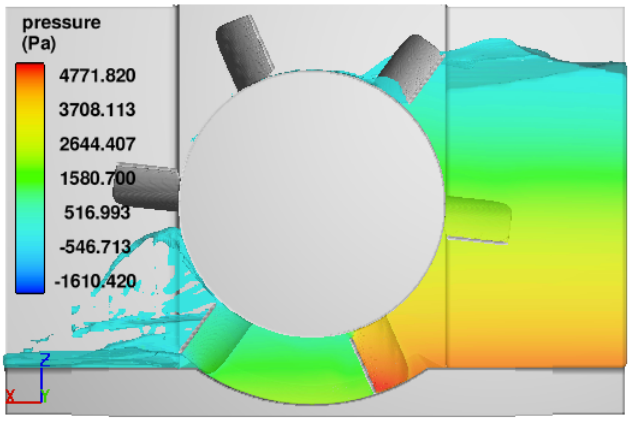

(d) 36°, $t = 15.75$ s

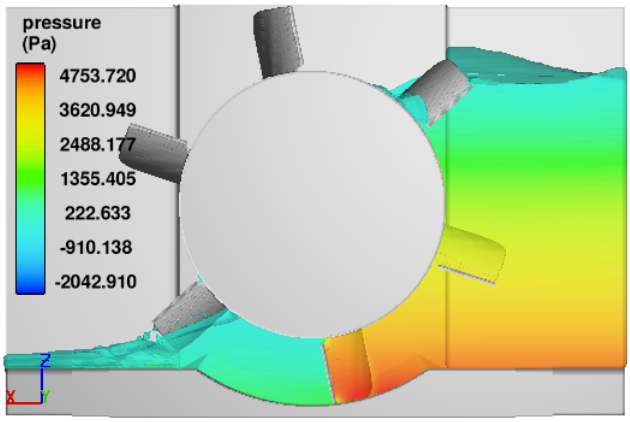

(e) 48°, $t = 16$ s

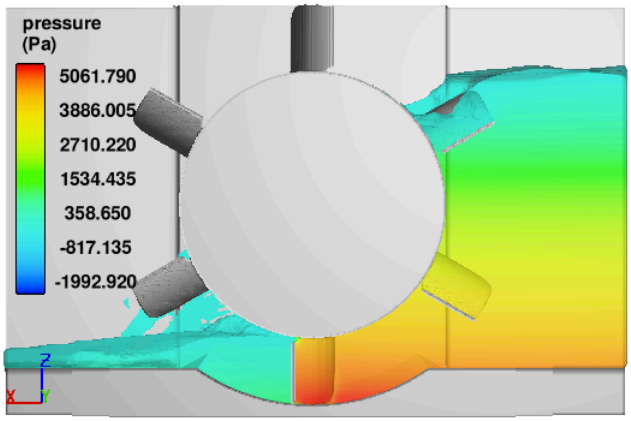

(f) 60°, $t = 16.25$ s

Figure 5.24: Pressure distribution for wheel with six curved blade BS1 at $N = 8$ rpm at different rotational positions of the wheel. Flow is from right to left.

The variation of total torque in one complete revolution of the wheel is shown in Fig. 5.25a. The distribution of blades resulted in a 60° angle between two consecutive blades. The torque cycle also resulted in a 60° period as expected. The amplitude of the torque oscillations remains nearly uniform in all cycles. The maximum torque of about 23 Nm occurs at every 30° rotational angle and the minimum torque occurs at every 60° interval with a magnitude of about 17.35 Nm. There are no occurrences of outlying peaks and drops on the total torque.

In Figure 5.25b, torque for wheel with eight sharp BS0 blades and six curved BS1 blades are shown in higher resolution. The details of fluctuations of the torque in both cases shows that the peaks and the torque fluctuations on the six curved blades wheel are smaller in comparison to the eight sharp blades wheel which implies that the torque quality has improved in case of wheel with six curved blades BS1.

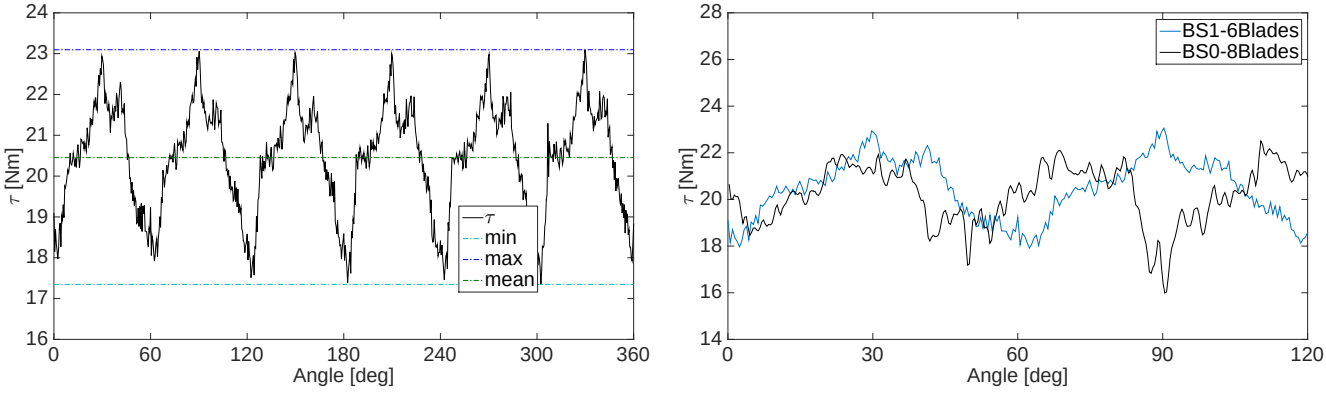

(a) (b)

Figure 5.25: (a) Torque for blade BS1 at different rotational angles and (b) Torque comparison for wheel with eight BS0 and six BS1 blades.

Output of the main variables are plotted in Fig. 5.26. On the left side, the time history development of flow rate, flow depths, total head and torque over the simulation time of 20 s is shown with the plot of oscillation, mean and standard deviation of the corresponding parameter at the right side. As expected, the frequency of the curves is decreased due to decreased number of blades. The oscillation on the upstream and downstream flow depths is much more reduced than in case of blade BS0. This could describe the reduced amount of splashing and flow separation in case of wheel with curved BS1 blades. Moreover, the oscillations on the total torque output is uniform. Total head however shows oscillations of greater magnitude. The fluctuation of exit flow velocity at different rotational angles of the wheel as noticed in Fig. 5.23 could explain these oscillations on the total head. The mean value of these parameters are taken from 10 to 20 s of simulation time and presented in Table 5.14.

Table 5.14: Numerical model output for blade BS1 for $N = 8$ rpm

Parameter	Mean	$\pm\sigma_s$
Q (l/s)	8.46	±3.19
τ (Nm)	20.45	±1.30
h_1 (cm)	44.59	±1.60
h_2 (cm)	5.23	±0.69
H (cm)	38.50	±7.35

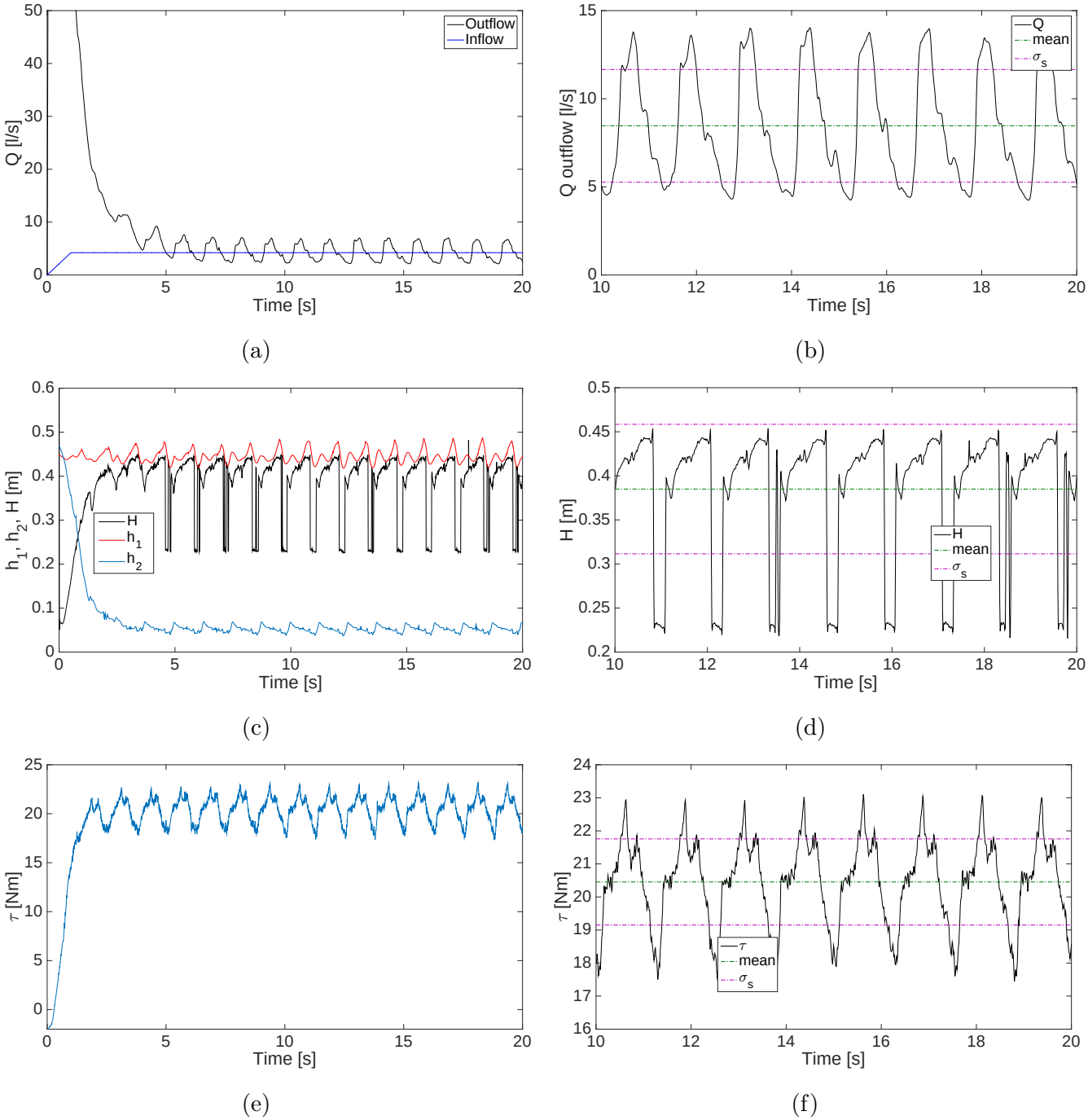

Figure 5.26: Model output for BS1 for $N = 8$ rpm as a function of simulation time. (a) Flow rates at the inlet and outlet boundary; (b) Outflow fluctuation, mean and standard deviation of Q; (c) Upstream and downstream water levels and the total head; (d) Total head fluctuation and its mean and standard deviation; (e) Total torque; (f) Torque fluctuation, its mean and standard deviation.

A restart simulation was performed for this case using the existing simulation of $N = 8$ rpm case of wheel model with six curved shape BS1 blades. The boundary conditions are changed accordingly and simulation was restarted from 15 s of simulation time. 5 s of simulation time was enough to get the converged solution.

The two dimensional x-velocity profiles at different rotational positions of $0 - 360°$ of the wheel are captured and shown in Fig. 5.27a-5.27f. These flow fields refer to the angular position of $0°, 10.2°, 15.6°, 31.8°, 48°$ and $60.96°$ at time step of 15.55, 15.65, 15.70, 15.85, 16 and 16.12 s respectively. The same cycle will repeat as the new blade enters the fluid. Zones of recirculation still persists at 15.6° and 31.8° rotational positions as shown in Figures 5.27c and 5.27d. The extent of fluid displacement and recirculation however is observed to be much reduced in comparison to the sharp BS0 blades (see Fig. 5.18). The flow velocity differs between -2.4 and 3.2 m/s.

A three dimensional flow field for $N = 18$ rpm is shown in Fig. 5.28 with the pressure contours. These pressure fields also refer to angular positions of the wheel at $0°, 10.2°, 15.6°, 31.8°, 48°$ and $60.96°$ at time step of 15.55, 15.65, 15.70, 15.85, 16 and 16.12 s respectively. Both negative and positive pressure increase as the speed of the wheel increases as compared to the previous case of wheel with BS1 blades at $N = 8$ rpm. In comparison to the wheel with sharp BS0 blades, the upstream surface disturbance due to the blade impact and the fluid taken upward by the blades at the exit is much reduced in this case due to curved shape of the blades. The smoother entry of the blades on the upstream side of the wheel created smaller surface waves than in the case of sharp BS0 blades. The curved shape of the blade also eased the blade cell emptying and minimised the fluid taken upwards on the blade cells at the exit. Leakage flow through the gaps seems to be smaller at increased flow rate than at the previous case of $N = 8$ rpm.

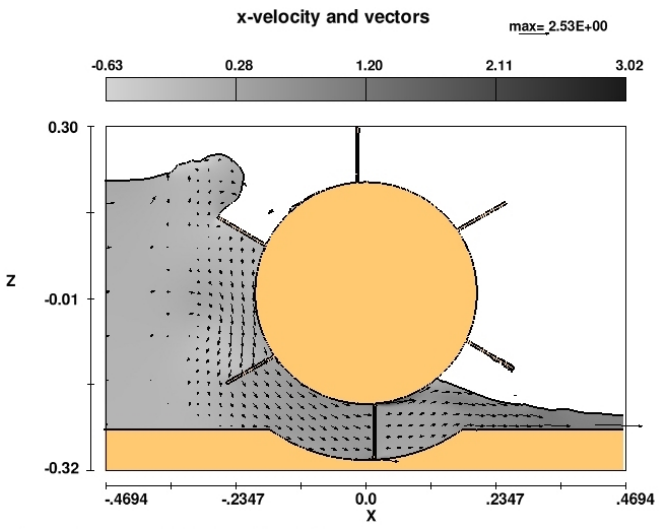

(a) $0^{\circ}, t = 15.55$ s

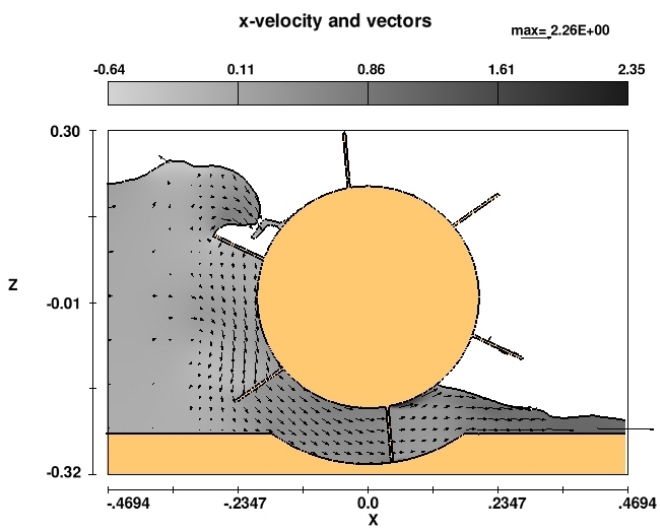

(b) $10.2^{\circ}, t = 15.65$ s

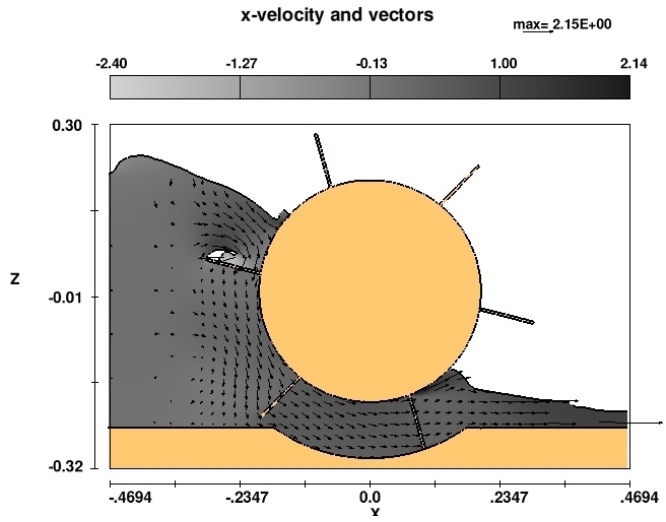

(c) $15.6^{\circ}, t = 15.70$ s

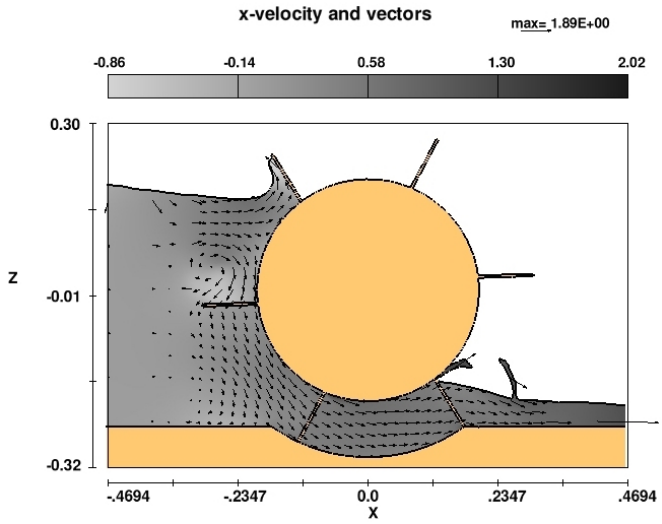

(d) $31.8^{\circ}, t = 15.85$ s

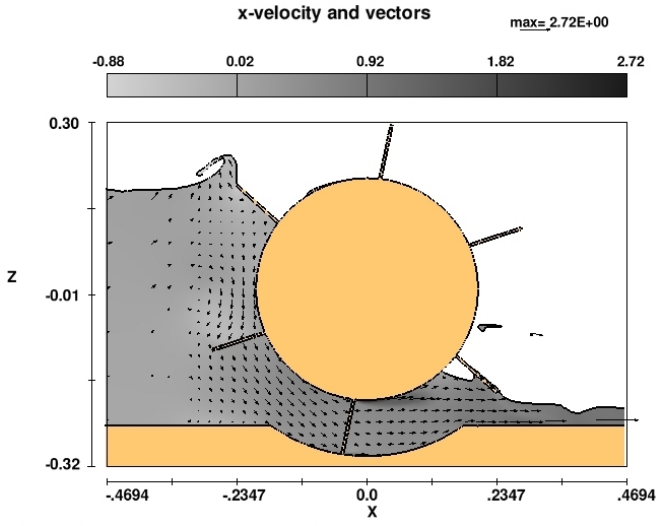

(e) $48^{\circ}, t = 16$ s

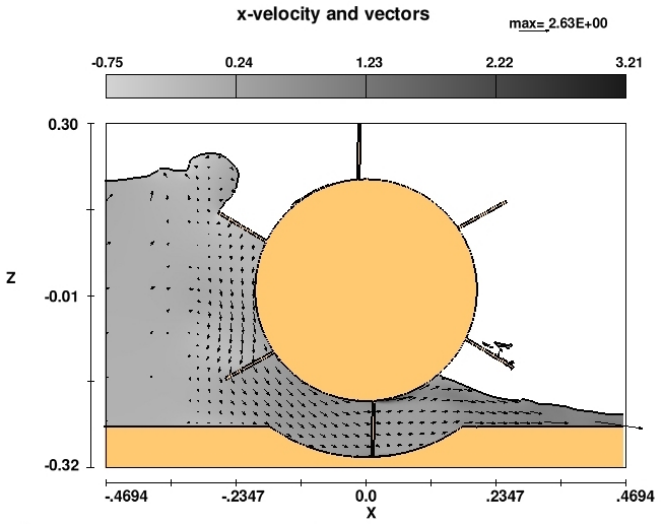

(f) $60.96^{\circ}, t = 16.12$ s

Figure 5.27: x-velocity contour and vectors for blade shape BS1 for $N = 18$ rpm at different rotational angle. The change in the flow field between rotational angle of $0° - 60^{\circ}$ is shown. Flow is from left to right.

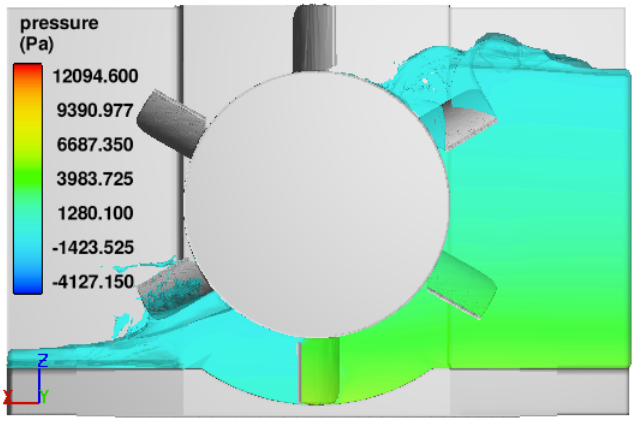

(a) $0°, t = 15.55$ s

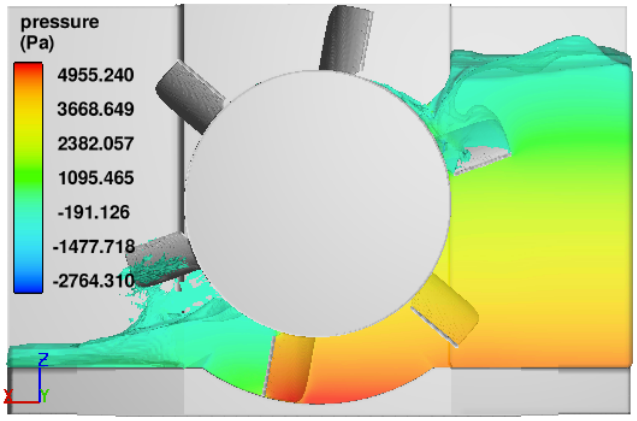

(b) $10.2°, t = 15.65$ s

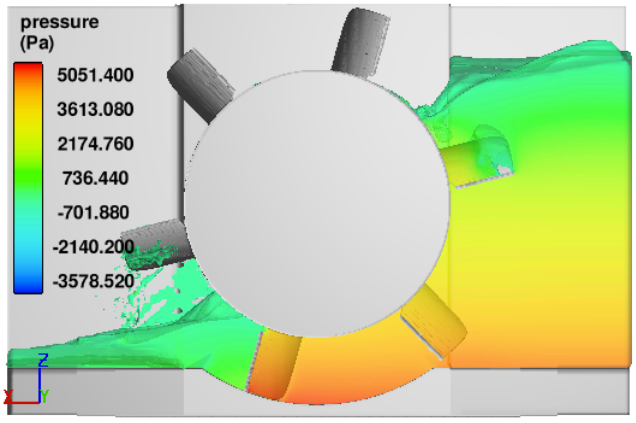

(c) $15.6°, t = 15.70$ s

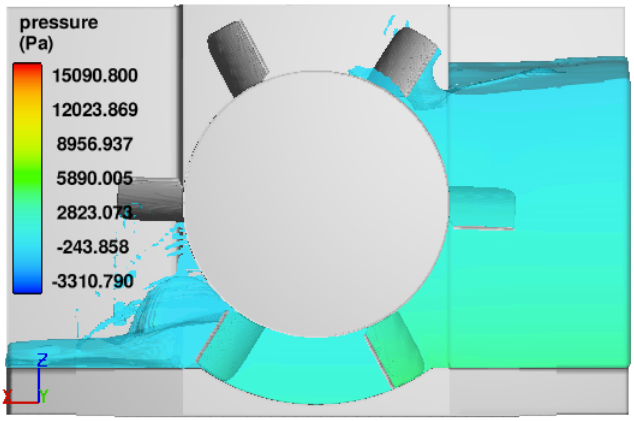

(d) $31.8°, t = 15.85$ s

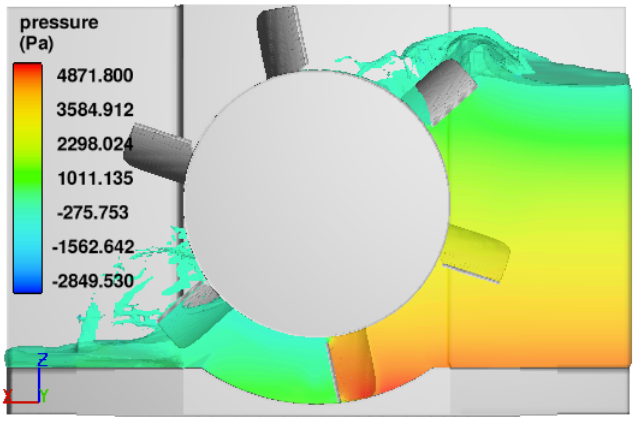

(e) $48°, t = 16$ s

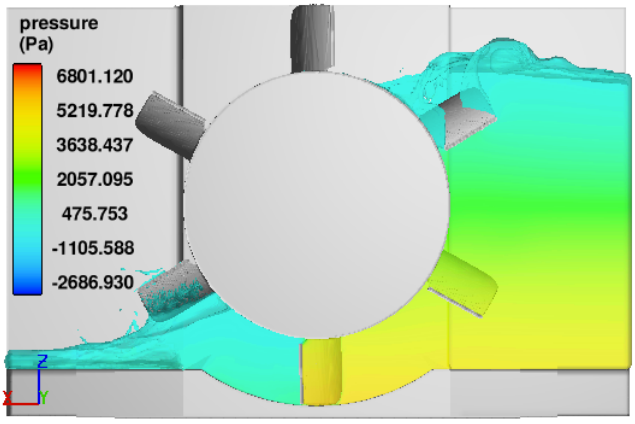

(f) $60.96°, t = 16.12$ s

Figure 5.28: Pressure distribution for wheel with six curved blade BS1 at $N = 18$ rpm at different rotational positions of the wheel. Flow is from right to left.

The torque fluctuation at different angular positions of the wheel is plotted in Fig. 5.29. The torque has a period of approximately 60° with six cycles in one complete revolution of the wheel and fluctuates with regular peaks and drops depending on the blade position. The minimum is at 0° position and increases with increasing angle and reaches peak at around 30° rotational angle (see Fig. 5.27d) and starts to drop again and reaches another minimum value at around 60° position.

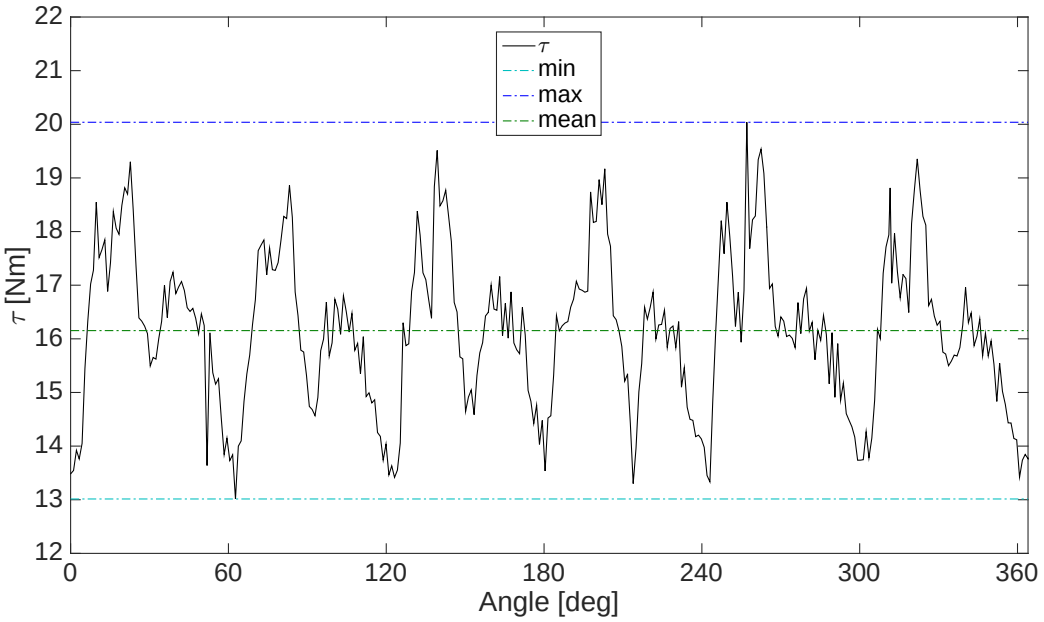

Figure 5.29: Torque versus rotational angle for blade BS1 at $N = 18$ rpm.

The model output for blades BS1 for $N = 18$ rpm are shown in Fig. 5.30. The time history development of flow rate (Q), head (H) and torque (τ) and their mean and standard deviation is shown. Only 6 s of simulation time was enough to get the statistically stationary solution. The mean is taken from 16 to 20.5 s simulation time. The mean and standard deviation of these variables is listed in Table 5.15. The fluctuation of the upstream flow depth (h_1), the total head (H) and torque (τ) is much smaller as compared to the blades BS0 shown in Fig. 5.21. This gives an indication that the flow disturbance at the entry is reduced due to the curved blade shape. Moreover, the curved blade shape could have possibly enhanced the blade evacuation process at the exit.

Table 5.15: Numerical model output for curved blade BS1 for $N = 18$ rpm

Parameter	Mean	$\pm\sigma_s$
Q (l/s)	14.29	±5.02
τ (Nm)	16.16	±1.36
h_1 (cm)	44.57	±2.45
h_2 (cm)	6.60	±0.34
H (cm)	38.58	±1.12

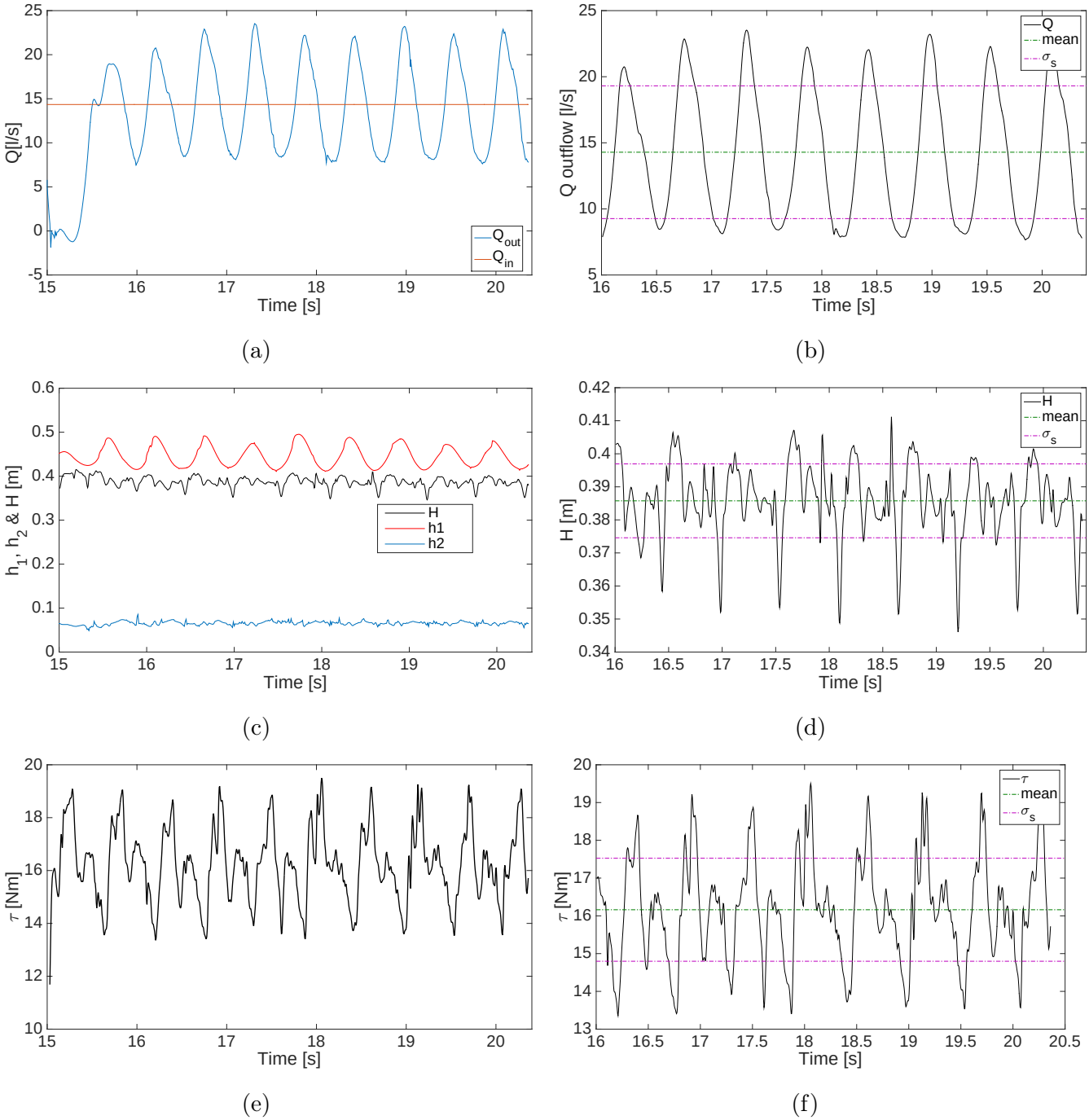

Figure 5.30: Model output for BS1 for $N = 18$ rpm as a function of simulation time. (a) Flow rates at the inlet and outlet boundary; (b) Outflow fluctuation, mean and standard deviation of Q; (c) Upstream and downstream water levels and the total head; (d) Total head fluctuation and its mean and standard deviation; (e) Total torque; (f) Torque oscillation, its mean and standard deviation.

Based on the above results of the computed cases for curved blades BS1, full performance curves for wheel with six BS1 blades are derived and plotted along with their uncertainties and compared with the wheel performance with six sharp BS0 blades in Fig. 5.31. The results show that both power output and efficiency of the wheel with BS1 is higher than the wheel with BS0 blades only at high rotational speeds. At low rotational speeds, the numerical model slightly under estimates the power output and efficiency. As discussed above, the increased leakage flow through the side gaps due to curved blade edges in BS1 blades could be the reason for this drop in performance. But at the same time, the uncertainties associated with the numerical model are also large which makes it difficult to conclude whether the BS1 blades performed better than the BS0 blades. Nevertheless, the qualitative performance of BS1 should not be overlooked from the operational point of view.

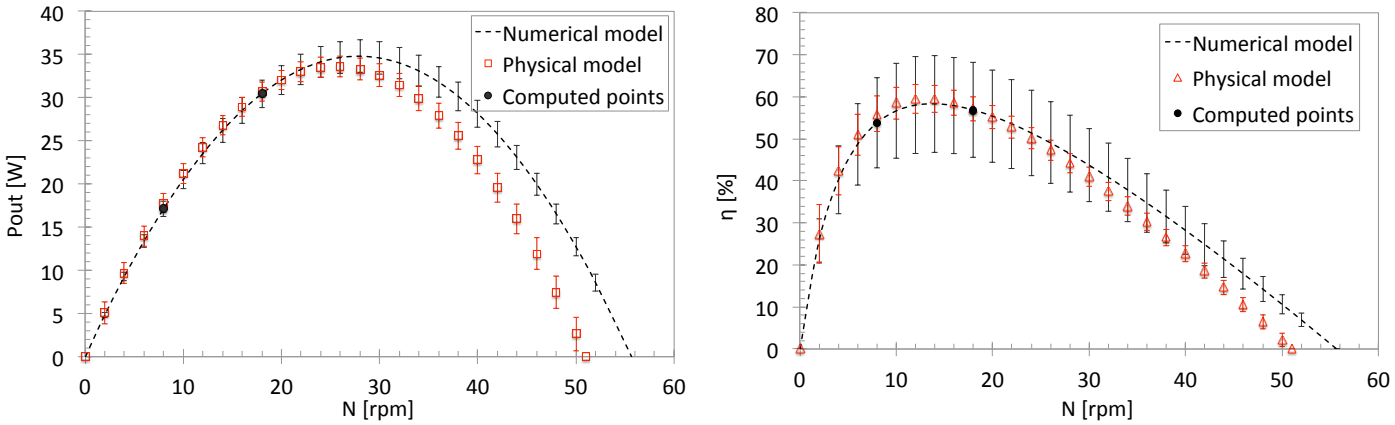

Figure 5.31: Numerical results comparison of six BS1 blades with physical model results of six BS0 blades wheel. The physical model refers to the wheel with six sharp BS0 blades and numerical results refers to the wheel with six curved BS1 blades (a) Power output (b) Efficiency

The BEP with efficiency of 59.57 ± 3.48% was at 12 rpm in case of physical model with sharp BS0 blades. The numerical model predicted the BEP of 55.44 ± 10.98% for the wheel with BS1 blades at $N = 14$ rpm. Power output and efficiency at the computed points for the wheel with six curved BS1 blades are compared with the physical model results for the wheel with six sharp BS0 blades and summarised in Table 5.16 along with their uncertainty bounds.

Table 5.16: Comparison of numerical model results of six BS1 blades wheel with physical model results of six BS0 blades wheel

Parameter	$N = 8$ rpm		$N = 18$ rpm	
	Measured (BS0)	Computed (BS1)	Measured (BS0)	Computed (BS1)
P_{out} (W)	17.78 ± 1.16	16.27 ± 0.85	30.72 ± 1.11	28.93 ± 1.53
η (%)	55.93 ± 4.26	51.10 ± 10.15	57.13 ± 2.87	54.03 ± 10.69

5.2.3 Numerical results of modified shroud shape SS1

A three dimensional numerical model of the wheel with six curved shape BS1 blades and the modified shroud shape SS1 shown in Fig. 3.11 is simulated. The shroud is modified to remove the downstream curvature and to allow the accelerated exit of the water on the downstream of the wheel. This modification of the shroud shape introduced a potential head to the wheel. To resolve the curved blades of the wheel properly, a finer mesh size with three nested mesh blocks of 8 mm, 4 mm and 2 mm were used, which required much longer computational time. Two different rotational speed of the wheel, 8 rpm and 18 rpm, were simulated. Performance of the wheel at these two operating points are elaborated in the following sections.

Model output for $N = 8$ rpm

The velocity distribution around the wheel at the rotational speed of $N = 8$ rpm is shown in Fig. 5.36. The angle between two blades is 60°, therefore velocity contours and vector fields are shown for rotational positions of 0°, 12°, 24°, 36°, 48° and 60° at the time step of 22.50, 22.75, 23.00, 23.25, 23.50 and 23.75 s respectively. The same cycle continues to make a complete revolution of the wheel. As noticed, there is a occurrence of minor flow recirculation within the blade cells at the angular position of 12°, 24° and 36° (Figures 5.32b, 5.32c and 5.32d). Within the blade cells, flow is streamlined and accelerated at the downstream. In comparison to the case of shroud shape SS0 at the same wheel speed of 8 rpm, the flow velocities are higher. Free surface disturbance seems to be reduced in this case.

A three dimensional pressure field for the new shroud shape SS1 and wheel with curved BS1 blades are shown in Fig. 5.33 at $N = 8$ rpm for different wheel positions of $0°-60^{\circ}$. These rotational positions refer to 0°, 12°, 24°, 36°, 48° and 60° at the time step of 22.50, 22.75, 23.00, 23.25, 23.50 and 23.75 s respectively. Unlike in previous cases, there is no presence of very low pressure zone at the inlet. Highest pressure is predicted at the lowermost position of the wheel blade and drops as the blade leaves the shroud and moves upward at the exit. Leakage flow through the air vent and side gaps is apparent. There is a very low or no occurrence of strong impact, splashing and the surface disturbance at the blade entry. However, losses through the air vent and the side gap looks remarkable.

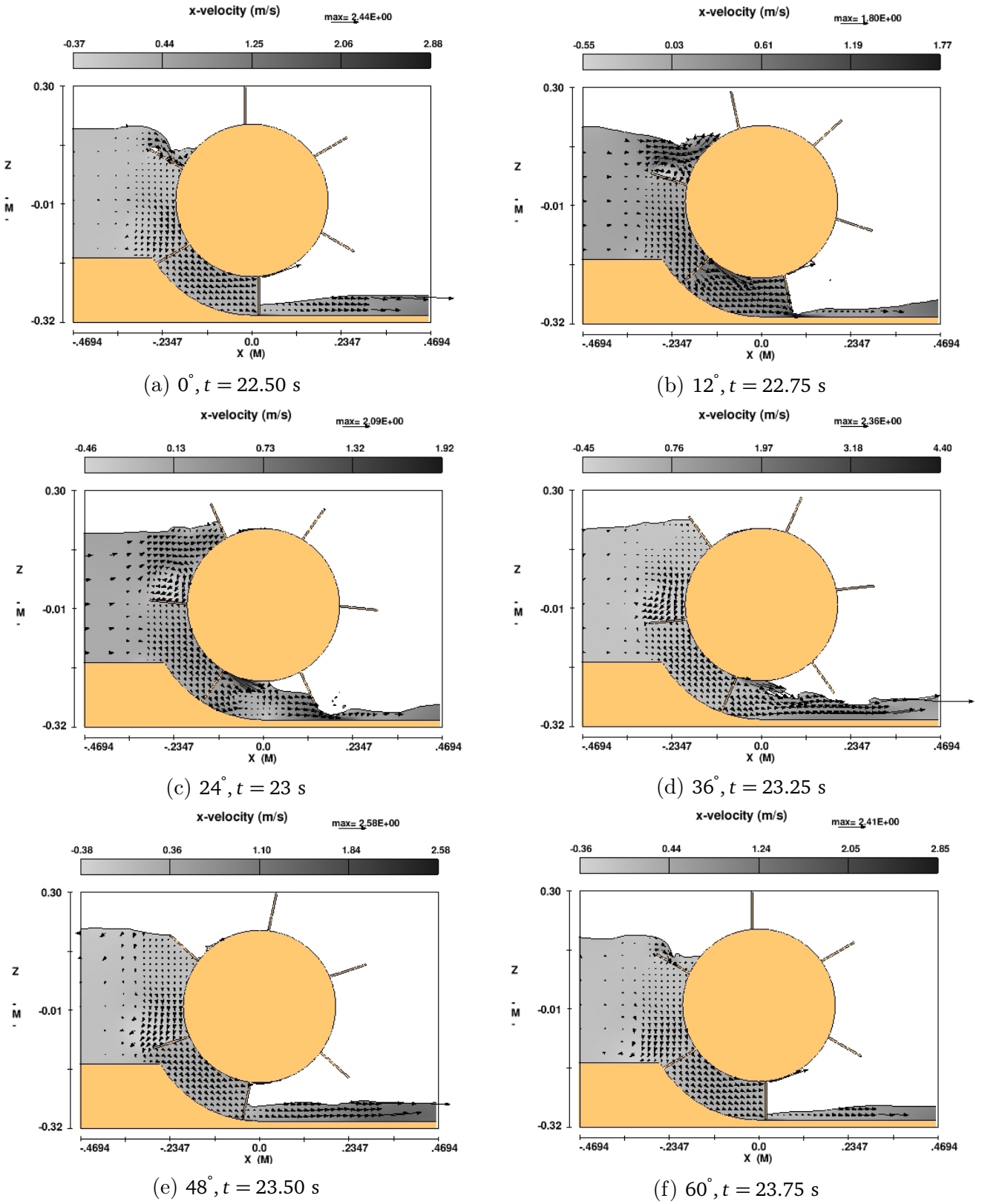

(a) $0^{\circ}, t = 22.50$ s

(b) $12^{\circ}, t = 22.75$ s

(c) $24^{\circ}, t = 23$ s

(d) $36^{\circ}, t = 23.25$ s

(e) $48^{\circ}, t = 23.50$ s

(f) $60^{\circ}, t = 23.75$ s

Figure 5.32: x-velocity contour and vectors for modified shroud shape SS1 and wheel with curved blade shape BS1 for $N = 8$ rpm at different rotational angles. The flow field is shown for rotational angle of $0° - 60^{\circ}$. Flow is from left to right.

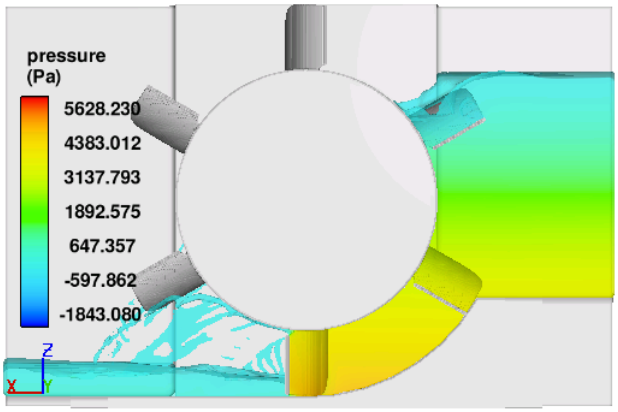

(a) 0°, $t = 22.50$ s

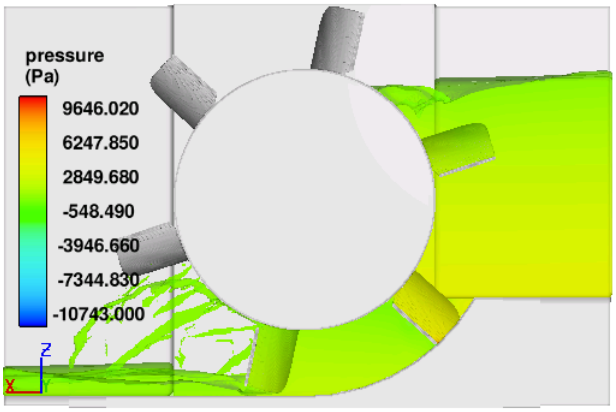

(b) 12°, $t = 22.75$ s

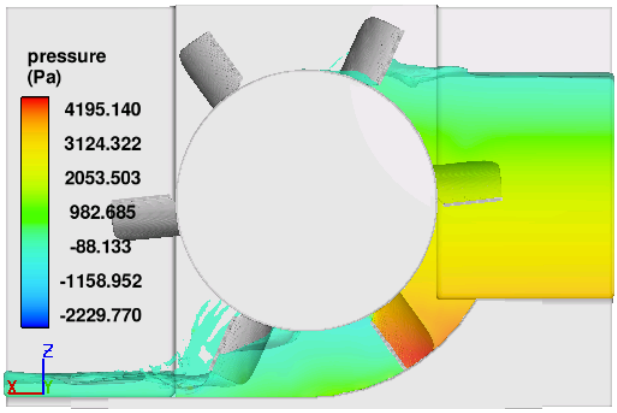

(c) 24°, $t = 23.00$ s

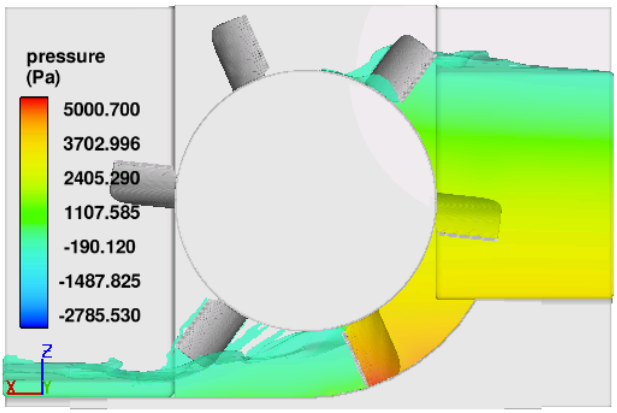

(d) 36°, $t = 23.25$ s

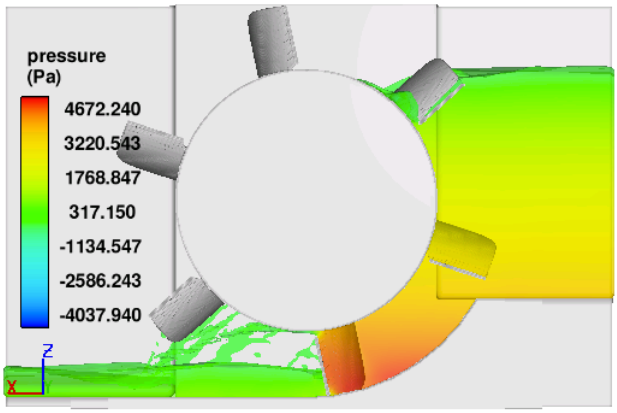

(e) 48°, $t = 23.50$ s

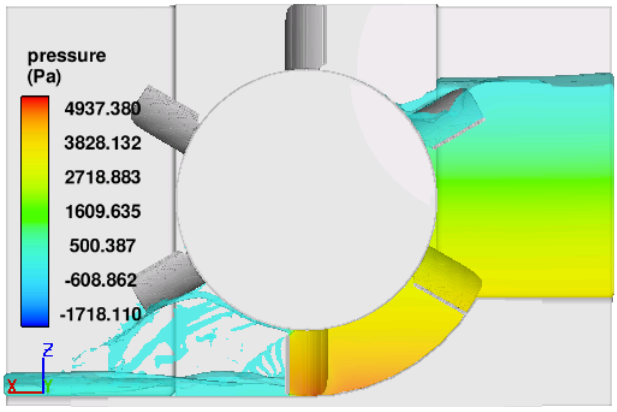

(f) 60°, $t = 23.75$ s

Figure 5.33: Distribution of pressure for the modified shroud shape SS1 and wheel with six curved blade BS1 at $N = 8$ rpm at different rotational angles of the wheel. Flow is from right to left.

Fluctuation of torque in one complete revolution of the wheel for the shroud shape SS1 at the rotational speed of $N = 8$ rpm is shown in Fig. 5.34. The period of torque shows rather unusual pattern than seen previously with curved six blade wheel model. Within 60° rotation, there are two distinct lower and higher peaks. Since the shroud shape is asymmetric and the wheel is rotating only with $N = 8$ rpm in this case, the evacuation of blade cell on the downstream could have led to this fluctuations on the torque at different rotational angles. The pattern and amplitude of the torque oscillation remains uniform in all cycles and fluctuates between maximum and minimum of about 24 Nm at every 15° and 19 Nm at every 30° interval respectively.

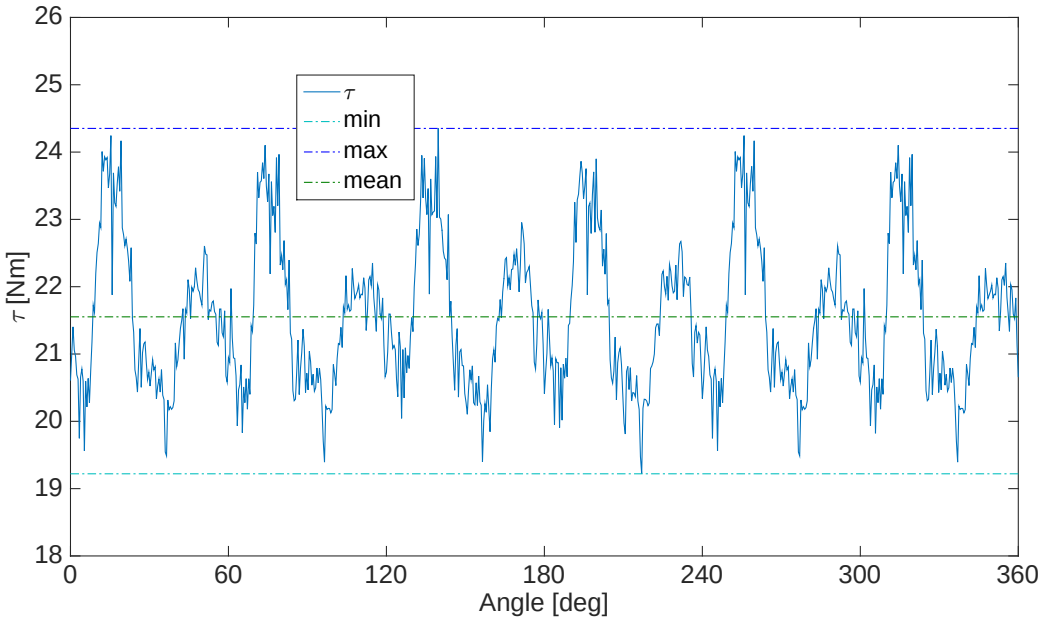

Figure 5.34: Torque versus rotational angle for wheel with shroud shape SS1 at $N = 8$ rpm

Figure 5.35 depicts the model output of the main variables at $N = 8$ rpm. The time history development of flow rate, upstream and downstream flow depths, total head and torque over the simulation time of 30 s is shown on the left and higher resolution plot of the variable and their mean and standard deviation is shown at the right side. The average of these variables are taken from 20 to 30 s of simulation time. The mean and standard deviation of these key variables is summarised in Table 5.17. Flow rate and the total head shows high fluctuation with the standard deviation of ±4 l/s and ±5.20 cm respectively.

Table 5.17: Numerical model output for shroud shape SS1 and wheel with blade BS1 at $N = 8$ rpm

Parameter	Mean	$\pm\sigma_s$
Q (l/s)	9.87	±4.00
τ (Nm)	21.56	±1.05
h_1 (cm)	33.81	±1.03
h_2 (cm)	3.61	±1.22
H (cm)	39.85	±5.20

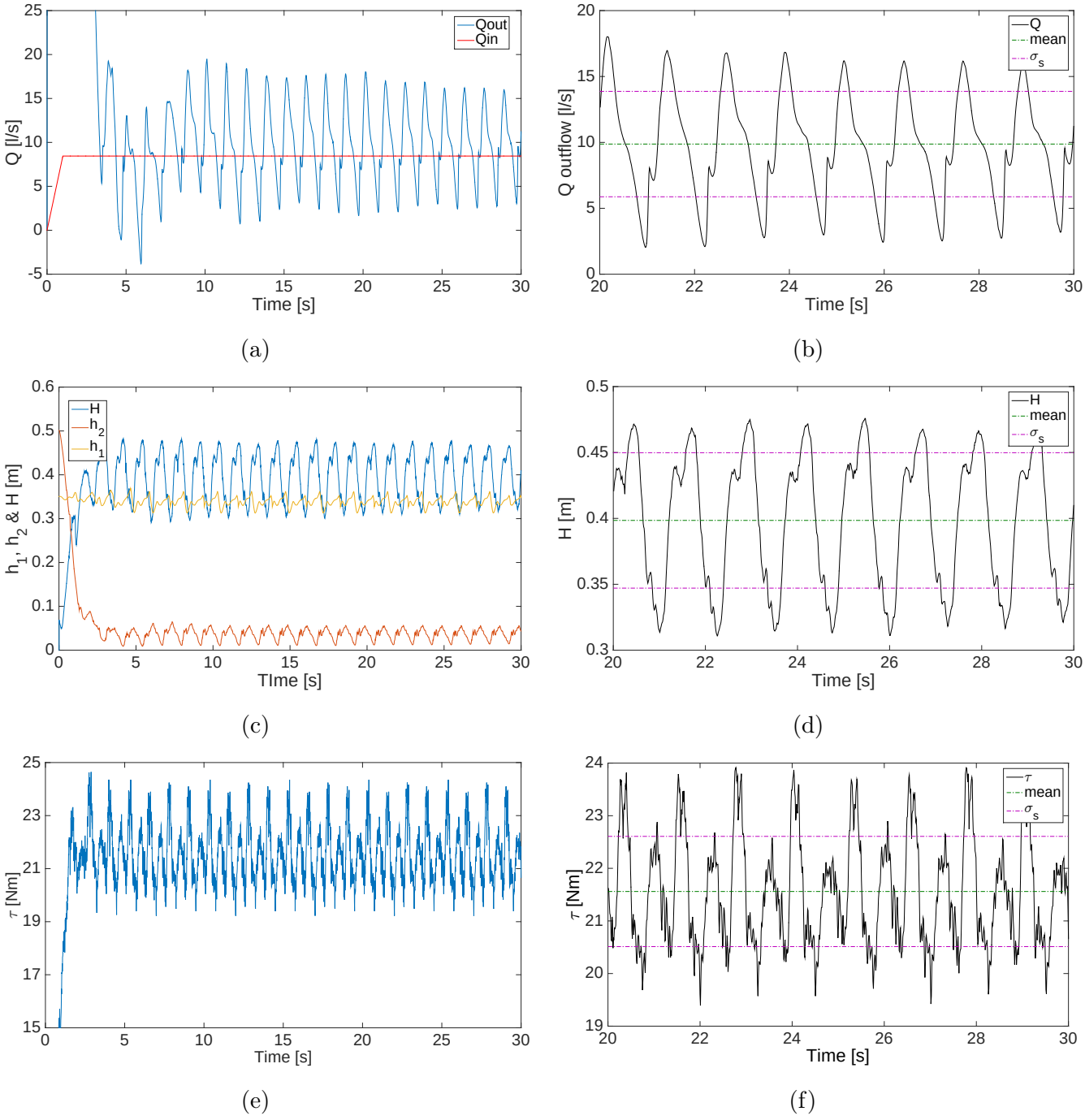

Figure 5.35: Model output for shroud shape SS1 with curved blade shapes BS1 at $N = 8$ rpm as a function of simulation time. (a) Flow rates at the inlet and outlet boundary; (b) Outflow fluctuation, mean and standard deviation of Q; (c) Upstream and downstream water levels and the total head; (d) Total head fluctuation and its mean and standard deviation; (e) Total torque; (f) Torque fluctuation, its mean and standard deviation.

Model output for $N = 18$ rpm

The previous simulation of modified shroud shape SS1 at rotational speed of $N = 8$ rpm is restarted with increased flow rate and rotational speed of $N = 18$ rpm from simulation time of 15 s. The convergence on the main variables were monitored, which showed good convergence within 22 s of simulation time.

A two dimensional x-velocity contour and vectors are shown in case of modified shroud shape SS1 and wheel with curved blade shape BS1 at the rotational speed of $N = 18$ rpm is shown in Fig. 5.36. These figures refers to the rotational positions of 0°, 12.49°, 24.38°, 36.26°, 48.13° and 60° at time step of 19.45, 19.56, 19.67, 19.78, 19.89 and 20.00 s respectively. Another five same cycles continue in one complete revolution of 360°. As the blade enters the flow at the angular position of 12.49° (Fig. 5.36b), the recirculation of flow appears within the blade cells with drop in velocity and continues to exists up to 36.26° position (Fig. 5.36d). However, flow is streamlined and no appearance of recirculation is observed within the blade cells. enclosed on the curvature of the shroud where high velocity. Surface disturbance and blade impact losses seem to be increased and the fluid depth on the upstream is dropped. The flow velocity ranges between −0.69 m/s to 2.96 m/s.

A three dimensional flow fields for the modified shroud shape SS1 at the rotational speed of $N = 18$ rpm are shown in Fig. 5.37 at different rotational positions of 0°, 12.49°, 24.38°, 36.26°, 48.13° and 60° at time step of 19.45, 19.56, 19.67, 19.78, 19.89 and 20.00 s respectively. Surface disturbance at the blade entry due to the blade impact is substantial than at the lower speed of $N = 8$ rpm. As expected, the highest pressure is predicted at the lowermost blade position and it drops as the flow leaves the blade cells at the exit. No occurrence of low pressure area can be noticed at the inlet area. As the speed of the wheel increased, the leakage losses through the v-shaped air vent and the side clearance gaps is reduced as compared to the previous case of wheel with SS1 shroud shape at $N = 8$ rpm rotational speed (see Fig. 5.33).

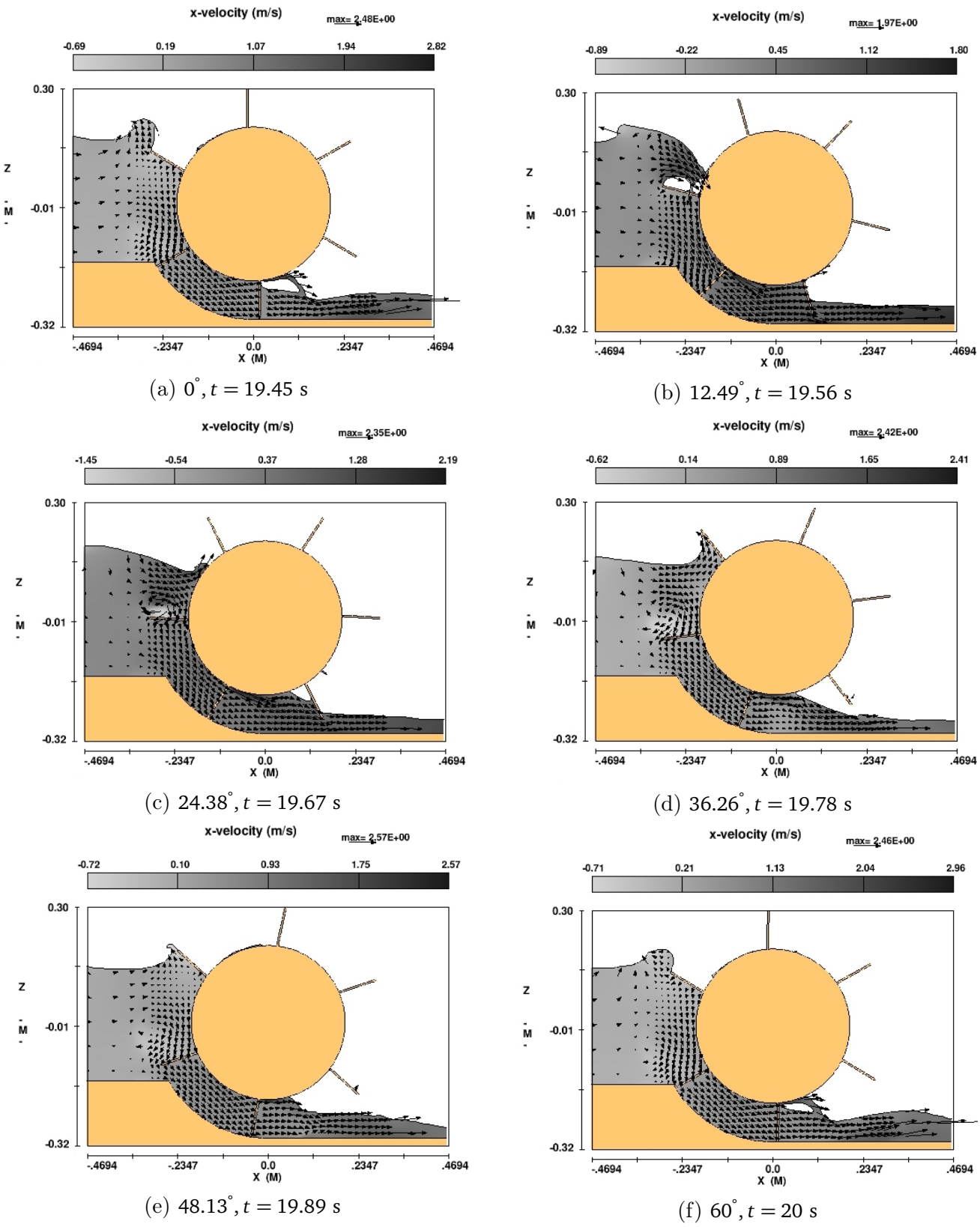

(a) $0^{\circ}, t = 19.45$ s

(b) $12.49^{\circ}, t = 19.56$ s

(c) $24.38^{\circ}, t = 19.67$ s

(d) $36.26^{\circ}, t = 19.78$ s

(e) $48.13^{\circ}, t = 19.89$ s

(f) $60^{\circ}, t = 20$ s

Figure 5.36: x-velocity contour and vectors for modified shroud shape SS1 and wheel with curved blade shape BS1 for $N = 18$ rpm at different rotational angles. The flow field is shown for rotational angle of $0° - 60°$. Flow is from left to right.

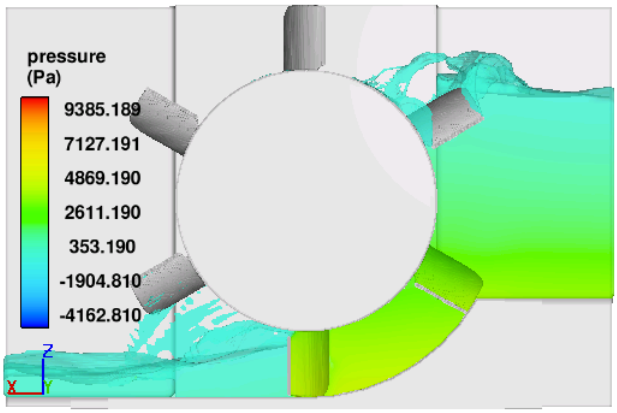

(a) 0°, $t = 19.45$ s

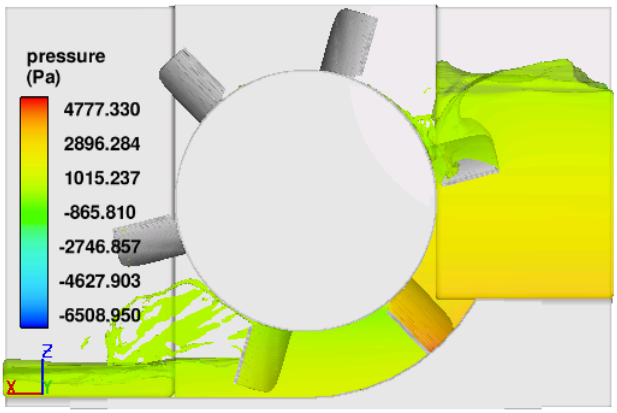

(b) 12.49°, $t = 19.56$ s

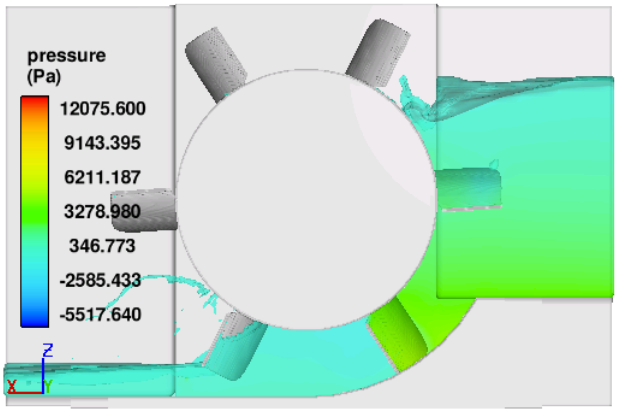

(c) 24.38°, $t = 19.67$ s

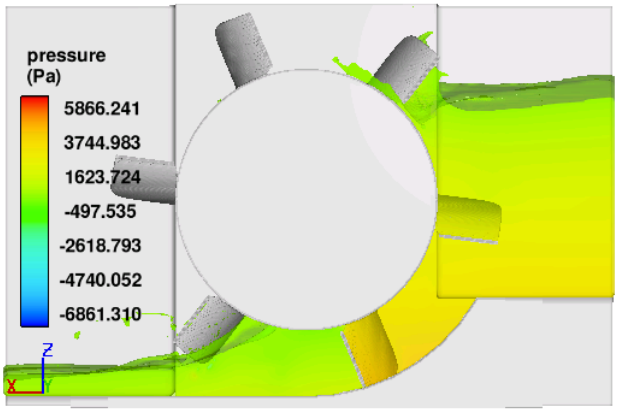

(d) 36.26°, $t = 19.78$ s

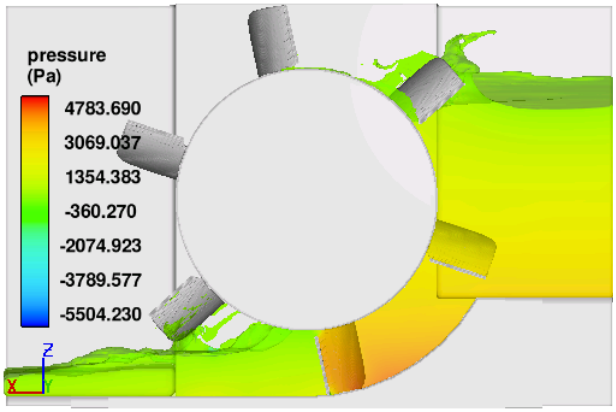

(e) 48.13°, $t = 19.89$ s

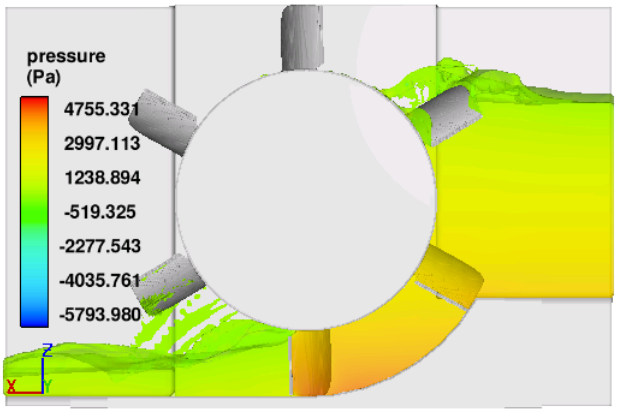

(f) 60°, $t = 20$ s

Figure 5.37: Distribution of pressure for the modified shroud shape SS1 and wheel with six curved blade BS1 at $N = 18$ rpm at different rotational angles of the wheel. Flow is from right to left in this figure.

The variation of total torque in one complete revolution of the wheel for the modified shroud shape SS1 at $N = 18$ rpm is shown in Fig. 5.38. Apart from the unusual peak at 90° position, the torque cycle showed a 60° period. The amplitude of the torque oscillations remains nearly same in all cycles. The maximum torque of 22 Nm occurred at angular position of 90° and a minimum of around 13 Nm at every 60° rotational angle.

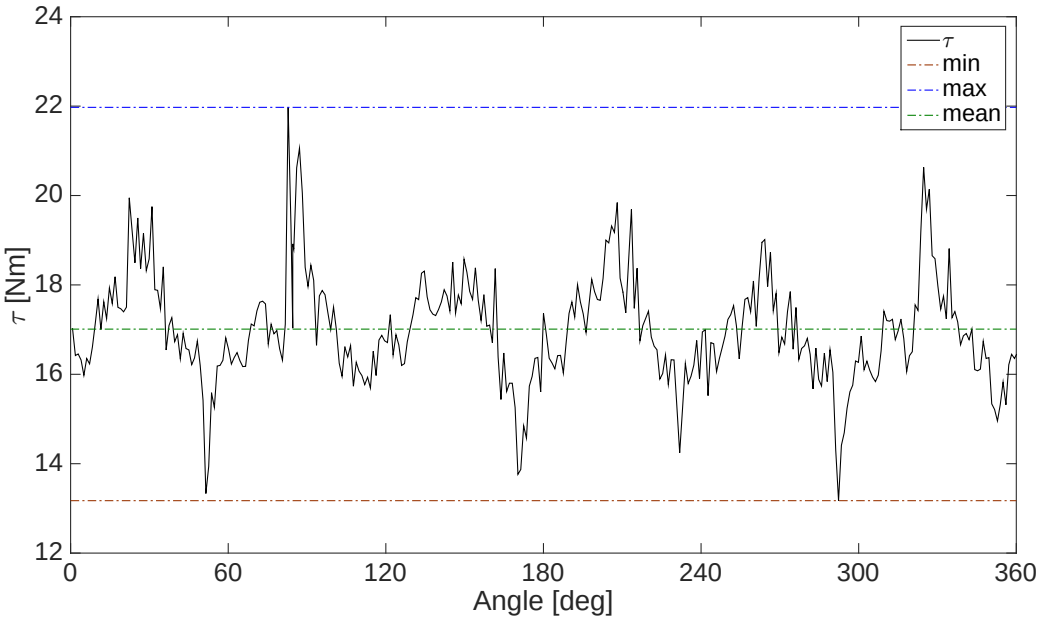

Figure 5.38: Torque versus rotational angle for wheel with shroud shape SS1 at $N = 18$ rpm

The numerical model output of the main variables and their time development is plotted in Figure 5.39. The model inflow and outflow, flow depths, total head and torque over the simulation time of 15 s to 22 s is shown on the left and higher resolution plot of the variable and their mean and standard deviation is shown at the right side. The mean value of these parameters are taken from 19 to 22 s of simulation time. The mean and standard deviation of these values are summarised in Table 5.18. The flow rate and total head show high fluctuation with standard deviation of ±3.86 l/s and ±3.59 cm respectively. Drop on the upstream water level is noticed. The initial fluid depth defined at the initial boundary condition might not be sufficient enough for the increased speed of the wheel to represent the desired upstream depth at the converged solution. However, trial and error procedure is required to get the desired water level by adjusting the wheel speed and the flow rate.

Table 5.18: Numerical model output for wheel with shroud shape SS1 and curved blade shape BS1 at $N = 18$ rpm

Parameter	Mean	$\pm\sigma_s$
Q (l/s)	15.45	±3.86
τ (Nm)	17.08	±1.19
h_1 (cm)	30.06	±1.76
h_2 (cm)	4.97	±0.82
H (cm)	33.28	±3.59

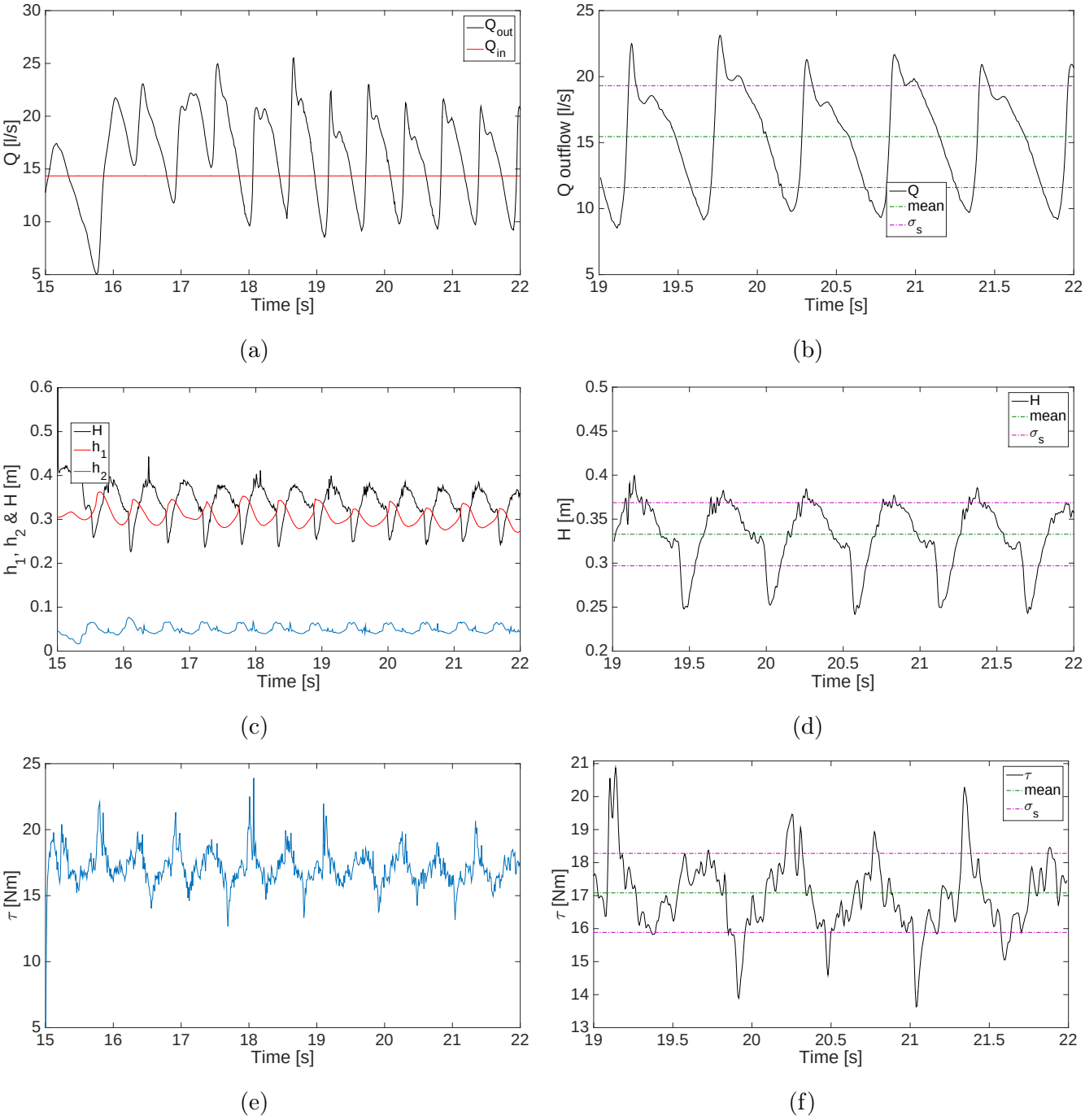

Figure 5.39: Model output for shroud shape SS1 and wheel with curved blade shapes BS1 at $N = 18$ rpm against simulation time. (a) Flow rates at the inlet and outlet boundary; (b) Outflow fluctuation, mean and standard deviation of Q; (c) Upstream and downstream water levels and the total head; (d) Total head fluctuation and its mean and standard deviation; (e) Total torque; (f) Torque fluctuation, its mean and standard deviation.

As seen above, the torque is improved in both cases of $N = 8$ rpm and $N = 18$ rpm. The torque at $N = 8$ rpm with shroud shape SS0 is 20.45 ± 1.30 Nm. This value increased to 21.56 ± 1.05 Nm in wheel with shroud shape SS1 at $N = 8$ rpm speed. Despite the drop in the upstream flow depth at $N = 18$ rpm, the torque output is higher than the shroud shape SS0 case at the same rotational speed. The torque output at $N = 18$ rpm is 16.16 ± 1.36 Nm in case of shroud shape SS0 which increased to

17.08 ± 1.19 Nm in case of shroud shape SS1. This increased torque and the lower head results in the improved efficiency of the wheel with shroud shape SS1.

5.2.4 Summary

On the physical model, wheel performance at different wheel housings, wheel to channel width ratios, transition shapes, blade numbers and losses were investigated. In order to be able to compare data of different tests and with the numerical model results, the upstream water level is fixed at 44.65 cm which refers to the top of the hub and the downstream water level is kept at 6.18 cm with the help of the downstream adjustable weir. At constant water levels, the rotational speed of the wheel holds a linear relationship with torque and the flow rate. These linear models are used to develop the full performance curves.

The original wheel housing provided an enclosure for the blade cells. On the modified wheel housing, the side enclosures are removed to allow the side filling and emptying of the blade cells. The side openings on the modified housing WH1 allowed the water filled on the blade cells to be emptied earlier as well as less entrapment of the air in the blade cells. The rotational quality of the wheel also improved in wheel housing WH1. The maximum power output is 22 W in WH0 which increased to 28 W in case of modified wheel housing WH1. The efficiency shows gain at rotational speed beyond 18 rpm, however a slight drop in efficiency can be noticed around the BEP region. These tests showed that side opening for the blade cells are necessary for a wider operating range and better performance of the wheel.

Blade number is an important geometrical design parameter which determines the hydraulic performance of the wheel. Four different number of blades $6, 8, 12$ and 16 are tested on the physical model. Power output and efficiency of the wheel both increased with decreased number of blades. Performance of the wheel reached the highest with least numbers of blades, i.e. six. The maximum efficiency reached to $59.57 \pm 3.48\%$ with six number of blades. This is explained by the reduced friction losses at lower number of blades. Moreover, the fluid displacement caused by the blade at the entry and exit from the fluid is reduced with smaller number of blades.

Performance of the wheel at different wheel to channel width ratios of $1:4, 1:3, 1:2$ and $1:1$ is measured. Results showed that wheel to channel width ratio is an important performance and economical criteria for the operation of the Dethridge wheel. In $1:1$ case, performance of the wheel dropped due to increased amount of hydraulic losses including splashing, air entrainment and high amplitude waves on the upstream. The optimum wheel to channel width ratio is found to be $1:2$ with an efficiency of $62.14 \pm 2.93\%$ at BEP. Therefore, a channel two times wider than the wheel would be necessary for more efficient operation of the wheel.

Gradual transition shapes with converging on the upstream and diverging shape on the downstream were tested for its effect on the wheel performance. Performance of these gradual transition shapes is compared with the case of sudden transition profiles. The difference in efficiency and power output between these two cases is found insignificant.

Furthermore, clearance gap is an important performance criteria. Tests with 1, 2 and 4 mm bottom gaps are accomplished on the physical model. Performance sharply dropped in 4 mm gap due to increased amount of leakage flow. At higher speed, 2 mm gap resulted in reduced hydraulic losses within the blade cells and therefore improved performance. But the uncertainties associated with these results overlap therefore drawing a concrete conclusion is difficult.

The physical model results of the eight sharp V-shaped BS0 blades are compared with the numerical model results. The measured and computed efficiency at $N = 7.971$ rpm is $55.46 \pm 4.72\%$ and $61.58 \pm 14.15\%$ respectively. At higher speed of $N = 25.181$ rpm, the measured and computed efficiencies are $39.74 \pm 2.79\%$ and $47.96 \pm 10.83\%$ respectively. This shows that numerical model is slightly over predicting the efficiency in both cases. However, the results are within the estimated uncertainty bounds. Similarly, physical model results of the wheel with six sharp V-shaped BS0 blades model is compared with the numerical model results of the wheel with six curved shaped BS1 blades. Even though the quantitative performance of wheel with BS1 blades does not differ much with the wheel with sharp BS0 blades, the qualitative performance of the torque variation is found to be improved with curved blades BS1. The performance of the wheel with modified shroud shape SS1 is numerically studied. The performance of the wheel showed improvement with shroud shape SS1. The torque at $N = 8$ rpm with shroud shape SS0 is 20.45 ± 1.30 Nm. This value increased to 21.56 ± 1.05 Nm in wheel with shroud shape SS1. Similarly, the torque output at $N = 18$ rpm is 16.16 ± 1.36 Nm in case of shroud shape SS0 which increased to 17.08 ± 1.19 Nm in case of shroud shape SS1. The numerical model results showed that CFD method could accurately predict hydrodynamic performance of the Dethridge wheel.

Chapter 6

Conclusions, Contributions and Future Work

6.1 Conclusions

The main objective of this thesis was to identify the potential of the Dethridge wheel for utilising very low head sites for hydropower in open channel flows. This study thus incorporated the detailed investigation of the Dethridge wheel, which was originally meant for flow measurement purposes, for developing power from very low head sites in open channel flow. Two different approaches were taken to assess the potential of the wheel for power production. The first was the experimental approach with a physical model of the wheel built and tested in the laboratory environment. The second approach was the numerical modelling of the wheel using a commercial Computational Fluid Dynamics (CFD) code Flow-3D.

The physical modelling approach involved the model tests of a $1:2$ scaled model of the original Dethridge wheel. Modifications on the shroud and wheel geometry were carried out to identify their effect on the wheel performance. The effect of modification on wheel housing, wheel to channel width ratio, blade numbers, channel transition shapes and the bottom clearance gap were investigated. Upstream and downstream water levels were kept constant for all the tests. Physical model tests have shown that at constant water levels the rotational speed of the wheel holds a linear relationship with torque as well as with flow rate. Using these linear regression models, full performance curves of the wheel were developed. Uncertainty analysis of all measured data was done using the constant odd combination method. Performance change was compared using the curves of relative change in performance between two different stages. Plots of flow rate, head, torque, power output and efficiency against rotational speed were used for studying the performance of the wheel. The velocity head term was very small and therefore the total head acting on the wheel was predominantly contributed by the pressure head term.

Side filling of the blade cells was observed to have significant impact on the performance of the wheel. Original wheel housing was modified to allow side filling and emptying of the blade cells. The effect of wheel housing modification has shown a mixed effect on the wheel efficiency. Efficiency increased only at higher rotational speeds but the power output was greatly increased over a wider operating range. Hydraulic losses within the wheel control volume including splashing and fluid displacement at the blade entry, air entrainment raised from turbulent disturbances at the free surface, and water carried upward at the blade exit were substantially reduced through the side openings of the blade cells in the modified housing.

Four different blade numbers of $6, 8, 12$ and 16 were tested on the physical model. The wheel with least number of blades (i.e. six) showed best performance among all blade numbers combinations.

This increase in power output and efficiency with reduced number of blades was expected to be contributed by the decrease in friction losses with decreased number of blades and reduced frequency of fluid displacement caused by the blade at the entry. Moreover, the frequency of water taken upward in the blade cells at the exit was also reduced with reducing number of blades. Other complex hydraulic losses inside the blade cells due to flow circulation and eddies were thought to be low in bigger cells, i.e. at lower blade numbers.

Performance at different wheel to channel width ratios of $1:4, 1:3, 1:2$ and $1:1$ were measured. Channel to wheel width ratio showed a vital role on the performance of the wheel. The splashing, size and amount of air bubbles and amount of water driven upward at the exit was observed to be reduced in $1:2$ and $1:3$ ratios with the increasing rotational speed. The $1:2$ width ratio showed highest efficiency among others. By having a wheel to channel width ratio of $1:2$, i.e. channel width two times greater than the width of the wheel, gain in performance was achieved.

Tests with sudden and gradual transition profiles were done on the physical model. Performance change between these profiles was found to be insignificant and remained within the defined uncertainty bounds. These observations suggests that there is no requirement of special channel transition profiles. Bottom clearance gap was found to be very important in controlling leakage losses and consequently wheel performance. A larger gap would be desired for sediment transport and for ecological reasons in these devices. However, performance of the wheel showed high dependency on the clearance gap. The least provision of bottom clearance gap showed highest performance in most of the operating region.

A three dimensional CFD model of a Dethridge wheel was developed. The Renormalization Group (RNG) model was employed for modelling the turbulence. The wheel motion was modelled using the General Moving Object (GMO) model. Numerical model results were assessed for numerical and model uncertainties. Effect of surface roughness, turbulence model, momentum advection scheme, blade thickness and domain symmetry was studied and validated against the measured results. A rigorous approach of numerical uncertainty analysis called Grid Convergence Index (GCI) method was employed for assessing the numerical uncertainty of the CFD model. A high resolution three dimensional time-dependent solution was obtained from the CFD model.

Through the development of a CFD model, a deeper understanding on the hydrodynamics of the Dethridge wheel has been acquired. Three dimensional hydraulics information from the CFD model provided the basis for qualitative analysis and visual examination of the flow field at the wake of the wheel and quantitative information on the wheel performance. The numerical model with eight sharp V-shaped blades (BS0) was numerically computed and compared with the physical model results, which supplemented the validation of the numerical model at distinct boundary conditions. The numerical model results appeared to be in good agreement with the measured values. Although the numerical model over predicted both the power output and the efficiency at higher rotational speeds, the computed results were within the defined uncertainty bounds. Following this, modified blade shape (BS1) and shroud shape (SS1) were numerically investigated. Modification of both blade and shroud shape led to an improvement on the performance of the wheel.

In light of the above findings, it can be concluded that Dethridge wheel is a potential machine for energy extraction from very low head sites in open channel flow. The simple and robust design of the wheel in combination with the efficiency of around 60% achieved in the laboratory scale physical model tests would make this wheel a viable option for decentralised pico hydropower generation from very low head sites in remote areas.

6.2 Contributions

This thesis examined the possibility of utilizing very low head sites for hydropower using simplistic technology. A new device, Dethridge wheel, is assessed for its suitability to use for power production from open channel flows. The outcome of this thesis contributed to the existing knowledge on very low head hydropower and the performance characteristics of Dethridge wheel. The results of this study enriched our understanding of the energy transfer mechanism in Dethridge wheel or machines with similar working principle.

A three dimensional numerical model of the Dethridge wheel is developed. Three dimensional modelling of the energy extraction devices in open channel flow using CFD is relatively new method for analysing the performance of such devices. Even though CFD modelling is computationally resource intensive, it can be much more efficient than the physical modelling process. This thesis explored the possibility and efficacy of using CFD model in studying complex hydrodynamics involved in a open channel energy extraction device.

6.3 Future work

The work presented in this thesis is a first model study of its kind developed and tested in the ideal laboratory settings. The results depicted here may provide adequate knowledge about the model wheel considered in the study. However, for the implementation in real life situation the prediction of performance is subjected to the nature and quality of the proposed site. For uninterrupted flow of natural water courses, the wheel diameter and width need to be sized according to the available head and the flow rate. This site specific sizing requirements of the machine will result in change in geometry and thus different dynamic performance of the machine. The results of the model tests can not be further elaborated for making predictions for geometrically dissimilar machines. Moreover, the performance characteristics of the machine in real life environment is not yet known. The upstream water level is determined by the amount of load on the wheel, while the downstream water level mainly depends on the flow rate. As the water level changes, the dynamic performance of the machine would be different. Following aspects will be worthwhile investigating for exploring the future development potential of the machine:

1. Different hub to overall diameter ratios of the wheel need to be investigated for further optimisation of performance.

2. Full scale prototype tests should be carried out to quantify the scale effects and the efficiency of bigger machines.

3. Further modification on the blade shape and shroud shape may lead to non-negligible improvement in performance. CFD approach would be very useful for initial performance assessment of different geometrical modifications.

4. Air entrainment and density change in the CFD model was not studied. There is a further potential to include these aspects into the numerical model study. A drift flux, density evaluation and air entrainment models could be utilised to study the losses due to air entrainment.

5. The economical viability of full scale installation needs be assessed. A comparative study of different very low head technologies would help in recognising the further development potential of the machine.

6. Slow rotation and large blade cells of the machine would mean uninterrupted flow and little or no disturbance on the original flow characteristics of natural water courses. However, small clearance gap desired for the optimum performance of this device could lead to increased risk of foreign object damage. Environmental impact of these machines needs to be investigated in greater detail.

References

ANCID (2002). *Know the flow training manual.* Australian National Committee on Irrigation and Drainage and National Program on Irrigation Research and Development.

Anderer, P., Dumont, U., Heimerl, S., Ruprecht, A., and Wolf-Schumann, U. (2010). Das Wasserkraftpotenzial in Deutschland [In German]. *WasserWirtschaft*, 9:12–16.

Anderson, J. D. (2009). *Computational fluid dynamics: An introduction*, chapter 2. Springer.

Ansar, A., Flyvbjerg, B., Budzier, A., and Lunn, D. (2014). Should we build more large dams? The actual costs of hydropower megaproject development. *Energy Policy*, 69:43–56.

ASTHC (1988). Measuring farm supplies - the Dethridge wheel, Published by Australian Science and Technology Heritage Centre. `http://www.austehc.unimelb.edu.au/tia/157.html`. [Last checked: 2015-06-23].

Bach, C. (1886). *Die Wasseräder [In German].* Konrad Wittwer Verlag, Stuttgart.

Basak, B. C. and Alauddin, M. (2010). Efficiency of an expansive transition in an open channel subcritical flow. *Dhaka University of Engineering and Technology Journal*, 1:27–32.

Basset, D. E. (1989). *A historical survey of low-head hydropower generators and recent laboratory based work at the University of Salford.* PhD thesis, Department of Civil Engineering, The University of Salford.

Biswas, G. (2002). *Turbulent flows: Fundamentals, experiments and modelling*, chapter 11. IIT Kanpur series of advanced texts. Narosa Publishing House, New Delhi, India.

Blindheim, B. (2015). A missing link ? The case of Norway and Sweden: Does increased renewable energy production impact domestic greenhouse gas emissions? *Energy Policy*, 77:207–215.

Botto, A., Claps, P., Ganora, D., and Laio, F. (2010). Regional-scale assessment of energy potential from hydrokinetic turbines used in irrigation channels. In *SEEP 2010 Conference Proceedings*, Bari, Italy.

Brada, K. (1996). *Schneckentrogpumpe als Mikroturbine, in Wasserkraftanlagen–Klein- und Kleinstkraftwerke [In German].* Expert-Verlag, Malsheim, 1st edition.

Brada, K. (1999). Wasserkraftschnecke ermöglicht Stromerzeugung über Kleinkraftwerke [In German]. *Maschinenmarkt Würzburg*, 14:52–56.

Brethour, J. M. (2009). Improved generalized minimal residual (GMRES) solver in Flow-3D – How it works and when to use it. Technical Note FSI-09-TN82, Flow Science.

Brinnich, A. (2001). Wasserkraft-Staudruckmaschine - Neues, konkurrenzlos wirtschaftliches Kraftwerkskonzept [In German]. *Wasserwirtschaft*, 91(2):70–74.

Brüdern, R. (2006). *Wie Man Wasseräder Baut [In German].* Richard Brüdern.

Butera, I. and Balestra, R. (2015). Estimation of the hydropower potential of irrigation networks. *Renewable and Sustainable Energy Reviews*, 48:140 –151.

Campbell, R. J. (2010). Small hydro and low-head hydro power technologies and prospects. CRS Report for Congress, Congressional Research Service.

Capecchi, D. (2013). Over and undershot waterwheels in the 18^{th} century. Science-technology controversy. *Advances in Historical Studies*, 2(3):131–139.

Castro-García, M., Rojas-Sola, J. I., and de la Morena-de la Fuente, E. (2015). Technical and functional analysis of Albolafia waterwheel (Cordoba, Spain): 3D modeling, computational-fluid dynamics simulation and finite-element analysis. *Energy Conversion and Management*, 92:207–214.

Chen, C.-F. A., Lotz, R. D., and Thompson, B. E. (2002). Assessment of numerical uncertainty around shocks and corners on blunt trailing-edge supercritical airfoils. *Computers & Fluids*, 31(1):25–40.

Chow, V. (1959). *Open Channel Hydraulics*. McGraw Hill, New York, USA.

Dai, Y. M. and Lam, W. (2009). Numerical study of straight-bladed darrieus-type tidal turbine. In *Proceedings of ICE, Civil Engineers*, Energy 162, pages 67–76.

Delabar, G. (1867). Zuppinger'schen wasserrades [in german]. *Polytechnisches Journal*, 185(LXX.):249–253.

Denny, M. (2004). The efficiency of overshot and undershot water wheels. *European Journal of Physics*, 25:193–202.

Dimke, S., Weichbrodt, F., and Froehle, P. (2011). Potential analysis for low head energy converters - exemplarily for irrigation canals in Pakistan. In *IAHR annual meeting 2011*.

DoECC (2010). England and Wales hydropower resource assessment- Final report. Technical report, Department of Energy & Climate Change.

Doig, A. (1999). Off-grid electricity for developing countries. *IEE Review*, 45(1):25–28.

Eça, L. and Hoekstra, M. (2009). Evaluation of numerical error estimation based on grid refinement studies with the method of the manufactured solutions. *Computers & Fluids*, 38(8):1580–1591.

Eça, L. and Hoekstra, M. (2014). A procedure for the estimation of the numerical uncertainty of CFD calculations based on grid refinement studies. *Journal of Computational Physics*, 262:104–130.

Elbatran, A., Yaakob, O., Ahmed, Y. M., and Shabara, H. (2015). Operation, performance and economic analysis of low head micro-hydropower turbines for rural and remote areas: A review. *Renewable and Sustainable Energy Reviews*, 43:40–50.

Flow-3D (2011). *Flow-3D User Manual*. Flow Science, USA.

Freitas, C. J. (2002). The issue of numerical uncertainty. *Applied Mathematical Modelling*, 26(2):237–248.

Furukawa, A., Watanabe, S., Matsushita, D., and Okuma, K. (2010). Development of ducted Darrieus turbine for low head hydropower utilization. *Current Applied Physics*, 10:S128–S132.

Gensler, D. and Kinzli, K. (2013). Examining the feasibility of hydropower generation in irrigation canals: Middle rio grande conservancy district. *Journal of Irrigation and Drainage Engineering*, 139(5):405–413.

Hasan, N. (2012). Validation of CFD models using Flow3D for a submerged liquid jet. In *Ninth International Conference on CFD in the Minerals and Process Industries*. CSIRO, Australia.

Hirt, C. (1992). Volume-Fraction techniques: Powerful tools for flow modeling. Report FSI-92-00-02, Flow Science, Santa Fe, NM.

Hirt, C. and Chen, K. S. (1996). Simulation of slide-coating flows using a fixed grid and a Volume-of-Fluid front-tracking technique. In *Eighth International Coating Process Science and Technology Symposium*, New Orleans, LA, USA.

Hirt, C. and Nichols, B. (1981). Volume of Fluid (VOF) method for the dynamics of free boundaries. *Journal of Computational Physics*, 39:201–225.

Hirt, C. and Sicilian, J. (1985). The porosity technique for the definition of obstacles in rectangular cell meshes. In *Fourth International Conference on Ship Hydrodynamics*, Washington DC.

Ikeda, T., Iio, S., and Tatsuno, K. (2010). Performance of nano-hydraulic turbine utilizing waterfalls. *Renewable Energy*, 35:293–300.

Isfahani, A. and Brethour, J. M. (2009). On the implementation of two-equation turbulence models in Flow-3D. Technical Report FSI-09-TN86, Flow Science, Inc.

Juhrig, L. (2011). Die Very-Low-Head-Turbine – Technik und Anwendung [In German]. *Wasser-Wirtschaft*, 10:327–333.

Kalitzin, G., Medic, G., Iaccarino, G., and Durbin, P. (2005). Near-wall behavior of RANS turbulence models and implications for wall functions. *Journal of Computational Physics*, 204(1):265–291.

Kang, S., Borazjani, I., Colby, J. A., and Sotiropoulos, F. (2012). Numerical simulation of 3D flow past a real-life marine hydrokinetic turbine. *Advances in Water Resources*, 39:33–43.

Kim, D. and Park, J. (2005). Analysis of flow structure over ogee-spillway in consideration of scale and roughness effects by using CFD model. *KSCE Journal of Civil Engineering*, 9(2):161–169.

Kim, K.-P., Ahmed, M. R., and Lee, Y.-H. (2012). Efficiency improvement of a tidal current turbine utilizing a larger area of channel. *Renewable Energy*, 48:557–564.

Kosnik, L. (2008). The potential of water power in the fight against global warming in the US. *Energy Policy*, 36(9):3252–3265.

Kosnik, L. (2010). The potential for small scale hydropower development in the US. *Energy Policy*, 38(10):5512–5519.

Kraatz, D. B. and Mahajan, I. K. (1975). Small hydraulic structures. Irrigation and drainage paper, Food and Agricultural Organization (FAO) of the United Nations, Rome.

Lane, S. N. (2005). Roughness –time for a re-evaluation? *Earth Surface Processes and Landforms*, 30(2):251–253.

Lane, S. N., Hardy, R. J., Elliott, L., and Ingham, D. B. (2002). High-resolution numerical modelling of three-dimensional flows over complex river bed topography. *Hydrological Processes*, 16(11):2261–2272.

Lashofer, A., Hawle, W., and Pelikan, B. (2013). Efficiency improvements of the Archimedean screw turbine. *WasserWirtschaft*, 103:29–34.

Linton, N. (2009). The design and development of hydrostatic pressure machines for small hydropower applications. Msc thesis, School of Engineering Sciences, University of Southampton, Sounthampton.

Linton, N. (2013). *Field trials and development of hydrostatic pressure machine*. PhD thesis, Faculty of Engineering and The Environment.

Loots, I., van Dijk, M., Barta, B., van Vuuren, S., and Bhagwan, J. (2015). A review of low head hydropower technologies and applications in a South African context. *Renewable and Sustainable Energy Reviews*, 50:1254–1268.

Lyons, M. and Lubitz, W. D. (2013). Archemedes screws for microhydro power. In *Proceedings of the ASME 2013 7th International Conference on Energy Sustainability*, pages 1–7, Minneapolis, MN, USA. ASME.

Mahat, I. (2004). Implementation of alternative energy technologies in Nepal: Towards the achievement of sustainable livelihoods. *Energy for Sustainable Development*, 8(2):9 –16.

Marsh, P., Ranmuthugala, D., Penesis, I., and Thomas, G. (2015a). Numerical investigation of the influence of blade helicity on the performance characteristics of vertical axis tidal turbines. *Renewable Energy*, 81:926–935.

Marsh, P., Ranmuthugala, D., Penesis, I., and Thomas, G. (2015b). Three-dimensional numerical simulations of straight-bladed vertical axis tidal turbines investigating power output, torque ripple and mounting forces. *Renewable Energy*, 83:67–77.

Mead, D. W. (1915). *Water Power Engineering*. McGraw Hill Book Co., New York, USA.

Meerwarth, K. (1935). *Experimentelle und theoretische Untersuchungen an oberschlächtigen Wasserrad [In German]*. PhD thesis, Technical University of Stuttgart, Germany.

Moffat, R. J. (1988). Describing the uncertainties in experimental results. *Experimental Thermal and Fluid Science*, 1:3–17.

Morvan, H., Knight, D., Wright, N., Tang, X., and Crossley, A. (2008). The concept of roughness in fluvial hydraulics and its formulation in 1D, 2D and 3D numerical simulation models. *Journal of Hydraulic Research*, 46(2):191–208.

Müller, G., Denchfield, S., and Shelmerdine, R. (2007). Stream wheels for applications in shallow and deep water. In *32nd IAHR Conference*, Venice, Italy.

Müller, G. and Kauppert, K. (2002). Old watermills- Britain's new source of energy? In *Proceedings of ICE, Civil Engineering*, volume 150, pages 178–186.

Müller, G. and Kauppert, K. (2004). Performance characteristics of water wheels. *Journal of Hydraulic Research*, 42(5):451–460.

Müller, G., Linton, N., and Schneider, S. (2012). Das Projekt HYLOW: Die Wasserdruckmachine [In German]. *Korrespondenz wasserwirtschaft*, 5(1):30–36.

Müller, G. and Senior, J. (2009). Simplified theory of Archimedean screws. *Journal of Hydraulic Research*, 47(5):666–669.

Müller, G. and Wolter, C. (2004). The breastshot water wheel: Design and model tests. In *Proceedings of the institutions of the civil engineers:Engineering Sustainability*, volume 157, pages 203–211.

Nicholas, A. P. (2001). Computational fluid dynamics modelling of boundary roughness in gravel-bed rivers: An investigation of the effects of random variability in bed elevation. *Earth Surface Processes and Landforms*, 26(4):345–362.

Nicholas, A. P. (2005). *Roughness parameterization in CFD modelling of gravel-bed rivers*, pages 329–355. John Wiley & Sons, Ltd.

Nuernbergk, D. (2012). *Wasserkraftschnecken: Berechnung und optimaler Entwurf von Archimedischen Schnecken als Wasserkraftmaschine [In German]*. Moritz Schäfer, 1 edition.

Nuernbergk, D. (2013). *Wasserräder mit Kropfgerinne: Berechnungsgrundlagen und neue Erkenntnisse [In German]*. Moritz Schäfer, 2 edition.

Nuernbergk, D. (2014). *Wasserräder mit Freihang: Entwurfs- und Berechnungsgrundlagen [In German]*. Moritz Schäfer, 2 edition.

Nuernbergk, D. and Rorres, C. (2013). Analytical model for water inflow of an Archimedes screw used in hydropower generation. *Journal of Hydraulic Engineering*, 139:213–220.

Nuernbergk, D. and Rorres, C. (2014). Bestimmung des Durchflusses in Archimedischen Schnecken [In German]. *Wasserkraft & Energie*, 3:37–47.

Oberkampf, W. L. and Roy, C. J. (2010). *Verification and validation in scientific computing*. Cambridge University Press, New York, USA.

Paish, O. (2002). Small hydro power: Technology and current status. *Renewable and Sustainable Energy Reviews*, 6:537–556.

Paudel, S., Linton, N., Zanke, U. C., and Saenger, N. (2013). Experimental investigation on the effect of channel width on flexible rubber blade water wheel performance. *Renewable Energy*, 52:1–7.

Paudel, S. and Saenger, N. (2014). Numerical simulation of a Dethridge wheel using Flow-3D. In Dittrich, A., editor, *LWI Mitteilungen - Wasserbau*, Heft 161/2014, pages 155–162. Technische Universität Braunschweig.

Pelliciardi, V. (2015). Overshot waterwheel to power an olive oil mill in Nepal. *Journal of Applied Water Engineering and Research*, 3(2):157–165.

Pujol, T. and Montoro, L. (2010). High hydraulic performance in horizontal waterwheels. *Renewable Energy*, 35(11):2543–2551.

Pujol, T., Montoro, L., and Silva, X. (2011). Hydraulic power of slow-rotating waterwheels: A novel analytical approximation. In *Proceedings of the Institution of Mechanical Engineers, Part C: Journal of Mechanical Engineering Science*, volume 225, pages 1495–1506. Institution of Mechanical Engineers.

Pujol, T., Solà, J., Montoro, L., and Pelegrí, M. (2010). Hydraulic performance of an ancient Spanish watermill. *Renewable Energy*, 35(2):387–396.

Pujol, T., Vashisht, A., Ricart, J., Culubret, D., and Velayos, J. (2015). Hydraulic efficiency of horizontal waterwheels: Laboratory data and CFD study for upgrading a western himalayan watermill. *Renewable Energy*, 83:576–586.

Quaranta, E. and Revelli, R. (2015a). Output power and power losses estimation for an overshot water wheel. *Renewable Energy*, 83:979–987.

Quaranta, E. and Revelli, R. (2015b). Performance characteristics, power losses and mechanical power estimation for a breastshot water wheel. *Energy*, 87:315–325.

Replogle, J. A. and Kruse, E. G. (2007). *Delivery and Distribution Systems*, chapter 11, pages 347–391. United States Department of Agriculture, 2nd edition.

Roache, P. J. (1994). Perspective: A method for uniform reporting of grid refinement studies. *Journal of Fluids Engineering*, 116(3):405–413.

Roache, P. J. (1997). Quantification of uncertainty in computational fluid dynamics. *Annual Review of Fluid Mechanics*, 29(1):123–160.

Roache, P. J. (1998). Verification of codes and calculations. *AIAA Journal*, 36(5):696–702.

Roache, P. J., Ghia, K., and White, F. (1986). Editorial policy statement on the control of numerical accuracy. *Journal of Fluids Engineering*, 108(1):2.

Roy, C. J. (2005). Review of code and solution verification procedures for computational simulation. *Journal of Computational Physics*, 205(1):131–156.

Roy, C. J. and Blottner, F. G. (2006). Review and assessment of turbulence models for hypersonic flows. *Progress in Aerospace Sciences*, 42(7-8):469–530.

Schneider, S., Saenger, S., Müller, G., and Zanke, U. C. E. (2011). Nutzung von geringen Fallhöhen zur Energiegewinnung: Untersuchungen an einer Wasserdruckmachine [In German]. *Korrespondenz Wasserwirtschaft*, 4(6):329–334.

Senior, J. (2009). *Hydrostatic pressure converters for the exploitation of very low head hydropower potential*. PhD thesis, School of Engineering Sciences, University of Southampton.

Senior, J., Müller, G., and Wiemann, P. (2007). The development of the rotary hydraulic pressure machine. Unpublished.

Senior, J., Saenger, N., and Müller, G. (2010). New hydropower converters for very low-head differences. *Journal of Hydraulic Research*, 48(6):703–714.

Sicilian, J. (1990). A "FAVOR" based moving obstacle treatment for Flow-3D. Technical Note FSI-90-00-TN24, Flow Science, Inc.

Sims, R., Schock, R., Adegbululgbe, A., Fenhann, J., Konstantinaviciute, I., Moomaw, W., Nimir, H., Schlamadinger, B., Torres-Martínez, J., Turner, C., Uchiyama, Y., Vuori, S., Wamukonya, N., and Zhang, X. (2007). Energy supply. In Metz, B., Davidson, O., Bosch, P., Dave, R., and Meyer, L., editors, *In Climate Change 2007: Mitigation. Contribution of Working Group III to the Fourth Assessment Report of the Intergovernmental Panel on Climate Change*, pages 253–315. Cambridge University Press, Cambridge, United Kingdom and New York NY, USA.

Sotiropoulos, F. (2005). Introduction to statistical turbulence modelling for hydraulic engineering flows. In Bates, P. D., Lane, S. N., and Ferguson, R. I., editors, *Computational Fluid Dynamics*, pages 91–120. John Wiley & Sons, Ltd.

Souders, D. T. and Hirt, C. (2002). Modeling roughness effects in open channel flows. Technical Note FSI-02-TN60, Flow Science.

Staus, A. (1928). Wasserradversuche [in German]. *Die Mühle*, 65(47).

Stern, F., Wilson, R. V., Coleman, H. W., and Paterson, E. G. (1999). Verification and validation of CFD simulations. Technical Report IIHR Report No. 407, Iowa Institute of Hydraulic Research.

Sternecker, A., Ulm, D., and Kühnke, T. (2013). Wasserkraft-staudruckmaschine [In German]. EP Patent App. EP20,110,738,388.

Steuernagel, J., Kraus, T., and Zanke, U. (2002). Wasserkraftnutzung in Kläranlagen [In German]. *Wasser und Boden*, Heft 3.

Sun, X., Chick, J., and Bryden, I. (2008). Laboratory-scale simulation of energy extraction from tidal currents. *Renewable Energy*, 33(6):1267–1274.

Swamee, P. and Basak, B. (1993). Comprehensive open-channel expansion transition design. *Journal of Irrigation and Drainage Engineering*, 119(1):1–17.

Swamee, P. K. and Basak, B. C. (1994). Design of open-channel-contraction transitions. *Journal of Irrigation and Drainage Engineering*, 120(3):660–668.

Tatsuki, U., Masahiro, G., Atsushi, N., and Yuichi, H. (2013). Perspectives of small-scale hydropower generation using irrigation water in Japan. *Japan Agricultural Research Quarterly*, 47(2):135–140.

Tevata, A. and Inprasit, C. (2011). The effect of paddle number and immersed ratio on water wheel performance. *Energy Procedia*, 9:359–365.

Ulm, D. (2014). Wasserkraft-staudruckmaschine [In German]. EP Patent 2,593,608.

Versteeg, H. and Malalasekera, W. (2007). *An introduction to computational fluid dynamics*. Pearson Education Limited, Harlow, England, second edition.

Vowles, A. S. (2012). *Experimental quantification of the response of fish to conditions associated with low-head hydropower and fish passage facilities*. PhD thesis, Faculty of Engineering and Environment, University of Southampton.

Vowles, A. S., Karlsson, S. P., Uzunova, E. P., and Kemp, P. S. (2014). The importance of behaviour in predicting the impact of a novel small-scale hydropower device on the survival of downstream moving fish. *Ecological Engineering*, 69:151–159.

Wahyudi, B., Faizin, A., and Supraman, S. (2013). Increasing efficiency of overshot waterwheel with Overflow Keeper Double Nozzle (OKDN) by using hydraulic ram system. *Applied Mechanics and Materials*, 330:209–213.

Ward, E. and Alexander, P. J. (1992). Further development of the Dethrige-Long Meter. In *Conference on Engineering in Agriculture*, volume 379. ACT: Institution of Engineers, Australia.

Wei, G. (2005a). A fixed-mesh method for general moving objects. Technical Note FSI-05-TN73, Flow Science, Inc.

Wei, G. (2005b). A fixed-mesh method for general moving objects in fluid flow. *Modern Physics Letters B*, 19(28n29):1719–1722.

Wei, G. (2006). An implicit method to solve problems of rigid body motion coupled with fluid flow. Technical Note FSI-05-TN76, Flow Science, Inc.

Weidner, C. (1913). Test of a steel overshot water wheel. *Engineering News*.

Williams, A. and Simpson, R. (2009). Pico hydro: Reducing technical risks for rural electrification. *Renewable Energy*, 34(8):1986–1991.

Williams, A., Upadhyay, D., Demetriades, G., and Smith, N. (2000). Chapter 306 - Low head pico hydropower: A review of available turbine technologies. In Sayigh, A., editor, *World Renewable Energy Congress VI*, pages 1475 – 1480. Pergamon, Oxford.

Williamson, S., Stark, B., and Booker, J. (2014). Low head pico hydro turbine selection using a multi-criteria analysis. *Renewable Energy*, 61:43–50.

World Energy Council (2015). World energy resources: Charting the upsurge in hydropower development 2015. Technical report, World Energy Council, London, United Kingdom.

Yakhot, V. and Orszag, S. (1986). Renormalization group analysis of turbulence. i. basic theory. *Journal of Scientific Computing*, 1(1):3–51.

Yakhot, V. and Smith, L. (1992). The renormalization group, the ε-expansion and derivation of turbulence models. *Journal of Scientific Computing*, 7(1):35–61.

Annex 1: Publications Related to the Research

Publications related to this research are attached below.

Renewable Energy 52 (2013) 1–7

Contents lists available at SciVerse ScienceDirect

Renewable Energy

journal homepage: www.elsevier.com/locate/renene

Technical Note

Experimental investigation on the effect of channel width on flexible rubber blade water wheel performance

Shakun Paudel [a,*], Nick Linton [a], Ulrich C.E. Zanke [b], Nicole Saenger [c]

[a] School of Civil Engineering and the Environment, University of Southampton, Highfield, SO17 1BJ Southampton, United Kingdom
[b] Institute of Hydraulic and Water Resources Engineering, Darmstadt University of Technology, Petersenstrasse 13, 64287 Darmstadt Germany
[c] Faculty of Hydraulic Engineering, Darmstadt University of Applied Sciences, Schöfferstrasse 3, 64295 Darmstadt, Germany

ARTICLE INFO

Article history:
Received 16 June 2012
Accepted 18 October 2012
Available online

Keywords:
Water wheel
Efficiency
Power output
Flexible blades

ABSTRACT

A laboratory scale flexible rubber blade water wheel has been investigated at the hydraulic laboratory of University of Southampton. The effect of channel width on water wheel performance has been studied. Different upstream and downstream channel widths are set for the tests. In this paper, the experimental set up, tested water wheel and the measurement procedure are described and the experimental results are shown. Results show significant improvement in power output and efficiency in reduced channel width.

1. Introduction

Hydropower plays an important role in the global renewable energy supply [1]. In 2011, hydropower accounted for 15% of the global electricity production [2]. Among all renewable energy sources, it is the most reliable and cost effective renewable source of energy [3,4]. Small hydropower schemes are getting increasingly popular because of its simplicity in design, ease in operation, lower environmental impacts, cheaper and easier installations and no requirement of heavy construction in comparison to large hydropower schemes [5–7].

There are often sites with very low head below 2.5 m in the irrigation canals, old mill sites, or weirs in the river [8]. Many of these hydropower sites still remain unexploited [9]. Conventional highly efficient low head hydraulic turbines such as *Kaplan* become economically unviable because of the large size of the turbine required for very low head installations, requirement of special flow control mechanism and the risk they impose on the ecology especially on fish and sediment transport [10]. However, the need for harnessing these sites for electrical power generation has been ever increasing because of the growing interest towards renewable energy and environmental protection [11,12]. Therefore, there exists a great potential of producing hydropower from those sites using appropriate technology.

Water wheels were used as a primary source of power in ancient times [13]. Water wheels are simple machines usually made of wood or steel with blades fixed at regular interval around their circumference. The blades are pushed by the water tangentially around the wheel. The thrust produced by the water on the blades produces torque on the shaft and as a result the wheel revolves. Wide variety of water wheel models have been evolved throughout the history [14]. Four commonly used water wheel models are overshot, undershot, breastshot and stream wheels. Overshot water wheels are driven by the potential energy created by the accumulated water in the buckets of the wheel. Water flows at the top of the wheel and fills into the buckets attached on the periphery of the wheel. These wheels are applicable for large heads of 2–10 m [13] whereas breastshot water wheels are applicable to the smaller head difference of 1.5–4 m. Water level on the breastshot water wheel is maintained approximately at the level of wheel axle. Weight of the water enclosed in the blade cell is the main driving force on this type of water wheel [8,15]. Undershot water wheels operate with very small head differences of less than 2 m head [11,13]. Water enters below the axis of the undershot water wheel and employs both kinetic and potential energy of the flowing water [13]. Stream wheels utilize only the kinetic energy of the flow. They are usually installed on shallow channels with their blades extended to the

* Corresponding author. Permanent address: Institute of Hydraulic and Water Resources Engineering, Darmstadt University of Technology, Petersenstrasse 13, 64287 Darmstadt, Germany. Tel.: +49 6151 16 8169; fax: +49 6151 16 3223.
E-mail addresses: paudel@wb.tu-darmstadt.de (S. Paudel), npl1e08@soton.ac.uk (N. Linton), zanke@wb.tu-darmstadt.de (U.C.E. Zanke), nicole.saenger@h-da.de (N. Saenger).

0960-1481/$ – see front matter © 2012 Elsevier Ltd. All rights reserved.
http://dx.doi.org/10.1016/j.renene.2012.10.014

bottom of the channel in order to utilize the available kinetic energy of the flow [11].

Research shows that water wheels are technically and economically favourable alternatives for low head sites with an efficiency of 75–85% over a wide range of flow. Slow speed of rotation and large sized cells of the water wheel reduce the risk to aquatic life as well as allow better sediment transport and tolerance to floating debris [11]. Moreover, robust and simple design of water wheels involves less effort in construction, operation and maintenance of the wheel resulting in lower initial, operation and maintenance costs [16].

Recently a novel water wheel named *Hydrostatic Pressure machine (HPM)* has been developed to exploit very low head sites [8]. Unlike conventional water wheels HPM is driven mainly by the hydrostatic pressure force created by the difference between upstream and downstream water level via a large hub (about 1/3 of the total diameter of the wheel). Different HPM models with rigid blades have been tested by Senior et al. [8] and Schneider et al. [17]. Potential hazard to foreign objects due to blade strike and sharp edges of the blades is witnessed as major concerns in larger scale models of rigid blade wheels. Schneider et al. [17] demonstrates that the use of flexible rubber on the blade edges improved sediment transport to the downstream as well as increased the efficiency of the water wheel through decrease in gap losses. Similarly, Muller et al. [18] recommended flexible blade edges to avoid damage of fish by the sharp blade edges as well as reduced gap losses. Moreover, rubber blade elements for turbines or fluid motors have been suggested in a number of patents [19–21]. Stenild [20] and Godsall et al. [21] utilise the flexibility of the rubber as a means of varying blade geometry during rotation; however, the close clearance between the blades and the housing which can be attained by the use of rubber elements is emphasized in Cherubim [19].

The flexible rubber blade water wheel in the hydraulic laboratory of University of Southampton is designed to work as hydrostatic pressure machine. The model was invented by Nick Linton and is applied for patent by the University of Southampton [22]. The water wheel is fitted with flexible rubber blades evenly around the circumference of the solid hub. This paper aimed to study the effect of upstream and downstream channel width on the flexible rubber blade water wheel performance. Optimum channel design is an important practical concern for increased performance of water wheels.

2. Theory

The total extractable hydraulic power from the flowing water is given by the following expression:

$$P_{in} = \rho \times g \times Q \times H \tag{2.1}$$

where P_{in} is the hydraulic power input to the wheel (W), ρ is the density of water (kg/m^3), g is the acceleration due to gravity (9.81 m/s^2), Q is the volumetric water flow rate (m^3/s), H is the difference in total energy line upstream and downstream of the wheel (m). The dynamic head difference $(v_2^2 - v_1^2)/2g$ between upstream and downstream sides is negligible, therefore not taken into account in the calculations. Therefore, the available head H is equal to the difference between upstream water depth H_u and downstream water depth H_d.

The angular velocity ω (rad/s) of the wheel is calculated from the number of revolutions N at the given load in revolutions per minute (rpm) of the wheel as:

$$\omega = 2 \times \pi \times N/60 \tag{2.2}$$

The shaft torque τ (Nm) is the product of the force F of water striking the blades of the water wheel (N) and the moment arm length (m) which, in this case, is the radius of the pulley r. Force F is equal to the differences in the mass obtained from the two load cells times the acceleration due to gravity.

$$\tau = m \times g \times r \tag{2.3}$$

Subsequently the mechanical power output P_{out} available at the wheel shaft is determined from the measured torque τ and the corresponding angular speed of the wheel ω as:

$$P_{out} = \omega \times \tau = 2 \times \pi \times N \times \tau/60 \tag{2.4}$$

With calculated power output and input, the mechanical efficiency η of the wheel is therefore:

$$\eta = P_{out}/P_{in} \times 100\% \tag{2.5}$$

3. Experimental set up

The test flume is a 2.7 m long, 0.74 m wide and 0.4 m deep with variable height bypass weir at the inlet; variable height downstream weir for downstream water depth regulation and a fixed sharp crested measurement weir at the outlet. The flume was originally developed by Senior [23] during his earlier work on the hydrostatic pressure machines for very low head hydropower potential and was later modified and optimized by Linton [24].

The water wheel consists of acrylic cylindrical hub of 150 mm diameter and 250 mm wide onto which 12 blades of 100 × 250 mm size have been fastened. Blades are made of flexible butyl rubber sheet of 1 mm thickness with aluminium edges at the outside blade edges for increased stiffness of the blade. Blade support beams of 15 mm aluminium strips together with aluminium angle section were bonded around the circumference at the both ends of the hub to transfer the load from the centre of each blade to the side beams as shown in Fig. 1.

The wheel was placed over a polystyrene curved shroud section designed to minimize losses through the bottom gaps (Fig. 2). The side gaps were as small as 0.6 mm whereas the bottom gap of 1 mm was maintained. Details of the test rig are shown in Fig. 3.

All tests were done keeping the head constant. The main variables are the load on the wheel, and the channel width. The resulting variables are rotational speed, the flow through the wheel and force on the wheel. The head H was kept constant at 150 mm

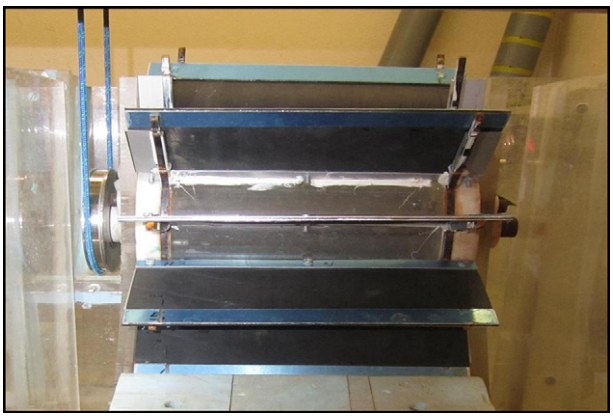

Fig. 1. Flexible rubber blade water wheel model (view from upstream).

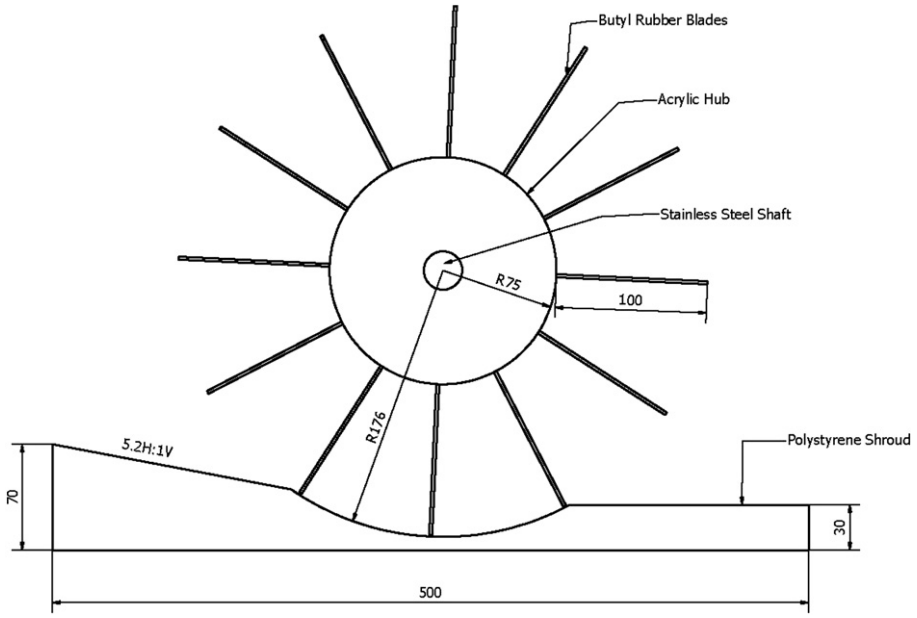

Fig. 2. Flexible rubber blade water wheel on the shroud.

for all test set ups by maintaining upstream water level H_u at 315 mm and downstream water level H_d at 165 mm and the flow was varied with the corresponding load on the wheel to maintain the constant water level. The variable height bypass weir at the inlet maintained the accurate level of water upstream while at the downstream, water level was dependent on the wheel rotation and the downstream adjustable weir height. During experiments, difficulty was experienced in accurately maintaining the target downstream water level which resulted in a net head fluctuation of 150 mm $\pm$ 5 mm. The upstream and downstream water levels were measured using the transparent graduated stilling tubes of diameter 100 mm within an accuracy of $\pm$1 mm. Three tubes were attached outside of the flume with 4 mm diameter tubing. One at 545 mm upstream from the wheel axle line; other one at 595 mm downstream of the wheel axle and the third one at 280 mm downstream of the downstream variable height weir.

Flow on the flume was regulated with adjustable pump of 25 l/s maximum flow capacity. The flow Q through the wheel is measured using the sharp crested measurement weir at the downstream of the test flume within an accuracy of $\pm$5%. All flow calculations are carried out using the methods described by British Standards Institution [25]. For the sharp crested rectangular weir Q is given by:

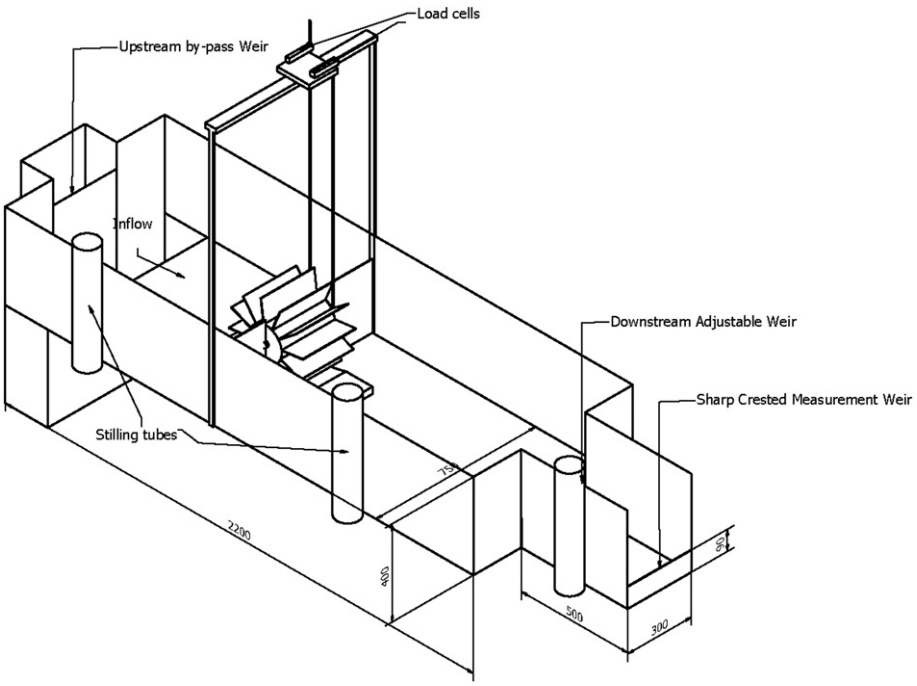

Fig. 3. The test rig assembly.

$$Q = C \times (2/3) \times \left(\sqrt{2g}\right) \times b_e \times h_e^{(3/2)} \quad (3.1)$$

where the constant C is given by the expression $C = 0.0602 + 0.075 \times (h/p)$ and h_e and b_e are calculated from $h_e = h + k_h$ and $b_e = b + k_b$. Where, h is measured head at the notch, p is the height of crest relative to the floor of the weir and b is the width of the notch in m. In this case, the values of b and p are 0.3 m and 0.09 m, respectively. Values of k_h and k_b are taken from the BSI graphs for the given ratio of b/B and are 0.001 m and −0.0008 m, respectively, where B is the width of the weir in m.

The torque was measured with the use of a Prony Brake. A 100 mm diameter plain low friction pulley was attached to one end of the wheel axle using a 6 mm keyway. Two calibrated cantilever beam load cells of 50 kg capacity were used for load application to the wheel. A brake rope was wrapped at 180° around the pulley, one end of which is fixed to one of the load cells and other end was used for load application. The readings were taken from the digital scales attached to each load cell which were accurate to ±0.007 kg. Load cells were calibrated against the dead weights to establish equations to quantify the corresponding values of mass for torque calculation. The difference in mass between two load cells was multiplied by the radius of pulley and acceleration due to gravity to get the torque values.

The revolutions of the wheel were recorded manually with the use of a stop watch and the numbers of revolution were within the accuracy of ±0.3 rpm. Three different time values for 10 revolutions were recorded for better accuracy and a mean value was taken for the calculations.

Following test set ups were investigated experimentally and compared with the full width set up of 740 mm both on upstream and downstream.

a. Full channel width of 740 mm both on upstream and downstream
b. Reduced upstream channel width tests
   i. Upstream 445 mm and downstream 740 mm
   ii. Upstream 350 mm and downstream 740 mm
c. Reduced downstream channel width tests
   i. Upstream full channel width of 740 mm and downstream 320 mm
   ii. Upstream 740 mm and downstream diverged at an angle of 12°

The channel width was varied symmetrically using the Plexiglas movable walls at the upstream and downstream of the channel.

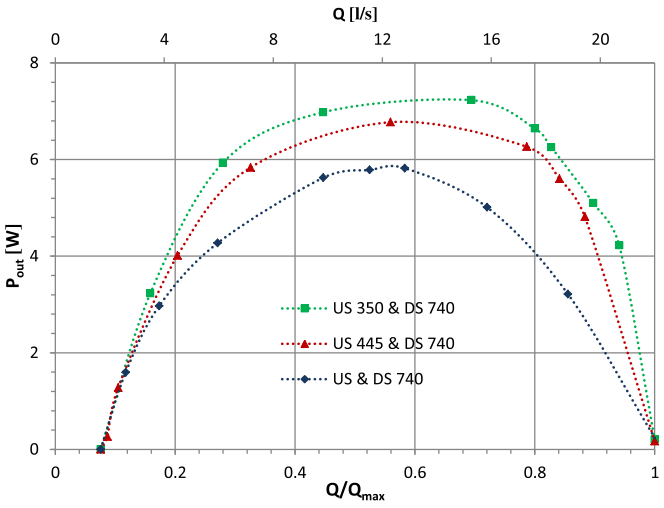

Fig. 4. Power output as a function of relative flow rate for changing upstream width.

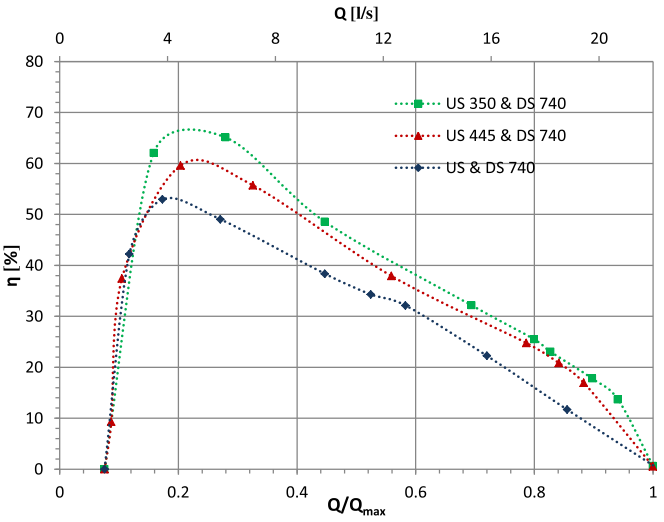

Fig. 5. Efficiency as a function of relative flow rate for changing upstream width.

These walls were fixed precisely in desired position with the help of wooden beams and G-clamps.

4. Results and discussion

4.1. Effects of upstream channel width variation

Power output, efficiency, torque and number of rotations are plotted against the relative flow rate (Q/Q_{max}). Where, Q_{max} (=22 l/s) is the maximum flow through the wheel when no load is applied to the wheel, i.e., at the runaway speed. The downstream channel width on these test settings is kept constant at 740 mm. The tests show increase in efficiency and power output with reducing channel widths (see Figs. 4 and 5). Improvement in performance is found to be occurred mostly due to the decrease in turbulent losses at the blade entry into the water. As channel width became narrower on the inlet, flow became confined and the rotational quality of wheel improved allowing smoother blade entry into water at higher flow rates than that of wider channels.

All curves follow similar trend for different upstream channel widths. Power output is constant for a wide range of flow between 5.5 l/s and 18 l/s. Decrease in load on wheel caused increased flow rate through the wheel and thus increased number of revolutions of

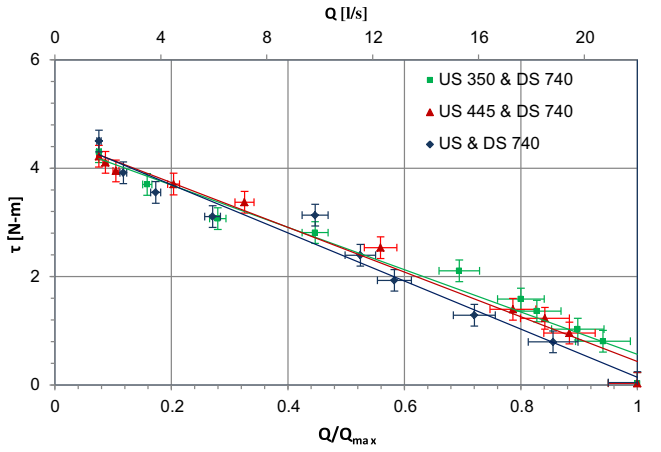

Fig. 6. Torque as a function of relative flow rate for changing upstream width.

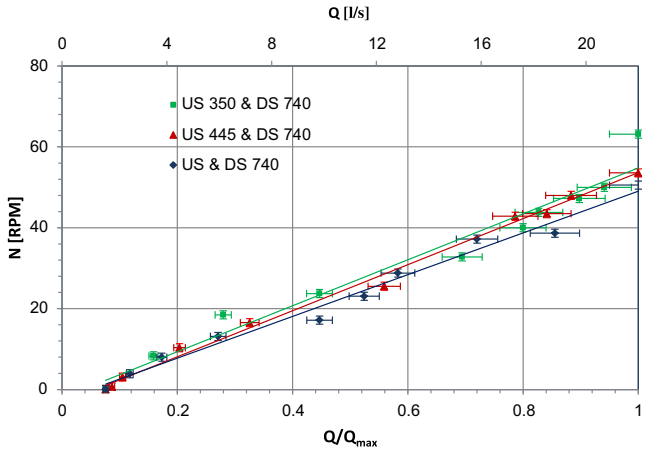

Fig. 7. Number of rotations as a function of relative flow rate for changing upstream width.

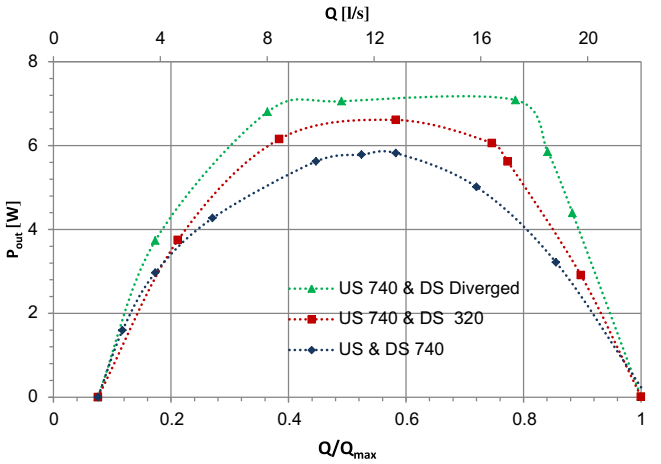

Fig. 9. Power output as a function of relative flow rate for changing downstream width.

water wheel but decreased torque. As the channel becomes narrower the range of flow ratio where power output stays almost flat becomes wider indicating improvement in power output over wider flow rates with reducing channel width. But when flow exceeds 18 l/s, blades start to splash on the water surface upstream then performance steeply drops. Fig. 4 reflects the behaviour of power output curves for different upstream channel width. The maximum power output accounts 5.82 W in 740 mm width at the flow rate of 12.82 l/s and efficiency 32.14%, which increases to 6.77 W in 445 mm width at the flow rate of 12.30 l/s and efficiency 37.92% and finally on the 350 mm width it reaches to 7.23 W at the flow rate of 15.27 l/s and efficiency 32.16%.

However, peak range in efficiency curve is narrower only for the flow rate of 4–9 l/s. Fig. 5 depicts the effect of upstream channel width on water wheel efficiency. As the flow increases beyond 9 l/s, power output remains almost constant but hydraulic power input increases continuously thus efficiency decreases continuously from the peak. The peak region slightly shifts towards the higher flow ratios as the channel width decreases. Maximum efficiency of 52.9% is achieved in 740 mm wide channel at a flow rate of 3.8 l/s with power output of 2.96 W which increases to 59.6% in 445 mm channel width at the flow rate of 4.48 l/s with power output of 4.01 W and finally it further increases to 65.11% in 350 mm channel at the flow rate of 6.15 l/s with power output of 5.93 W. At higher flows, blades create splashes on the water surface generating turbulence on the upstream side, air bubbles were trapped in the cell dropping the efficiency down with increasing flow rate. Therefore, performance curves are not clear in this region. Similarly, minimum data points can be obtained at the lower flow rates as the wheel rotates slowly and unevenly at very low flow rates.

The rotational speed of the wheel and the torque continuously increase with decrease in the channel width. As shown in Figs. 6 and 7, increase in torque with reducing channel size on the upstream is smaller compared to the increase in number of rotations with decreasing channel size at any given flow. Performance improvement is found to be mostly contributed by the increase in rotational speed than by the increase in torque. Increase in torque and number of rotations become more apparent with increasing flow rates. At low flow rates all curves tend to coincide showing almost no increase in torque with changing channel width. The trend lines are added for more clarity with error bars showing the extent of measurement errors.

Fig. 8 shows a plot of torque against number of rotations. At given number of wheel rotation, there are three torque values, the highest being the narrowest channel width and vice versa. This behaviour clearly demonstrates increase in performance with reducing upstream channel widths. But at lower number of rotations all curves tend to overlap showing no improvement in torque in different channel widths at the given rotational speed.

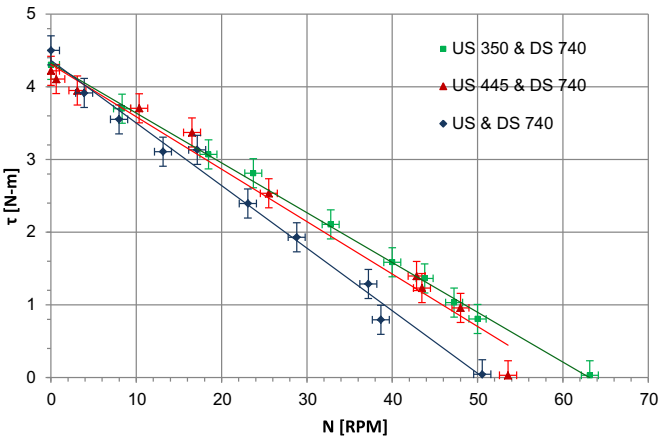

Fig. 8. Torque as a function of number of rotations for changing upstream width.

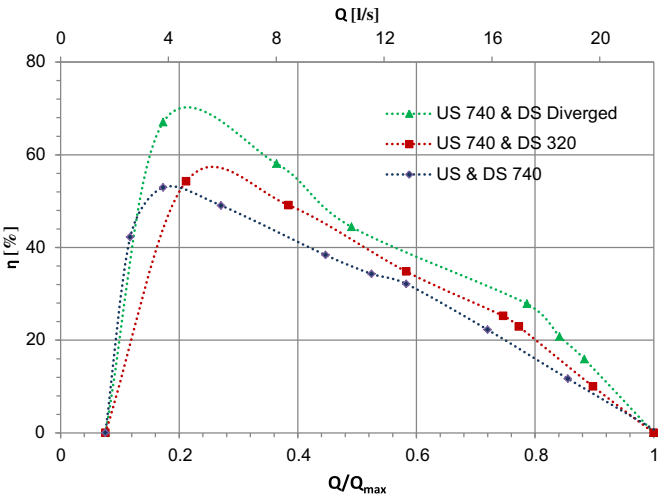

Fig. 10. Efficiency as a function of relative flow rate for changing downstream width.

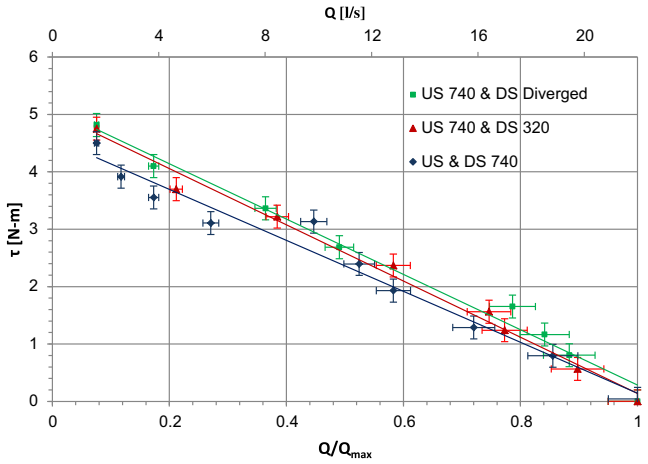

Fig. 11. Torque as a function of relative flow rate for changing downstream width.

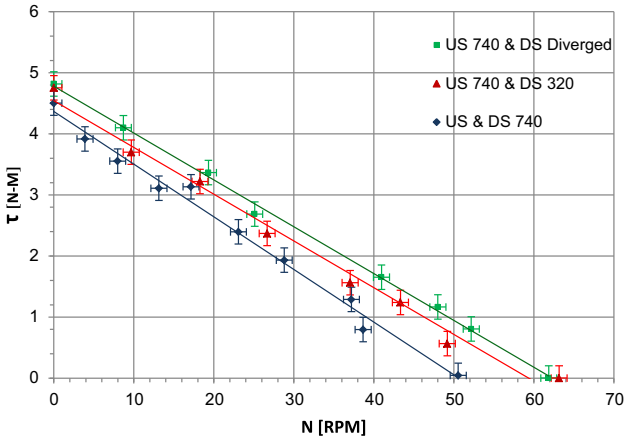

Fig. 13. Torque as a function of number of rotations for changing downstream width.

4.2. Effects of downstream channel variation

To investigate the effect of downstream channel width on wheel performance, upstream width is kept constant at 740 mm. Power output, efficiency, torque and number of rotations are plotted against the relative flow rate (Q/Q_{max}).

The power output curves reflect broad range of flow at the maximum power output. The power output has a flat range between the flows of 8 l/s and 18 l/s. As shown in Fig. 9, the maximum power output of 5.82 W at the flow rate of 12.82 l/s with efficiency 32.14% in 740 mm wide channel increases to 6.61 W at the same flow rate of 12.82 l/s with efficiency 34.81% in 320 mm channel width and finally to the 7.08 W at the flow rate of 17.3 l/s with an efficiency of 27.83% on the diverged channel set up. This increase in performance is caused slightly due to the increase in effective head acting on the wheel because of the reduction in water depth immediately downstream of the water wheel. As the channel narrows down on the downstream side, flow velocity increases creating a strong hydraulic jump on the downstream side and thus creating supercritical flow immediately downstream of the water wheel. Moreover, the amount of load application required to rotate the wheel at any number of rotations became higher in narrower channel width than in full channel width setting. This implies increase in torque at constant rotational speed thus improvement in wheel performance.

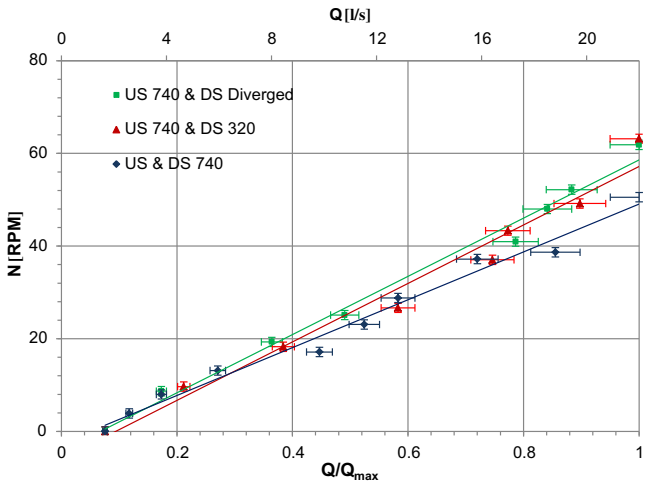

Fig. 12. Number of rotations as a function of relative flow for changing downstream width.

Efficiency curves are steeper than the power curves and have a narrower band of peak efficiency between the flow rates of 4 and 9 l/s as shown in Fig. 10. All lines follow the similar trend. The efficiency trend shows only a slight increase from the 52.9% at the flow rate of 3.8 l/s and with power output of 2.96 W in 740 mm width to the 54.26% at the flow rate of 4.66 l/s and with power output of 3.74 W in 320 mm width. On the diverged downstream settings efficiency reaches to 67.35% at the flow rate of 3.8 l/s with power output of 3.71 W Figs. 9 and 10 depict comparison of measured performances in various downstream channel widths. It is apparent that the downstream channel width also influences power output and efficiency of the wheel.

Torque and number of rotations of the wheel are plotted against relative flow rate in Figs. 11 and 12. Increase in torque with reducing channel size on the downstream is smaller compared to the increase in number of rotations with decreasing channel size at any given flow. In this case as well, performance improvement is found to be contributed by the increase in rotational speed than by the increase in torque. Increase in torque is clearer in lower flow rates in contrast to the upstream reducing channel width set up described earlier. Increase in number of revolutions has however a similar trend as in the case of upstream channel width set up. At the low flow rates the behaviour of rotational speed seems unclear.

Fig. 13 shows torque against number of rotations. In contrast to the reducing upstream set up, at lower number of rotations the increase in torque for given rotational speed at different widths of the downstream channel is significant.

5. Conclusion

Performance characteristics of the flexible rubber blade water wheel at different channel width have been experimentally investigated. Performance is observed to be improved with reducing channel size both on upstream and downstream side of the water wheel. On the upstream, performance improvement is found to occur mainly due to reduced turbulent losses. This improvement in performance with reducing channel size confirms that side filling of cells does not play an important role in the flexible rubber blade water wheel performance. Therefore, there is no need for a wider channel on the upstream side of the wheel. Among other set ups, the diverged channel shape on the downstream minimised the effect of downstream flow on the wheel by creating supercritical flow immediately downstream of the water

wheel and resulted in increased net head acting on the wheel thus increased performance.

Among the tests settings mentioned above, upstream 350 mm and downstream 740 mm, and upstream 740 mm and diverged downstream has shown maximum improvement over other test set ups with wider channel widths. The maximum efficiency of 65.11% is achieved on the narrowest upstream set up. This is 32.75% increase in efficiency as compared to the full channel width set up at the same flow rate. Similarly, maximum power output of 7.23 W has been attained on the same test set up. This is 2.22 W increase in comparison to the upstream and downstream 740 mm set up at the same flow rate. Similarly on the upstream 740 mm and diverged downstream set up, efficiency reached to 67.02% which is 14.08% increase in comparison to the full channel width set up for the same flow rate. Power output increased to 7.08 W which is 3.8 W increase in comparison to the full channel width set up at the same flow rate.

According to the Froude scaling laws, three times the diameter of the model investigated here would produce maximum power of 338 W on the narrowest upstream set up and 331 W on the diverged downstream set up. It is assumed that the combination of these two set ups would produce improved results.

Acknowledgement

This research is financially supported by the German Ministry of Education and Research. Authors would like to acknowledge Hydraulics Laboratory of the School of Civil and Environmental Engineering, University of Southampton for providing resources to accomplish this research.

References

[1] Bartle A. Hydropower potential and development activities. Energy Policy 2002;30:1231–9.
[2] International Energy Agency (IEA). World energy outlook 2011: executive summary. Available at: http://www.iea.org/weo/docs/weo2011/executive_summary.pdf; 2011 [accessed 18.02.12].
[3] Leijon M, Skoglund A, Waters R, Rehn A, Lindahl M. On the physics of power, energy, and economics of renewable electric energy sources – part 1. Renewable Energy 2010;35(8):1729–34.
[4] Kosnik L. The potential of water power in the fight against global warming in the US. Energy Policy 2008;36(9):3252–65.
[5] Kosnik L. The potential for small scale hydropower development in the US. Energy Policy 2010;38(10):5512–9.
[6] Paish O. Small hydro power: technology and current status. Renewable and Sustainable Energy Reviews 2002;6(6):537–56.
[7] Yassi Y, Hasemloo S. Improvement of the efficiency of the Agnew micro hydro turbine at part loads due to installing guide Vane mechanism. Energy Conversion and Management 2010;51(10):1970–5.
[8] Senior J, Saenger N, Muller G. New hydropower converters for very low-head differences. Journal of Hydraulic Research 2010;48(6):703–14.
[9] Shimokawa K, Furukawa A, Okuma K, Matsushita D, Watanabe S. Experimental study on simplification of Darrieus-type hydro turbine with inlet nozzle for extra-low head hydropower utilization. Renewable Energy 2012; 41:376–82.
[10] Mosonyi E. Low-head power plants. In: 3rd enlarged and completely revised edition, vol. 1. Budapest: Akademiai Kiado; 1987.
[11] Muller G, Kauppert C. Performance characteristics of water wheels. Journal of Hydraulic Research 2004;42(5):451–60.
[12] Furukawa A, Watanabe S, Matsushita D, Okuma K. Development of ducted Darrieus turbine for low head hydropower utilization. Current Applied Physics 2010;10(2):S128–32.
[13] Denny M. The efficiency of overshot and undershot water wheels. European Journal of Physics 2004;25:193–202.
[14] Farret FA, Simoes MG. Integration of alternative sources of energy. Hoboken, NJ: Wiley-IEEE Press; 2006.
[15] Muller G, Wolter C. The breastshot water wheel: design and model tests. Proceedings of the Institutions of the Civil Engineers: Engineering Sustainability 2004;157(ES4):203–11.
[16] Woods G, Tickle A, Chandler P, Beardmore J, Pymm R. Peak power: Developing micro hydro power in the peak district, friends of the peak district, UK. Available at: http://www.friendsofthepeak.org.uk/download/files/HYDRO/PEAKPOWERMainreportAppA.pdf; 2010 [accessed: 30.09.12].
[17] Schneider S, Saenger N, Muller G. Nutzung von Geringen Fallhohen zur Energiegewinnung: Untersuchungen an einer Wasswerdruckmaschine. Korrespondenz Wasserwirtschaft 2011;4(6):329–34 [in German].
[18] Muller G, Linton N, Schneider S. Das project HYLow: Die Wasserdruckmachine. Korrespondenz Wasserwirtschaft 2012;5(1):30–6 [in German].
[19] Cherubim JL. Lightweight radial fluid flow machine with fluid bearing sealed flexible blades. US patent number 4302147; 1981.
[20] Stenild EL. Positive displacement fluid motor with flexible blades. US patent number 5456585; 1995.
[21] Godsall TG., Innes DE, Innes MC. Low head water turbine. US patent number 6877968b2; 2005.
[22] Linton N. Flexible blades for water wheels and hydrostatic pressure machines, application number GB1007134.8. UK patent application; 2011.
[23] Senior J. Hydrostatic pressure converters for the exploitation of very low head hydropower potential. PhD thesis, University of Southampton; 2009.
[24] Linton N. The design and development of hydrostatic pressure machines for small hydropower applications. MSc thesis, University of Southampton; 2009.
[25] British Standards Institution. Methods of measurement of liquid flow in open channels, part 4A – methods using thin plate weirs, BS 3680-4A 1981. London: British Standards Institution; 1981.

Numerical Simulation of a Dethridge Wheel Using Flow-3D

S. Paudel[1] & N. Saenger[2]

[1]Institute of Hydraulics and Water Resources Engineering, Darmstadt University of Technology, Franziska-Braun-Str. 7, 64287, Darmstadt, Germany
Email: paudel@wb.tu-darmstadt.de

[2]Faculty of Hydraulic Engineering, Darmstadt University of Applied Sciences, Schofferstr. 3, 64295, Darmstadt, Germany
Email: nicole.saenger@h-da.de

Abstract

Dethridge wheel is primarily used for measuring flow in irrigation canals. Working in a similar principle as the conventional undershot waterwheel, this wheel could be a viable option of power generation for decentralized application in remote areas. The potential of Dethridge wheel for electricity generation is investigated experimentally and numerically. A physical model is built in 1:2 scale and for simulation, a commercial CFD tool Flow-3D is used.

In this paper, the physical model is briefly described and an example of Computaional Fluid dymanics (CFD) model of a Dethridge wheel is presented. Two different cases involving coupled and prescribed motion cases are compared with the experimental results. Preliminary analysis suggests that computed values are in good range with the observed values. Further investigation with advanced numerical options and different mesh characteristics is ongoing and is believed to produce better results.

Introduction

Dethridge wheel has been in use since early 20th century for measuring flow in irrigation canals. Being robust and simple in design, this technology served as a reliable flow metering solution for more than a century now. There are still thousands of these wheels working as a flow meter in the irrigation canals of Australia and also found in use in the USA and other Asian countries (Kraatz & Mahajan, 1982).

The wheel works in a similar principle as the conventional undershot water wheel (Kraatz & Mahajan, 1982), in which water enters below the axle of the wheel and as a result the wheel rotates (Muller & Kauppert, 2004). The big hub of the wheel acts as a dam and creates a head difference by itself. Therefore, it could be a potentially viable option for very low head applications in irrigation canals for remote and decentralised pico-scale hydropower application.

The potential of the Dethridge wheel for power generation is investigated at the hydraulics laboratory of Darmstadt University of Applied Sciences. Two different methods are used for the optimisation. A laboratory scale physical model is tested and a numerical model of the wheel is simulated in a commercial Computational Fluid Dynamics (CFD) code Flow-3D. Two different cases of simulations are compared with the physical model results and are pre-

sented in this paper.

Experimental Set-up

A laboratory scale physical model of Dethridge wheel is built and tested within the 20 m long, 1 m wide and 1.5 m deep flume for its potential as a power converter. The slope of the flume is adjustable and contains inlet tank at the upstream and a control weir at the downstream. Side walls of the flume are made up of a glass and the bottom is a smooth concrete floor. Flow (Q) in the channel is regulated through an automated flow meter.

The hub of the wheel is made up of polyvinyl chloride (PVC) piping, which is 40 cm in diameter and 25 cm wide. Eight v-Shaped steel blades of 2 mm thickness are mounted along the circumference of the wheel and are 10 cm long and are bent in V-shape to acquire an angle of 127°. At the apex of each blade, a V-shaped air vent is located to facilitate the filling and emptying of adjacent compartment as they enter and exit the water surface under the wheel. The both ends of the blades are chamfered to match the fillets at the junction of the side walls and the floor. The apex of the V is leading in the direction of rotation. Figure 1 shows the physical model of the Dethridge wheel placed in a test flume.

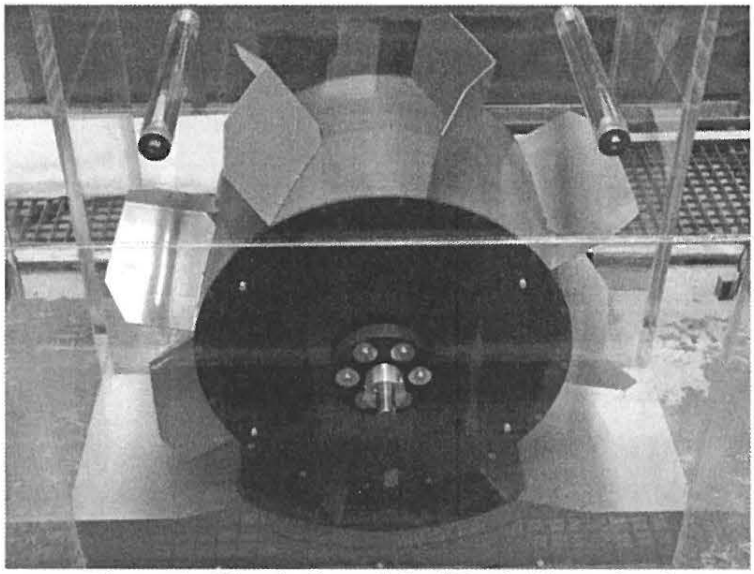

Figure 1: Physical model of Dethridge wheel

The shroud is made up of concrete with smooth surface finishing. The curvature of the shroud makes an arc of 70° to the wheel's circumference and is symmetrical in both x- and y-direction. Side and bottom gaps are 1 mm. The shroud and wheel assembly with key dimensions (in mm) is shown in Figure 2.

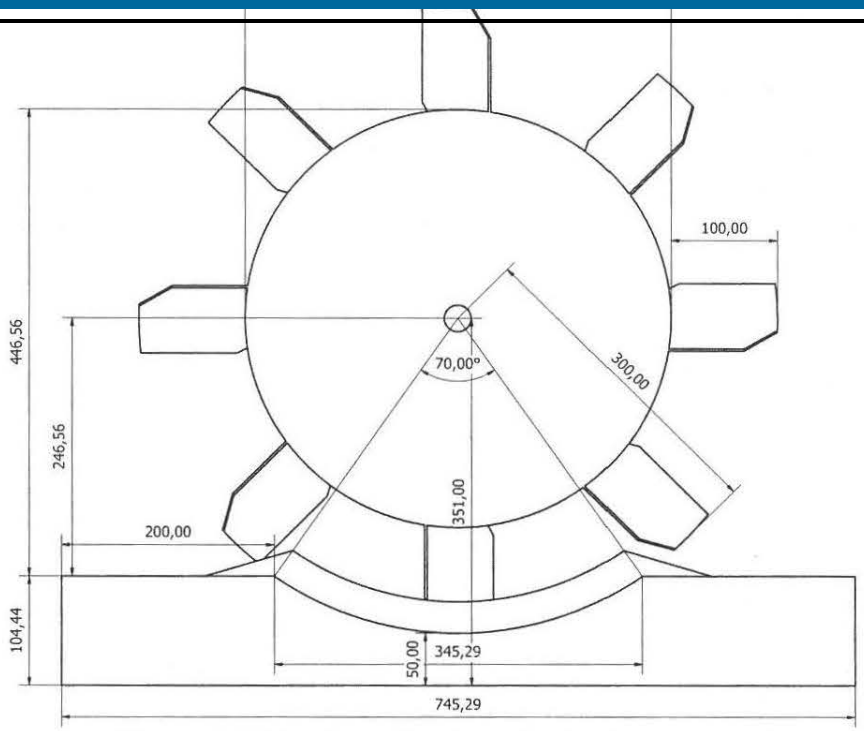

Figure 2: Side view of a shroud wheel assembly

For the given flow condition, number of revolutions (N), the shaft torque (τ), upstream water depth (h_1) and the downstream water depth (h_2) are measured from which power output and the efficiency of the wheel is calculated. A torque transducer is used for measuring the torque and the shaft speed is measured using a pulse sensor. A lab view based computer program is used for data acquisition. Water level on the upstream and downstream is measured using the stilling tubes and graduated scale and is manually recorded.

Computational Fluid Dynamics (CFD) Model

For CFD simulation of the Dethridge wheel, a commercial CFD code Flow-3D is used. The geometry of flume, shroud and the wheel is prepared as STL files and are imported as individual components into Flow-3D. Figure 3 below shows a sectional view of CAD model within the test flume.

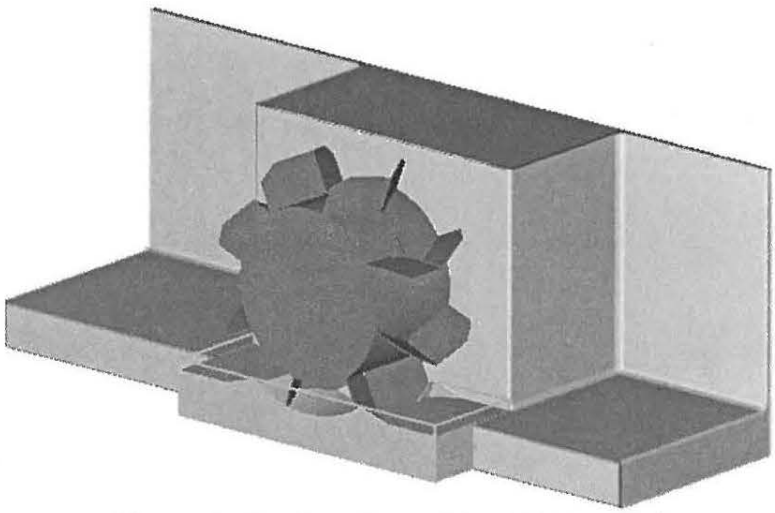

Figure 3: Section view of the CAD model

In order to reduce the computational time, only symmetrical half of the model is simulated. Three nested mesh blocks of cell size 10 mm, 5 mm and 2.5 mm are used to define the computational domain. The nested meshing allowed the area around the wheel to be refined and thereby reduced the computational effort to a great extent. Among the 4.8 million total cells, only 3.8 million were active. The rendered view of the computed domain is shown in Figure 4.

For modelling the turbulence, the Renormalized Group (RNG) model is used with the default no-slip condition imposed at the solid surfaces and dynamically computed turbulent length scale option. Wheel motion is modelled using the moving objects model (GMO) with implicit solver option. The model is calibrated with the data obtained from the experiments. Volume flow rate with uniform pressure distribution is introduced on the upstream boundary. The downstream mesh boundary condition is characterized by the pressure boundary with experimentally known fluid depth. Two different simulation cases are presented here. Firstly a coupled motion case is simulated and compared with the identical test on the physical model. Then the case of a prescribed motion is simulated and compared with corresponding measured values. Mesh characteristics remain the same in both cases.

Case I Coupled Motion

In the case of coupled motion, there is no external control on the motion of the wheel and the wheel rotates freely under the effect of moving fluid. The upstream water level (h_1) should adjust itself according to the flow rate and downstream losses. The number of revolution of the wheel (N) for given flow rate should also match with the measured value. A volume flow rate (Q) of 5 l/s and a downstream fluid height (h_2) of 42 mm are introduced at the upstream and downstream boundaries respectively.

Case II Prescribed Motion

In this case, motion of the wheel is pre-defined with a counter-clockwise angular velocity (ω) of 1.047 rad/sec, which corresponds to 10 revolutions per minute. At steady state, the upstream and downstream water depths (h_1 & h_2) and the torque (τ) value should match with the measured results. In this case, the flow rate (Q) is 5 l/s and the downstream water depth (h_2) is 46 mm.

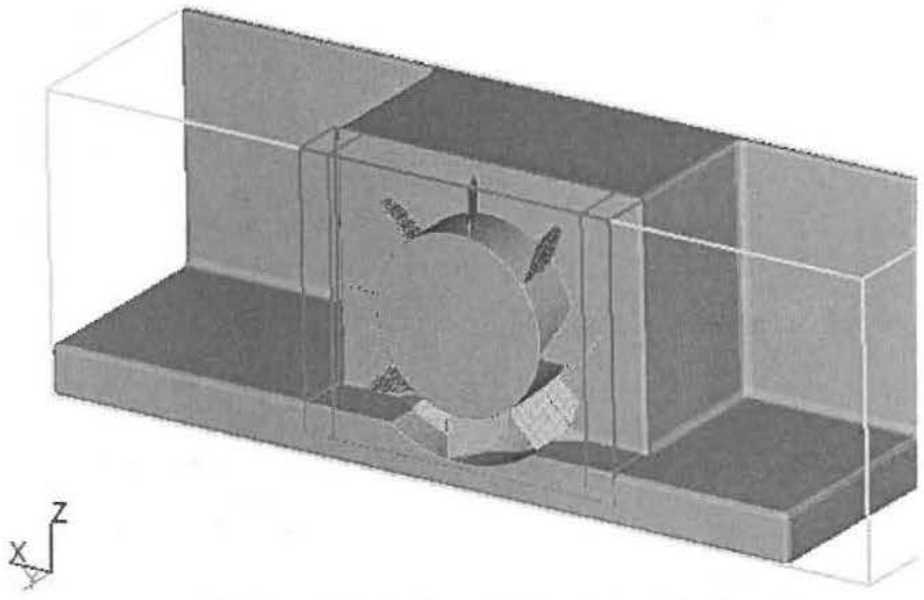

Figure 4: The rendered view of computational domain

Results and Discussion

Computed results show a good agreement with the measured values. However, there are still considerable discrepancies between measured values and computed results in both cases indicating a need of further simulation runs with different mesh sizes, boundary conditions or numerical options. The results of case I and II are presented and discussed separately in the following paragraphs.

Case I Coupled motion

The simulation took around 4 days for 30 seconds of simulation time and steady state is reached at around 26 seconds of simulation time. The flow rate at the downstream is close to the flow introduced on the upstream boundary as shown in Figure 5.

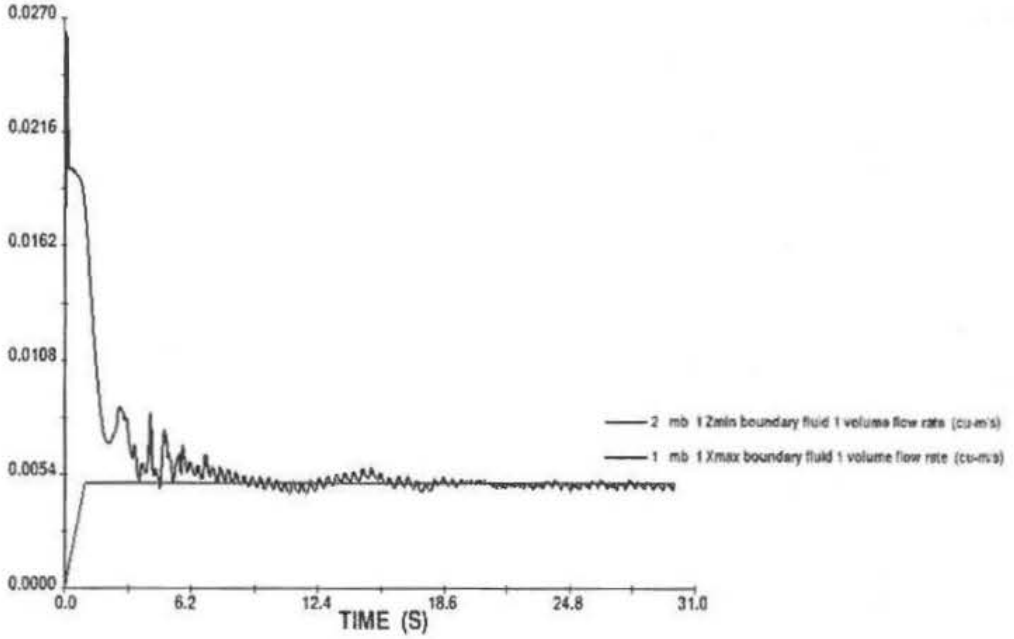

Figure 5: Flow rates for coupled motion case

The angular velocity of the wheel is calculated by the solver, which is then converted to the number of revolutions per minute (rpm). As shown in Table 1, the computed value of the number of revolutions (N) and the downstream flow depth (h_2) are quite close to the measured values. However, upstream water depth (h_1) is much less than the measured value.

Table 1: Comparison of parameters for coupled motion

Variables	Experiment	Computed	% Error
N (rpm)	15.196	16.23	- 6.77 %
h_1 (cm)	12.70	10.279	19.06 %
h_2 (cm)	4.20	4.41	- 5.00 %

In Figure 6, the velocity magnitude at the time frame of 30 seconds is shown. Here, a flow of 5 l/s is flowing through the wheel and as a result the wheel is rotating at 16.23 rpm. The upstream part and the areas close to the boundaries have very small magnitude of velocity. As water enters the wheel, velocity rises and reaches supercritical at the downstream. This velocity distribution is intuitive and similar to what is observed on the physical model.

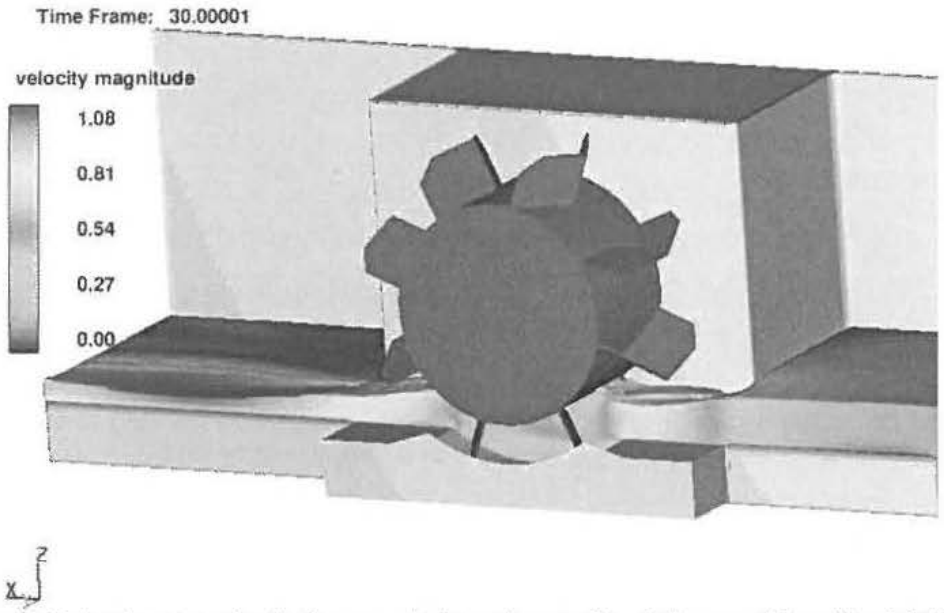

Figure 6: Velocity magnitude for coupled motion at $Q = 5$ l/s, resulting $N = 16.23$ rpm

Case II Prescribed motion

The simulation time was longer in this case, which took around 7 days for 30 seconds of simulation time. The upstream and downstream flow rate is compared in Figure 7. The downstream flow rate is close to the flow rate introduced at the upstream, however there is about 10 % of volumetric losses and considerable fluctuation on the flow rate.

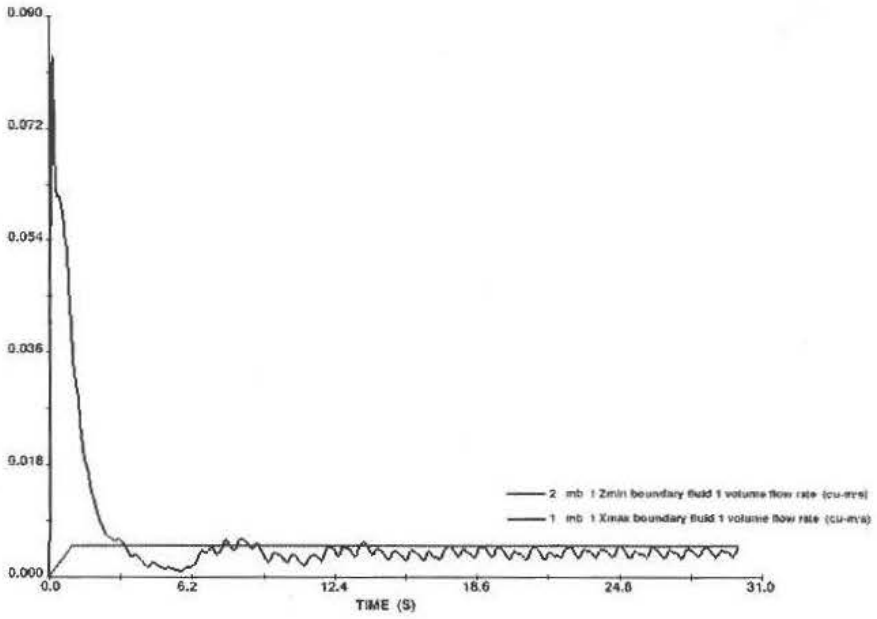

Figure 7: Flow rate for prescribed motion case

The computed values of torque (τ), upstream and downstream flow depths (h_1 & h_2) are compared in Table 2. The computed value of torque differs considerably from the measured value. Sensitivity study including different numerical options, mesh characteristics, turbulence models would help to improve these results.

Table 2: Comparison of parameters for prescribed Motion

Variables	Experiment	Computed	% Error
τ (N-m)	11.818	8.491	28.15 %
h_1 (cm)	34.65	32.71	5.59 %
h_2 (cm)	4.60	4.15	9.78 %

In Figure 8, the velocity magnitude for prescribed motion of 10 rpm and 5 l/s of flow is shown. As wheel slows down than in case 1 above, the water is dammed up on the upstream and becomes subcritical. Waves are generated as the blades enter and splash the flow on the upstream. Due to the pressure built on the upstream side of the wheel, stream of flow rises up through the V-shaped air vent on the downstream. This phenomenon was also observed during experiments. As water leaves the wheel, flow on the downstream becomes supercritical.

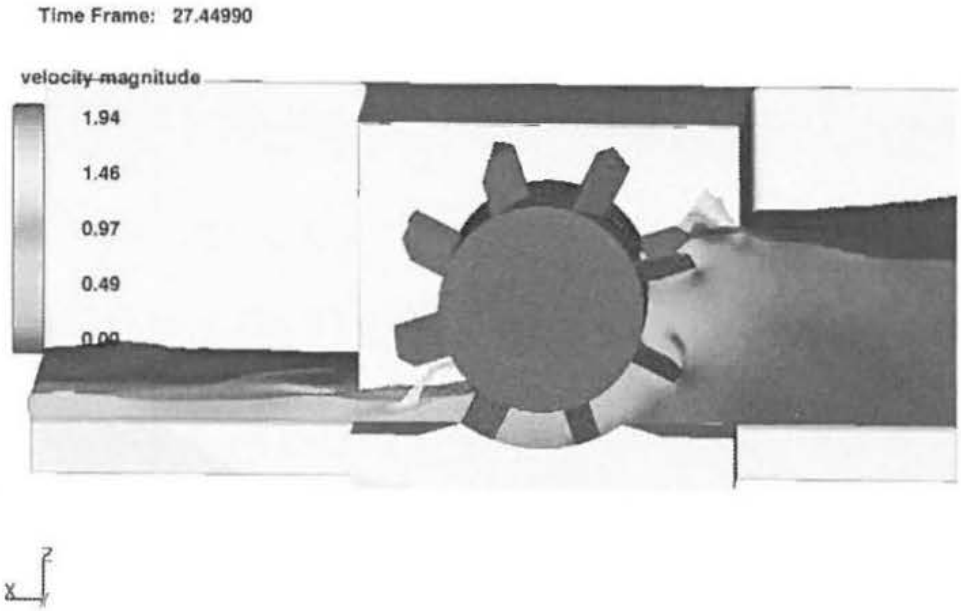

Figure 8:Velocity magnitude at $N = 10$ rpm; $Q = 5$ l/s

Conclusion

Dethridge wheel holds a potential to be utilised in remote areas for decentralised power application. The initial findings suggest that a full-scale machine would produce the power in the range of 200 to 300 watts. When optimised for power, this technology could become a potential solution for many rural households to meet their basic energy need such as for lighting and battery charging facility. The powerful numerical tool Flow-3D proves to be advantageous option in reducing the costs and time constraints involved in the optimisation process. This simple example presented in this paper shows how complex flow phenomena can be conveniently captured with the aid of a powerful CFD tool. Further simulation runs with different numerical options, boundary conditions and mesh sizes are necessary to improve these results.

References

Kraatz, D., & Mahajan, I. (1982). *Small Hydraulic Structures* (Vol. 26/1). Rome: Food and Agricultural Organisation of the United Nations.

Muller, G., & Kauppert, K. (2004). Performance Characteristics of Water Wheels. *Journal of Hydraulic Research , 42* (5), 451-460.

Matthias von Harten, Shakun Paudel und Nicole Saenger

Nutzung kleiner Fallhöhen – ein Beitrag aus Forschung und Entwicklung

Die Energiewende und der steigende Energiebedarf führen auch zur Modernisierung und zum Neubau von Wasserkraftanlagen mit kleinen Fallhöhen. Die Nutzung dieser Fallhöhen wird durch die Forschungsarbeit an Wasserrädern an der Hochschule Darmstadt unterstützt. Dieser Beitrag beschreibt die Untersuchungen an einem Wasserrad nach Zuppinger und einem Dethridge Wheel hinsichtlich der ökologischen (Durchgängigkeit) und energetischen (Leistung) Optimierung.

1 Motivation

Die Nutzung kleiner Wasserkräfte wird seit der deutschen Energiewende in 2012 wieder in einem anderen Licht betrachtet. Die Steigerung der Energiewandlung in Deutschland durch die Nutzung von Standorten an kleinen und mittelgroßen Fließgewässern wird von Anderer et al. [1] bei nur knapp 20 % gesehen. Diese Erhöhung wird insbesondere durch die Steigerung des Wirkungsgrades durch Modernisierung bzw. die optimierte Steuerung der Anlagen möglich. Der Neubau von Wasserkraftanlagen und den damit verbundenen Querbauwerken muss konform mit dem Wasserhaushaltsgesetz des Bundes und der Wassergesetze der Länder bzw. der europäischen Wasserrahmenrichtlinie geschehen und wird daher von Anderer et al. [1] als eher nachrangig eingeschätzt. Wenn es um die Modernisierung von Anlagen geht, muss deren Optimierung im Hinblick auf ökologische Parameter und Prozesse berücksichtigt werden. Sediment- und Fischdurchgängigkeit der Anlagen sind ein wichtiges Thema, und können nicht allein durch den Bau von funktionstüchtigen Fischwegen (Auf- bzw. Abstieg) erfolgen.

An der Hochschule Darmstadt werden derzeit hydraulische Versuche und numerische Simulationen zur ökologischen Optimierung von Wasserrädern durchgeführt. Die Untersuchungen werden an dem maßstäblichen Modell des Rades nach Zuppinger der Firma Walter Schuhmann, Bad Kissingen, durchgeführt. Wasserräder können mit einem weiten Abflussspektrum arbeiten und gelten nach Gerhardt [2] als fischdurchgängig. Die Aussage von Gerhardt wird jedoch nicht näher belegt. Auswertungen von Versuchen aus dieser Zeit liegen nicht vor. Erst in den letzten Jahren wurden einige wenige Untersuchungen des Fischdurchgangs durchgeführt. Diese Untersuchungen bestätigen die Aussage von Gerhardt nicht; auch beim Durchgang durch Wasserräder werden Fische verletzt oder getötet, jedoch in einem geringeren Maße als bei Turbinen (z. B. Tombek & Holzner [3]). Jedoch sind die wenigen bekannten Untersuchungen nach Ansicht der Verfasser Einzelbeispiele und belegen nicht ausreichend die Mortalität von Fischen beim Durchgang durch Wasserräder. Zudem fehlt diesen Untersuchungen die Analyse der hydraulischen Verhältnisse, die die Schwimmwege der Fische prägen. In den Modellversuchen der Hochschule Darmstadt wird untersucht, wie sich beispielsweise variierende Durchflüsse, Spaltweiten zwischen Schaufeln und Bodensegment, Schaufelanzahl, Drehzahl und Schaufelform auf den Wirkungsgrad bzw. die Leistung des Wasserrades auswirken und wie sie die ökologische Durchgängigkeit beeinflussen.

Die neuen Erkenntnisse aus den Untersuchungen an einem Zuppinger-Wasserrad werden auch auf andere Wasserradarten übertragen. Denn Wasserräder werden nicht allein zur Wandlung von Wasserkräften in mechanische bzw. elektrische Energie verwendet. Das australische Dethridge Wheel misst in Bewässerungskanälen den durchgeleiteten (bzw. entnommenen) Abfluss. Erste Untersuchungen [4] zeigen, dass eine Wandlung der Wasserkräfte in mechanische oder elektrische Energie mit dieser simplen Wasserradkonstruktion möglich ist. Da Entwicklungspotenzial in der Leistungsausbeute dieser sehr einfachen Maschine gesehen wird, wird nun an deren Wirkungsgradoptimierung gearbeitet. Ziel ist es, bei optimierter Zu- und Ableitung sowie Schaufelform und -anzahl einen einfach zu bauenden Wandler zu entwickeln, der insbesondere in Entwicklungsländern vor Ort aus ortsüblichen Materialien gebaut werden kann.

2 Ansätze zur ökologischen Optimierung des Wasserrades nach Zuppinger

Aufgebaut wurde ein Wasserrad der Firma Mühlenbau Schumann, Bad Kissingen, nach Zuppinger-Bauart im Maßstab 1:5 (**Bild 1**). Das Modell hat einen Durchmesser von 1,80 m und eine Breite von 0,90 m. Die 50 Schaufeln besitzen eine Holzbeplankung mit einer Stärke von 8 mm; das Rad besteht aus drei Segmentkränzen. Das Spaltmaß zwischen Schaufeln und Bodensegment sowie zu den Seiten beträgt 0,005 m. Es werden Wasserstände über Drucktransmitter (Keller:

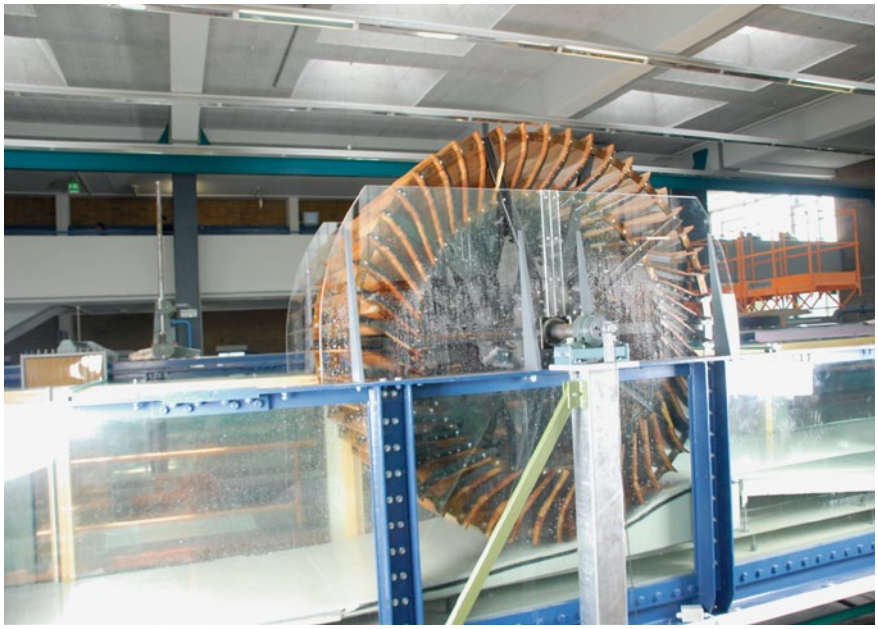

Bild 1: Das Modellwasserrad in der Zuppinger-Bauweise

PR-41X), Radumdrehungen pro Minute über Drehgeber (ifm electronic: RB1015), Durchfluss über ein MID (Krohne: AQUAFLUX F/6) und Drehmoment über Drehmomentaufnehmer (ETH-Messtechnik: DRFL-VI-1000-A) gemessen. Die Fallhöhe wird aus der Differenz des Oberwasserstandes und des Wasserstandes im Unterwasser direkt dort bestimmt, wo das Wasser aus der Schaufel „fällt". Unterstrom dieser Stelle hat die Kraft des Wassers keinen Einfluss mehr auf die Leistung des Rades.

Erste Ergebnisse (**Bild 2**) zeigen, dass das Modellrad seinen optimalen Maschinen-Wirkungsgrad von über 80 % bei der vorgesehenen Drehzahl von 7,6 U/min hat. Wirkungsgradverluste durch Getriebe und Generator treten im Versuchsaufbau nicht auf. Der Verlauf des maximalen Wirkungsgrades ist hoch und flach. Üblicherweise haben Wasserräder der Zuppinger-Bauart Gesamtwirkungsgrade von etwa 70 bis 76 % [5], [6]. Gründe für die höheren Wirkungsgrade des Wasserrades der Firma Mühlenbau Schuhmann sind neben den zu berücksichtigenden Laborbedingungen die optimale Einströmung des Wassers in das Wasserrad, der gewählte Schaufelstellungswinkel und die Eintauchtiefe der Schaufeln im Unterwasser.

Zur ökologischen Optimierung werden die Spaltmaße variiert, um die gängige Meinung zu validieren, dass die Spaltweite, die ausschlaggebend für die Durchgängigkeit von Sedimenten und Fischen ist, maßgeblich den Wirkungsgrad steuert. Ziel des Forschungsvorhabens ist es, die Durchgängigkeit von Wasserrädern für Fische und Sedimente zu steigern, ohne den Wirkungsgrad erheblich zu reduzieren. Erste Versuchsergebnisse lassen bereits Rückschlüsse auf den Einfluss des Spaltmaßes auf den Wirkungsgrad zu: bei einer Verdopplung des Spaltmaßes behält das Wasserrad seinen hohen Wirkungsgrad; bei einer Verdreifachung nimmt er ab.

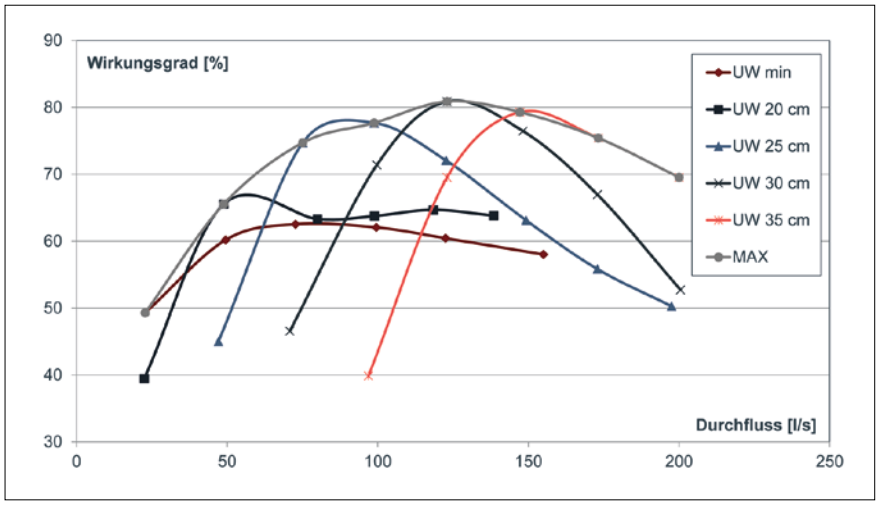

Bild 2: Wirkungsgradverlauf am Zuppinger-Wasserrad bei 7,6 U/min (UW: Unterwasserstände).

Weiterhin werden unterschiedliche Drehzahlen untersucht. Niedrigere Umfangsgeschwindigkeiten reduzieren vermutlich das Verletzungsrisiko von Fischen bei der stromabwärts gerichteten Durchwanderung des Wasserrades. Eine Variation der Umdrehungszahlen führt zu einer Verschiebung der Wirkungsgradkurven. Die Wirkungsgrade der niedrigen Drehzahlen liegen im Durchflussbereich unterhalb des Ausbaudurchflusses (125 l/s) oberhalb der hohen Drehzahlen. Etwa im Ausbaudurchfluss tauschen diese ihre Reihenfolge, was dazu führt, dass die Wirkungsgrade der hohen Drehzahlen deutlich über denen der niedrigen Drehzahlen liegen.

Eine weitere Versuchsreihe besteht aus der Erhöhung des Schaufelabstandes durch eine reduzierte Schaufelanzahl. Das Rad besitzt mit den vorgesehenen 50 Schaufeln einen Wirkungsgrad, der selbst unter Berücksichtigung der Laborbedingungen außerordentlich hoch ausfällt. Durch eine reduzierte Schaufelanzahl würde für Fische, Sedimente und Störkörper die Wahrscheinlichkeit erhöht, das Rad unbeschadet zu passieren. In Zusammenarbeit mit der Firma Schuhmann wurde diese Variation vorgesehen, um deren Auswirkung auf die Leistungsausbeute zu untersuchen.

Mit der CFD-Software FLOW-3D wird die Durchströmung des sich drehenden Rades simuliert. Das numerische Modell wird derzeit anhand der Ergebnisse des hydraulischen Modells kalibriert. Weitere Optimierungspotenziale werden anhand der Software untersucht und am physikalischen Modell überprüft (hybride Modellierung). Es soll gezeigt werden, dass Optimierungen von vorhandenen Wasserradanlagen mit numerischen Modellen kostengünstiger und schneller durchgeführt werden können, als dies mit Versuchsständen zu erreichen ist.

Bild 3: Dethridge Wheel im Einsatz als Durchflussmesser [7]

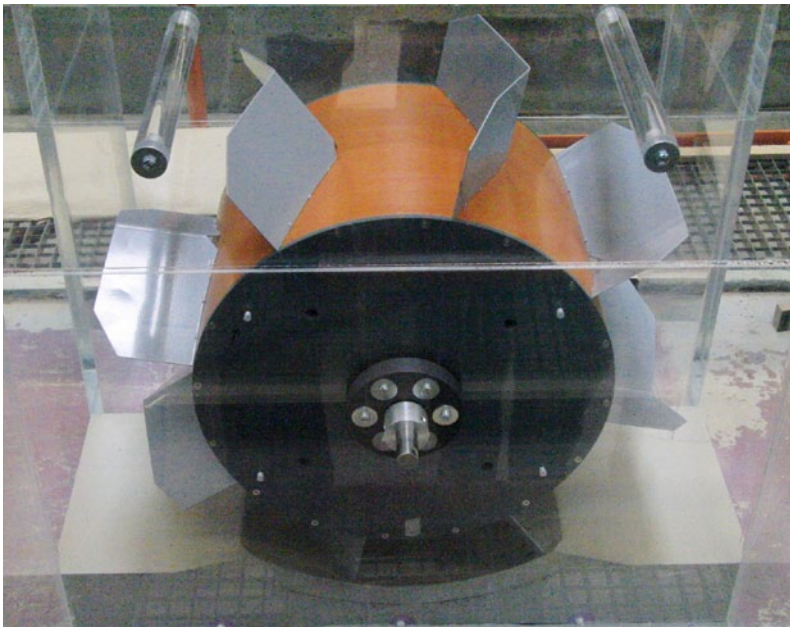

Bild 4: Das Modellwasserrad eines Dethridge Wheels

3 Nutzung des Dethridge Wheels in Bewässerungskanälen

Das Dethridge Wheel ist ein Wasserrad mit 8 Schaufeln, das insbesondere in Australien und Afrika zur Durchflussmessung in Bewässerungskanälen eingesetzt wird (**Bild 3**). Es wird meist aus Metall gebaut und dreht sich in einem standardisierten, betonierten Kanalsegment. Erste Untersuchungen zur Nutzung des sehr einfach gebauten und hydraulisch nicht optimierten Rades zur Wandlung der Wasserkraft in mechanische bzw. elektrische Energie wurden an der TU Darmstadt durchgeführt [4]. Diese zeigten, dass sich das Dethridge Wheel durch hydraulische Veränderungen zu einem Energiewandler mit einem Wirkungsgrad von bis zu 65 % optimieren lässt. Mit Dethridge Wheels in Schwellenländern und Entwicklungsgebieten, wie Indien, Afrika und auch Australien, befinden sich tausende potentielle Energiewandler im Einsatz. Diese werden zurzeit allerdings nur zur Durchflussmessung eingesetzt. Ein Wasserrad in dieser Größe eignet sich besonders für die dezentrale Energieversorgung ländlicher und schwer zugänglicher Gebiete, wie beispielsweise Nepal. Umfangreiche Investitionen in die Erweiterung der Infrastruktur elektrischer Netze lassen sich dadurch vermeiden.

Eine Fortführung der Untersuchungen an der Hochschule Darmstadt beinhaltet insbesondere die Optimierung des Dethridge Wheels, der An- und Abströmbedingungen sowie des Kropfgerinnes. Zu deren Untersuchung wurde ein Modell eines Dethridge Wheels im Maßstab 1:2 aufgebaut (**Bild 4**). Das Modell besitzt einen Durchmesser von 0,60 m, wobei die Nabe einen Durchmesser von 0,40 m hat, und einer Breite von 0,25 m. Das Funktionsprinzip entspricht dem einer Wasserdruckmaschine: Nabe und Schaufeln bilden einen geschlossenen Verbund, wodurch der Anteil an potentieller Energie erhöht wird. Die Untersu-

Matthias von Harten, Shakun Paudel and Nicole Saenger

Investigation of Very Low Head Differences in Research and Development of Hydropower Converters

Due to the switch to sustainable energies and the increasing energy demand, construction and updating of hydro power plants with low heads received a new understanding. The utilization of these low heads is supported by the research on water wheels at the Darmstadt University of Applied Sciences. This paper describes studies conducted at a Zuppinger waterwheel and a Dethridge Wheel in order to examine and optimize ecological consistency and energetic performance.

Маттиас фон Хартен, Шакун Паудель и Николь Заенгер

Использование малых высот напора – научно-исследовательские и опытно-конструкторские разработки

Перелом в энергетической политике и растущая потребность в энергии требуют модернизации и строительства новых гидроэнергетических установок, использующих малую высоту напора. В Высшей школе города Дармштадт проводятся научные исследования, касающиеся использования таких высот напора и применения водяных колес. Данная статья описывает исследования водяных колес Зуппингера (Zuppinger) и Детриджа (Dethridge Wheel) в отношении проблем экологической (проходимость) и энергетической (работоспособность) оптимизации.

chungen werden neben der hydraulischen Modellierung auch am numerischen Modell durchgeführt.

4 Zusammenfassung und Ausblick

Wasserräder stellen sehr alte Wandler von kleinen Wasserkräften zu mechanischer bzw. elektrischer Energie dar, die bis vor ca. 100 Jahren noch eine weite Verbreitung an kleinen und mittleren Fließgewässern hatten. Sie wurden von der großen Wasserkraft und anderen Energieträgern verdrängt, erlangen jedoch aufgrund der Energiewende 2012 wieder eine Bedeutung.

Die systematischen hydraulischen Versuche zeigen, dass das Potenzial eines konventionellen Wasserrades nach Zuppinger weiter verbessert werden kann, obwohl dieses Rad bereits als wirkungsgradoptimiert angesehen wird. Die Konstellation von Umdrehungen, Fallhöhen und Spaltmaßen spielt hierbei eine wichtige Rolle. Zudem kann die ökologische Durchgängigkeit durch bestimmte Maßnahmen (Optimierung von Drehzahlen, Spaltmaßen und Schaufelabständen) verbessert werden, ohne wesentliche Einbußen im Wirkungsgrad hinnehmen zu müssen. In Naturversuchen gilt es dies zu bestätigen und insbesondere die Fischdurchgängigkeit zu analysieren.

Am Beispiel des Dethridge Wheels wird deutlich, dass unkonventionelle Wasserräder, die eigentlich zur Durchflussmessung entwickelt wurden, durchaus zur Energiegewinnung genutzt werden können. Die Optimierung der Zuleitungs- und Ableitungskanäle werden weitere Verbesserungen bringen, so dass der Einsatz in Kanälen durchaus vielversprechend ist. Auch hier gilt es die Erkenntnisse im Naturmaßstab zu verifizieren.

Autoren

Dipl.-Ing. Matthias von Harten
Shakun Paudel, M. Sc.
Prof. Dr.-Ing. Nicole Saenger
Hochschule Darmstadt
Fachgebiet Wasserbau
Haardtring 100
64295 Darmstadt
nicole.saenger@h-da.de

Literatur

[1] Anderer P.; Dumont, U.; Heimerl, S.; Ruprecht, A.; Wolf-Schumann, U.: Das Wasserkraftpotenzial in Deutschland. In: WasserWirtschaft 100 (2010), Heft 9, S. 12-16.
[2] Gerhardt, P.: Fischwege und Fischteiche. Die Arbeiten eines Ingenieurs zum Nutzen der Fischerei. Leipzig: Verlag Wilhelm Engelmann, 1904.
[3] Tombek, B.; Holzner, M.: Untersuchungen zur Effektivität alternativer Triebwerkstechniken und Schutzkonzepte für abwandernde Fische beim Betrieb von Wasserkraftanlagen. Studie im Auftrag des Landesfischereiverbands Bayern, (ohne Datum).
[4] Von Harten, M.: Untersuchung und Optimierung eines Wasserrades zur simultanen Energiegewinnung und Durchflussmessung. Diplomarbeit an der TU Darmstadt, 2010.
[5] Müller, W.: Die Wasserräder. Detmold: Verlag Moritz Schäfer, 1939.
[6] Nuernbergk, D. M.: Wasserräder mit Kropfgerinne. Detmold Verlag Moritz Schäfer, 2005.
[7] N. N.: Dethridge water meter wheel (www.nma.gov.au; Aufruf: 19.07.13).

SHAKUN PAUDEL

	2010-2015	Darmstadt University of Technology, Germany
Doctor of Philosophy		Faculty of Hydraulic Engineering Thesis: *Experimental and Numerical Study of Dethridge wheel for Pico-scale Hydropower Generation*
	2009–2010	Tribhuvan University, Nepal
Lecturer of Civil Engineering		Institute of Engineering
	2006-2008	Karlsruhe Institute of Technology, Germany
MSc in Resources Engineering		Department of Civil Engineering, Geo and Environmental Sciences
	2001-2005	Tribhuvan University, Nepal
Bachelor's Degree in Civil Engineering		Institute of Engineering
	1998-2001	Tribhuvan University, Nepal
Diploma in Civil Engineering		Institute of Engineering
	1998	Tal Barahi Higher Secondary School, Nepal
School Leaving Certificate		